Towards Gated Quantum Emitters from Undoped Nano-LEDs

by

Nachiket Sunil Sherlekar

A thesis
presented to the University of Waterloo
in fulfillment of the
thesis requirement for the degree of
Doctor of Philosophy
in
Physics (Quantum Information)

Waterloo, Ontario, Canada, 2024

Examining Committee Membership

The following served on the Examining Committee for this thesis. The decision of the Examining Committee is by majority vote.

External Examiner	Akira Oiwa Professor, Dept. of Physics, Osaka University
Supervisor	Michael E. Reimer Associate Professor, Dept. of Electrical and Computer Engineering, University of Waterloo
Internal Member	Thomas Jennewein Associate Professor, Dept. of Physics and Astronomy, University of Waterloo
Internal Member	Raffi Budakian Professor, Dept. of Physics and Astronomy, University of Waterloo
Internal-external Member	Na Young Kim Associate Professor, Dept. of Electrical and Computer Engineering, University of Waterloo

Author's Declaration

This thesis consists of material all of which I authored or co-authored: see Statement of Contributions *included in the thesis. This is a true copy of the thesis, including any required final revisions, as accepted by my examiners.*

I understand that my thesis may be made electronically available to the public.

Statement of Contributions

Nachiket Sherlekar is the primary author of Chapters 4, 5 and 6, and the sole author of Chapters 1, 2 and 7 (excluding figures reused from third-party content in Chapter 2, see Letters of Copyright Permission). All thesis chapters were written under the supervision of Prof. Michael Reimer. The experimental results from Chapters 3, 4, 5 and 6 were collected as part of a project that is a joint collaboration between the Quantum Photonic Devices lab, the Coherent Spintronics Group and the Molecular Beam Epitaxy (MBE) research group. Day-to-day supervision for the project was provided by Prof. Michael Reimer, Prof. François Sfigakis, and Prof. Jonathan Baugh.

MBE growth of heterostructure wafers that served as the basis for all results was conducted by Dr. Man Chun (Alan) Tam and Dr. Ho-Sung Kim under the supervision of Prof. Zbig Wasilewski. Nachiket Sherlekar commissioned the attoDRY2100 optical cryostat used for a majority of cryogenic optical characterization. Additional breakdowns of contributions for Chapters 3 to 6 are listed below.

Chapter 3: The results in this chapter, initially published on August 7, 2023, have been reproduced from L. Tian, F. Sfigakis, A. Shetty, H.-S. Kim, N. Sherlekar, S. Hosseini, M. C. Tam, B. van Kasteren, B. Buonacorsi, Z. Merino, S. R. Harrigan, Z. Wasilewski, J. Baugh, and M. E. Reimer, "Stable electroluminescence in ambipolar dopant-free lateral p–n junctions", Applied Physics Letters 123, 061102 (2023) with the permission of AIP Publishing.[*] Lin Tian, François Sfigakis and Arjun Shetty are co-first authors of this work.

- **Text and figures:** François Sfigakis, Lin Tian
- **Review and copy editing:** François Sfigakis, Lin Tian, Nachiket Sherlekar, Arjun Shetty, Jonathan Baugh, Michael Reimer
- **Sample design:** François Sfigakis
- **Sample fabrication:** Arjun Shetty, François Sfigakis
- **Transport characterization:** Stephen Harrigan, François Sfigakis
- **Optical setup:** Lin Tian, support from Sara Hosseini, Nachiket Sherlekar
- **Electroluminescence measurements:** Lin Tian, support from Nachiket Sherlekar
- **Modelling and simulation:** Zach Merino, Arjun Shetty
- **Custom cryogenic wiring:** Brad van Kasteren, Brandon Buonacorsi, support from Nachiket Sherlekar

[*] https://publishing.aip.org/resources/researchers/rights-and-permissions

Chapter 4:

- **Text and figures:** Nachiket Sherlekar
- **Review and copy editing:** Nachiket Sherlekar, François Sfigakis, Michael Reimer
- **Sample design:** François Sfigakis
- **Sample fabrication:** Stephen Harrigan, François Sfigakis
- **Optical setup:** Nachiket Sherlekar, Lin Tian
- **Electroluminescence measurements:** Nachiket Sherlekar

Chapter 5:

- **Text and figures:** Nachiket Sherlekar
- **Review and copy editing:** Nachiket Sherlekar, François Sfigakis, Michael Reimer
- **Sample design:** Nachiket Sherlekar, François Sfigakis
- **Sample fabrication:** Nachiket Sherlekar, Stephen Harrigan (*mesa*, p-ohmics), support from François Sfigakis
- **Transport characterization:** Stephen Harrigan
- **Optical setup:** Nachiket Sherlekar, support from Lin Tian
- **Electroluminescence measurements:** Nachiket Sherlekar
- **Modelling and simulation:** Nachiket Sherlekar
- **Custom cryogenic wiring:** Brady Cunard, support from Nachiket Sherlekar, François Sfigakis

Chapter 6:

- **Text and figures:** Nachiket Sherlekar
- **Review and copy editing:** Nachiket Sherlekar, François Sfigakis, Michael Reimer
- **Sample design:** Nachiket Sherlekar
- **Modelling and simulation:** Nachiket Sherlekar
- **Sample fabrication:** Nachiket Sherlekar
- **Optical setup:** Nachiket Sherlekar, support from Tarun Patel, Lin Tian
- **Optical measurements:** Nachiket Sherlekar (primary), Tarun Patel (support), Lin Tian (reflection measurements from bare unpatterned wafers)

Abstract

Quantum light emitters have the potential to transform emerging quantum technologies and their applications, such as secure quantum communication, metrology, and quantum computing. Ideally, these light sources emit on-demand at high rates and efficiencies with high degrees of single-photon indistinguishability. Additionally, these emitters can emit entangled photon pairs, are position-controllable, and wavelength-tunable. Current state-of-the-art single- and entangled-photon sources based on spontaneous parametric down-conversion (SPDC) and on-demand (or deterministic) implementations suffer from various drawbacks that make them deviate from ideality. SPDC sources emit probabilistically, and increasing their brightness degrades their single photon purity, indistinguishability, and entanglement fidelity. Of the various deterministic sources, optically-driven semiconductor quantum dots have very high single-photon efficiencies ($\simeq 71\%$), purities ($> 99\%$) and indistinguishabilities ($> 99\%$), are position-controllable and wavelength-tunable. However, complex synchronized optical routing between the pump laser, sources and detectors is required to scale their usage. This would occupy a large footprint, restricting them to a laboratory setting. Quantum dots may be current-injected instead, but while gigahertz (GHz) emission frequencies are possible, the electron injection number is not controllable. This inability to control the electron injection is akin to non-resonant optical excitation in which there are many charges in the environment around the quantum dot, thus making current-injected quantum dots inferior to optically-driven quantum dots.

This thesis proposes a novel design for a high-rate, deterministic, electrically-driven quantum emitter that combines a gate-defined lateral planar p–n junction (or nano-light-emitting-diode or nano-LED) with a quantized charge pump along a quasi-one-dimensional channel in dopant-free GaAs/AlGaAs heterostructures. In contrast to other electrically-driven sources, our implementation allows for a precise control of the injected electron number via the quantized charge pump. In addition, by using gates to define the p-type and n-type regions of the junction instead of intentional dopants (as in conventional vertical p–n junctions), the charge carrier mobility in these heterostructures is much higher. The lack of dopants also allows p-type and n-type regions to exist simultaneously on both sides of the device (such devices are termed 'ambipolar'), in turn allowing flexible operation. By operating the charge pump at GHz frequencies, this source could emit a billion photons per second. Integrating a cavity at the site of emission would boost the rate of emission and the efficiency, and could also increase the single-photon indistinguishability.

The following research obstacles were identified over the course of developing our

nano-LED (the prerequisite for our quantum emitter):

- quenching of device electroluminescence (EL) and time-instability of emissions due to parasitic charge accumulation, necessitating thermal cycling to reset the device;
- alternate current pathways (both radiative and non-radiative) through the device *mesa* that reduce both internal and external quantum efficiency;
- delocalized emission at *mesa* edges due to minority currents under the topgate edges, affecting extraction efficiency and position-controllability; and
- multimode emission and slow rate of spontaneous emission that reduce extraction and collection efficiencies.

Descriptions of our nano-LEDs and their emissions as well as solutions to the above obstacles obtained through experiment are summarized below.

The nano-LEDs discussed in this thesis are gate-induced either in GaAs *rectangular quantum wells* or at GaAs/AlGaAs *single heterojunction interfaces*. All nano-LEDs reported in literature are induced using the former and not the latter. In fact, a recent theoretical study concluded that radiative electron-hole recombination was impossible in nano-LEDs induced at single heterojunction interfaces. Our demonstration of EL from nano-LEDs induced at GaAs/AlGaAs single heterojunction interfaces is the first of its kind. Since the fabrication yield using single heterojunction wafers is higher than when using rectangular quantum wells, they offer an alternative for easier fabrication of the nano-LEDs.

To understand how the EL quenches in our nano-LEDs, we propose a scenario of localized parasitic charging that results in enhanced non-radiative recombination and causes a gating of the p–n channel that suppresses the diode current. To address this issue, we have devised a gate voltage sequence that we call the 'Set-Reset' protocol. This protocol clears away accumulated parasitic charge, extending the lifetime of device operation without the need for thermal cycling.

Our nano-LEDs can be operated in four distinct circuit measurement configurations, depending on whether the left side is p-type or n-type (with the right side being n-type or p-type, respectively), and whether the left side is grounded or floating (with the right side being floated or grounded, respectively). EL from our nano-LEDs (induced at both quantum wells and single heterojunctions) is observed not only around the p–n junction interface, but also as far as the edges of the etched *mesa*, indicating the presence of unwanted radiative recombination pathways. The p-side is consistently brighter in the single heterojunction samples while the n-side was brighter for the quantum well devices.

A neutral and a negatively charge exciton peak was observed in the spectra from

the n-side of the nano-LEDs. Spectra from the p-side were measured only for the single heterojunction devices, and showed the neutral exciton peak as well as a lower energy peak. The narrowest neutral exciton emission linewidths (0.70 meV) from lateral p–n junctions to date were recorded from the quantum well nano-LEDs. Our nano-LEDs were also shown to be compatible with radio frequency operation, necessary for quantized charge pump integration to create a quantum emitter.

To address the issue of delocalized emission and time-instability of EL, we fabricated and tested a nano-LED with a novel gate architecture that included two wide surface gates placed adjacent and perpendicular to the p–n channel. The extra gates add a degree of freedom that along with standard DC operation and the Set-Reset protocol opens up many measurement configurations. A downside is that these surface gates are prone to current leakage. Several measurement configurations were explored, with two standing out—one yielded *localized* emission at the junction interface while using the Set-Reset protocol; another yielded *time-stability* of emission in DC operation. A conceptual model has been laid out that is compatible with the results from these various operating configurations. From the time-stable measurements of EL intensity and p–n current, the internal and external quantum efficiencies were estimated to be $\sim 1.19\times10^{-3}$ and $\sim 1.95\times10^{-5}$, respectively. These values may be boosted in future designs by incorporating *insulator-separated* side gates, blocking gates, and a cavity around the emission region. The side gates and blocking gates will respectively time-stabilize and localize the EL emission during DC operation, and the cavity will increase the rate of spontaneous emission and shape the mode.

A long-standing problem in the field of deterministic quantum emitters is the fact that they emit light omnidirectionally and into multiple modes. Various confining structures such as tapered nanowires, micropillar cavities, photonic crystals, solid immersion lenses and circular Bragg gratings have been proposed and implemented in literature. We identified the circular Bragg grating cavity etched into a heterostructure with a Bragg mirror grown below the rectangular quantum well as the optimum solution for our nano-LED. Through simulation, both the Bragg mirror and circular Bragg grating designs were tuned to match the quantum well emission wavelength (~ 807.5 nm). The circular Bragg cavity etched into the Bragg mirror wafer around the emission region enhances the rate of spontaneous emission via the Purcell effect, and simultaneously funnels the emission into a single elliptical Gaussian mode for efficient collection. A split was included in the circular Bragg grating to make it compatible with our proposed emitter design. Theoretically, for in-plane exciton dipoles oriented parallel to this split, the cavity enhances the spontaneous

emission rate by a factor of 5.3 at a center wavelength of 807.4 nm and a bandwidth of ~ 3.7 nm or ~ 7.0 meV. The split in the cavity causes emission to be linearly polarized. This linear polarization is unfortunately incompatible with the emission of polarization entangled photon pairs. The effective collection efficiency (from simulation) is $\sim 30\%$, which is ~ 52 times greater than that of a device without a cavity. The inclusion of our cavity also boosts the internal and external quantum efficiencies by factors of 4.5 and 89, yielding values of $\sim 5.32\times10^{-3}$ and $\sim 1.74\times10^{-3}$, respectively. Design validation of the Bragg mirror using reflection measurements yielded a Bragg stopband frequency and bandwidth that closely match simulation. Simulated and measured reflection spectra from the circular Bragg gratings indicated a linear relationship between the ring width of the grating and the cavity resonance wavelength, with a consistent wavelength offset between simulation and measurement of ~ 16.3 nm. From these results, a cavity with a ring width of ~ 94.8 nm would most closely match the emission wavelength of ~ 807.5 nm.

Through our proposed and implemented solutions for the obstacles facing our nano-LEDs, we pave the way for the realization of a high-rate, electrically-driven quantum emitter.

Acknowledgments

I have spent the duration of my PhD on the campus of the University of Waterloo, situated on the Haldimand Tract, the land granted to the Six Nations that includes six miles on each side of the Grand River. The existence of this academic institution (and indeed the city of Waterloo and the country of Canada as a whole) would be impossible without the ongoing colonization of Turtle Island and the Indigenous peoples that live here. The First Nations groups that occupied the lands on which the university resides include the Attawandaron, Anishinaabeg and the Haudenosaunee peoples. By continuing to educate myself about them and other First Nations groups on Turtle Island, I hope to aid in their goal of reclamation—of land, culture, language and the right to self-govern.

The supportive, driven, and fun research culture at the core of the Quantum Photonic Devices (QPD) lab has been established thanks to the supervision and leadership of its Principal Investigator, Prof. Michael Reimer. It has been a pleasure and privilege to witness the growth of the group and its individual members (including myself) since nearly its inception, and I am so proud to become one of its alumni. Michael—thank you so much for the opportunity to work with you on the cutting-edge of quantum science.

It is my good fortune that my network of collaborators and professional support extend well beyond my own research group. My PhD would not have been possible without the unwavering support and guidance of Prof. François Sfigakis. Throughout my PhD, François has been endlessly giving with his time and energy, and has taught me so much about a range of topics from cleanroom fabrication to cryogenic systems to charge transport. The overarching project this thesis contributes to was conceived by principal investigators Prof. Jonathan Baugh, Prof. Zbig Wasilewski, Prof. Reimer and Prof. Sfigakis in a proposal to Defence Research and Development Canada (DRDC). Frequent and informative team discussions with the project leads as well as project members Dr. Lin Tian, Dr. Arjun Shetty, Dr. Brandon Buonacorsi, Dr. Sara Hosseini, Dr. Ho-Sung Kim and Stephen Harrigan were very helpful in keeping me on track and up to speed.

My long hours spent inside the Quantum Nanofabrication and Characterization Facility (QNFCF) would probably be even longer if not for the practical knowledge gained through discussions with Dr. Buonacorsi, Dr. Shetty, Andrew Jordan, Dr. Pardis Sahafi, and Stephen Harrigan. As well, their active presence during fabrication procedures in the cleanroom has always been greatly appreciated. The hard-working staff of the QNFCF do a fantastic job operating a world-class fabrication facility while maintaining high standards of safety, for which I am grateful. Dr. Greg Holloway—thanks especially for your help in utilizing

the electron-beam lithography tool. To my collaborators from the MBE research group, Dr. Alan Tam, Dr. Ho-Sung Kim and Prof. Wasilewski—thank you for growing the wafers that form the basis of all the devices that I have fabricated. Sincere thanks to my qualifying exam and defense committee members Prof. Raffi Budakian, Prof. Thomas Jennewein, Prof. Baugh, Prof. Na Young Kim, Prof. Akira Oiwa and Prof. Reimer, for all their time and insightful feedback. Several members of the Institute for Quantum Computing (IQC) community have helped me in countless ways over the years, including Christine and John Dietrich, Harmeny Toope, Sarah Wang, Alex Mitrovic, Dr. John Donohue, Roberto Romero, Steve Weiss, Dr. Jean-Phillipe Bourgoin, Dr. George Nichols and Don Carkner—thank you all so much. I am also grateful to the remaining IQC staff as well as the entire staff of the Physics & Astronomy department for all they do to help students such as myself.

Establishing friendships with my fellow group members has been easy—they are kind, smart and fun to be around. Importantly, they are always ready to lend a hand, both intellectually and physically. Stimulating scientific discussions with Dr. Tian, Matteo Pennacchietti, Sayan Gangopadhyay, Dr. Sasan Vosoogh-Grayli, Stephen Harrigan and Dr. Tarun Patel have helped me get out of my head and find solutions to problems from different perspectives. Also, getting to share an office with Dr. Mohammed Zeeshan, Dr. Arash Ahmadi, Sayan Gangopadhyay, Sathursan Kokilathasan and Sarah Odinotski at various points over the last several years has been a true joy.

This degree is my first experience seeing a long-form project to completion. It has been very interesting charting my growth as an individual and as a scientist over the course of the last several years. There have been ups and downs and ups again, and I could not have navigated them without the help of some exceptional people I get to call friends. What follows is an attempt to list all their names: my current and former housemates—Evan (and his cats Amelie and David), Anand, Irene, and Nikhil; the rest of los friendos—Aditya, Jérémy, Manjit, Daniel, Rahul, and Júlia; my extended IQC (and IQC-adjacent) fam—Kristine, Doug, Kimia, Noura, Laura, Claire, Nidhi, Sonell, Brady, Burak, Merve, Brad, Maeve, Hannah, Collin, Devashish, Prathamesh, Ramy, Rhyse, Bidushi, Connor, Carl, Ena, Andrew, Maggie, Justin, Joanna, Meenu, Pranav, Pritam, Khushmeet, Michael, Harmen, and Alex; my extended Waterloo (and beyond) fam—Felicia, Tristan, Krishna, Nikole, Kristina, Matt, Rana, Chantelle, Rachel, Geoff, Johan, Morgan, Katherine, Meaghan, and Marcus; and my D&D crew—Romain, Vic, Cliff, and Manuel.

Of course, none of this would have been possible without the love and support of my family throughout this journey. Amma, Papa, Apu, Shamik, and Naomi—thank you so much, and so much love to you all.

Table of Contents

List of Figures

List of Tables

List of Abbreviations

2DEG two-dimensional electron gas 21, 23, 24, 27, 29–31, 33, 34, 36, 37, 42–47, 49, 52, 53, 61–63, 65, 66, 69, 78, 85, 87, 90, 113, 122, 123, 127

2DHG two-dimensional hole gas 23, 24, 29, 31, 33, 34, 36, 37, 42–47, 49, 53, 61–63, 65, 66, 113, 122

APD avalanche photodiode 64, 76, 90, 94, 96, 97

CBG circular Bragg grating 6, 99, 105–119, 124–129, 156, 162, 164

DBR distributed Bragg reflector 99–104, 106–108, 112, 118, 119, 129, 163

EL electroluminescence 7, 10, 11, 36, 37, 39, 42, 44, 48–57, 59–72, 75, 76, 79–93, 97, 98, 107, 120–126, 128

EQE external quantum efficiency 93, 94, 97, 112, 119, 124

HEMT high-electron-mobility transistor 10, 11, 13, 14, 20–22, 24, 25, 27–29, 31, 43, 74

IQE internal quantum efficiency 93, 94, 97, 108, 112, 119, 124

LED light-emitting diode 1, 4, 7–11, 31, 32, 35, 63, 72, 73, 98, 99, 106, 107, 112, 118–124, 126, 128, 129

MBE Molecular Beam Epitaxy 13, 26–28, 43, 45, 52, 54, 55, 58, 65, 74, 99, 101–104, 119, 121, 128, 129

MIS metal-insulator-semiconductor 21–23, 25, 26, 29, 34

PL photoluminescence 37, 42, 44, 51–60, 63, 64, 100–102, 104, 105, 123–125, 128, 155

QCP quantized charge pump 10, 38

QW quantum well 11, 52, 63, 101–104, 108, 117, 119, 121, 123–129, 157, 161

RF radio frequency 5, 8, 11, 35, 38–41, 44, 63, 64, 124

RQW rectangular quantum well 21, 65, 68, 69, 71, 72, 106

SAW surface acoustic wave 32, 36–39

SHJI single heterojunction interface 11, 13, 20, 25, 26, 65, 66, 68–72, 74, 75, 78, 85, 95, 96, 106, 112, 121–124, 126, 128, 157

SR Set-Reset 80–84, 87–90, 92, 122–124

1. Introduction

For most of modern history, our understanding of all observable phenomena in nature relied on a 'classical' picture, based on the discoveries of Newton, Leibniz, Euler and others. This was upended in the 20th century starting with Planck's model of black-body radiation, that relied on energy being emitted in discrete packets or 'quanta'.[1] Planck's mathematical formulation was validated soon after by Einstein's description of the photoelectric effect, which states that light is *itself* quantized into individual particles called photons that are each generated and detected as a whole.[2] This particle nature of light was in opposition to the conventional wave nature of light that came from classical theory. However, it is now understood that describing quantum objects using classical terms such as 'wave' or 'particle' can be misleading, since these objects behave unlike any classical object and can only be approximated as such. Quantum field theory (QFT) attempts to find a more accurate description of photons and their interaction with matter by applying the quantization to a field—formally, in QFT, a photon is defined as an elementary excitation of a single mode of the quantized electromagnetic field.[3] For a quantized field mode k with frequency ν_k, the energy E of a photon associated with this mode is

$$E = h\nu_k, \tag{1.1}$$

where h is the Planck constant.

The deepening of our understanding of light-matter interaction over the course of the 20th century led to the development of several ground-breaking technologies including light-emitting diodes (LEDs), transistors and lasers. More recent advances in this century have allowed us to harness quantum phenomena such as superposition and entanglement to engineer devices that aim to revolutionize the fields of imaging, metrology, remote sensing, communication and computation. Quantum photonic devices fall under this category, and are based on the generation, manipulation and detection of single photons

or entangled photon pairs. Devices that generate quantized light—referred to as quantum emitters or single-photon sources—are the focus of this thesis.

1.1 The ideal quantum emitter

An ideal quantum light source possesses the following properties:[4,5,6,7]

- on-demand (or deterministic) photon generation—only one photon at a time is generated in a predictable manner with high probability;
  - triggered photon generation—a photon is generated at the push of a button;
  - single-photon purity—null probability of multi-photon emission;
  - high internal quantum efficiency—efficient conversion of electrons to photons;*
  - efficient extraction and collection of emitted photons into a single spatial mode;
- high emission rate (or high brightness)—short radiative emission lifetime (with a pre-requisite of on-demand generation);
- single-photon indistinguishability—all emitted photons indistinguishable from each other in terms of wavelength, polarization and spatio-temporal mode;
- high *measured* entanglement fidelity (in the case of an entangled photon source);
- position-controllability—the emission may be localized and the source location possible to control; and
- wavelength-tunable emission—emission wavelength from one indistinguishable source may be tuned to match another, enabling two-photon interference.

It is important to emphasize that the above properties belong to an *ideal* quantum emitter—practical implementations can only strive for *near-ideality*. Engineering near-ideal quantum emitters has the potential to transform emerging quantum optical technologies and their applications. An on-demand source of single and entangled photons could extend the distance of quantum communication[8] or increase the key exchange rate for secure communication,[9,10] and also allows for all-on-chip, scalable photonic integrated circuits for quantum computing.[11] Depending on the type of emitter, there is an interplay and trade-off between some of the properties that constitute ideality. The early workhorse for entangled photon generation was not on-demand; it relied on the *probabilistic* generation process of spontaneous parametric down-conversion (SPDC) in a non-linear crystal excited by a

* specifically applies to electrically-driven sources

high-powered laser.[12] Probabilistic single-photon sources rely on correlated photon pair emission—the detection of one photon in the pair is used to 'herald' the emission of the other. This drastically reduces the number of 'useful' photons emitted. Near-unity fidelity entangled photons as well as indistinguishable single photons with high purity have been produced in SPDC sources.[13] However, increasing the source emission rate by increasing the power of the excitation laser leads to a higher probability of multi-photon emission relative to single photons. This of course degrades single-photon purity but also lowers measured indistinguishability and measured entanglement fidelity, thus limiting the emission rate (brightness) to levels where multi-photon emission is less likely, in turn limiting their applications. Photon multiplexing mitigates this problem but only to an extent, and requires an array of sources that adds cost and reduces scalability.

Broadly, emitters that are in principle *deterministic* (any two-level quantum system) may be categorized as optically-driven or electrically-driven. Optically-pumped semiconductor epitaxial quantum dots are the current state-of-the-art—they possess the highest purities (>99%[14]), indistinguishabilities (>99%,[15] resonant excitation) and system efficiencies ($\simeq 71\%$[16]) of any source. Gigahertz emission rates have been achieved using these sources[17,18] with no compromise to the purity and indistinguishability, unlike in non-linear crystals. Generation of entangled photon pairs is also possible via the biexciton-exciton cascade. Several fabrication techniques have been developed to control the quantum dot emitter position and place confining structures such as waveguides or microcavities around the dot to shape the emission mode and enhance the spontaneous emission rate. Strain and external fields to tune the emission wavelength have also been incorporated. A trade-off is that scaling up the number of sources requires complex optical routing between between the sources, ultrafast pump laser and detectors, all of which need to operate in synchronization. The infrastructure required for this would occupy a large footprint, restricting optically-driven quantum dots to a laboratory setting. Emission rates are limited by the optical pump rate; achieving GHz pump rates is a technical and technological challenge. Exciting the dots *resonantly* is the best way to drive them, however the spectral overlap makes it harder to filter the emission from the high-powered excitation laser in order to utilize it.

Deterministic electrically-driven emitters are not limited by a large infrastructure footprint, making them more scalable than their optically-driven counterparts. Electrical driving can constitute *mesoscopic current injection* or *quantized charge pumping*. The former is when a current is driven through a two-level system such as defect centres in diamond[19] or in strained thin films,[20] or in epitaxial or colloidal quantum dots. GHz emission rates in

current-injected quantum dots is possible,[21,22] but the photon number is not controllable, and their entanglement fidelity suffers from dephasing mechanisms during charge carrier injection in an incoherent process. A quantized charge pump can be used to control current flow down to the single- or few-electron level. Integrating such a device with a lateral p–n junction could in theory create a single photon source. To date, the only example in literature of such a device was published in 2020 by Hsiao et. al.,[23] and consists of an undoped lateral p-n junction whose current is driven by surface acoustic waves that act as the quantized charge pumping mechanism. They boast a pump frequency of over 1 GHz that translates to a high emission rate. Their post-selected value for second-order correlation function $g^{(2)}(0)$ is less than 0.5, indicating single photon emission; however, their $g^{(2)}(0)$ value from raw data is between 0.5 and 1—while this does not indicate single photon emission, it still indicates photon antibunching (see Section 2.2.2.1 for some additional details).

In the next section, I propose a novel deterministic electrically-driven quantum emitter design that utilizes a gate-controlled quantized charge pump to drive the current in an undoped lateral p-n junction.

1.2 Design proposal for a novel quantum emitter

The results presented in this thesis are part of a broader goal to develop a novel quantum emitter that combines a **nano-LED** or a gate-defined lateral planar p–n junction[†] with a **one-parameter electron pump**[‡] in dopant-free heterostructures consisting of Gallium Arsenide (GaAs) and Aluminum Gallium Arsenide (AlGaAs) layers. Fig. 1.1 shows the cross-sectional schematic of the proposed device at different stages of operation. Voltages of opposite polarities applied to two insulator separated topgates simultaneously 'induce' a 2D electron gas on the left and a 2D hole gas on the right, creating a lateral p–n junction. The charges are supplied by an n-type (AuGeNi) and p-type (AuBe) ohmic contact respectively. A source-drain or p–n current can be induced by applying a bias across these ohmic contacts. The quantized charge pump is defined by an 'entrance' and 'exit' gate placed closer to the substrate on the n-side. A high-frequency signal on the entrance gate modulates the formation of a dynamic quantum dot between the barriers created by the two gates, resulting in a precise number of electrons n being pumped through

[†] see Section 2.2.1
[‡] see Section 2.2.2.2

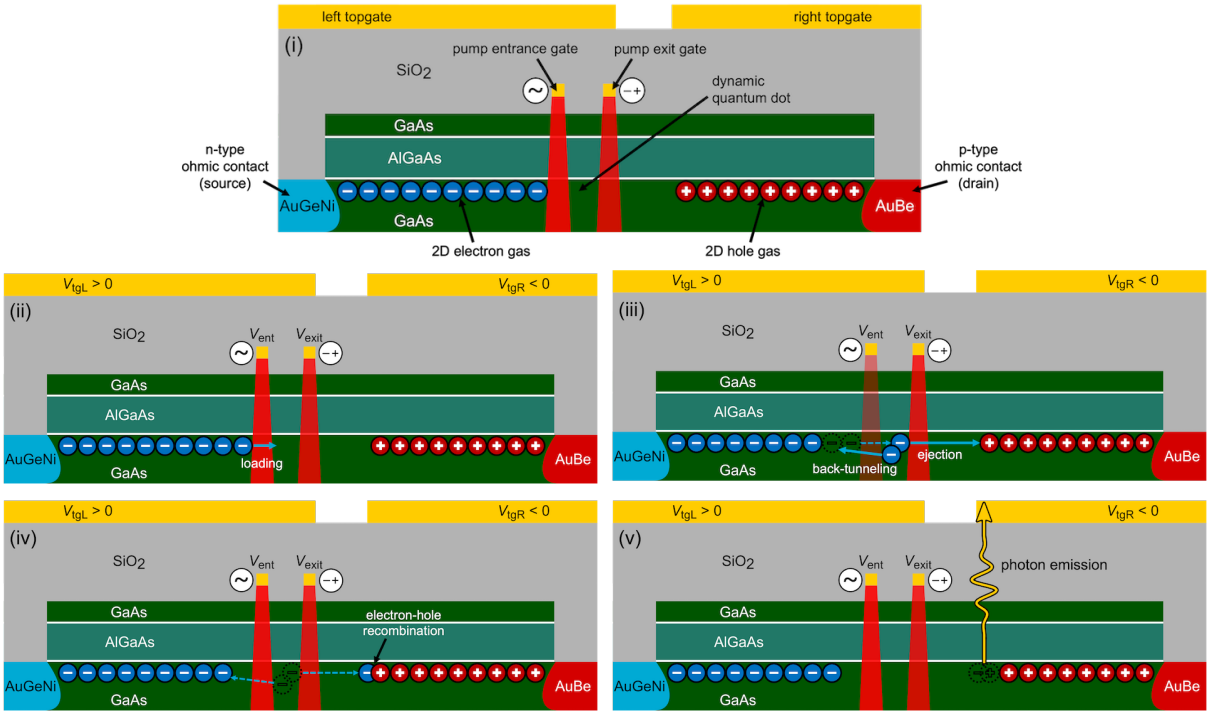

Figure 1.1: (i) Vertical cross-section schematic of our proposed quantum emitter comprising an undoped lateral p–n junction driven by a gated electron pump. A 2D electron gas and a 2D hole gas are induced on either side of the device by the left and right topgates. The pump entrance gate is modulated by a radio frequency (RF) signal and the exit gate is set to a fixed DC potential; these gates create a dynamic quantum dot at the interface between the AlGaAs barrier and GaAs. The source and the drain of the p–n junction are defined by the n-type ohmic contact (AuGeNi) and the p-type ohmic contact (AuBe) respectively. (ii) The bias on the pump entrance gate (V_{ent}) reduces, and m electrons load into the dynamic quantum dot. (iii) As V_{ent} begins to increase, $m-n$ electrons back-tunnel out of the dot while n electrons are captured in the dot ($n=1$ for single-photon emission and $n=2$ for entangled photon emission). A further increase in V_{ent} causes ejection of the n electrons towards the holes. (iv) The ejected electrons reach the hole gas, where they recombine. (v) n electron-hole pairs recombine to emit n photons.

the junction. Deterministic quantum light emission is achieved when these n electrons recombine with holes on the p-side to emit n photons. Gate-defined quantized charge pumps have been demonstrated to work at GHz frequencies, opening up the possibility for this type of source to generate a billion photons per second, matching the current state-of-the-art. A value of $n=1$ corresponds to a single-photon source; however most charge pumps can operate with $n=2$ or higher. In 2021, our team (Buonacorsi et. al., Ref. [24][§]) demonstrated a quantized charge pump with up to $n=3$. Setting $n=2$ for the charge pump and tuning the entrance and exit potentials can generate a spin singlet entangled electron pair state.[25] Since radiative emission preserves spin information, this

[§] note that the author of this thesis did not contribute to this publication

in principle translates to the emission of polarization-entangled pairs of photons that have applications in quantum communication and quantum key distribution. Integrating a CBG cavity into the device at the electron-hole recombination site, as well as a 'blocking gate' just past the recombination site would enhance the overall efficiency of the source (Fig. 1.2).

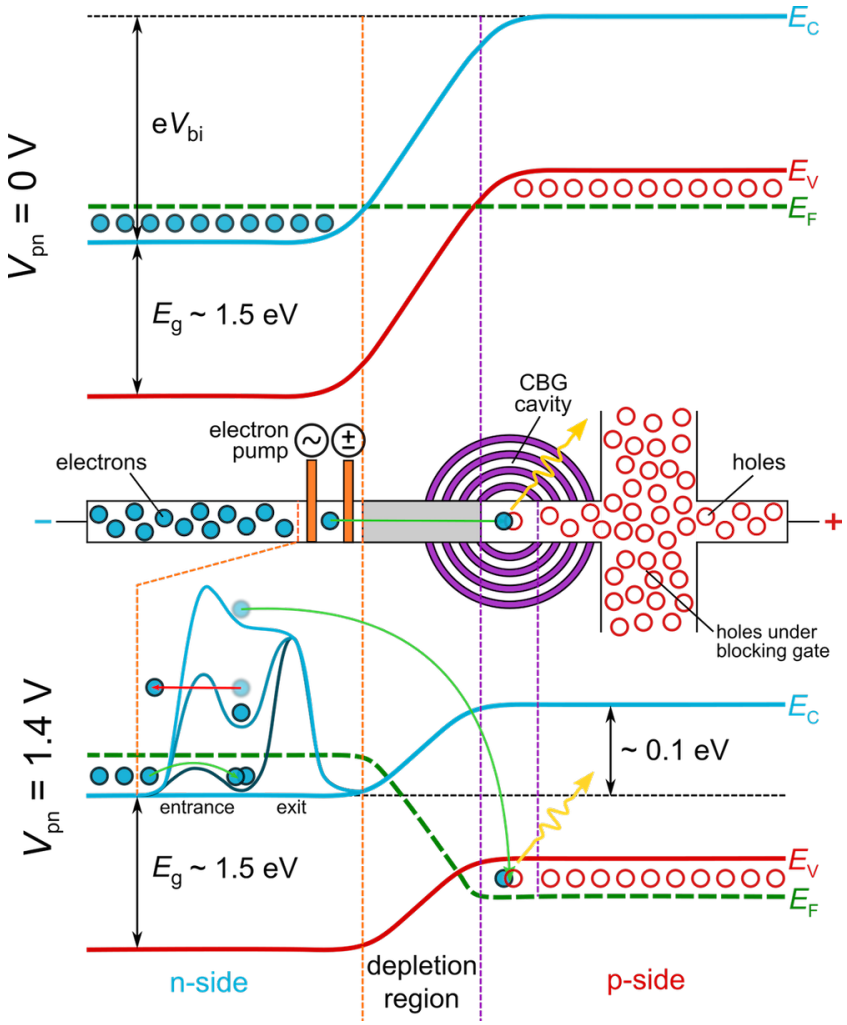

Figure 1.2: Proposed quantum emitter schematic along with band diagrams for *off* and *on* states. The band gap E_g of the device is 1.5 eV. Note that these schematics are not to scale. (TOP) The device is OFF at forward bias $V_{pn} = 0$ V; the Fermi level E_F is flat and the conduction band E_C and valence band E_V are bent due to the built-in potential V_{bi}. (MIDDLE) The horizontal cross-sectional schematic shows the electron pump on the n-side and the circular Bragg grating (CBG) cavity and the holes under the blocking gate on the p-side. The electron pump shuttles n electrons at a time across the junction ($n = 1$ in this schematic; see Section 2.2.2 for a detailed explanation of the mechanism). Electron-hole recombination occurs at the center of the cavity. The blocking gate prevents electrons from migrating past the recombination site and recombining elsewhere. (BOTTOM) In the ON state, V_{pn} is increased until E_C and E_V are nearly flat. The pump voltages help the electrons overcome the remaining V_{bi} and eject them onto the p-side where they form electron-hole pairs in the cavity and radiatively recombine.

In short, our proposed novel design for a quantum emitter will yield several advantages over the competition—it is electrically-driven, deterministic, position-controlled, has a high emission rate, and offers precise control of the photon number in the few-photon regime.

1.2.1 Juxtaposition with near-ideality

In designing this novel quantum emitter, we must keep in mind the traits corresponding to near-ideality, how our device can achieve these traits, and where it may fall short. Firstly, regarding **deterministic/on-demand** generation—quantized charge pumping allows for triggered photon generation, since single electrons can be pumped on-demand to recombine with holes. Single-photon purity is characterized by how close the measured value of $g^{(2)}(0)$ is to zero.* Measuring the electron number uncertainty for single-electron pumping gives us a lower limit to $g^{(2)}(0)$. For our pump,[24] we measured a one-electron error rate of ~ 64.4 ppm at a pump frequency of 850 MHz, and an error rate of just ~ 0.7 ppm at a frequency of 500 MHz (see Section 2.2.2.2). These are very small lower bounds for $g^{(2)}(0)$, suggesting promising numbers for single-photon purity.

Adding a cavity at the site of electron-hole recombination enhances the rate of spontaneous emission of photons via the Purcell effect. By coupling the emission to the cavity mode, the probability of radiative recombination is boosted relative to non-radiative recombination. This in turn makes electron-to-photon conversion more efficient, i.e. higher **internal quantum efficiency** (see Section 6.3). A cavity can also enhance the **extraction efficiency** (the ratio of the external and internal quantum efficiencies) as well as the **collection efficiency** by funneling the emission into one direction and shaping it into a single mode.

Since our pump rates are high, they will not limit the **brightness** or rate of emission from our sources. Also, from our measurements (see Fig. 3.17), we know that the electroluminescence (EL) lifetime for our nano-LEDs is compatible with GHz operation. Cavity Purcell enhancement can further reduce radiative lifetimes, increasing brightness.

Our source may unfortunately fall short when it comes to single-photon **indistinguishability**. For two successively emitted photons to be indistinguishable, they must have the same wavelength, polarization and spatio-temporal mode. Indistinguishability

* refer to Section 2.2.1 for an explanation of the second-order correlation function $g^{(2)}(0)$

is measured by the coherence (or dephasing) time T_2 of the emitted photons, which is inversely proportional to the linewidth of the emission—the full-width at half maximum (FWHM)—in the energy or frequency domain. Generally, $T_2 \leq 2T_1$, where T_1 is radiative lifetime or the average time an emitter spends in the excited state before radiative decay. An ideal, perfectly indistinguishable source has a Fourier-limited or transform-limited linewidth, which means that $T_2 = 2T_1$. Emitters with linewidths closer to the Fourier-limited linewidth will have longer coherence times and better indistinguishability. On the other hand, the presence of noise (for example due to phonon scattering or dephasing due to phonon absorption/emission) broadens the linewidth, reducing coherence times and indistinguishability. State-of-the-art quantum dot emitters have achieved linewidths that are Fourier-limited,[26] the best corresponding to 0.75 μeV in energy (or 181 MHz in frequency). In contrast, the spread of electron energies leaving quantized charge pump devices has been observed to be quite large ($\sim$ 3.5 meV/846 GHz by Waldie et. al.[27]). This would translate to very broad emission linewidths—almost four orders of magnitude larger than the linewidth for quantum dots. In our nano-LEDs, which do not have an electron pump, the emission linewidth is smaller (0.7 meV,[28] see Chapter 3), but this is still three orders of magnitude larger than the best quantum dot linewidth. Including a cavity tuned to the emission wavelength at the recombination site in the regime of *weak coupling* between the emitter and cavity could help with this issue.[29,30,16] A cavity with a high quality factor Q would enhance the spontaneous emission rate into the cavity mode via the Purcell effect, reducing the impact of phonon dephasing. In a well-tuned cavity, this would spectrally filter the emission, reducing the linewidth. A static gated quantum dot at the recombination site on the p-side of the device to quantize holes could help even more in reducing the linewidth. However, for radiative recombination, the spin of the hole loaded into this static gated dot must be opposite to the spin of the pumped electron. There is only a 50% probability of this being the case, meaning half the counts are lost due to probabilistic emission.

As mentioned, entangled electron pair emission is theoretically possible in the $n = 2$ regime of the electron pump, where electron pairs can form a spin singlet. According to Wenz et. al. (Ref. [25]), tuning the entry and exit gate potentials to a specific regime can force the dynamic quantum dot to energetically allow initialization of only ground-state singlet pairs and *no* triplet pairs. Unlike our pump,[24] they utilize a pulsed RF waveform instead of a sinusoidal one. Although our sinusoidal RF waveforms are sufficient for single electron pumping and single photon emission, switching to an AWG (Arbitrary Waveform Generator) to drive the pump entrance gate with a pulsed waveform should

be possible for us in the future when we investigate the generation of entanglement. The pumped electron spin singlet recombines with holes on the p-side of the nano-LED to emit polarization-entangled photons. The dynamics of this process can be quite complicated. Before recombining, electrons and holes form bound states of electron-hole pairs called excitons. If spin is conserved, a singlet electron pair could form two singlet excitons that are themselves entangled to each other. However, before this is possible, Coulombic interaction of the electron spin singlet with the sea of holes as well as interaction with the nuclear spin bath in GaAs may cause decoherence and degradation of **entanglement fidelity**. The presence of external fields (electric or magnetic) and the shape of the cavity at the recombination site also affect the entanglement fidelity (discussion in Chapter 6). The extent of entanglement fidelity degradation would depend on the timescale of decoherence for each of these cases.

The source is **position-controllable** by virtue of the radiative recombination being concentrated at the center of the cavity. Stray recombination due to migration of minority electrons past the cavity can be curtailed with the use of a blocking gate.

Finally, **wavelength-tunability** of our emitter may be possible by applying an external magnetic field. A drawback, however, is that this would lift the spin-degeneracy of entangled electrons, leading to lower fidelity of entangled photon pair emission—this would need to be investigated in future work.

1.3 Research goals and obstacles

The development of a new type of optoelectronic device with a novel architecture is a slow and iterative process involving many hours of labour. In our case, a large chunk of those hours were devoted to perfecting the fabrication recipe for our nano-LEDs in the cleanroom, while the rest went into characterizing prototypes electrically and optically, and thinking of ways to tweak and improve the design for future fabrication runs. Along the way, several milestones were achieved, and novel device architectures and new regimes of operation were conceived. Our ultimate goal for this project is to fabricate an integrated, on-demand, electrically-driven source of single and entangled photons, characterize the emission, and explore ways to utilize them for applications. While we have not yet achieved this ultimate goal, we have passed two major milestones—the development of lateral two-dimensional (2D) nano-LEDs, and the realization of one-parameter single-electron pumps along quasi-one-dimensional (1D) channels, both in

dopant-free GaAs heterostructures. However, deficiencies in the performance of the nano-LEDs have prevented us from integrating them with the single-electron pumps to create a quantum light source. The focus of my doctoral research, summarized in this thesis, has been to identify the obstacles created by these deficiencies in our nano-LEDs, suggest solutions, and try to implement them. The main obstacles we need to overcome when operating undoped nano-LEDs are:

(i) quenching of device EL and time-instability—occurs due to unwanted charge accumulation around the p–n junction during standard forward-bias operation and can be reversed only by thermal cycling (warming up the device from cryogenic to room temperature, letting it thermalize, and then cooling it back down) which is time-consuming and impractical;
(ii) alternate current pathways (both radiative and non-radiative) through the device—reduce both internal and external quantum efficiency;
(iii) delocalized emission—affects extraction efficiency and position-controllability; and
(iv) multimode emission and slow rate of spontaneous emission—reduces extraction and collection efficiency.

Solutions to overcome each of these obstacles are laid out in Chapters 3, 4, 5 and 6 of this thesis; however, the nuances of some of these obstacles were identified only during the course of experimentation, and their corresponding solutions must be implemented in future work. These obstacles are reiterated in the conclusions (Chapter 7), along with their corresponding solutions as uncovered in the preceding chapters.

1.4 An overview of this thesis

The theory behind dopant-free gate-induced devices [including the high-electron-mobility transistor (HEMT), lateral planar p–n junctions and quantized charge pumps (QCPs)], as well as a review of the corresponding literature is laid out in Chapter 2—Section 2.1 covers gated undoped semiconductor transistors (that serve as precursors to the p–n junctions), Section 2.2.1 covers undoped lateral planar p–n junctions, and Section 2.2.2 covers quantized charge pumps. Our charge pumps were developed by Buonacorsi et. al. (Ref. [24]) in 2021; the results from this publication are summarized briefly in Section 2.2.2. Note that the author of this thesis did not personally contribute to these results, hence their exclusion from the main experimental chapters. Instead, the

experimental results compiled in Chapters 3, 4 and 5 focus on the latest developments and improvements of our dopant-free nano-LEDs.

In 2023, our team (Tian et. al., Ref. [28]) demonstrated a new operating protocol—the Set-Reset protocol—to overcome the obstacle of EL quenching in nano-LEDs *without* the need for a thermal cycle. The results from this publication (both the main text and supplementary information) are reproduced in Chapter 3. Section 3.1 briefly lists the sample fabrication and optical and electrical characterization methods. Section 3.2 shows some band structure simulation results, while Sections 3.3 and 3.4 show transport characterization in control HEMTs and rectifying diode behaviour through diode I–V traces respectively. The Set-Reset sequence is introduced in Section 3.5. A detailed spectral analysis of the emission from several devices is covered in Section 3.6. Section 3.7 discusses the mechanism by which the Set-Reset protocol overcomes EL quenching. The observed EL linewidths are the narrowest reported to date in lateral p–n junctions. Also, our devices are shown to be compatible with RF operation, indicating they can be integrated with the high-frequency quantized charge pumps.

Chapter 4 shows results from a nano-LED that is fabricated using a heterostructure with a GaAs/AlGaAs single heterojunction interface (SHJI). This is in contrast to the devices in Chapter 3 that were fabricated using a heterostructure wafer with a narrow (15 nm) rectangular GaAs quantum well (QW) (see Section 2.1 for more background). We are the first to demonstrate lateral 2D p–n junctions at SHJIs; in fact, it was recently theorized that such devices are impossible to fabricate.[31] Section 4.1 briefly lists the sample fabrication and optical and electrical characterization methods. The experimental results in Section 4.2 include top-down optical images of the device center and emission spectra from the n-side and p-side in all electrical measurement configurations. Fabrication of nano-LEDs is easier using SHJIs than quantum wells, although the spectra are harder to analyze since the peak energies match those of luminescence from the substrate.

The SHJI-based nano-LED in Chapter 5 includes side gates adjacent to (but not overlapping) the p–n channel on either side. The purpose of this device was to localize the emission and make it stable in time. Section 5.1 briefly lists the sample design, fabrication, and optical and electrical characterization methods. HEMT transport and diode I–V curves are shown in Sections 5.2 and 5.3. Device center images and optical spectra along with a map of emission across the sample are presented in Section 5.4. Section 5.5 explores the effect of applying potentials to the side gates. Regimes corresponding to localized emission during Set-Reset operation and time-stable emission in conventional operation are described in Sections 5.6 and 5.7. These new modes of operation offer interesting

ways to make these devices compatible with the integration of quantized charge pumps.

Chapter 6 shows results from a prototype wafer with a bottom Bragg mirror and Bragg ring microcavity fabricated to be compatible with our lateral 2D p–n junction and quantized charge pumps. Section 6.1 discusses sample characterization methods. The simulation, fabrication and design validation of the bottom mirror and microcavity are detailed in Sections 6.2 and 6.3. These structures will enhance the photon emission and extraction efficiency from our sources by redirecting any downward propagating emission back up and shaping the emission into a single Gaussian-like mode.

Finally, Chapter 7 summarizes the results from the main experimental chapters while contextualizing them within the broader scope of our project, and recommends future work needed to achieve the ultimate goal of a bright, deterministic, electrically-driven quantum emitter.

2. Background

2.1 Two-dimensional charge gases in GaAs/AlGaAs heterostructures

A system of charges (electrons/holes) is said to be dynamically two-dimensional (2D) if it is subject to strong quantum confinement along one spatial direction but is free to move along the other two.[32] III–V semiconductor heterostructure devices grown using Molecular Beam Epitaxy (MBE) are well-suited to host these types of systems. Due to a relatively smaller effective mass of their conducting electrons, the electron mobility in these materials is higher.[33] Devices made using undoped Gallium Arsenide (GaAs) and Aluminum Gallium Arsenide ($Al_xGa_{1-x}As$) semiconductor heterostructures are the focus of this section. In GaAs/$Al_xGa_{1-x}As$ heterostructures, there are few interface defects between successive layers as there is little variation in the lattice constant; the resulting ease of growth further contributes to higher charge mobility since scattering off of defects is lower.[34]

Appropriate doping or the application of an electric field normal to the heterostructure can modify its band structure, creating a confinement region in the lower bandgap material at the SHJI between two layers. Charges supplied to this region can accumulate and form a planar charge 'gas'. Applying a source-drain bias across this conducting channel results in a specific type of field-effect transistor (FET) known as the HEMT.[35]

The first HEMT devices were modulation-doped, meaning that the dopants are spatially separated from the conduction channel. This offered a significant advantage over older 2D FETs made using conventionally doped semiconductors, since charge scattering due to ionized dopant impurities was eliminated (hence the descriptor 'high-electron-mobility'). An alternative to modulation-doped HEMTs are so-called 'induced' HEMTs—a potential is

applied to a conductive gate on one side of the structure and a 2D charge carrier region is induced via ohmic contacts to the conduction channel.[36] Induced HEMT devices are undoped and offer several advantages over their modulation-doped counterparts. Unlike in modulation-doped HEMTs, 2D charge systems in induced HEMTs are superior in quality since they are not affected by scattering due to remote ionized dopants.[37] Another key advantage of induced HEMTs is that the polarity on the inducing gate determines the carrier type in the conduction channel, allowing either electrons or holes in the *same* device (and on the *same side* of a device). In contrast, the carrier type in modulation-doped HEMTs is fixed by the type of dopant used.[38] This section covers the theory, design, fabrication and operation of induced HEMTs in undoped GaAs/AlGaAs heterostructures.

2.1.1 Theory

2.1.1.1 Quantum description

It is first useful to understand how electrons[‡] are confined within a 2D quantum well. A single electron with wavefunction $\psi(x, y, z)$ in the presence of a potential V and under the effective mass approximation obeys the Schrödinger equation[39]

$$-\frac{\hbar^2}{2m^*}\nabla^2\psi + V\psi = E\psi, \tag{2.1}$$

where E is the energy of the electron, m^* is its effective mass, and $\hbar$ is the reduced Planck constant. An electron confined to a quantum well parallel to the xy-plane is restricted in motion along z. The Schrödinger equation in this case can be decoupled along the three axes as

$$-\frac{\hbar^2}{2m^*}\frac{\partial^2\psi_x}{\partial x^2} = E_x\psi_x, \tag{2.2}$$

$$-\frac{\hbar^2}{2m^*}\frac{\partial^2\psi_y}{\partial y^2} = E_y\psi_y, \text{ and} \tag{2.3}$$

$$-\frac{\hbar^2}{2m^*}\frac{\partial^2\psi_z}{\partial z^2} + V(z)\psi_z = E_z\psi_z, \tag{2.4}$$

where $V(z)$ is the confining potential due to the quantum well, $E = E_x + E_y + E_z$, and $\psi(x, y, z) = \psi_x(x)\psi_y(y)\psi_z(z)$. Since the electron's motion is unrestricted along x and y,

[‡] the same description can be applied to holes.

we can use the form of a standard travelling wave to describe the electron and solve the Schrödinger equation to obtain the components of its energy along these axes;

$$\psi_{x,y}(x,y) = \frac{1}{\sqrt{A}} e^{i(k_x x + k_y y)}, \tag{2.5}$$

$$E_{x,y} = \frac{\hbar^2 |\vec{k}_{x,y}|^2}{2m^*}. \tag{2.6}$$

Here, $\vec{k}_{x,y}$ is the electron momentum along x, y. A is a normalization constant equal to the area of the quantum well. For an infinitely large well, we use a finite normalization area and assume periodic boundary conditions.

Along z, the Schrödinger equation takes the form of a standard 1D infinite well, and solving it yields wavefunctions $\psi_{z,n}(z)$ with discrete energies $E_{z,n}$;

$$\psi_{z,n}(z) = \sqrt{\frac{2}{w}} \sin(k_z z) = \sqrt{\frac{2}{w}} \sin\left(\frac{n\pi z}{w}\right), \text{ and} \tag{2.7}$$

$$E_{z,n} = \frac{\hbar^2 k_z^2}{2m^*} = \frac{n^2 \pi^2 \hbar^2}{2m^* w}. \tag{2.8}$$

Here, n is an integer greater than or equal to zero and represents an individual energy 'subband',* and w is the width of the quantum well. This gives us the expression for the total wavefunction and energy,

$$\psi(x,y,z) = \frac{1}{\sqrt{A}} e^{i(k_x x + k_y y)} \sqrt{\frac{2}{w}} \sin\left(\frac{n\pi z}{w}\right), \text{ and} \tag{2.9}$$

$$E_{\text{total}} = \frac{n^2 \pi^2 \hbar^2}{2m^* w} + \frac{\hbar^2 |\vec{k}_{x,y}|^2}{2m^*}. \tag{2.10}$$

2.1.1.2 Density of states and subband populations

When considering multiple charge carriers, understanding how they are distributed in terms of energy E and momenta k is useful. The density of states ρ tells us the number of

* a state confined along one dimension but broadened along the other two

states a charged particle can occupy at a particular energy, and is defined as[39]

$$\rho(E) = \frac{\mathrm{d}N}{\mathrm{d}E} = \frac{\mathrm{d}N}{\mathrm{d}k}\frac{\mathrm{d}k}{\mathrm{d}E}. \tag{2.11}$$

In the two-dimensional case, the number density $N = N_{2D}$ is the number of states per unit area in real space, and can be derived as

$$N_{2D} = \frac{k^2}{2\pi} = \frac{1}{2\pi}\frac{2m^*E}{\hbar^2}, \tag{2.12}$$

yielding the 2D density of states

$$\rho_{2D}(E) = \frac{m^*}{\pi\hbar^2}. \tag{2.13}$$

Charge carriers like electrons and holes are *fermions*, and obey Fermi-Dirac statistics. The probability of a fermion occupying a state with energy E is given by the Fermi-Dirac distribution

$$f_{FD}(E) = \frac{1}{e^{\frac{E-E_F}{k_B T}} + 1}, \tag{2.14}$$

where k_B is the Boltzmann constant, E_F is the quasi-Fermi energy and describes carrier population *within* a subband, and T is the lattice temperature at equilibrium.

The total number of carriers in a subband is found by multiplying the probability of state occupation with the corresponding density of states and integrating over all energies in the subband,

$$N_{total} = \int f_{FD}(E)\rho_{2D}(E)\mathrm{d}E = \int_{E_{min}}^{E_{max}} \frac{1}{e^{\frac{E-E_F}{k_B T}} + 1}\frac{m^*}{\pi\hbar^2}\mathrm{d}E. \tag{2.15}$$

Solving this, we get

$$N_{total} = \frac{m^* k_B T}{\pi\hbar^2}\left\{\left[\frac{E_{max} - E_F}{k_B T} - \ln\left(1 + e^{\frac{E_{max}-E_F}{k_B T}}\right)\right] - \left[\frac{E_{min} - E_F}{k_B T} - \ln\left(1 + e^{\frac{E_{min}-E_F}{k_B T}}\right)\right]\right\}. \tag{2.16}$$

E_{min} can be taken as the subband minima while E_{max} can be set to $E_F + 10k_B T$ (more stable at low temperature). If N_{total} is known, the only unknown E_F can be evaluated.

2.1.2 Influence of electric and magnetic fields

Applying an electric field F along the wafer growth direction z creates a slope in the heterostructure potential and is equivalent to applying a perturbation $V' = -eFz$ to the potential. The first-order correction to the ground state energy level ψ_1 of an electron is given by[39]

$$\Delta E^{(1)} = \langle \psi_1 | V' | \psi_1 \rangle = \int_{-\infty}^{+\infty} \psi_1^*(z)(-eFz)\psi_1(z)\mathrm{d}z. \tag{2.17}$$

Due to symmetry, the value of this integral is zero, implying that for small fields, there is no change to the ground state energy level. Larger electric fields would necessitate calculating the second-order correction term

$$\Delta E^{(2)} = \sum_{m=2}^{\infty} \frac{|\langle \psi_m | V' | \psi_1 \rangle|^2}{E_m - E_1}. \tag{2.18}$$

Since $V' = -eFz$, and since a charge would want to lower its energy, we get $\Delta E^{(2)} \propto -F^2$. Physically, this means that an electron and a hole trapped in a quantum well would become spatially separated, decreasing their overlap and the exciton binding energy. The energy levels also come closer together, causing a redshift in the optical transition, but only when the external field is significant. The phenomenon associated with this redshift is called the Quantum Confined Stark Effect.

An electric field F applied *in-plane* as opposed to perpendicular can also result in a shift in energy, as per the Franz-Keldysh effect. This energy shift is given by[40]

$$\Delta E = \left(\frac{\hbar^2 e^2 F^2}{2m_r^*} \right)^{1/3}, \tag{2.19}$$

where m_r^* is the reduced effective mass, i.e. $1/m_r^* = 1/m_e^* + 1/m_h^*$.

Applying a strong external magnetic field with magnitude B along the growth direction z quantizes the x- and y-components of the carrier energies in addition to the existing z-quantization due to confinement in the quantum well. These quantized energy levels are called Landau levels. Under this external magnetic field, the Schrödinger equation takes the form of that of a 1D simple harmonic oscillator with frequency $\omega_c = eB/m^*$; this parameter is known as the cyclotron frequency of the charge (with effective mass m^*)

arising due to the field B. The solution for the total energy given by Eqn. 2.10 becomes[39]

$$E_{\text{total}} = E_{z,n} + \frac{\hbar^2 k_l^2}{2m^*} = E_{z,n} + \left(l + \frac{1}{2}\right)\hbar\omega_c, \tag{2.20}$$

where k_l is the wavevector of a charge in the l^{th} Landau level, l being zero or a positive integer. Landau quantization causes the density of states to become a series of delta peaks at discrete energies,

$$\rho(E) = \sum_l g\delta(E - E_l), \tag{2.21}$$

where g is the degeneracy of each Landau level. Assuming the cyclotron motion of an electron covers an area A, the magnetic flux Φ through this area is

$$\Phi = B \cdot A. \tag{2.22}$$

This magnetic flux is quantized; the number of flux quanta is equivalent to the total number of states per Landau level. This is in fact the degeneracy of each level, and is given by

$$g = \frac{\Phi}{\Phi_0}, \tag{2.23}$$

where $\Phi_0 = h/e$ is the magnetic flux quantum. For an infinitely large quantum well plane, the degeneracy is infinite; in a practical device the area is finite but the degeneracy is still very large, making it easier to think in terms of area densities. For a fully occupied Landau level, the carrier density per unit area per Landau level is

$$\frac{g}{A} = \frac{\Phi}{A\Phi_0} = \frac{eB}{h}. \tag{2.24}$$

In turn, we get the expression for the total 2D carrier density

$$n_{2D} = \nu\frac{eB}{h}, \tag{2.25}$$

where ν is the fill factor, or the number of occupied Landau levels. Depending on convention, ν may include a factor of 2 accounting for two electron spin states per flux quantum. In the case of high magnetic fields, Zeeman splitting of these two spin states in each Landau level can occur; in this case ν does *not* include the factor of 2, but instead corresponds to the number of occupied spin-split *half* Landau levels. The total energy in this case is

modified as

$$E_{\text{total}} = E_{z,n} + \left(l + \frac{1}{2}\right)\hbar\omega_c \pm \frac{1}{2}g^*\mu_{\text{B}}B, \tag{2.26}$$

where g^* is the Landé g-factor related to the quantum numbers of the particle in consideration (2 for free electrons), and $\mu_B = e\hbar/2m$ is the Bohr magneton.

For a longitudinal source-drain bias V_{sd}, longitudinal and transverse conductivities (σ_{xx} and σ_{xy} respectively) are affected differently in the presence of the perpendicular magnetic field B. The transverse or Hall conductance G_{H} is given by[†]

$$G_{\text{H}} = \frac{I_{\text{sd}}}{V_{\text{H}}}, \tag{2.27}$$

where I_{sd} is the longitudinal current driven by V_{sd} and the Hall voltage V_{H} is related to the magnetic field as

$$V_{\text{H}} = \frac{I_{\text{sd}}B}{n_{\text{2D}}e}. \tag{2.28}$$

The above expression is derived by using the Lorentz force equation for an electron in a steady-state two-dimensional system. The Lorentz force due to B deflects charge carriers perpendicular to B and I_{sd}, resulting in non-zero V_{H}. We thus get

$$G_{\text{H}} = \frac{n_{\text{2D}}e}{B} = \nu\frac{e^2}{h}, \tag{2.29}$$

implying quantization of the Hall conductance—when ν is an integer (assuming spin-split half Landau levels), the conductance plateaus. Also, the Fermi energy in this case is above the ν^{th} half Landau level, meaning all levels are completely occupied and there are no accessible empty states, making σ_{xx} drop to zero. At half-integer values of ν, the ν^{th} half Landau level is passing through the Fermi energy, and the material is now able to conduct meaning σ_{xx} peaks. Since increasing B increases ω_c, the energy of each Landau level increases linearly with B. It follows that sweeping B while fixing the electron density n_{2D} will make the quantized energy levels successively pass through the Fermi energy, leading to discrete peaks in σ_{xx} at half-integer values of ν (and dips at integer values of ν) called Shubnikov-de Haas oscillations. There will simultaneously be plateaus in G_{xy} corresponding to integer values of ν; these plateaus are the hallmark of the integer quantum Hall effect.

[†] note that this is a special quantity and not indicative of conductance as per Ohm's law, since I_{sd} and V_{H} are perpendicular to each other

Carrier mobility μ is related to conductivity σ as

$$\sigma = en\mu, \tag{2.30}$$

where n is the carrier density. This expression can be derived from first principles using Newton's second law, Ohm's law and the current drift equation. Applying this to our model, we get

$$\mu = \frac{\sigma_{xx}}{en_{2D}}. \tag{2.31}$$

Here, μ is the longitudinal mobility parallel to the source-drain bias. σ_{xx} can be calculated at $B = 0$ using

$$\sigma_{xx} = \frac{I_{sd}(L/W)}{V_{sd}}, \tag{2.32}$$

in turn yielding

$$\mu = \frac{I_{sd}(L/W)}{en_{2D}V_{sd}}. \tag{2.33}$$

Although this equation suggests an inverse relation between μ and n_{2D}, in practice σ_{xx} generally goes up for higher n_{2D}. This is because at higher carrier densities, there is more screening of the charges in the 2DEG from impurities in and around the plane of the 2DEG. This increase in σ_{xx} more than compensates for the higher n_{2D}, resulting in a raising of μ instead. The precise manner of this scaling depends on the impurity scattering mechanisms present in the system (see Section 2.1.4.1 for more details).

2.1.3 Induced HEMT architecture

Induced HEMTs are fabricated using *undoped* semiconductor heterostructure wafer substrates. The majority carrier (electron/hole) is 'induced' at a SHJI via an electric field applied perpendicular to the heterostructure. Carrier mobilities are high due to the lack of dopants and are limited only by scattering due to background impurities. The key components of an induced device are:

- a heterostructure wafer substrate with a HJI at a depth of several tens to a few hundred nanometres,
- a reservoir of charge carriers (electrons/holes) in electrical contact with the HJI;
  - this 'ohmic contact' must be isolated from the inducing gate,[41] and

  - may be composed of either p- or n-type material to supply holes or electrons respectively,
- a conductive gate on the front or back of the structure to induce and tune the density of the 2D charge carrier region at the HJI, spatially separated from the conduction channel.

GaAs-based HEMTs utilize heterostructure wafers that generally include a thick GaAs buffer as the channel layer, followed by a higher bandgap AlGaAs[†] barrier, and finally a GaAs spacer or cap layer at the top.[36] Alternatively, a thin GaAs channel layer may be sandwiched between two thick AlGaAs barriers. Applying a positive or negative voltage on a top gate bends the band structure, forming a triangular quantum well[‡] in the GaAs channel at the GaAs/AlGaAs HJI, or a rectangular quantum well (RQW) in the case of a sandwiched GaAs layer.

Molecular Beam Epitaxy can yield GaAs heterostructure wafers with low background impurities, making them ideal for use in undoped devices in which high carrier mobilities are required.[42] Heterostructures with the GaAs channel grown on top of a layer of AlGaAs have lower mobilities *unless* a GaAs/AlAs short-period superlattice is grown prior to the AlGaAs layer[43]—this applies to devices with RQWs and also back-gated inverted HEMTs (described below).

Various designs and fabrication techniques have been reported for GaAs-based induced devices (Fig. 2.1). The inducing gate may either be heavily doped GaAs[36,49] or a metal,[47,50] and may be either located at the front (top)[36,41,49,50,51] or back (bottom).[42,52] The contact it makes with the semiconductor can be a Schottky[47] (metal-semiconductor) contact or a MIS[47,53] contact. The ohmic contacts to the HJI are created by etching a recess into the wafer and depositing either p-type (usually AuBe[45]) or n-type (usually NiAuGe[54,55,51]) material followed by thermal annealing.[36,56] This may be preceded by implanting ions of an appropriate element around the contact region (e.g. Si^{2+} or Be^{+} for n- and p-type contacts respectively[46]). The depth of the induced charge gas can vary—ultra-shallow conduction channels are necessary when defining nanostructures using a fine-featured inducing gate, since feature resolution is poor for deeper channels.[57,58] Architectures with simultaneous n- and p-type ohmic contacts are termed *ambipolar*.[59,38] Changing the polarity of the top gate voltage in such devices changes the polarity of the induced charge gas. A positive voltage induces a two-dimensional electron gas (2DEG) by bending the conduction band

[†] the Al ratio for such devices tends to be around 0.3.
[‡] this shape is an approximation.[32]

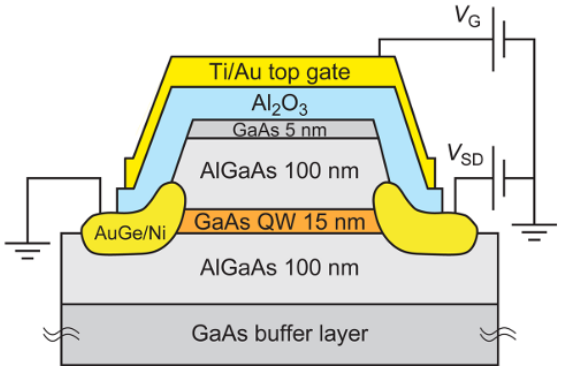

(a) metal-insulator-semiconductor (MIS) contacted metal top gate, sandwiched GaAs channel, n-type ohmic contacts[44]

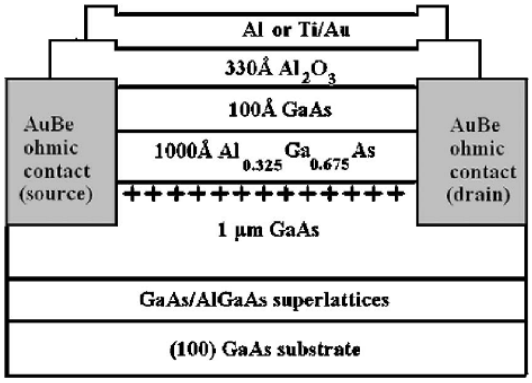

(b) MIS contacted metal top gate, single HJI, p-type ohmic contacts[45]

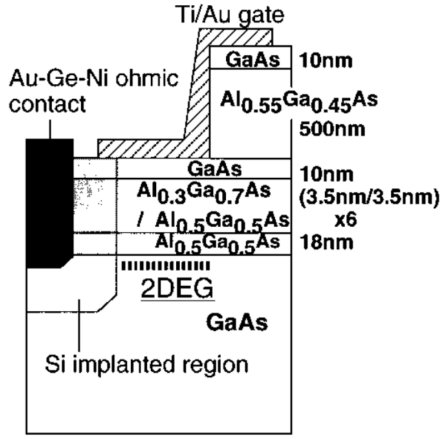

(c) Schottky contacted metal top gate, single HJI, ion-implanted n-type ohmic contacts[46]

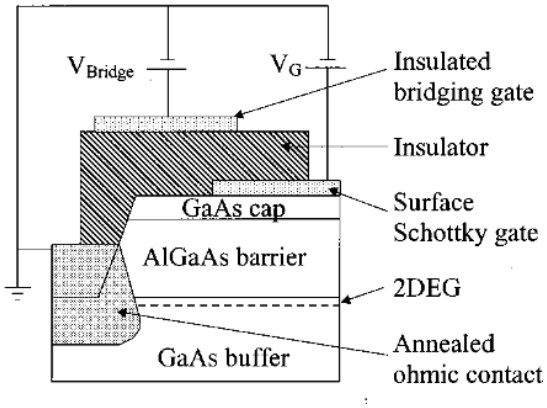

(d) Schottky and MIS contacted metal top gates, single HJI, n-type ohmic contacts[47]

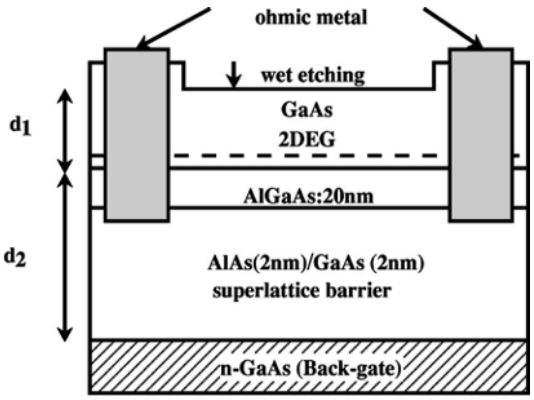

(e) Schottky contacted doped GaAs back gate, single HJI, n-type ohmic contacts[48]

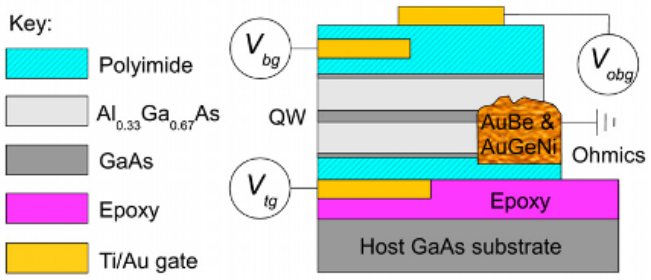

(f) MIS contacted metal top and back gates, sandwiched GaAs channel, ambipolar ohmic contacts[38]

Figure 2.1: HEMT devices with several different architectures.

downwards in energy until it crosses the Fermi level. Inversely, a negative voltage bends the valence band upwards until it crosses the Fermi level, inducing a two-dimensional hole gas (2DHG).

Each of these design choices has pros and cons. Using heavily-doped GaAs (grown *in situ* as the final layer during wafer fabrication) as a top gate can result in good quality devices—the AlGaAs barrier above the 2DEG is a high quality single crystal with few surface defect states. Metallic gates generally cannot be deposited *in situ*,[†] therefore impurities may be introduced on the surface of the GaAs cap layer prior to metal deposition, introducing surface charges and disorder at the contact.[41] For Schottky devices, the metal could also diffuse past the cap layer and into the AlGaAs barrier, diluting the Al ratio and causing non-uniformity in the contact.[41] On the other hand, devices with heavily-doped GaAs top gates have poor yield—alloyed ohmic material requires a thermal anneal to diffuse (or 'spike') to the 2DEG channel layer and form an electrical contact,[60] but there is a high chance (especially in shallower devices) of the ohmic material spiking and shorting to the doped top gate as well, causing current leakage.[61,62] Additionally, defining nanostructures using doped GaAs gates is not possible since patterning fine features in doped gates results in their charge being depleted, rendering them nonfunctional.[50]

Back-gating is achieved by growing the heterostructure on n-type GaAs.[63] Since the ohmic contacts require front-side processing, fabrication is simpler compared to top-gated devices.[42] However, the yield of back-gated devices tends to be low for the same reason as devices with doped GaAs as a topgate—spiking of ohmic material during annealing can easily extend to the back gate,[64] causing shorts. Devices using a MIS-type topgate avoid this issue—the caveat is that a high-quality insulating dielectric material is required.[53,45]

Using Schottky contacts limits device operation to low voltages and thus low charge gas densities, since there is a risk of shorting through the AlGaAs barrier to the charge gas at higher potentials.[45] MIS devices can operate at higher voltages without gate leakage, but may also yield low carrier densities if using thin insulators. Another advantage of MIS devices is the ability to dual-gate—a second 'local' gate located closer to the surface (and insulated from the first 'global' gate) can be used to realize nanoscale features[65] or induce and control charge densities independently.[47] As mentioned previously, doped GaAs Schottky gates deposited *in situ* result in few surface charges. This is not the case for MIS devices, where the presence of surface states reduces transport and quantum scattering lifetimes[66] of carriers in shallow devices, and affects the latter even in devices with deeper

[†] In 2022, Ashlea Alava et. al.[50] demonstrated an *in-situ* epitaxial Al gate.

conduction channels (a few hundred nanometers).[67]

Ion implantation prior to ohmic contact deposition necessitates a very high temperature anneal, about 800 °C.[46] This is very harmful to the integrity of the heterostructure and introduces defects that severely limit carrier mobility,[59] and as a result usually avoided.

2.1.4 Operation of induced HEMTs

As mentioned, the polarity of an induced charge carrier depends on the polarity of the voltage V_{tg} on the inducing gate—a positive V_{tg} induces electrons in the channel layer while a negative V_{tg} induces holes, as long as n-type or p-type ohmic material respectively is contacting the channel to supply carriers. A temperature T of at most a few Kelvin is required to operate these devices to prevent phonon-charge scattering. Charges are induced only beyond a certain voltage called the 'pinch-off', 'turn-on' or 'threshold' voltage, typically represented by[33,36,46]

$$V_{tg}^{thr} = (U_F^c - U_F^g)/e + E_{sub} t_{ins} + eN_{imp} t_{ins}^2/2\epsilon, \tag{2.34}$$

where U_F^c and U_F^g are the Fermi energies of the carrier and gate material respectively; E_{sub} is the electric field from the substrate; t_{ins} is the insulator thickness; N_{imp} is the density of impurities in the insulator and ϵ is the dielectric constant of the insulator. Past this voltage threshold, the two-dimensional electron (hole) density n_{2D} (p_{2D}) increases linearly with increasing (decreasing) V_{tg}. Experimentally, V_{tg}^{thr} is obtained by extrapolating the V_{tg} vs n_{2D} plot to intersect with the voltage axis and reading the value of the intercept. Nominally, the difference between the V_{tg}^{thr} values for a 2DEG and 2DHG in the same device equals the bandgap of GaAs (1.52 eV).[46] However, impurities and charge traps present within and at the interfaces adjoining the insulator or substrate could cause a shift in the V_{tg}^{thr} values and alter this difference.[36,46,44]

A source-drain bias V_{sd} applied between two ohmic contacts leads to conduction in the 2D channel. The channel current I_{sd} and charge mobility $\mu_{e,h}$ generally increase with increasing carrier density, while the ohmic contact resistance R_c and resistivity of the 2D charge gas $\rho_{e,h}$ decrease. Carrier densities and mobilities can be obtained by the measurement of a Hall bar device made using the substrate as the induced HEMT (see

Section 2.1.2). Their values are calculated using Eqns. 2.28 and 2.33,[68] reproduced below–

$$n_{2D} = \frac{I_{sd}B}{eV_H}, \text{and} \tag{2.35}$$

$$\mu = \frac{I_{sd}(L/W)}{en_{2D}V_{sd}}, \tag{2.36}$$

Table 2.1 lists data from various induced HEMT devices in chronological order of publishing. To fruitfully compare them, mobility data at carrier densities of 0.5×10^{11}, 1×10^{11} and $2\times10^{11}\text{cm}^{-2}$ are chosen.

Table 2.1: Summary of data from several GasAs/AlGaAs induced devices. ABBREVIATIONS: BG = back gate, TG = top gate, x = Al ratio in $Al_xGa_{1-x}As$ barrier, d = depth of conduction channel from surface, w = vertical width of channel.

Author, Year	**Gate type**	**Conduction channel**	***T* (K)**	**(V_{tg}^{thr}) (V)**	**$\mu_{e,h}$ (1e5 cm^2/Vs) [n_{2D}=5e10 cm^{-2}]**	**$\mu_{e,h}$ (1e5 cm^2/Vs) [n_{2D}=1e11 cm^{-2}]**	**$\mu_{e,h}$ (1e5 cm^2/Vs) [n_{2D}=2e11 cm^{-2}]**
Linfield '93[64]	Schottky n^+ GaAs BG	SHJI, n-type, d=1367nm	4.2	−4.7	–	1	2.8
Kane '93[36]	Schottky n^+ GaAs TG	SHJI, n&p-type, d=600nm	4.2	n:0.00, p:-1.66	μ_e=15, μ_h=1.5	μ_e=22, μ_h=2	μ_e=31, μ_h=2.4
Kane '95[41]	Schottky Al TG	SHJI, n-type, d=40nm	4.2	–	0.5	2	8
Kane '95[41]	Schottky n^+ GaAs TG	SHJI, n-type	4.2	–	10	16	25
Hirayama '96[46]	Schottky metal TG	SHJI, n&p-type, d=70nm	1.6	n:+1, p:−0.72	–	–	μ_e=3, μ_h ~1.5
Harrell '99[47]	Schottky metal TG	SHJI, n-type, induced, d=317nm	1.5	+1.1	16.8	23.2	3.4
Harrell '99[47]	Schottky metal TG	SHJI, n-type, doped	1.5	+1.1	12.3	21.9	3.4
Kawahara-zuka '00[48]	Schottky n^+ GaAs BG	SHJI, n-type, d=420nm	1.6	+0.8	8.3	14.6	23.1
Willett '06[53]	MIS metal TG	SHJI, n-type, d=105nm	0.29	+0.7	2.9	4.6	7.4
Lu '07[45]	MIS metal TG	SHJI, p-type, d=143nm	0.3	−1.25	1.2	3.1	5.8
Sarkozy '07[61]	MIS metal TG	SHJI, n-type, d~150nm	–	+1.1	1.3	2.3	–
Sarkozy '09[65]	Schottky TG & MIS metal TG	SHJI, n-type	1.4	+1	14.7	24.5	35.2
Mak '10[57]	MIS metal TG	SHJI, n-type, d=40nm	1.5	~ +2	2	5	11.2
Mak '10[57]	MIS metal TG	SHJI, n-type, d=310nm	1.5	~ +2	10.9	19	29.8
Chen '12[59]	MIS metal TG	SHJI, n-&p-type	0.24	n:+1.09, p:−0.52	μ_e=33.2, μ_h=5.4	μ_e=61.6, μ_h=8	μ_e=55.6, μ_h=6.5

Croxall '13[38]	MIS metal TG & BG	RQW, n&p-type, w=10nm	0.05	–	μ_e=1.3, μ_h=0.74	μ_e=2.3, μ_h=1.7	μ_e=4.4, μ_h=3.3
Croxall '13[38]	MIS metal TG & BG	RQW, n&p-type, w=25nm	0.05	–	μ_e=12.1, μ_h=5.5	μ_e=20.4, μ_h=11.7	μ_e=34.3, μ_h=16.8
Mak '13[34]	MIS metal TG	SHJI, n-type, d=60nm, x=0.33	4	~ +2	11.3	24.1	42.9
Mak '13[34]	MIS metal TG	SHJI, n-type, d=30nm, x=0.9	4	~ +2	1.4	4.7	11.5
Wang '13[67]	MIS metal TG	SHJI, n-type	0.025	~ +1	23.9	41.9	>56
MacLeod '15[49]	Schottky n^+ GaAs & MIS metal TGs	SHJI, n-type, d=50nm	0.229	+0.2	4.9	10.1	20
MacLeod '15[49]	Schottky n^+ GaAs & MIS metal TGs	SHJI, n-type, d=160nm	0.229	+0.2	12.7	24.9	50.3
Taneja '16[51]	MIS metal TG	SHJI, n&p-type	1.4	–	μ_e=3.4, μ_h=2.1	μ_e=5.3, μ_h=3.8	μ_e=8.1, μ_h=4.0
Taneja '17[69]	MIS metal TG	SHJI, n&p-type	0.3	n:+1.8, p:-1.8	μ_e=3.4, μ_h=3.1	μ_e=5.3, μ_h=4.5	μ_e=8.1, μ_h=4.8
Ashlea Alava '22[50]	MIS TiAu TG	SHJI, n-type	0.25	+0.76	–	3.4	11.4
Ashlea Alava '22[50]	Schottky evaporated Al TG	SHJI, n-type	0.25	+0.8	–	1.2	–
Ashlea Alava '22[50]	Schottky MBE 50nm Al TG	SHJI, n-type	0.25	+0.88	–	0.3	2.3
Ashlea Alava '22[50]	MIS evaporated Al TG	SHJI, n-type	0.25	+0.78	–	2.4	7.5
Ashlea Alava '22[50]	Schottky MBE 8nm Al TG on GaAs	SHJI, n-type	0.25	+0.71	–	4.8	8.9
Ashlea Alava '22[50]	Schottky MBE 8nm Al TG on AlAs	SHJI, n-type	0.25	+0.69	–	2.7	6.5
Ashlea Alava '22[50]	Schottky MBE 8nm Al TG on AlGaAs	SHJI, n-type	0.25	+0.67	–	3.3	–
Shetty '22[68]	MIS metal TG	SHJI, n-type, d=160nm	1.4	+0.8	16	31	56

2.1.4.1 Scattering

Various scattering mechanisms have been theorized to explain drop-offs in charge carrier mobility observed experimentally at different carrier density regimes. The mobility μ is related to the transport scattering time τ[†] by $\mu = e\tau/m^*$, with e being the elementary charge and m^* the effective mass.[68] The total rate of scattering $1/\tau_{tot}$ can be obtained by summing over the individual rates due to each mechanism, according to Matthiessen's rule,[70] given by

$$\frac{1}{\tau_{tot}} = \sum_i \frac{1}{\tau_i}, \tag{2.37}$$

[†] The average time between successive scattering events, also called relaxation time.

and thus, the mobility is modeled as

$$\frac{1}{\mu} = \frac{m^*}{e} \sum_i \frac{1}{\tau_i}. \tag{2.38}$$

Broadly, scattering in 2D HEMTs can be ascribed to (i) background ionized impurities, (ii) remote dopants, (iii) surface charges, (iv) interface roughness, (v) alloy disorder, and (vi) phonons. Phonon scattering can be due to acoustic[†] or optical[‡] phonons. The latter is the dominant source of scattering in devices from room temperature down to $\sim 100\,\mathrm{K}$.[71] Both types of phonon scattering are negligible at temperatures of a few Kelvin and under (the Bloch-Grüneisen regime[72]), which is why devices must be operated at these cryogenic temperatures.

The remaining scattering mechanisms all contribute to carrier mobility reduction to different extents in 2D HEMT devices with differing architectures. Modulation-doped HEMTs require *intentional* doping in thin layers (δ-doping) around the 2DEG. These remote dopants act as scattering sites and also introduce charge noise into the device.[73] Devices with shallower 2DEGs require the δ-doping layers to be closer to the 2DEG, causing more scattering.[71] Background ionized impurities are the result of *unintentional* doping of the semiconductor wafer material (both GaAs and AlGaAs) during growth in the MBE chamber. These impurities are distributed evenly throughout the material. Undoped devices avoid scattering due to remote dopants, but cannot escape background impurity scattering. Both scattering types are more prominent at $n \sim 10^{11}\,\mathrm{cm}^{-2}$, although remote dopant scattering is greater in significance. At very low densities,[‡] the density fluctuates and is inhomogeneous, and transitions to an insulating phase below $n \sim 5 \times 10^{10}\,\mathrm{cm}^{-2}$.[71]

Coulomb scattering due to surface charges is another source of carrier mobility degradation. Surface charges may occur for several reasons: dangling bonds or excited states, redistribution of free charges (from the wafer or an insulating material), or a local reorganization of the semiconductor lattice, to name a few.[68] Since these charges are confined to a single layer on the surface, they behave similarly to remote δ-dopants in modulation doped devices, and can be modelled as such.[57,67] Transport lifetimes in shallower devices are naturally impacted more—2DEGs shallower than 200 nm show deviation from expected values,[67] but the effect is more noticeable for depths of 100 nm or less.[57,68] The single-particle scattering rate (distinct from the transport scattering rate) is increased even

[†] Atoms vibrate coherently around equilibrium lattice positions.
[‡] Adjacent atoms vibrate out of phase—common in lattices with more than one type of atom.
[‡] Note that the exact density regimes vary from device to device.

in deep devices ($> 200\,\text{nm}$), causing issues when working at the one-particle quantum level.[67] Preventing surface oxide formation by epitaxially growing gates[§] in-situ in the MBE wafer growth chamber can prevent surface charges.[41,47,49,74,50] An interesting phenomenon is that illumination can cause surface charge density to build up in a device, further hampering mobility (see Section 2.1.4.2).

Fitting the carrier mobility vs density plot to a power-law, $\mu \propto n^{\alpha}$, and extracting the exponent α helps identify the dominant scattering mechanism in a device.[75,71] The exponent is calculated from $\alpha \equiv d\ln(\mu/d)\ln(n)$, where d is the separation between 2D remote dopants (or surface charges modelled as remote dopants) and the 2D charge gas. In the absence of all background impurities, α increases with increasing d at lower carrier densities, but saturates around $\alpha \sim 1.5$ for $n = 3 \times 10^{11}\,\text{cm}^{-2}$ at all values of d. Increasing the separation to $d \gtrsim 100\,\text{nm}$ eliminates the influence of remote ionized/surface charge scattering altogether, also yielding $\alpha \sim 1.5$ at all densities. When only background impurities are present (with a conservative volume density $N_{\text{BI}} \sim 10^{13}\,\text{cm}^{-3}$), $\alpha < 1$ for $n < 2 \times 10^{11}\,\text{cm}^{-2}$, and increases to $\alpha \sim 1.2$ for $n = 3 \times 10^{11}\,\text{cm}^{-2}$. In the absence of all impurities (except for some background impurities in the barrier), $\alpha \sim 1.5$ for $n \gtrsim 5 \times 10^{10}\,\text{cm}^{-2}$.[75] In short, the value of the power-law exponent α can tell us how great an effect different scattering mechanisms may have on carrier mobility. Increasing d or decreasing N_{BI} can enhance μ; very large μ is possible when $d \gtrsim 100\,\text{nm}$ and $N_{\text{BI}} \lesssim 10^{-13}\,\text{cm}^{-3}$. Increasing n can also increase μ up to a certain point, beyond which interface roughness and alloy disorder scattering mechanisms kick in.

Asymmetrically gating an induced HEMT device causes the carrier wavefunction to be pulled against the interface between the channel and barrier. Roughness at the interface thus causes charge carrier scattering that is more noticeable at higher densities ($n \gtrsim 3 \times 10^{11}\,\text{cm}^{-2}$).[75,51,68] Alloy disorder in the AlGaAs barrier can also cause scattering. It only affects the tail of the carrier wavefunction that penetrates the barrier and is thus also more prominent at higher densities.[38] Carriers in GaAs quantum wells sandwiched between two AlGaAs barriers are naturally affected more by interface roughness and alloy disorder scattering, which goes up as the well width decreases.[38]

Expressions for scattering rates due to background impurities in the GaAs channel and AlGaAs barrier, interface roughness, and surface charge (which are the primary contributors to scattering in undoped HEMTs) can be found in Ref. [68].

[§] The gates can be either metal (Al) or doped-GaAs.

2.1.4.2 Effect of unbiased and biased illumination

Low-temperature illumination of HEMT devices at above-bandgpap energies has a marked impact on their characteristics. While there have been several studies on the effect of illumination on modulation-doped HEMTs, only a handful have been conducted using induced HEMTS—some with doped GaAs Schottky gates,[62,63,76] (henceforth referred to as semiconductor-insulator-semiconductor[§] FETs or SISFETs) and others with MIS top gates (henceforth referred to as MISFETs)[44,68]—with conflicting reports. The present understanding is that illumination alters the disorder potential in induced devices by ionizing or neutralizing impurities; potential mechanisms are inferred via measurement of transport characteristics such as the inducing gate voltage threshold V_g^{thr}[¶] and the carrier density n and mobility μ. A known advantage of using induced HEMTs over modulation-doped HEMTs in this context is that device characteristics observed in the dark prior to illumination can be recovered in the former (and not the latter) by thermally cycling the device, i.e., warming up the device to room temperature, since this allows charges to overcome the energy barrier around impurities caused by lattice deformation.[76,68] This allows us to study the effect of illumination on undoped HEMTs and gain a further understanding of the influence of impurities on transport without permanently altering the device. The process of illuminating a device with a zero (non-zero) voltage bias on the inducing gates is called unbiased (biased) illumination.

With **unbiased illumination**, a buildup of positive or negative charge in the barrier[62,63,76], substrate[44] or at the surface[68], coupled with a change in carrier density in the 2DEG/2DHG, can shift the value of V_g^{thr} up[68] or down.[62,63,76] In SISFETs, surface charges are completely screened by the presence of the doped GaAs gate, so a change in surface potential has no effect. MISFETs on the other hand tend to have charge traps at the semiconductor-insulator interface that cannot be screened. The carrier mobility of the device is also affected by the shift in disorder potential. The mobility tends to increase for a given carrier density unless the device is a shallow MISFET with surface charge that induces scattering.[68] This increase in μ due to illumination is known as *persistent photoconductivity*—the changes persist until the device is thermally cycled.

The effects of **biased illumination** have so far been reported only in MISFETs.[44,68] The chosen insulator must not allow current leakage when under a bias, so SiO_2 is a good choice while polyimide is not.[68] Similar to unbiased illumination, biased illumination also

[§] Note that the insulator in this case is AlGaAs.

[¶] The 't' is dropped from the subscript of V_{tg}^{thr} to allow it to refer to both top and back gate thresholds.

shifts the n-V_g curve (without altering its slope) and the μ–n curve. Assuming the initial state of the device is set using an extended period of unbiased illumination (6 min)[68], illuminating the device with a positive or negative bias V_0 (for 1 min) shifts the n–V_g curve by V_0. Simultaneously, at a fixed value of n, μ increases when $V_0 > 0$ and decreases when $V_0 < 0$; these changes are greater in shallower devices, but regardless of channel depth, the shift in mobility saturates beyond a certain magnitude of V_0. Two possible mechanisms are involved: charging effects in the insulating oxide layer and ionization of surface states. Ref. [68] posits that the n–V_g curve is affected by the former and the μ–n curve by the latter. Changing surface charge densities would affect the scattering rate and thus the mobility, even more so in shallower devices. The shift in mobility saturates when all surface states have been ionized. Charging of defects in the insulator will not impact mobility since they are isolated from the 2DEG and the oxide dielectric constant is lower than that of AlGaAs. These charged oxide defects will, however, shift the n–V_g curve in either direction by populating/depopulating with electrons. Interestingly, the device can be reset to the initial state if subject to more unbiased illumination, but only when the device is ambipolar. In unipolar samples, the μ–n curve stays shifted if attempting to reverse the effects of biased illumination, implying a permanent change in the surface charge density. In the absence of p-type ohmic contacts, there is no way for the holes generated during photoexcitation of electron-hole pairs to be swept away, allowing them to recombine with photogenerated electrons. This leaves no electrons to re-neutralize the ionized surface states, causing the permanent shift in surface charge density. This in turn causes a small shift in the 'reset' n–V_g curve relative to the initial state.

Understanding the mechanisms behind unbiased and biased illumination is crucial to the development of quantum light sources based on lateral 2D p–n junctions, since these devices may be subject to self-illumination: the emitted light energy matches the bandgap of the semiconductor and can be easily re-absorbed, causing impurity charge densities to shift and alter carrier transport characteristics and the efficiency of photon emission.

2.2 Lateral planar light-emitting diodes, quantized charge pumps and single-photon sources in undoped GaAs/AlGaAs heterostructures

Modern conventional LEDs such as laser diodes are constructed by sandwiching an intrinsic direct bandgap[‖] semiconductor layer between heavily-doped p-type and n-type layers. By applying a forward bias across this three-dimensional (3D) vertical LED, electrons and holes are pumped into the intrinsic layer (also called the active region) where they recombine radiatively. To maximize the probability of light emission, the bandgap of the active region is smaller than the surrounding layers to create confinement. This means that carriers are forced to pass through high-bandgap material before reaching the active region where they can recombine. The carriers thus end up with a surplus of energy and need time to thermalize before recombining—this broadens the emission linewidth.[77] The architecture of vertical LEDs also prevents them from being integrated with lateral devices such as quantized charge pumps[78,79,80,81] that could yield high-frequency on-demand sources of single photons.

Lateral planar LEDs do not suffer from this issue—electrons (from the 2DEG) and holes (from the 2DHG) are directly injected into the intrinsic active region without passing through a higher bandgap material.[†] Charge mobility is high, as well as radiative recombination rates and quantum efficiency. Due to the small cross-sectional area of the 2D planar charge gases, these devices have a relatively low intrinsic capacitance. Mobile charges in 3D vertical LEDs are more spread out, screening the junction electric field. Since charges in 2D lateral LEDs are confined to a plane, the junction field is weakly screened, causing the depletion region to be extended and not fully depleted at the edges where the electrostatic potential slowly transitions to the n- or p-side. This in turn causes these devices to have a high reverse breakdown voltage relative to 3D vertical LEDs.[82] As in HEMTs, the charge carriers in lateral LEDs can either be due to modulation doping or gate induction. There are several examples of modulation-doped lateral planar LEDs in literature.[77,83,84,85,86,87] Normally, only one type of charge carrier can exist in a modulation-doped transistor; modulation-doped p–n junctions are realized by using selective doping or selective etch

[‖] the direct bandgap nature of III–V semiconductors makes them favourable for use in optoelectronic devices.
[†] this is because the n-type (2DEG), p-type (2DHG) and intrinsic regions are all in the same material layer and have the same bandgap.

techniques that are clever but greatly complicate the fabrication procedure. Emission linewidths from these LEDs are broadened due to dopant scattering,[86,88,87] making them a poor candidate for an electrically-driven single-photon source.

The first *dopant-free* gate-induced planar LED was realized in 2009.[89] Since then, only a handful of papers on this topic have been published,[90,91,92,23,28] with very few follow-up studies showing reproducibility.

The coplanar geometry of lateral planar LEDs allows them to be integrated with quantized charge pumps, potentially creating high-rate, on-demand, and efficient sources of single photons. A useful parameter to characterize a single-photon source is the second-order correlation function at zero time delay. The second-order correlation function is written as

$$g^{(2)}(\tau) = \frac{\langle n(t)n(t+\tau)\rangle}{\langle n(t)\rangle^2}, \tag{2.39}$$

where $n(t)$ is the number of emitted photons detected using a single-photon detector at time t, and τ is the time delay between detection events. $g^{(2)}(\tau)$ effectively gives us the probability of a photon detection event at time $(t+\tau)$ given that a photon has been detected at time t. At $\tau = 0$, Eqn. 2.39 simplifies to $g^{(2)}(0) = 1-(1/n)$. $g^{(2)}(0) < 1$ corresponds to photon antibunching which is a purely nonclassical phenomenon, while $g^{(2)}(0) < 0.5$ confirms that single photons are being emitted. For a near-ideal single-photon source, the value of $g^{(2)}(0)$ is very close to zero.

The two main types of quantized charge pumps in literature are (i) surface acoustic wave (SAW) generators,[78] and (ii) electrostatically-driven single-electron pumps that quantize charge using a gated dynamical quantum dot.[79,80,81] There have been several attempts over the last two decades to realize single photon emission using SAWs; in 2020, Hsiao et. al.[23] successfully fabricated and characterized single photon emissions from a dopant-free GaAs quantum well SAW device. Single-electron pumps (as well as SAWs) have long been used in metrology as a potential candidate for the standard definition of the SI unit of current, the Ampere. Gated single-electron pumps tend to be fabricated using n-type modulation-doped GaAs/AlGaAs because of ease of fabrication and operation. The only example using *undoped* GaAs/AlGaAs was published by us* in 2021 (Buonacorsi et. al., Ref. [24]).

The following sections cover the operation of lateral planar LEDs, SAWs and one-parameter single-electron pumps, and summarizes the progress of these devices in recent

* The author of this thesis did not personally contribute to this publication.

years.

2.2.1 Dopant-free lateral planar light-emitting diodes

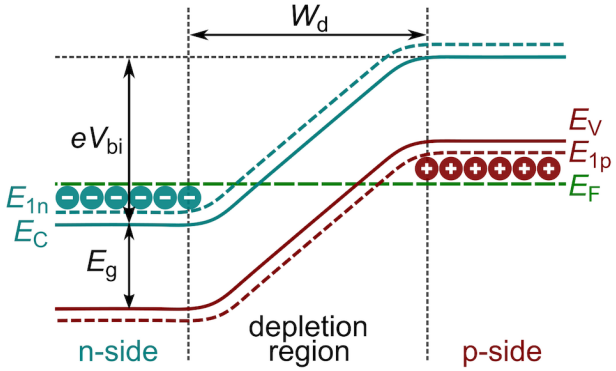

Figure 2.2: Schematic band structure of a lateral 2D p–n junction at zero forward bias. The n-side (2DEG), p-side (2DHG) and depletion region between the two are indicated. Due to weak screening of the junction field, the depletion region is extended and not fully depleted at the edges. The Fermi energy E_F is denoted by the flat dashed green line. The solid maroon and teal lines denote the valence and conduction band energies E_V and E_C respectively. The dashed maroon and teal lines denote the ground state energies of the holes (E_{1p}) and electrons (E_{1n}) respectively. Also indicated are the bandgap E_g and the energy corresponding to the built-in potential V_{bi}.

This section borrows from a complete analytical treatment of gate-induced lateral 2D p–n junctions found in Refs. [93, 94]. When a 2DEG and 2DHG are simultaneously induced adjacent to each other using two gates in an undoped heterostructure at cryogenic temperatures, a fraction of majority carriers from each side pass to the opposite side and neutralize, forming an intrinsic depletion region at the junction interface.[82] The resulting electric field between the n- and p-sides bends the energy band structure until a new state of equilibrium is reached. In this state, the Fermi level (with energy E_F) is constant, while the bent conduction and valence bands introduce a 'built-in' potential barrier eV_{bi}[**] for the electrons and holes (Fig. 2.2). The magnitude of the built-in potential varies with a parameter known as the 'overdrive gate voltage' V_g',

$$V_g' = V_g - \frac{1}{e}\left(\Phi_g - X_{sc} - \frac{E_g}{2}\right), \tag{2.40}$$

where V_g[‡] is the gate voltage magnitude on each inducing gate, Φ_g is the work function of

[**] e is the elementary charge

[‡] we assume for the sake of simplicity a symmetric junction where the gate voltage magnitude on each

the metal gate, X_{sc} is the semiconductor electron affinity, and E_g is the bandgap energy. $\Phi_g - X_{sc} - E_g/2$ is the potential corresponding to the flat-band configuration. V_{bi} varies linearly with V'_g for low values,

$$eV_{bi} = 2eV'_g = E_g + 2\left(eV_g + X_{sc} - \Phi_g\right); \tag{2.41}$$

above a certain threshold V'_{gth} (defined as $0.6E_g/(2e)$) this relationship becomes nonlinear—

$$eV_{bi} = E_g + 2k_BT\log\left\{\exp\left[\frac{(V'_g - V'_{gth})C_{ins}}{e\rho_{2D}k_BT}\right] - 1\right\}, \tag{2.42}$$

where C_{ins} is the insulator capacitance and ρ_{2D} is the 2D density of states at the band edge.

The width W_d of the 2D intrinsic depletion region can be tuned by changing the inducing gate voltage magnitude V_g on either side, the separation between the gates, and the thickness of the insulator in the case of MIS-type devices. Ref. [93] derives the expression for the depletion width of a gate-induced lateral 2D p–n junction from numerical simulations as

$$W_d = 0.6t_{ins}\left(2\frac{V_{bi}}{V'_g} + 1\right). \tag{2.43}$$

where t_{ins} is the insulator thickness. This tells us that the depletion width is linearly dependent on the insulator thickness and the ratio between the built-in potential and the gate voltage. For small gate separations $l_{gap} \ll W_d$, the two parameters are independent; this assumption holds for Eqn. 2.43. W_d increases linearly with l_{gap} for larger values. An analytical expression for the depletion width has also been derived (see Ref. [94] for details), which like Eqn. 2.43 shows a linear dependence on the insulator thickness, but **no** dependence on its dielectric constant, which is in contrast to doped devices. Note that in the case of heterostructure devices, t_{ins} will include the thicknesses of the heterostructure layers above the 2DEG/2DHG in addition to the insulator thickness.

Applying a potential difference V_{pn} ($> V_{bi}$) across the junction drives it out of equilibrium, resulting in a flow of current. As with conventional diodes, gated lateral 2D p–n junctions also display rectifying behaviour—the reverse bias current density is much smaller than that of the forward bias.[93] Also, the simulated ideality factor of this type of diode is close to two, implying that the current should be dominated by carrier recombination in the depletion region[§] as opposed to diffusion in the induced charge regions.[93] The

inducing gate is V_g but the polarities are opposite

[§] Note that we did not see this behaviour in our fabricated p–n junctions. Instead, light is mostly emitted

recombination current density exponentially increases with V_{pn} as[93]

$$J_R \approx \sqrt{\frac{\pi}{2}} \frac{k_B T n_i}{\tau F_0} \exp\left(\frac{eV_{pn}}{2k_B T}\right), \tag{2.44}$$

where n_i is the intrinsic carrier density of the semiconductor, τ is the carrier lifetime (assuming the electron and hole lifetimes are equal), and F_0 is the magnitude of the in-plane electric field at the point where the recombination rate is maximum; the two in the denominator of the exponential term is the ideality factor. F_0 itself increases with decreasing V_{pn} and increasing V_g. It follows that for a given V_{pn}, J_R decreases as the magnitude of V_g increases. Finally, when the gap between the two inducing gates increases, the depletion width W_d increases, in turn decreasing the field in the depletion region for a given V_{pn}—thus, F_0 reduces and J_R increases. Not that this equation assumes that the device is free of interface trapped charge, and that $eV_{pn} > k_B T$.

A brief summary of the differences between doped 3D vertical LEDs and undoped 2D lateral LEDs is listed below—

- 2D LEDs have a **coplanar geometry** that allows them to be integrated with other types of devices such as lateral quantized charge pumps;
- unlike 3D junctions, there is **direct injection** of charge carriers into the active region without passing through higher bandgap materials in 2D LEDs, **reducing carrier transit times**;
- since charges are confined to a plane, the junction electric field is weakly screened in 2D LEDs relative to 3D—this **extends the width of the depletion region**, resulting in a gentle transition of the potential at the edges causing them to not be fully depleted;
- **charge scattering** is high in doped 3D vertical LEDs since dopant impurities are present everywhere including the site of recombination, but undoped 2D LEDs have **higher carrier mobilities** since there is very low probability of scattering off of impurities;
- the presence of a quantum well in the 2D LED increases the rate of radiative recombination and **quantum efficiency**;
- 2D LEDs have a **smaller capacitance** than 3D LEDs due to the small cross-sectional thickness, favoring them for use in devices operating at **high-frequencies** (RF).

from under the p-side topgate; see Chapters 4 and 5.

2.2.1.1 Summary of literature

The first realization of a dopant-free lateral 2D p–n junction was in 2009 by De Simoni et. al.[89] Dai et. al. were the next to do so in 2013,[90] with a follow-up publication in 2014.[91] The most recent work (excluding our own) on dopant-free junctions is found in two related papers from 2019 and 2020 by Chung et. al.[92] and Hsiao et. al.[23] respectively; the latter corresponds to a SAW-driven single-photon source whose results are discussed in Section 2.2.2. Results from the remaining publications are compared in this section. The results from *our* dopant-free junction (detailed in Chapter 3) were published in 2023,[28] and are also included here for the sake of comparison.

	De Simoni '09	**Dai '13**	**Dai '14**	**Chung '19**	**Tian '23**
p–n current driver	SAW	voltage	voltage	SAW	voltage
***w* (nm)**	20	20	20	15	15
***d* (nm)**	40	303	303	110	90
n-type ohmics	Ni/AuGe/Au	Ni/Au/Ge/Ni	Ni/Au/Ge/Ni	Ni/Au/Ge/Ni/Au	Ni/AuGe/Ni
p-type ohmics	Au/Zn/Au	Pd/AuZn	Pd/AuZn	AuBe	AuBe
gate	Cr/Au	Ti/Au	Ti/Au	Ti/Au	Ti/Au, Ti
insulator	PMMA	polyimide	polyimide	polyimide	SiO_2
λ_{EL}, E_{EL} (nm, eV)	–	811, 1.529	815.4, 1.5207	809, 1.5326	808, 1.5344

Table 2.2: A comparison of all the existing dopant-free lateral 2D p–n junctions in literature. w is the RQW width, d is the depth of the RQW from the surface, and λ_{EL} and E_{EL} are the wavelength and energy of the quantum well EL emission peak.

These devices were all realized in GaAs/AlGaAs heterostructures with RQWs. The p–n current in the junctions from De Simoni '09 and Chung '19 are SAW-driven, while the rest are driven by a voltage bias. The width w of the RQWs and their depth d from the wafer surface are shown in Table 2.2. Ni, Au and Ge are collectively the standard n-type ohmic contact materials, while AuZn or AuBe serve as p-type materials. The EL emission wavelengths for these sources are all similar; there are however some intricacies that will be covered below. The results from De Simoni '09 did not include spectrally-resolved EL data. Chung '19 include one spectral plot but this corresponds to using voltage and not SAWs as the p-n current driver.

The gate structures for these devices are varied but share some features. All devices have a insulator-separated metallic topgate to induce a 2DEG/2DHG. De Simoni '09 adds two lateral (side) gates to constrict the current channel. Dai '14 includes additional etch-recessed surface gates closer to the junction for greater potential resolution when

controlling charge carriers. Chung ’19 uses both surface gates *and* two side gates. Tian ’23 includes transparent thin Ti topgates near the junction for more efficient light collection, which was a suggestion in Dai ’14.

Comparing the SAW devices, both use a small source-drain bias (less than the bandgap) and apply the SAW potential over this DC bias to drive current. Both use lateral gates to constrict the electron channel to one dimension. The observed EL spot size at the junction was 700 nm for De Simoni ’09 and 6–10 µm for Chung ’19. Using just a source-drain voltage of 2.5 V as the current driver, Chung et. al. observed stray EL along the length of a surface gate for $w = 15$ nm, which they attribute to electrons escaping the junction due to the high bias voltage. This stray EL was observed in our devices as well; the results presented in Chapter 5 offer solutions to this problem. The corresponding EL spectrum showed one major peak at 809 nm (1.5326 eV), and a smaller peak at a higher energy.

Next, we compare the voltage-driven sources. Normally, the magnitude of the threshold voltage for inducing 2DEGs is smaller than that of 2DHGs, as seen in the supplementary of Tian ’23. The opposite trend was observed in Dai ’13 and ’14—this is attributed to surface state pinning at the GaAs/insulator polyimide interface, i.e., negative charge accumulates at this interface and screens the n-side topgate. In relation to this, the charging effects of unbiased and biased illumination on the threshold voltages are alluded to in Dai ’13, which have an influence on our devices as well. For standard DC operation, Tian ’23 reports EL instability and fast quenching. Dai ’13 claims stable EL, but this requires very large source-drain currents $\geqslant 100$ µA compared to a few µA in Tian ’23. Two ways to solve this problem of EL quenching are detailed in Chapters 3 and 5.

The EL spot is observed at and around the junction interface in Dai ’13, whereas most of the EL in Tian ’23 arises from under the n-side topgate. Although the well widths w for Dai ’13 and ’14 are both 20 nm, the wavelengths of their peaks differ significantly, by 4.4 nm (8.3 meV). It may instead be possible that the EL (and photoluminescence (PL)–photoluminescence) peaks from Dai ’14 are due to defect states on the etched regions of the surface gate recess. The process of etching the recess also exposes unpassivated AlGaAs, which is prone to reacting and deteriorating the integrity of the surface. Until more samples are made replicating these spectra, this gate architecture remains untenable. On the other hand, both w and λ_{EL} match closely for Chung ’19 and Tian ’23. In addition to the main peak, a lower energy charged exciton peak is reported in Tian ’23. The details of this paper and its supplementary information are compiled in Chapter 3.

2.2.2 Quantized charge pumps

QCPs work by modulating the current I_{sd} along a quasi-one-dimensional channel between a source and drain such that $I_{sd} = nef$, where f is the pump frequency, e is the elementary charge, and n is an integer. This modulation hinges on the presence of tunnel potential barriers that allow for the shuttling of charge via the Coulomb blockade effect down to the single-electron level. Changing the voltage parameters of these QCP tunnel barriers can change the value of n, leading to current quantization. In practical implementations, the value of n is more well-defined in low conductance regimes to suppress charge fluctuations. The trade-off is that the pump frequency f should not be compromised due to the lower current.[79]

QCPs can be classified as turnstiles[95,96] or single-parameter pumps.[24,97,79] By operating at frequencies lower than the timescale needed for charges to settle, turnstile pumps are always in a state of equilibrium. To allow for this equilibration, the quantum dot formed by the tunnel barriers of turnstile pumps needs to be as open as possible, whereas the opposite it true for one-parameter pumps. One-parameter QCPs are so-called because they work by fixing the exit barrier potential while dynamically tuning just the entrance barrier. Both SAWs and gate-defined pumps can fall into either of these categories, although the nomenclature varies in literature.

2.2.2.1 SAW devices

Surface acoustic waves at high frequencies are supported in Gallium Arsenide due to its piezoelectric properties.[81,79] These SAWs are generated from electric signals using an interdigitated transducer (IDT), a metallic structure deposited on the semiconductor surface composed of several interleaving finger electrodes. SAWs are essentially vibrations in the crystal lattice that decay going into the bulk; they are confined to two dimensions at the surface and can thus travel over longer distances. Applying an RF signal to the IDT induces a train of SAWs; the strain caused by these SAWs in the crystal lattice creates an electrostatic potential trap in the semiconductor that propagates with the SAW. If the IDT is adjacent to a charge reservoir (source), and a sub-bandgap source-drain bias is applied, the SAW potential can quantize the current and transport individual or a few charges at a time. The period of the finger electrodes in the IDT influences the SAW frequency.

Foden et. al.[98] were the first to propose a single-photon source using SAWs, which were realized in 2020 by Hsiao et. al.[23]. Their device is fabricated using a GaAs/AlGaAs

heterostructure with a 15 nm wide GaAs RQW at a depth of 110 nm from the surface. A 1.2 µm wide 1D channel guiding the SAWs is etched into the substrate. EL spectral measurements from SAW transport show a single peak with energy 1.531 eV (that matches the well width) and a linewidth of ~ 1 meV. The carrier lifetime from time-resolved EL measurements is 94 ps; this low value and the resulting low quantum efficiency is attributed to non-radiative recombination at surface states.

From second-order correlation measurements, a value of $g^{(2)}(0) = 0.39 \pm 0.05$ is reported. However, this value is obtained after post-selecting 30% of the coincidences. The need for post-selection is due to the instability of the quantized current that is reported to fluctuate despite the presence of a PID control loop. For the raw data, $g^{(2)}(0) = 0.63 \pm 0.03$, which still indicates nonclassical photon antibunching.

2.2.2.2 One-parameter single-electron pumps

One-parameter single electron pumps work by using two electrical gates—with one of them tunable—to generate the barriers of a dynamic quantum dot. The tunable gate is referred to as the entrance gate (potential V_{ent}) since it opens the dot to the charge reservoir source, while the fixed-barrier gate is termed the exit gate (potential V_{exit}). The two barrier gates are placed perpendicular to the channel direction. The channel is quasi-one-dimensional and may be defined by ion bombardment, etching, or gating. An RF potential V_{RF} is applied over a base DC bias V_{DC} to tune the entrance gate, such that $V_{\text{ent}} = V_{\text{DC}} + V_{\text{RF}}\sin(2\pi f t)$, where f is the pump frequency and t is time.

A schematic of the charge pumping mechanism is shown in Fig. 2.3 (adapted from Ref. [24]). Within one RF cycle, quantized charge pumping can be broken down into three stages—loading, capture and ejection. In the loading stage, V_{ent} dips below the Fermi level E_{F}, and a large number of electrons *load* into the dot. V_{ent} is then raised, and as this happens, most electrons back-tunnel into the charge reservoir, with higher energy electrons tunneling at a faster rate ($\Gamma_{i+1} > \Gamma_i$). The remaining few electrons are *captured* in the dot as V_{ent} raises further. Next, as V_{ent} increases past V_{exit}, the dot is unable to confine electrons anymore and they are *ejected* to the drain. Finally, V_{ent} lowers for the cycle to start once again.

Measuring the source-drain current I_{sd} for increasing values of V_{exit} yields current quantization plateaus $I_{\text{sd}} = nef$, where n is the number of pumped electrons—a larger V_{exit} allows more electrons to be captured in the dot per RF cycle. By fitting the I_{sd}–V_{exit}

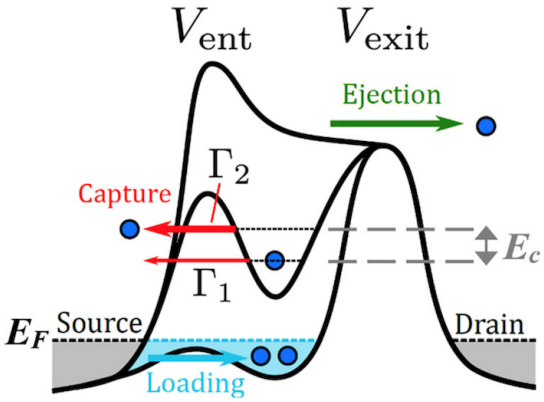

Figure 2.3: Potential energy diagram showing the quantized charge pumping mechanism in a one-parameter single electron pump. V_{ent} and V_{exit} are the voltages on the entrance and exit gates of the dynamic quantum dot. E_F and E_c refer to the Fermi level and maximum charging level of the dot. Γ_i is the back-tunneling rate of the i^{th} captured electron. The $i = 2$ electron has a higher energy and back-tunneling rate than the $i = 1$ electron. The pump mechanism consists of three stages—loading, capture, and ejection, described in the text (adapted from Ref. [24]).

plot to the universal decay cascade model,[99] a fitting parameter δ may be extracted. This parameter is used as a figure of merit—a larger value of δ implies better current quantization, i.e. flatter plateaus and steeper transitions between plateaus. In practice, the value of δ may depend on a lot of external factors, including temperature, pump frequency, external magnetic field, gate voltage configurations, and the waveform of the RF signal. Although δ as a figure of merit is abstract, it can be related to the uncertainty or error in single electron pumping using[79]

$$P_{error} = P_0 + P_2 = 1 - P_1 \approx 2\delta \exp(-\delta), \tag{2.45}$$

where P_n is the probability of capturing n electrons in the dynamic quantum dot per RF cycle. P_1 is maximized when P_0 and P_2 are equal (Fig. 2.4). P_{error} sets a baseline for the second order correlation function $g^{(2)}(0)$. In fact, since the probability of null-photon emission P_0 does not contribute to single photon purity, the baseline for $g^{(2)}(0)$ is half the uncertainty, i.e. $P_{error}/2$.

Results from several one-parameter single electron pumps in dopant-free GaAs/AlGaAs fabricated and measured by our team were published in Ref. [24]. All other experimental conditions being similar, these pumps have similar values of δ compared to other pumps in literature. The authors estimated a theoretical requirement of $8 \lesssim \delta \lesssim 10$ to obtain a *lower bound* to the value of $g^{(2)}(0)$ between 0.0004 and 0.003 in a single-photon source

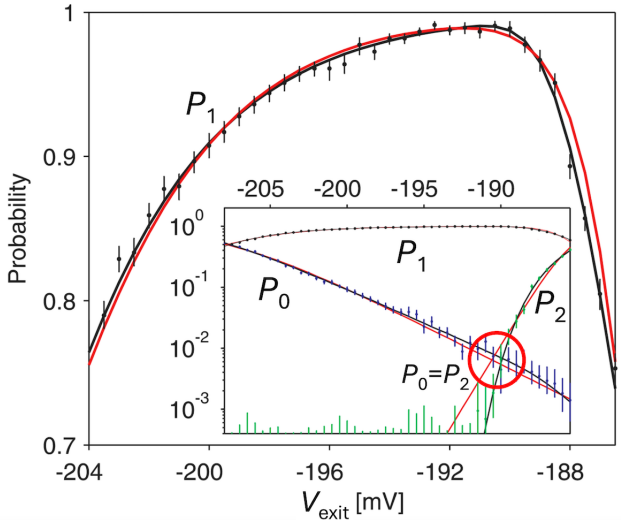

Figure 2.4: Probabilities of capturing 0, 1 and 2 electrons (P_0, P_1 and P_2) in a dynamic quantum dot as a function of exit gate barrier potential V_{exit}. P_1 is maximum (in this case $\sim$98%) when V_{exit} is set to a value where $P_0 = P_2$, indicated by the red circle (adapted from Ref. [100]).

that utilizes these pumps. By plugging the various estimated values of δ into Eqn. 2.45, their uncertainties can be calculated. $\delta = 12.9$ for operation at $f = 850$ MHz, and thus $P_{error} = 64.4$ ppm, while $\delta = 17.8$ for operation at $f = 500$ MHz, giving us a P_{error} of just 0.7 ppm ($P_1 = 99.99993\%$ for the latter). The corresponding lower bounds for $g^{(2)}(0)$ are extremely small—32.2 ppm for $f = 850$ MHz and 0.35 ppm for $f = 500$ MHz. This indicates that the pump error rates will not be a contributing factor to the degradation of single-photon purity. Optimistically, our single-photon emitter created by integrating these quantized charge pumps with lateral p–n junctions could possess $g^{(2)}(0)$ values that compete with the current state-of-the-art.

As mentioned in Chapter 1, for $n = 2$, pumping of a spin singlet pair of electrons is possible for a certain tuning of V_{ent} and V_{exit} when the RF waveform on the entrance gate is pulsed.[25] By using an Arbitrary Waveform Generator (AWG) to generate a pulsed RF voltage signal, pumping of entangled electron pairs may be possible, and in turn we could theoretically generate polarization entangled pairs of photons.

3. The Set-Reset protocol for extending the lifetime of electroluminescence

A major obstacle to the integration of GaAs/AlGaAs heterostructure-based dopant-free lateral p–n junctions with quantized charge pumps and other components has been the unwanted accumulation of charge at the p–n junction gap that causes a rapid decay or *quenching* in the EL, either via enhanced non-radiative recombination or an inhibition of p–n current. Typically, samples need to frequently be thermally cycled, i.e. warmed up to room temperature and left to thermalize to dissipate this built-up charge in order to restore electrical properties and brightness in a subsequent cooldown.[23,87]

This chapter discusses a novel technique that implements a sequence of gate voltages *in-situ* at low temperature to completely restore EL in dopant-free GaAs/AlGaAs rectangular quantum wells without the need for thermal cycling. We recorded the narrowest EL linewidths observed to date in lateral p–n junctions, whether doped or undoped. Well-defined EL emission peaks are visible up to a temperature of $T = 85\,\mathrm{K}$, which we unambiguously identify as the ground state of neutral free excitons (labeled X^0 for heavy holes and LH for light holes), and the ground state of a heavy hole trion. In all samples, the free exciton emission energies for both PL and EL are found to be nearly identical, with a symmetric lineshape. Using pulsed EL, we recorded an exciton lifetime of 237 ps, much shorter than the lifetime of 419 ps obtained by pulsed PL. The implemented gate voltage sequence, which we call the Set-Reset sequence, is a significant step towards realizing viable quantum light sources based on dopant-free 2DEGs and 2DHGs.[101,24]

3.1 Experimental methods

3.1.1 Sample fabrication

Data from five dopant-free lateral p–n junctions (labelled A, B, C, D, and E) is reported in this chapter. These p–n junctions along with control Hall bars (dopant-free ambipolar induced HEMTs, see Section 2.1.3 for a review of literature) were fabricated using two quantum well heterostructures, wafers G0375 (samples A–D) and G0569 (sample E), and oriented along the high mobility crystal direction $[1\bar{1}0]$. The wafers were grown by MBE on semi-insulating (SI) GaAs (100) substrates. Wafer G0375 (Fig. 3.1 (a)) has the following layer sequence (starting from the substrate): a 200 nm GaAs buffer, a 20-period smoothing superlattice (SL) composed of a 2.5 nm GaAs layer and 2.5 nm $Al_{0.3}Ga_{0.7}As$ layer, a 500 nm $Al_{0.3}Ga_{0.7}As$ bottom barrier, a 15 nm wide GaAs quantum well, a 80 nm $Al_{0.3}Ga_{0.7}As$ top barrier, and a 10 nm GaAs cap layer. Wafer G0569 is nominally identical to G0375 except that the 20-period smoothing superlattice buffer was replaced by a 500 nm LT-GaAs buffer followed by a 1000 nm GaAs buffer. There was no intentional doping anywhere in either heterostructure.

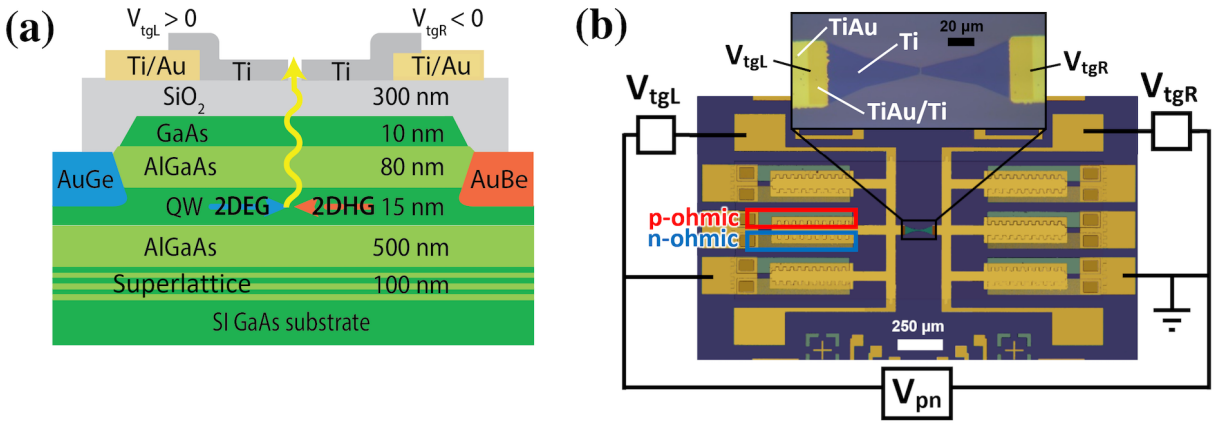

Figure 3.1: (a) Schematic cross-sectional diagram of our dopant-free lateral p–n junctions, including the epitaxial layers of the quantum well (QW) heterostructure G0375 (samples A–D). (b) Composite top-view optical image of one of our dopant-free lateral p–n junctions, along with the electrical circuit used in all low-frequency measurements. Both sides of the junction have ambipolar ohmic contacts, allowing a 2DEG or a 2DHG to form on either side. V_{tgL} and V_{tgR} are the topgate voltages on the left and right sides respectively. V_{pn} is the forward bias, used to drive current across the p–n junction. (INSET) The black labels V_{tgL} and V_{tgR} identify the left and right topgates in the vicinity of the p–n junction located at the center of the photograph. The white labels identify the topgate materials (opaque TiAu and semi-transparent Ti). Their overlap region is labeled TiAu/Ti.

The fabrication of unipolar/ambipolar Hall bars on dopant-free wafers is described in Refs. [57, 59, 102, 103, 51]. A step-by-step recipe for our lateral p–n junctions is also listed in Appendix C, and images from pattern mask files with annotated dimensions are included in Appendix B. Briefly, after a *mesa* etch, Ni/AuGe/Ni n-type recessed ohmic contacts and AuBe p-type recessed ohmic contacts were deposited and annealed at 450 °C for 180 s and at 520 °C for 180 s, respectively. A 300 nm thick SiO_2 insulator layer was deposited by plasma-enhanced chemical vapor deposition (PECVD). Above the SiO_2 insulator layer, a TiAu topgate covers the entire surface of the 2DEG or 2DHG (overlapping the ohmic contacts). Near the p–n junction, the topgate is composed of a single 5 nm thin semi-transparent Ti layer ($\sim$ 70% transmission) in samples A–D and composed of a single 30 nm thin semi-transparent indium-tin-oxide (ITO) layer ($\sim$ 85% transmission) for sample E. The topgate gap is the distance between the left topgate (V_{tgL}) and right topgate (V_{tgR}), and is also the distance between the p-type and n-type regions. The topgate gap varies from 200 nm to 2000 nm in samples A–E (Table 3.1).

Sample	Wafer	TG material	TG gap (µm)
A	G0375	Ti	0.2
B	G0375	Ti	0.4
C	G0375	Ti	1.2
D	G0375	Ti	1.2
E	G0569	ITO	2.0

Table 3.1: Wafer IDs, topgate material, and topgate gaps for all samples. The topgate gap is the gap between the p-type and n-type regions, i.e., the distance separating the V_{tgL} and V_{tgR} topgates in Fig. 3.1 (a).

3.1.2 Optical and electrical characterization

All spectra were acquired with a spectrometer grating with a groove density of 1800 lines/mm, except for Fig. 3.5 (a) (150 lines/mm). Devices were cooled down either to $T = 3$ K in an Oxford Instruments OptistatDry BLV closed-cycle cryostat or to $T = 1.6$ K in an attocube attoDRY2100 closed-cycle cryostat, both with in-house customized DC and RF electrical feedthroughs. Unless specified otherwise, continuous-wave PL was generated from photoexcitation with a Thorlabs Stabilized Red HeNe Laser (632.8 nm) at 1 mW optical output power. Pulsed photoexcitation for time-resolved photoluminescence was provided by a Coherent Mira900 Ti:Sapphire laser operating at 800 nm. The electrical circuit for all the low-frequency EL measurements is shown in Fig. 3.1 (b).

3.2 Self-consistent band structure simulations

Fig. 3.2 shows the calculated band structures and wavefunction profiles in the MBE growth direction of a dopant-free GaAs/AlGaAs quantum well using nextnano®, a commercial Schrödinger-Poisson solver.[104,105†] As-grown, the wafer is not conductive—a gated

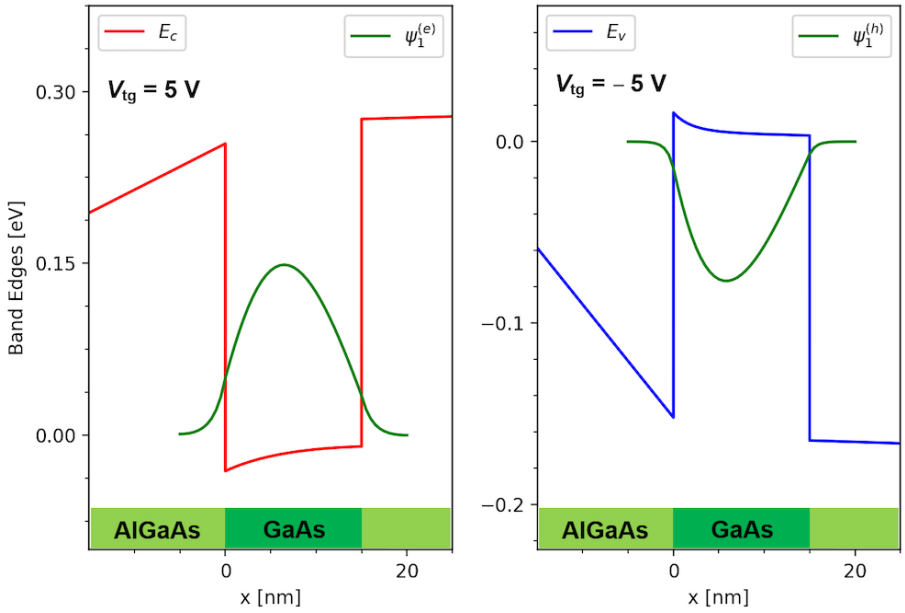

Figure 3.2: Band structure simulations of an ambipolar dopant-free quantum well heterostructure for: (a) a 2DEG wavefunction with $V_{tg} = +5\,\text{V}$, and (b) a 2DHG wavefunction with $V_{tg} = -5\,\text{V}$. The GaAs/AlGaAs quantum well is represented at the bottom of the panels. E_c is the conduction band edge, E_v is the valence band edge, and V_{tg} is the topgate voltage.

field-effect transistor (FET) must be fabricated. As seen in Fig. 3.3, such a FET does not conduct at a topgate voltage of $V_{tg} = 0\,\text{V}$, because the band structure along the growth direction is essentially flat. At $V_{tg} = +5\,\text{V}$ ($-5\,\text{V}$), the lowest 2D subband of the GaAs quantum well is populated and a 2DEG (2DHG) has formed.

3.3 Transport characterization, mobility and density

Fig. 3.3 shows the gating and mobility characteristics of wafers G0375 and G0569. In all cases, the electron/hole density (n2D/p2D) versus topgate voltage (V_{tg}) relation is linear and reproducible, with no time drift or voltage hysteresis [Figs. 3.3 (a, b, c, d)]. Typical mobilities for both wafers are (3–6)$\times 10^5$ cm^{2}V^{-1}s^{-1} for 2DEGs and (1.7–3.0)$\times 10^5$ cm^{2}V^{-1}s^{-1} for 2DHGs [Figs. 3.3 (e, f)]. The electron mobilities increase with rising carrier densities because the 2DEG is more efficiently screened from impurities located in and around the charge plane. The electron mobilities in general are relatively low compared to maximum values achieved in dopant-free GaAs 2DEGs,[68,92,38] because their quantum well width is too narrow (only 15 nm) to maximize electron mobility.[38] Hole mobilities are consistent with those achieved in other dopant-free narrow quantum well heterostructures.[92,38] In

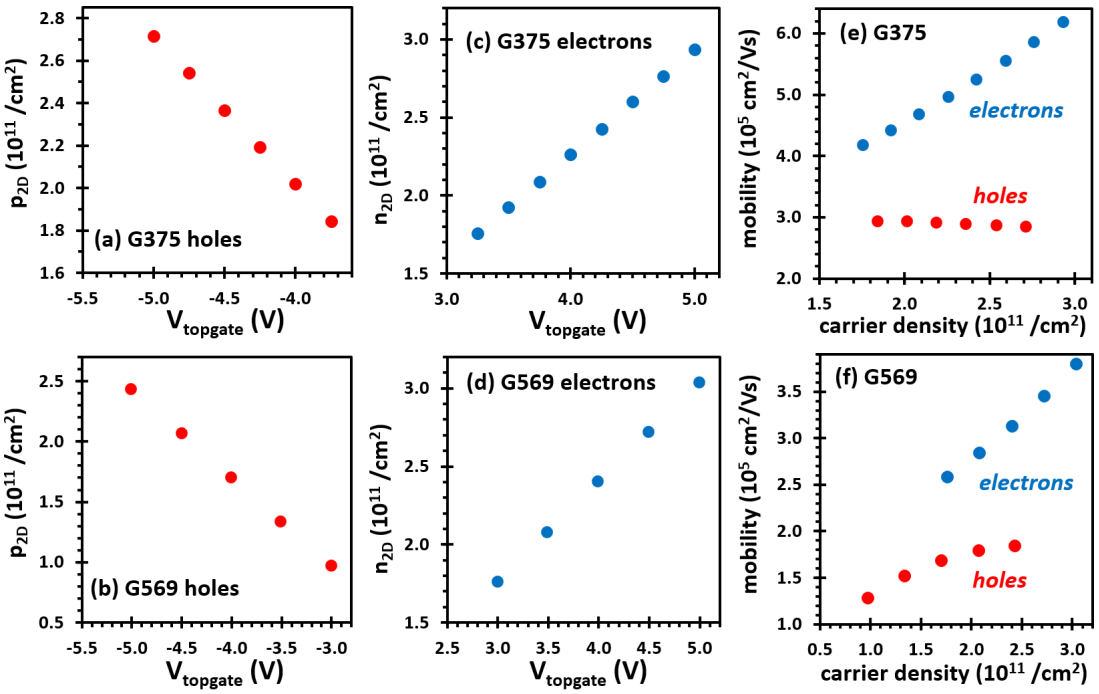

Figure 3.3: All four-terminal measurements shown above were taken at $T = 1.5$ K on dedicated gated Hall bars. Hole density (p_{2D}) versus topgate voltage V_{tg} for wafer: (a) G0375 and (b) G0569. Electron density (n_{2D}) versus V_{tg} for wafer: (c) G0375 and (d) G0569. Electron and hole mobilities versus carrier density for wafer: (e) G0375 and (f) G0569.

† https://www.nextnano.de

both G0375 and G0569, the electron mobility exceeds the hole mobility because of the difference in effective mass between electrons ($m_e^* = 0.067m_0$) and holes ($m_h^* = 0.35m_0$; m_0 is the electron rest mass). Because of their smaller size, holes are in general more susceptible than electrons to the GaAs/AlGaAs interface roughness scattering mechanism (see Section 2.1.4.1), and thus hole mobility saturates at a much lower carrier density than it does in electrons. In G0375, the hole mobility has already peaked for the density used in the experiments described in the rest of this chapter, whereas it is just reaching its peak in wafer G0569.

3.4 Ambipolar diode I–V traces

Due to their ambipolar functionality, our dopant-free lateral p–n junctions can be operated in the PN, NP, NN, or PP configurations. When V_{pn}, V_{tgL}, and V_{tgR} are kept

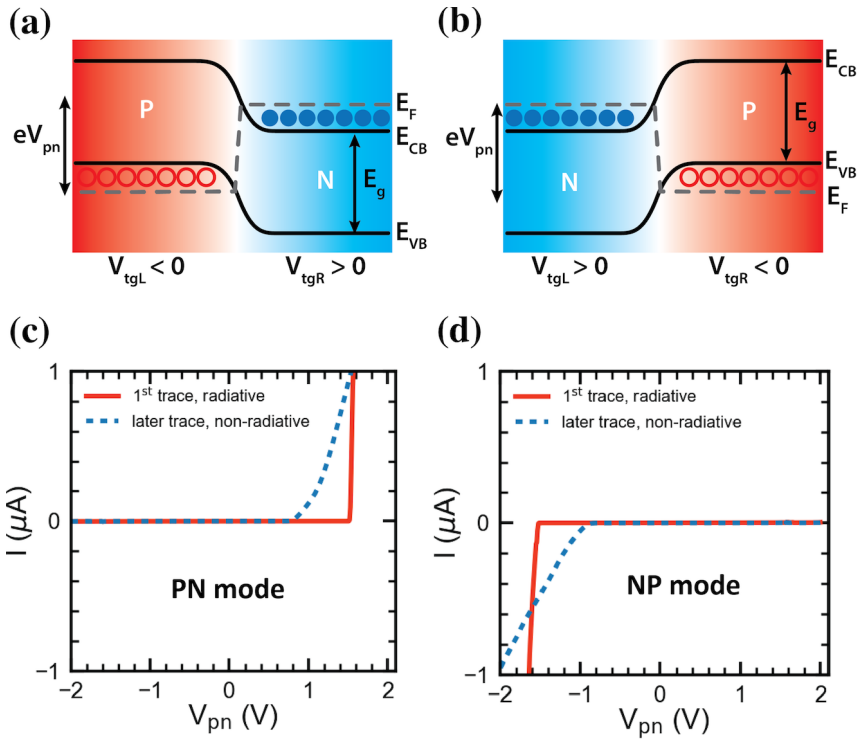

Figure 3.4: Band structure schematic across the p–n junction in the quantum well plane, when the device is operated in: (a) PN mode and (b) NP mode; filled blue circles represent electrons in a 2DEG, and empty red circles represent holes in a 2DHG. Diode current when sample C is operated in: (c) PN mode with $V_{\mathrm{tgL}} = -5\,\mathrm{V}$ and $V_{\mathrm{tgR}} = +5\,\mathrm{V}$, and (d) NP mode with $V_{\mathrm{tgL}} = +5\,\mathrm{V}$ and $V_{\mathrm{tgR}} = -5\,\mathrm{V}$.

constant, the device is in *DC mode*. EL occurs only in the *PN mode* ($V_{tgL} < 0$ and $V_{tgR} > 0$) or in the *NP mode* ($V_{tgL} > 0$ and $V_{tgR} < 0$). Figs. 3.4 (a, b) show schematic band structures of a device operated in the PN and NP modes respectively.* Fig. 3.4 (c) demonstrates the measured diode behavior when the lateral p–n junction is operated in PN mode (red solid trace). Current only flows when $V_{pn} > +1.5$ V in forward bias, and no current flows in reverse bias (i.e., $V_{pn} < 0$). The diode turn-on threshold is at the expected value for the GaAs bandgap (~ 1.5 eV). The ambipolar device behaves identically when operated in the NP mode [Fig. 3.4 (d)]. However, all samples showed strong hysteretic behavior after the first V_{pn} sweep—each subsequent sweep had a different turn-on V_{pn} bias and diode ideality factor. The blue dashed lines in Figs. 3.4 (c,d) are examples of such non-reproducible sweeps. Most importantly, radiative electron-hole recombination only occurred during the *first* V_{pn} sweep. Subsequent V_{pn} sweeps usually did not produce any light emission, unless either V_{pn} or V_{tg} (we use V_{tg} to refer to either V_{tgR} or V_{tgL} or both) were increased beyond values used in previous sweeps. After a thermal cycle to room temperature and back down to cryogenic temperatures, device characteristics are fully restored—red traces in Figs. 3.4 (c, d), with the associated light emission.

3.5 The Set-Reset sequence

Operating one of our dopant-free lateral p–n junctions in the PN or NP mode results in EL emission [Fig. 3.5 (a)]. Fig. 3.5 (b) illustrates the principle problem in dopant-free lateral p–n junctions—EL decays with time and vanishes within seconds. This quenching of

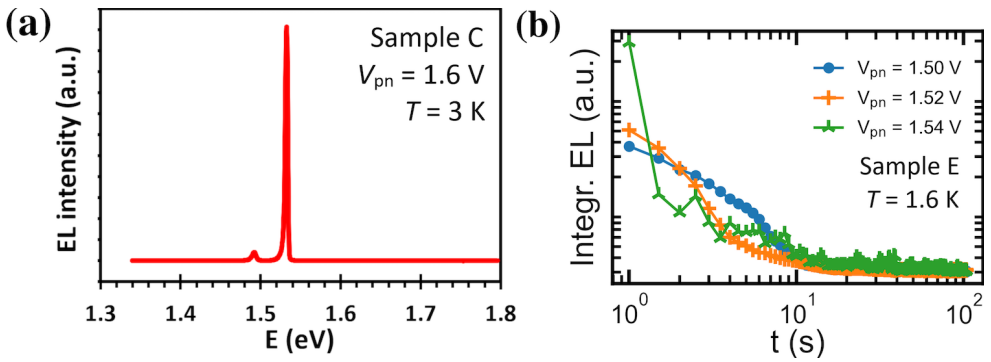

Figure 3.5: (a) Typical EL spectrum. (b) Decaying EL of a device in DC mode (see text).

* in Chapters 4 and 5, PN and NP are each further divided into two configurations based on whether the ground reference is on the left or right side of the device

EL is almost always accompanied by a similar quenching of the p–n current. Significantly, with higher forward bias V_{pn} (and hence with higher initial p–n currents), light emission is suppressed more quickly. This is indicative of charging effects, either enhancing non-radiative electron-hole recombination or suppressing current altogether. Light emission can only be recovered in a subsequent cooldown if quenched samples are warmed up to room temperature and electrically grounded for several hours.

As an alternative to a full thermal cycle, applying our 'Set-Reset' voltage sequence to both V_{tgL} and V_{tgR} topgates can completely reset a dopant-free lateral p–n junction in-situ at low temperatures, such that light emission is fully recovered in the same cooldown. The Set-Reset sequence involves alternating the polarities of V_{tgL} and V_{tgR}, while keeping V_{pn} fixed. The periodicity of the voltage sequence is determined by the Set-Reset frequency f_{SR}. In effect, the device alternates between PN mode and NP mode. For the reset to be most effective, (i) the magnitude of the topgate voltages must be large enough to alternately induce a 2DEG and 2DHG on each side of the p–n junction, and (ii) the voltage sequence must contain many cycles (50–500), where each cycle switches the topgate voltage polarities back and forth once. Note that alternating the polarity of V_{pn} while holding V_{tgL} and V_{tgR} constant does *not* reset a device.

After resetting, a device can degrade once again. Instead of applying the Set-Reset sequence before or after a set of measurements, one can continuously apply the Set-Reset voltage sequence with a fixed $V_{pn} > 1.52\,\mathrm{V}$ (i.e., the bandgap of bulk GaAs) *during* optical data acquisition. In this configuration, the Set-Reset sequence modulates the on/off states of the p–n junction by switching between forward bias ('set') and reverse bias ('reset') without changing V_{pn} [see inset of Fig. 3.6 (a)]. We call this operating regime the **Set-Reset mode**. Fig. 3.6 (a) shows a typical diode I–V trace when a device is operated in this mode. The measurement is very noisy because 2DEGs and 2DHGs continuously form and dissolve on both sides of the p–n junction, causing currents to flow in/out to (de)populate the 2DEG/2DHG. Overall however, the diode turn-on remains at the correct threshold, $\sim 1.5\,\mathrm{V}$ for GaAs.

Fig. 3.6 (b) illustrates the dramatic difference between the DC and Set-Reset modes. In DC mode, EL emission disappears very rapidly ($< 10\,\mathrm{s}$). In stark contrast, the Set-Reset mode yields an EL intensity that does not decay over at least $10^4\,\mathrm{s}$. In fact, it can remain bright for at least 48 h, the longest period over which EL intensity was continuously tracked. Crucially, optical characteristics are reproducible for a given set of experimental parameters.

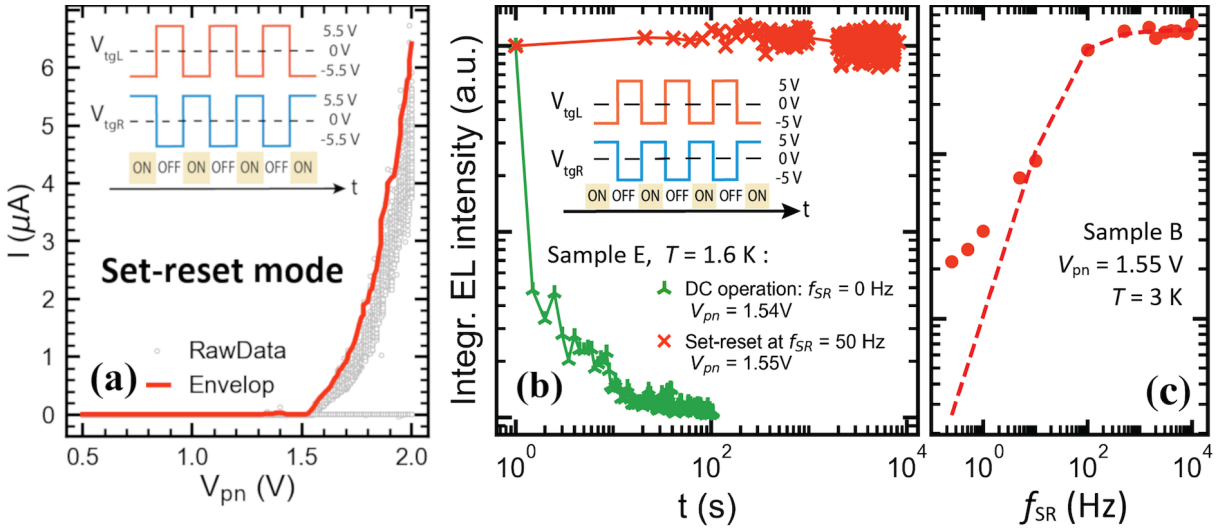

Figure 3.6: (a) (INSET) Diagram of the Set-Reset voltage sequence for topgates with time; V_{pn} is constant. If $V_{pn} > +1.5\,\mathrm{V}$, then the diode switches between ON/OFF states, as indicated by the highlighted labels. (a) (MAIN) Raw diode I–V curve in Set-Reset mode. The grey circles are the raw data, twenty data points for each value of forward bias V_{pn}. Current is measured for both ON and OFF cycles. The red line is the highest current at a given V_{pn} (the 'envelop' of the dataset). Our instrument undersampled the data: measurements were performed below the Nyquist frequency (with respect to the set-reset frequency f), and suffered from a long RC time constant (exceeding $1/f$). We believe that even the envelop current is an under-estimate of the true p–n current. (b) (INSET) Diagram of the Set-Reset voltage sequence for topgates with time; V_{pn} is constant. (b) (MAIN) EL in DC mode (green triangles) and in Set-Reset mode (red crosses). (c) EL (red circles) as a function of f_{SR}. The dashed line is a fit to Eqn. (3.2).

As f_{SR} increases from 0.25 Hz to 500 Hz, Fig. 3.6 (c) shows EL becomes brighter—the average intensity during the light emitting portion ('set') of a single set-reset cycle increases as the frequency becomes larger. Assuming emission intensity I_{EL} decays as $I_{EL}(t) = I_0\, e^{-t/\tau_d}$, where I_0 is the EL intensity at time $t = 0$ and τ_d is the EL decay's mean lifetime (or half-life $\tau_d \ln 2$), the integrated intensity is

$$I_\Sigma = \frac{\Delta t}{T_{SR}} \int_0^{T_{SR}} I_{EL}(t)\, dt, \tag{3.1}$$

where Δt is the data acquisition integration time, T_{SR} is the period of a single Set-Reset cycle ($T_{SR} = 1/f_{SR}$), and the condition $T_{SR} < \Delta t$ is met. Performing the integral in Eqn. (3.1) on our ansatz for $I_{EL}(t)$ yields

$$I_\Sigma(f_{SR}) = I_0\, \Delta t\, \tau_d\, f_{SR}\, (1 - e^{-1/\tau_d f_{SR}}). \tag{3.2}$$

When $\tau_d f_{SR} \gg 1$, Eqn. (3.2) predicts I_Σ will saturate. In other words, when the set-reset period is very short ($T_{SR} \ll \tau_d$), the EL emission does not significantly decay during a

single set-reset cycle, and I_Σ becomes independent of f_{SR}. When the set-reset period is very long ($T_{SR} \gg \tau_d$), the EL emission decays significantly during a single set-reset cycle, and Eqn. (3.2) predicts I_Σ grows linearly with f_{SR}. The experimental data in Fig. 3.6 (c) is broadly consistent with Eqn. (3.2), but in the regime $T_{SR} > \tau_d$, the experimental I_Σ is not a simple linear function of f_{SR}. Nevertheless, fitting Eqn. (3.2) to this experimental data yields $\tau_d \approx 0.2\,\text{s}$, which implies that the signal strength has already reduced by two orders of magnitude during the first second of data acquisition (from $t = 0$ to $t = 1\,\text{s}$) when operating in DC mode.

3.6 Analysis of spectra

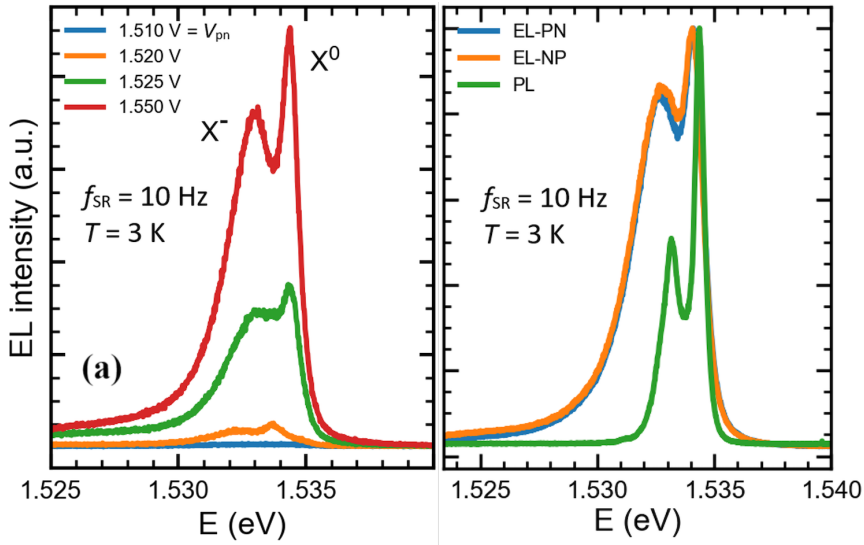

Figure 3.7: Sample C in the Set-Reset mode. (a) EL as a function of V_{pn}. (b) Comparison of EL spectra between PN mode and NP mode with $V_{pn} = 1.55\,\text{V}$, and between PL and EL spectra.

Fig. 3.7 (a) shows EL spectra at different V_{pn}, with light emission occurring only once the forward bias exceeds the bandgap of bulk GaAs ($V_{pn} > 1.519\,\text{eV}$). Fig. 3.7 (b) shows EL spectra from the same p–n junction in the PN and NP mode configurations.[†] From their characteristic behavior in a detailed temperature dependence (see Section 3.6.4), we can unambiguously attribute the narrowest peak ($E \sim 1.534\,\text{eV}$) to the ground state

[†] Because of the continuous Set-Reset topgate voltage sequence, without physically changing any electrical connections, the 'ON' state of the PN configuration corresponds to $V_{pn} = +1.55\,\text{V}$, $V_{tgL} < 0$, and $V_{tgR} > 0$, whereas the 'ON' state of the NP configuration corresponds to $V_{pn} = -1.55\,\text{V}$, $V_{tgL} > 0$, and $V_{tgR} < 0$. Not all samples emit in PN and NP modes with equal EL intensities.

neutral exciton X^0 for a 15 nm wide GaAs QW, and the lower-energy peak ($E \sim 1.533$ eV) to a negatively-charged exciton (trion) X^-.[106,107] A complete justification for these two assignments can be found in Sections 3.6.1 and 3.6.4. Of note, the PL and EL emission energies for X^0 match very well (within 0.3 meV or 0.2 nm). The emission energies of PL X^0 for both heterostructures G0375 and G0569 are nearly identical and consistent with literature (see Section 3.6.3 for the characterization of PL, including lineshape fits).[108,109,110,111,112,113,114,115,116]

3.6.1 EL lineshape fits and peak identification

The two EL peaks at ~ 1.533 eV and ~ 1.534 eV are present in the spectra from samples A, B, C and D, shown in Fig. 3.8. Neither peak corresponds to light emission from the semi-insulating (SI) GaAs substrate (~ 1.519 eV), nor from the MBE growth buffer's superlattice [see Fig. 3.1 (a)] containing twenty GaAs quantum wells 2.5 nm wide (roughly corresponding to emission at ~ 1.64 eV), nor from any of the well-known donor/acceptor impurities ($E < 1.516$ eV) in GaAs.[106,107] The temperature dependence of both peaks (no saturation from 85 K down to 3 K), described in Section 3.6.4, also rules out emission from impurities/traps. The temperature dependence also revealed another peak, whose energy difference from the ~ 1.534 eV peak is consistent with the energy difference between heavy and light holes (see Figs. 3.13 and 3.14). We thus attribute the narrowest peak ($E \sim 1.534$ eV) to the neutral exciton X^0 ground state for a 15 nm wide GaAs quantum well. We assign the lower-energy peak ($E \sim 1.533$ eV) to charged excitons (trions), due to its characteristic temperature dependence [see Fig. 3.13 (a) in Section 3.6.4], its lower energy, and its linewidth being wider than that of X^0. Its charge is likely to be negative (X^-), since there are more electrons than holes in the quantum well for the same topgate voltage magnitude (see plot of carrier density versus topgate voltage in Fig. 3.3), and most of the EL emanated from underneath the thin, semi-transparent Ti topgate on the 2DEG or n-side.

3.6.2 Binding energies of EL X^0 and EL X^-

Table 3.2 lists the emission energies and full width at half maximum (FWHM) of X^0 in all samples reported here, obtained from the EL lineshape fits. As the p–n junction gap between the V_{tgL} and V_{tgR} topgates decreases from 2000 nm to 200 nm, both X^- and X^0

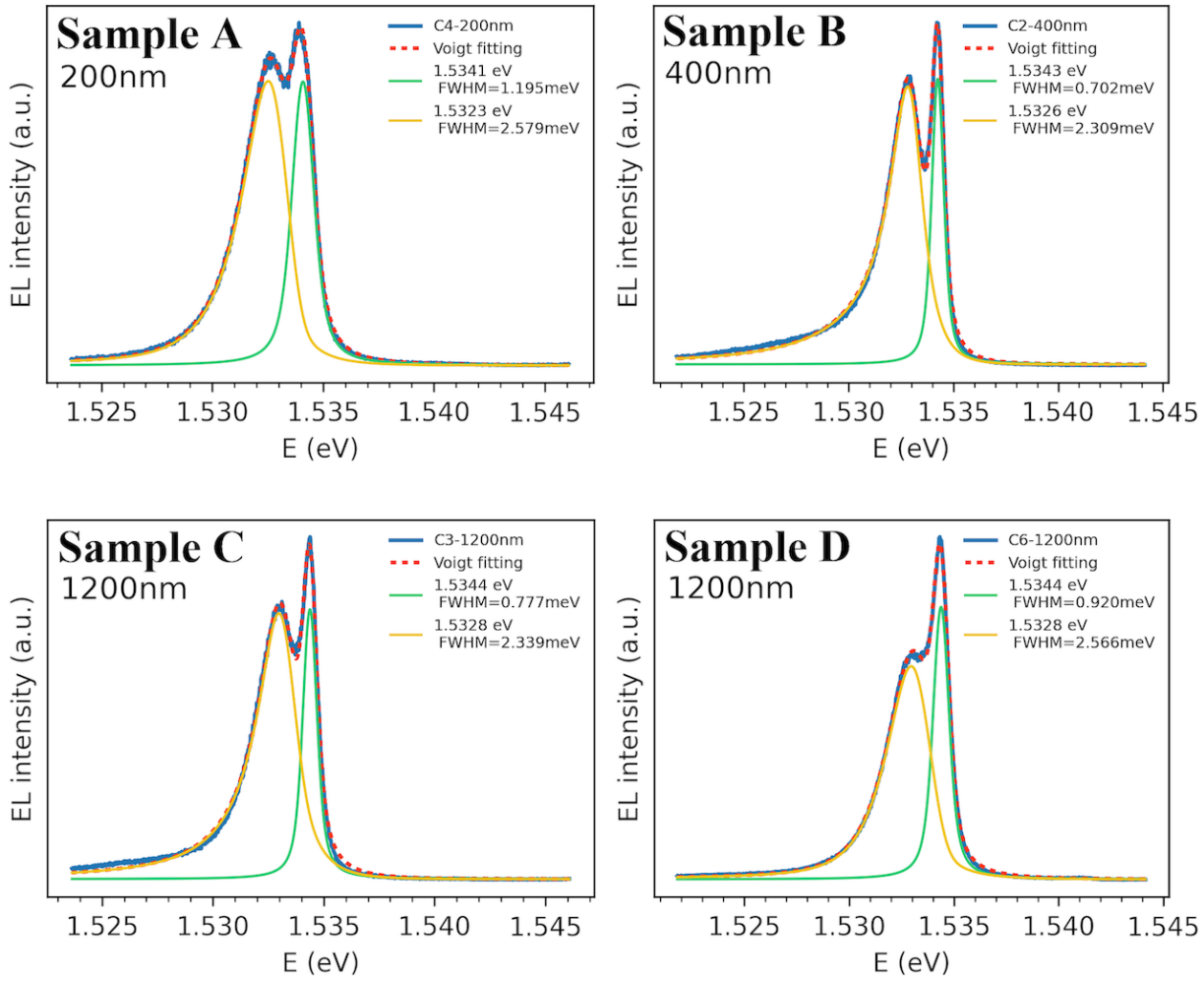

Figure 3.8: EL spectra at $T = 3$ K for samples A–D (see Table 3.1), including lineshape fits. The resulting fitting parameters are listed in each panel for both X^0 and X^- peaks. The solid blue lines are experimental data, and the dashed red lines are the integrated fits, including contribution from both peaks. Symmetric pseudo-Voigt functions[117] (green solid lines) were used for fitting the free exciton peaks X^0. The EL trion X^- peaks are asymmetric (unlike the PL trion), so asymmetric pseudo-Voigt functions[117] (yellow solid lines) were used instead. The physical origin of the long-tail on the low-energy side of the trion peak is most likely inelastic trion-electron scattering,[114] considering that trions form in an electron-rich environment. Below each sample label, the p–n junction gap between topgates is stated.

show a very weak Stark shift (0.6 meV) to lower EL energies due to the increasing in-plane electric field $|\vec{E}_{\text{ext}}| = V_{\text{pn}}/\text{gap}$, ranging from 7.8 kV/cm (in sample E) to 78 kV/cm (in sample A) in the 2DEG/2DHG plane.

Four of the five samples listed in Table 3.2 have narrower linewidths (0.7–0.9 meV) than the narrowest EL linewidths (1.0–1.6 meV) of any lateral p–n junctions reported in

Sample	Gap (μm)	$E_{EL}(X^0)$ (meV)	$E_{EL}(X^-)$ (meV)	E_{bx} (meV)	ΔE_{X^-} (meV)	FWHM (meV)
A	0.2	1534.1	1532.3	8.8	1.8	1.20
B	0.4	1534.3	1532.6	8.8	1.7	0.70
C	1.2	1534.4	1532.8	8.8	1.6	0.78
D	1.2	1534.4	1532.8	8.8	1.6	0.92
E	2.0	1534.7	1533.3	8.8	1.4	0.92

Table 3.2: EL emission energies of X^0 and X^- in all samples reported here. Also listed are the gaps between their p-type and n-type regions (i.e., the distance separating the V_{tgL} and V_{tgR} topgates in Fig. 3.1 (a)), their X^0 binding energies E_{bx}, their X^- dissociation energies $\Delta E_{X^-} = E_{EL}(X^0) - E_{EL}(X^-)$, and the full width at half maximum (FWHM) of their X^0 peaks.

the literature, whether undoped[90,91,92,23] or modulation-doped.[85,84,118,119,86] Our narrow EL linewidths in turn allowed the observation of the small but noticeable shift[†] in E_{EL}; this small shift would likely have been masked by the rapid and large linewidth broadening reported in the original PL experiments. The most likely reason for such narrow linewidths is the high quality MBE growth, as evidenced by the clean PL spectrum shown later in Fig. 3.12, and the high electron/hole mobilities shown in Fig. 3.3. Additionally, we speculate that in the vicinity of the p–n junction, the Set-Reset voltage sequence clears away parasitic charge that causes additional scattering, and hence reduces the broadening of EL emission (details in Section 3.7).

The emission energy of EL X^0 can be decomposed into the following contributions—

$$E_{EL}(X^0) = E_g - \vec{p} \cdot \vec{E}_{ext} + E_{e\text{-}QW} + E_{h\text{-}QW} - E_{bx}, \tag{3.3}$$

where E_g is the GaAs bandgap energy, $\vec{p}$ is the free exciton dipole moment, $\vec{E}_{ext}$ is the in-plane electric field, $E_{e\text{-}QW}$ ($E_{h\text{-}QW}$) is the lowest-energy bound state in the quantum well conduction (valence) band, and E_{bx} is the binding energy of the neutral exciton. Energies used in our calculations are shown in Fig. 3.9. The conduction band offset at the GaAs/AlGaAs interface is assumed to be $\sim 0.6\Delta E_g$.[121,122] The quantum well bound state energies are numerically found from the standard textbook finite barrier square well transcendental equation. We use the isotropic mass $m_e^* = 0.067\, m_0$ for electrons in our 15 nm wide quantum well, where m_0 is the electron rest mass 9.11×10^{-31} kg. Heavy

[†] The decrease in $E_{EL}(X^0, X^-)$ is not due to Joule heating (which would cause the bandgap to decrease)—sample A, which has the smallest p–n junction gap and hence the smallest electrical resistance across the gap (i.e. the smallest heat dissipation), has the largest decrease in E_{EL}, whereas the converse is true for sample E (i.e. the largest p–n junction gap but the smallest decrease in E_{EL}).

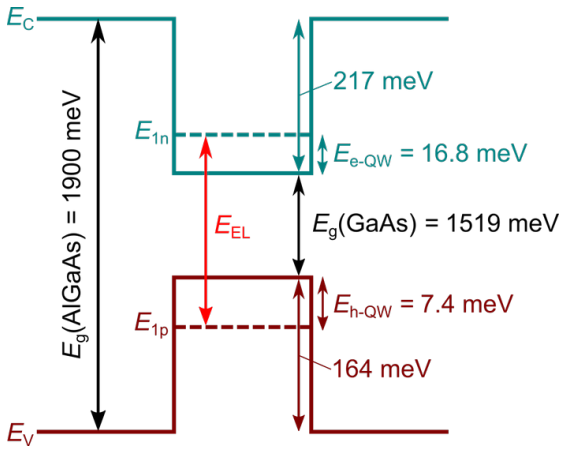

Figure 3.9: Energy band diagram of the GaAs QW sandwiched by $Al_{0.3}Ga_{0.7}As$ barriers at cryogenic temperatures. E_C and E_V are the conduction and valence band energies. The bandgap energy (E_g) of GaAs is 1519.0 meV[107] and of AlGaAs is 1900.0 meV.[120] The energy offsets between GaAs and AlGaAs in the conduction and valence band are 217 meV and 164 meV respectively. E_{1n} and E_{1p} are the ground state energies of the electrons and holes in the quantum well. The quantum well bound state energies for electrons is $E_{e\text{-}QW} = [E_{1n} - E_C(\text{GaAs})] = 16.8$ meV and for holes is $E_{h\text{-}QW} = [E_V(\text{GaAs}) - E_{1p}] = 7.4$ meV. E_{EL} is the EL (or PL) emission energy.

holes have different masses in different crystal directions;[123] we use an average effective hole mass, the optical mass[107] $m^*_{hh} = (m^*_z\, m^*_y\, m^*_x)^{1/3}$, where $m^*_z = 0.377\, m_0$ in the [001] crystal direction (MBE growth direction) and $m^*_y = m^*_x = 0.112\, m_0$ in the [110] and [1$\bar{1}$0] crystal directions (Eqn. (24) in Ref. [124]). Thus, taking into account the small redshift $\vec{p} \cdot \vec{E}_{ext}$ due to the Franz-Keldysh effect,[125,126] the spatial asymmetry in the effective mass of heavy holes, the bandgaps of GaAs and $Al_{0.3}Ga_{0.7}As$ and their band offsets,[107,120,121,122] and the energy of the ground state for holes and electrons in the GaAs quantum well, the binding energy of EL X^0 is calculated to be $E_{bx} = (8.8 \pm 0.2)$ meV (see Table 3.2). The same calculations and results apply to PL X^0 from wafers G0375 and G0569 (Section 3.6.3).

Fig. 3.10 shows that our E_{bx} values for PL/EL X^0 are consistent with reported experiments[108,109,127] and theory[108,123,124,128] on PL X^0. Our experimental values are slightly larger than the experimental PL E_{bx} values from Ref. [127], but fall well within the maximum/minimum theoretical values (solid black lines in panels a and b). These theoretical values are dictated by the choice of isotropic/anisotropic hole effective mass symmetry.

Unexpectedly, the trion dissociation energy appears to increase with higher in-plane electric field (see Table 3.2). There is no ambiguity as to whether ΔE_{X^-} is increasing or not with in-plane electric field, since it is directly obtained from the difference in emission energies $\Delta E_{X^-} = E_{EL}(X^0) - E_{EL}(X^-)$. The emission energy of EL X^- can be decomposed

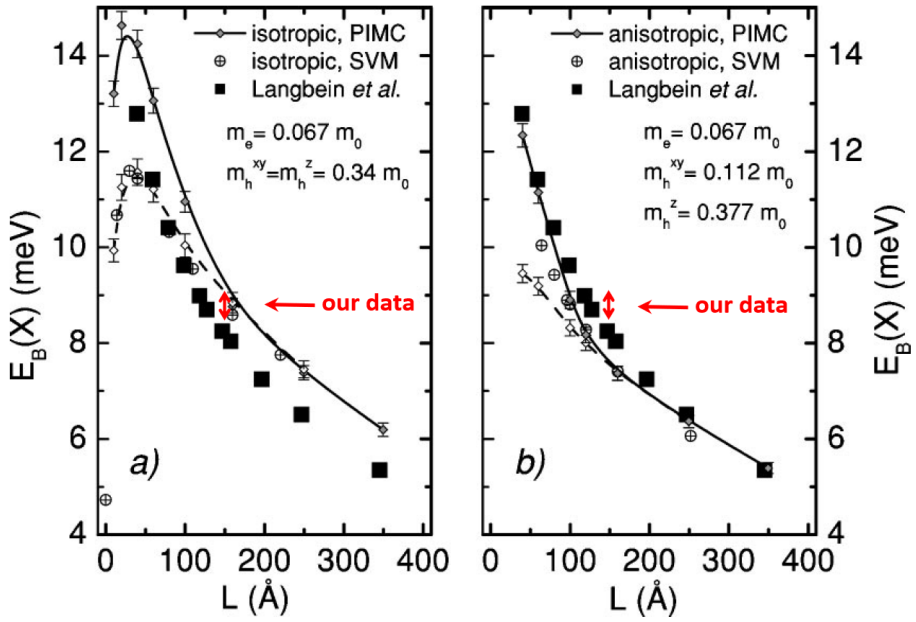

Figure 3.10: Comparison of our EL exciton binding energy with theory. The EL X^0 energies range from 1,534.1 to 1,534.7 meV (see Table 3.2). Using those values and Eqn. (S1), we find that $E_{bx} = (8.8 \pm 0.3)$ meV for samples A–E. Our result (with its uncertainty represented by the red double-ended vertical arrow) is compared to experiment[127] (filled black squares) and theory[123] (circles and lines) in Fig. 10 from Ref. [123] (shown above), where theoretical calculations used (a) isotropic and (b) anisotropic hole effective masses.

into the following contributions:

$$E_{EL}(X^-) = E_g - \vec{p} \cdot \vec{E}_{ext} + E_{e\text{-}QW} + E_{h\text{-}QW} - E_{bx} - \Delta E_{X^-}. \tag{3.4}$$

An increase in the dissociation energy of trions with larger in-plane electric field has been experimentally observed and theoretically justified in InGaAs/GaAs quantum dots,[129] in the presence of strong spin-orbit coupling.

3.6.3 Comparison of non-resonant PL and EL

Fig. 3.11 (a) compares G0375's non-resonant PL spectrum and the EL spectrum from sample B; the comparison in Fig. 3.7 (b) was between PL from G0375 and EL from sample C. Fig. 3.11 (b) shows the lineshape fits of the two PL peaks, the neutral exciton X^0 and negatively-charged trion X^-, with symmetric Voigt functions. The emission energies for X^0 match very well, with $E_{EL} = 1534.4$ meV and $E_{PL} = 1534.6$ meV (same E_{PL} for both wafers G0375 and G0569). The FWHM of the PL X^0 peak is 0.51 meV from the lineshape fit. It is

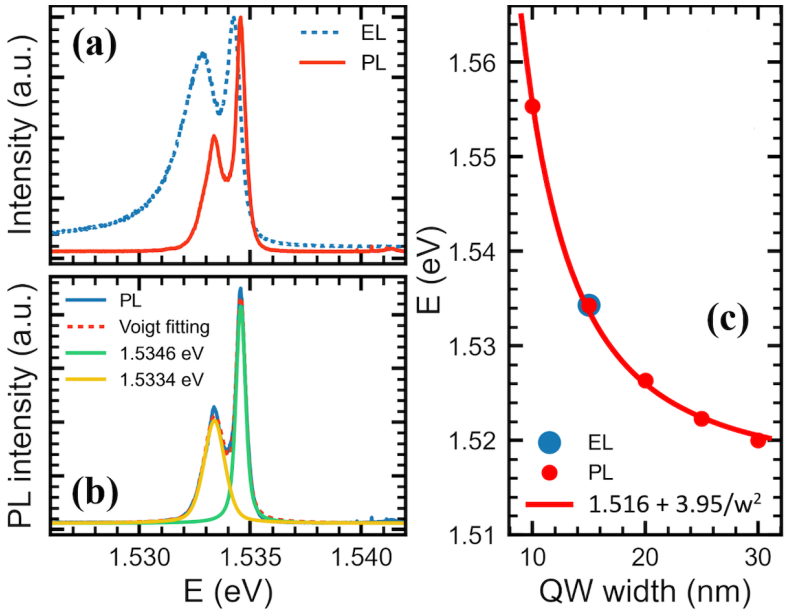

Figure 3.11: (a) Comparison of PL and EL spectra from sample B at $T = 3$ K. (b) Peak fitting of the two PL peaks shown in (a). The solid blue line is experimental data. The dashed red line is the integrated fit, including contribution from both peaks. The green solid line is the fit to X^0, and the yellow solid line is the fit to X^-. (c) (MAIN) PL emission energies of X^0 from a series of six nominally identical dopant-free GaAs quantum well heterostructures except for a varying well width w, ranging from 10–30 nm (red circles).

smaller than any of the FWHM values for EL X^0 listed in Table 3.2, because EL occurs at much higher carrier densities (causing more electron-exciton scattering), higher electric fields (from both V_{pn} and V_{tg}), and possibly higher temperatures (due to Joule heating from the p–n current). On the one hand, a similar trend is observed for the PL and EL X^- trions, where the FWHM of EL X^- is much larger than that of PL X^-, presumably for the same reasons as EL X^0. On the other hand, the emission energies for the PL and EL trions do not match; the lineshape of EL X^- is asymmetric whereas it is symmetric for PL X^-, and EL X^- occurs at a much lower energy than PL X^-. The latter implies the binding (dissociation) energy of EL X^- is larger than that of PL X^-. These differences between EL X^- and PL X^- are the same for all samples A–E and for both wafers G0375 and G0569.

The two heterostructures used (G0375 and G0569) both had a quantum well width of 15 nm, and have identical PL emission energies. Both wafers were part of a series of six nominally identical dopant-free GaAs quantum well heterostructures except for a varying well width w, ranging from 10 nm to 30 nm. Fig. 3.11 (c) shows the PL emission energies (red circles) for each wafer in the series. The PL X^0 energies scale as $1/w^2$ (best fit represented by solid red line), as expected for bound states in a square quantum well.

Fig. 3.12 shows a wide PL spectrum of wafer G0375, from 1.35 eV (918 nm) to 1.82 eV

(681 nm). The main peak at ~ 1.534 eV is in reality the merger of two peaks—one peak from free neutral excitons involving heavy holes (X^0) and the other from charged excitons (trions, X^-). The peak on the high-energy side of the main peak, near ~ 1.541 eV, is from neutral free excitons involving light holes (LH). The emission line near ~ 1.634 eV is from the superlattice (SL) of twenty thin (2.5 nm wide) GaAs quantum wells in the MBE growth buffer. Finally, the very broad peak near ~ 1.493 eV comes from C acceptors throughout the heterostructure (including the substrate) and Be acceptors in the layers grown using MBE (the chamber contains a Be cell). Overall, the PL spectrum is very clean, with the main peak two orders of magnitude brighter than the next brightest peak. A high-resolution scan of the dominant peak near ~ 1.534 eV can be found in Fig. 3.11 (b), where the PL X^0 and X^- peaks can be fully resolved.

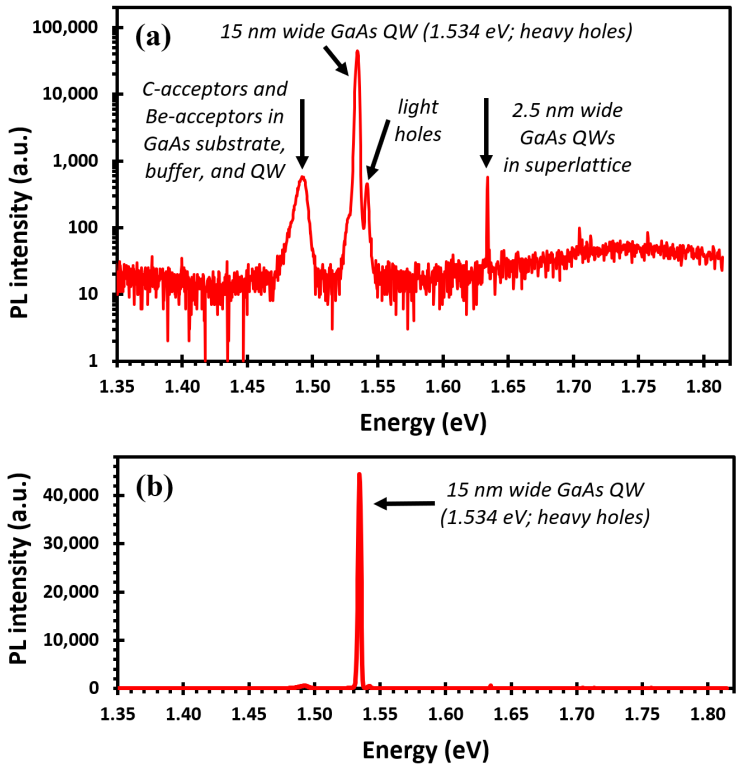

Figure 3.12: Wide-energy PL spectrum of quantum well (QW) heterostructure G0375. (a) Data shown on a log scale. (b) Same data, shown on a linear scale. No cleanroom processing was performed on the wafer sample shown here. Unlike all other data in this paper, the data shown above was acquired with a low-resolution grating of 400 lines/mm.

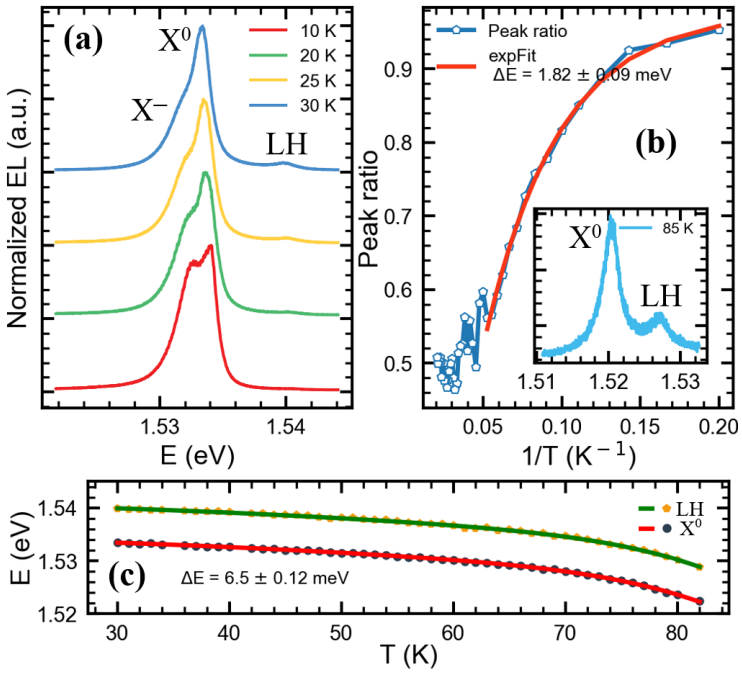

Figure 3.13: Temperature dependence of EL in sample A. (a) Temperature dependence of EL from sample A operated at Set-Reset frequency of $f_{SR} = 1$ KHz. The four spectra shown have been normalized so that the X^0 peak height is constant. The spectra have been vertically offset for clarity. (b)(main) Fit of the peak intensity ratio X^-/X^0 as a function of temperature. (b)(inset) EL intensity as a function of energy in eV at 85 K: the X^0 peak can still be resolved. The light hole (LH) peak is evident at higher temperatures, but not at lower temperatures. (c) EL energies of X^0 and LH as a function of temperature, from experiments (circles) and theory (lines). The latter uses Pässler's semi-empirical model[130,131] for the GaAs bandgap.

3.6.4 Detailed temperature dependence of EL

Fig. 3.13 (a) shows the temperature dependence of the X^0 and X^- EL peaks. As expected for a charged exciton, the X^- peak disappears above a much lower temperature threshold ($T > 30$ K) than the X^0 peak, which survives up to $T \approx 85$ K as shown in the inset of Fig. 3.13 (b). The PL energy separation between X^0 and X^- in Fig. 3.11 (b) suggests a dissociation energy of 1.2 meV for the trion's second electron, consistent with similarly obtained energies with PL in GaAs quantum wells.[132] The EL energy separation between X^0 and X^- for all samples in Fig. 3.8 (see Table 3.2) show a range of dissociation energies spanning 1.4–1.8 meV for the trion's second electron, for the same quantum well width. Another experimental method for measuring the dissociation energy involves fitting the ratio of integrated peak intensity between X^0 and X^- with $e^{-\Delta E/kT}$ for a wide range of temperatures.[133] Using this method for the EL spectra, Fig. 3.13 (b) yields (1.8±0.1) meV for the trion's dissociation energy, consistent with the 1.8 meV value obtained from Fig. 3.8 (a)

at $T = 3$ K in sample A. For both X^0 and X^-, the EL intensity decreases as the temperature increases, due to some combination of exciton dissociation, activation of non-radiative recombination centers, and thermally-induced escape of carriers from the quantum well [Fig. 3.13 (c)]. From $T = 3$ K to $T = 85$ K, the emission energy of both X^0 and LH redshifts by ~ 14 meV, mostly due to the temperature-dependent decrease of the GaAs bandgap.[130,131]

3.6.5 Identifying light holes in EL

The light hole (LH) peak, visible in Fig. 3.13, appears ~ 6.5 meV above X^0 for a wide range of temperatures. It also appears at the same emission energy in the PL spectra of Fig. 3.11 (a) (barely visible, just above $E \sim 1.541$ eV) and of Fig. 3.12 (a), also 6.5 meV above X^0. Excitons composed of an electron bound to a light hole can co-exist with excitons composed of an electron bound to a heavy hole, and have higher PL emission energies than the latter due to their smaller effective mass ($m^*_{\mathrm{lh}} = 0.082 m_0$).[107] Characteristically, the ratio of the PL intensity of the light-hole free exciton to that of the heavy-hole free exciton increases with temperature, due to the thermally-driven transfer of holes from the heavy-hole band to the light-hole band.[134,135,110] This behavior is indeed observed in the EL shown in Fig. 3.13 (a), and continues until the highest temperature attempted ($T = 85$ K) in the inset of Fig. 3.13 (b). The 6.5 meV energy difference between EL X^0 and LH [see Fig. 3.13 (c)] for our 15 nm quantum well is consistent with those observed with PL in modulation-doped quantum wells of various widths (see Fig. 3.14).[111,108,110,136] This

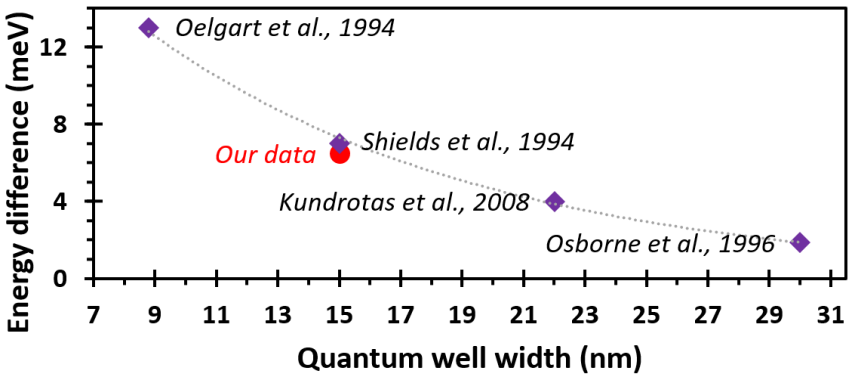

Figure 3.14: Comparison with literature of the difference in emission energies between heavy/light hole free excitons. Literature values for PL (purple diamonds) come from Refs. [111,108,110,136]. The dotted line is a guide to the eye. Our EL data (red circle) is consistent with the trend.

6.5 meV difference is also consistent with the calculated energy difference (≈ 6.4 meV)

between the heavy-hole and light-hole square-well bound states in the valence band (see Fig. 3.9). We therefore identify the LH peak with the ground state of light-hole free excitons. This peak also appears in other dopant-free devices (but is not identified as such)—see EL spectrum in Fig. 4b of Ref. [92], the peak nearest wavelength 806 nm.

3.7 Parasitic charge clearance in the Set-Reset mode

Five key observations support the scenario of localized parasitic charging in lateral p–n junctions:

(1) quenching of EL with time [Fig. 3.5 (b)];
(2) faster quenching of EL with larger initial forward bias currents [Fig. 3.5 (b)];
(3) brighter EL when operating a device in the Set-Reset mode [Fig. 3.6 (a)];
(4) the 'reset' requiring the alternating presence of both 2DEG and 2DHG in the same location to be most effective (see below); and
(5) the 'reset' not requiring a finite V_{pn} to be effective.

Regarding observations (1–3): Without current flowing across the p–n junction, the 2DEG and 2DHG carrier densities are otherwise stable, before or after EL is quenched. This suggests that the charging mechanism making devices unstable is only associated with current flowing across the p–n junction,[‡] and is localized near the p–n junction since the 2DEG/2DHG themselves are not suppressed. We note that electrons or holes can escape the quantum well confinement in significant numbers at/near the p–n junction when the forward bias provides energies ($eV_{pn} > 1.5$ eV) much larger than the QW confinement potential, which is defined by the GaAs/AlGaAs conduction band offset for electrons (~ 0.217 eV) or GaAs/AlGaAs valence offset for holes (~ 0.164 eV). Another possible escape mechanism could be biased self-illumination due to EL emission—electrons (holes) from the QW or from charge traps due to background impurities are photoexcited into the GaAs cap layer by emitted EL photons, since the EL photon energy (1.534 eV) exceeds the AlGaAs barrier heights (band offsets).

[‡] From our own experience and that of others,[90,137] at very high p–n currents (0.1–0.5 mA), dopant-free p–n junctions can be stable in time. In that case, we speculate that any parasitic charge build-up is cleared away by the high currents. We believe this high-current regime is not applicable to the single photon regime, where currents are expected to be six orders of magnitude smaller.

Regarding observation (4): If the Set-Reset sequence is only applied to one side (say, V_{tgR} but not V_{tgL}) of an ambipolar p–n junction, then light emission lasts longer than in DC mode but not as long as when the Set-Reset sequence is applied to both V_{tgR} and V_{tgL}. In addition to the five ambipolar p–n junctions reported here, 'unipolar' p–n junctions were also fabricated, with only n-type ohmic contacts on one side of the p–n junction and only p-type ohmic contacts on the other side. These were also unstable with time (i.e., EL quenching) in DC mode operation, similar to their ambipolar cousins. However, the Set-Reset sequences failed to reset these unipolar devices—only full thermal cycles could reset them. These two results together strongly suggest an efficient 'reset' mechanism must involve the presence of alternating 2DEGs and 2DHGs in the same physical location, with its associated reversal of the electric field direction.

Regarding observation (5): The 'reset' is effective whether $V_{pn} = 0$ or $V_{pn} \neq 0$. Thus, unlike the mechanism behind parasitic charging, the 'reset' mechanism does not involve any phenomena associated with $V_{pn} \neq 0$.

A scenario for parasitic local charging in dopant-free lateral p–n junctions is illustrated in Fig. 3.15. During EL emission, driven by photoexcitation and/or the electric fields from V_{pn}, V_{tgL}, and V_{tgR} present at the p–n junction, electrons (holes) tunnel/escape from their 2DEG (2DHG) QW into the surrounding GaAs/AlGaAs material and to the GaAs/SiO_2 interface at the wafer surface. This parasitic charge build-up either enhances non-radiative electron-hole recombination, or counters the forward bias enough to altogether suppress current across the p–n junction. By reversing the directions of the electric fields stemming from the topgates during the 'reset' cycle of the Set-Reset sequence, all or most of the trapped electron (hole) charges at the GaAs/SiO_2 interface are dislodged from their metastable traps and 'push-pulled' to recombine with the newly-formed 2DHG (2DEG) below. We note the two tunneling processes in the 'Set' and 'Reset' cycles are not complementary/reversed processes—one requires $V_{pn} > 1.5\,\text{V}$ (i.e., photoexcitation) to occur while the other does not (it can occur at $V_{pn} = 0$).

3.8 Conclusion and outlook

In conclusion, we have outlined a mechanism (localized parasitic charging) for quenched EL in lateral p–n junctions, and demonstrated an operating regime (the Set-Reset mode) that dissipates this parasitic charge. The Set-Reset mode allowed the observation of the narrowest EL linewidths (0.70 meV) achieved to date in lateral p–n

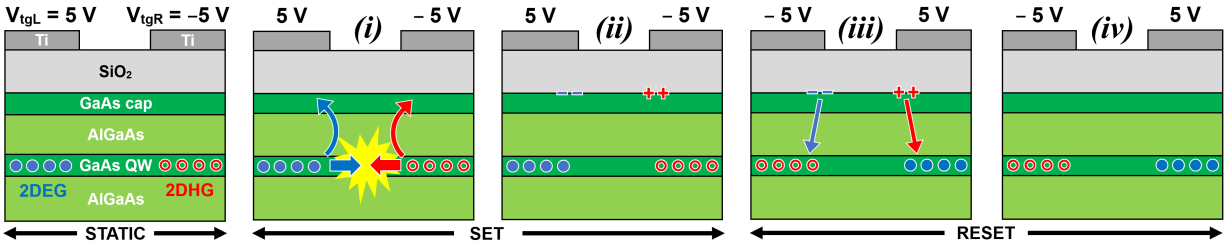

Figure 3.15: Illustration of the parasitic charging and set-reset mechanisms. (STATIC) The leftmost panel shows the device in DC mode with $V_{pn} = 0$, and is the starting point of all optical experiments. This panel is not part of the Set-Reset sequence. The Set-Reset sequence is shown in panels *(i)* through *(iv)*, with $V_{pn} = +1.5\,V$ remaining constant in all four panels. (SET) The next two panels show events during the 'set' cycle of the Set-Reset sequence; the p–n junction is in the *forward-bias* regime. *(i)* Radiative electron-hole recombination with finite p–n current occurs (EL). A small proportion of electrons and holes escape the QW confinement, and head towards the GaAs/SiO_2 interface where they get trapped. *(ii)* As the parasitic charges trapped at the GaAs/SiO_2 interface build up, EL decays. Eventually, the p–n current and light emission vanish altogether. (RESET) The two rightmost panels show events during the 'reset' cycle of the Set-Reset sequence; the p–n junction is in the *reverse-bias* regime. *(iii)* The polarity of both topgates has been reversed. The metastable electron (hole) charges trapped at the GaAs/SiO_2 interface are dislodged, repelled by the topgate above and attracted to the 2DHG (2DEG) below. *(iv)* All previously built-up parasitic charges have now been drained to the 2DEG/2DHG nearby, and the p–n junction has been restored to its original state. The 'reset' cycle ends, and the next 'set' cycle can start.

junctions, and the indefinite operation of ambipolar lateral p–n junctions at cryogenic temperatures (up to 85 K), obviating the need for frequent thermal cycles to room temperature. In turn, this enabled the unambiguous identification of the heavy-hole free exciton X^0, the light-hole free exciton LH, and charged exciton X^-. The emission energies for free excitons EL X^0 and PL X^0 were closely matched (within 0.3 meV or 0.2 nm) and both their lineshape were symmetric in all observed samples.

Fig. 3.17 demonstrates that our nano-LEDs are compatible with RF operation when run in Set-Reset mode.[§] The shorter lifetime of EL relative to PL is consistent with the wider FWHM observed in EL relative to PL [see Fig. 3.7 (b)]. Hypothetically, in the single-photon regime, an exciton lifetime $\tau_{EL} = 237\,ps$ would be compatible with a 1 GHz emission rate for the single photon source proposed in Refs. [101, 24].

An important point is that while Set-Reset operation does work well to clear parasitic charge and extend the lifetime of EL *in-situ* in our nano-LEDs, it would not be compatible single-photon operation in a quantum emitter built by integrating the nano-LED with a quantized charge pump. This is because quantum emitters need time-stable photon

[§] The electrical circuit used is shown in Fig. 3.16. The lineshape of the EL peaks in Fig. 3.17 is dictated in part by the limitations of the RF equipment (max. rise time of 0.95 ns/0.6 $V_{p\text{-}p}$); the attenuated RF pulses reaching the samples are very unlikely to be square-shaped pulses. Nevertheless, the lateral p–n junction is clearly responsive on timescales of less than 1 ns [see Fig. 3.17 (a)].

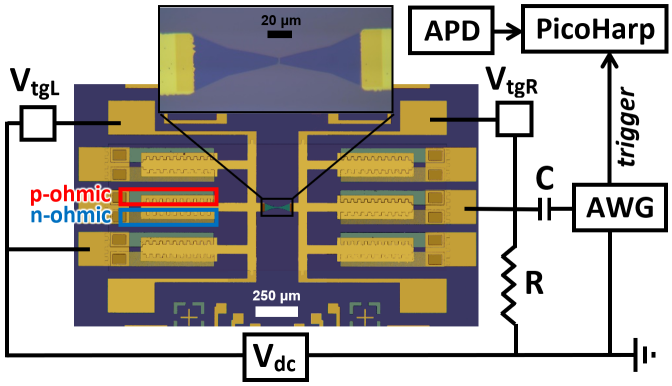

Figure 3.16: Electrical RF circuit used for all time-resolved EL. Forward bias $V_{pn} = V_{DC} + V_{RF}$, the latter being supplied by an arbitrary waveform generator (AWG) Tektronix 5014B. The RF pulse was a square wave with repeat frequency 100 MHz (10 ns period) with a nominal 10% duty cycle. However, the AWG has a max. rise time of 0.95 ns/0.6 $V_{p\text{-}p}$, and outputs RF pulses that are Gaussian-shaped. A PicoHarp 200 provided time tagging using signals from the AWG and the avalanche photodiode (APD). Periodic RF-pulsed EL was obtained with $V_{pn} = 1.47\,\text{V}$ (DC) + $0.5\,V_{p\text{-}p}$ (RF).

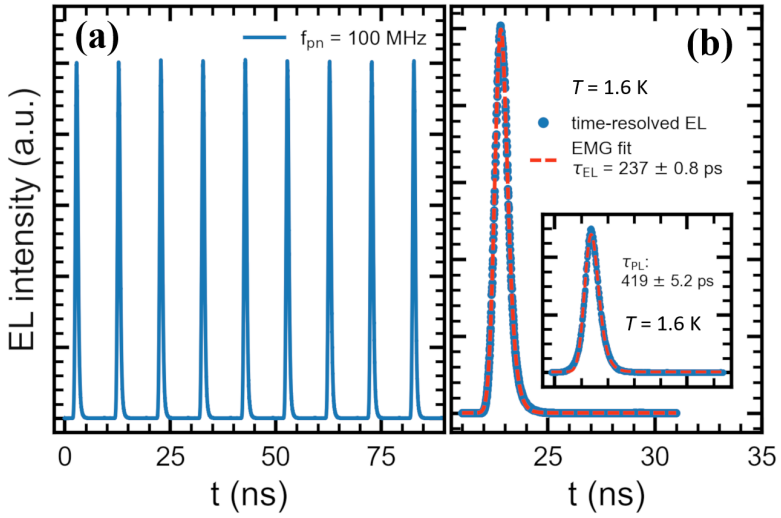

Figure 3.17: Time-resolved EL at $T = 1.6\,\text{K}$ from sample E in Set-Reset mode with $f_{SR} = 10\,\text{Hz}$. (a) Periodic RF-pulsed EL with $V_{pn} = 1.47\,\text{V}$ (DC) + $0.5\,V_{p\text{-}p}$ (RF). (b) Fitting the experimental data (blue circles) to an exponentially modified Gaussian (EMG; dashed red line), an EL exciton lifetime $\tau_{EL} = 237\,\text{ps}$ is obtained. (INSET) The PL exciton lifetime from the same QW heterostructure is $\tau_{PL} = 419\,\text{ps}$.

statistics at the one-photon level to be favorably characterized as a single photon source. Set-Reset operation cannot guarantee this, so alternative solutions are required—Chapter 5 discusses one possible solution.

4. Lateral 2D p–n junctions defined at single heterojunction interfaces

The 2DEG and 2DHG that form the lateral 2D p–n junctions measured in Chapter 3 are induced in the rectangular GaAs quantum well layer of the GaAs/AlGaAs heterostructure wafer stack. Until now, none of the lateral 2D p–n junctions discussed in literature utilize 2DEGs and 2DHGs induced at the SHJI between two semiconducting materials. In fact, a theoretical study published by Kim et. al. in 2022 (Ref. [31]) concludes that it is impossible for electron and hole wavefunctions to overlap and allow for recombination in the case of SHJIs. They argue that since electrons traveling to the p-side to recombine with holes will no longer be under the voltage-induced 2D confinement from the n-side topgate, they will instead escape into the substrate rather than recombine. In this chapter, we discuss experimental results that prove otherwise—lateral 2D light-emitting diodes *can* in fact be realized at GaAs/AlGaAs SHJIs. These devices show characteristics typical of 2D p–n junctions, and like the RQW devices in Chapter 3, they are ambipolar and can be operated using the Set-Reset protocol to clear away built-up parasitic charge and improve the stability of their EL. From our experience, fabricating ohmic contacts to SHJIs in induced devices and lateral planar diodes is easier and more reproducible than in RQWs, making SHJI devices a useful substitute/alternative.

4.1 Experimental methods

Data from one of our SHJI devices is reported in this chapter. The device was fabricated using the MBE-grown heterostructure wafer G0265, with the p–n junction oriented along the high-mobility crystal direction $[1\bar{1}0]$. The details of each layer in the wafer stack (starting from the substrate) are as follows (see Fig. 4.1)—a 200 nm GaAs buffer, a 500 nm

LT-GaAs layer, a 1700 nm GaAs buffer, a 300 nm GaAs channel layer, a 300 nm $Al_{0.3}Ga_{0.7}As$ top barrier, and a 10 nm GaAs cap layer. The fabrication recipe used for this device is

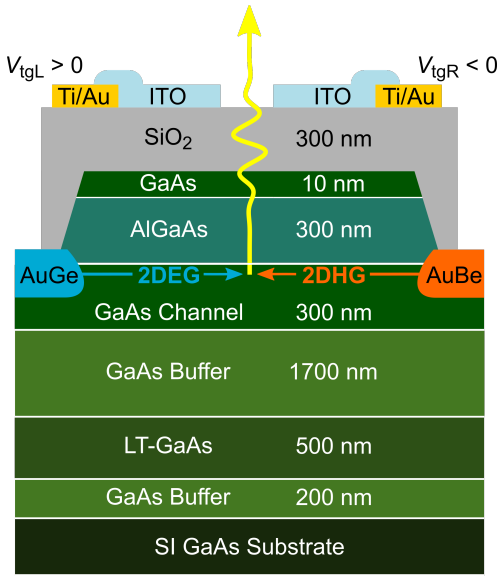

Figure 4.1: Vertical cross-section of our ambipolar dopant-free lateral p–n junction showing the layers of the SHJI GaAs/AlGaAs heterostructure G0265. The SHJI is at a depth of 310 nm from the wafer surface. Also shown are the left and right topgates (opaque Ti/Au and semi-transparent ITO) separated from the surface by SiO_2. $V_{tgL} > 0$ and $V_{tgR} < 0$, inducing a 2DEG and 2DHG underneath them respectively. A forward source-drain bias drives electron-hole recombination and light emission.

essentially identical to the recipe described in Chapter 3, with some minor difference with regards to the fabrication of the n-type ohmic contacts (see Appendix C). The pattern masks for each significant lithography step are shown in Appendix B. A 30 nm semi-transparent ITO layer is used as the topgate material close to the p–n junction, and induces the charge carriers at a depth of 310 nm from the surface. The device was designed to have a topgate gap of 3 µm, which in reality was smaller due to overexposure during photolithography.

4.1.1 Optical and electrical characterization

The EL spectra reported in this chapter (Figs. 4.4, 4.5) were frequency-selected using a Princeton Instruments Acton Series SP-2750 optical spectrometer with the chosen grating having 1200 grooves/mm, and acquired with the integrated Princeton Instruments PIXIS 100 CCD camera thermoelectrically cooled to −70 °C. The SHJI device itself was placed in an attocube attoDRY2100 closed-cycle optical cryostat, and cooled to 1.6 K. The objective lens used has a numerical aperture of 0.81 and a working distance of 0.70 mm.

Optical video of the electroluminescing device was captured using a Watec WAT-910HX CCIR miniature camera with a 0.5 inch black and white CCD; still images from these videos are reported in this chapter (Fig. 4.3). These images are qualitative, and are used as a way to infer the EL distribution over the device.

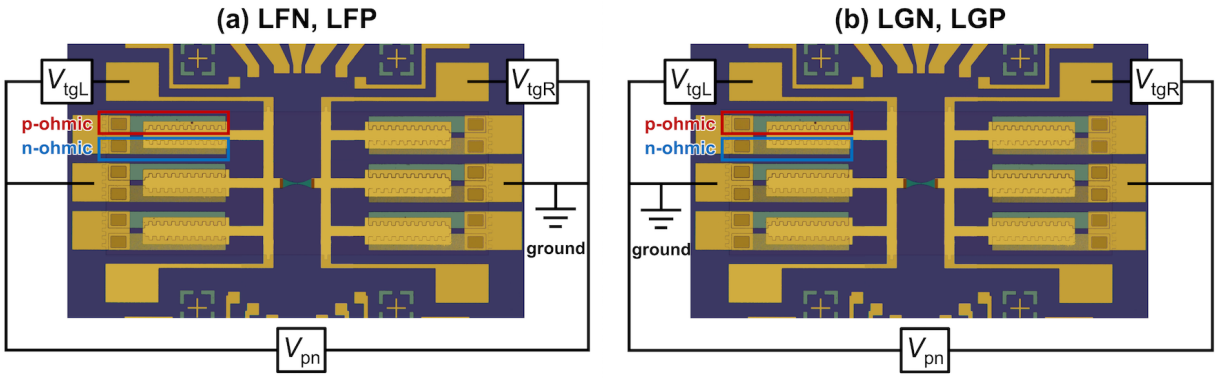

Figure 4.2: Circuit diagrams showing the different configurations our ambipolar lateral 2DPN devices can be connected in. Note that the sample images are purely representative and do not correspond to the actual device measured. V_{tgL} and V_{tgR} are the voltages applied on the left and right topgates respectively. V_{pn} is the forward bias applied to the diode. (a) LFN or LFP configurations. The left side of the device is floating, and can be n-type or p-type, while the right is grounded, and can be p- or n-type. (b) LGN or LGP configurations. The left side is grounded (n- or p-type), and the right side is floating (p- or n-type).

Electrical connections were made to the device using in-house custom electrical feedthroughs paired with existing cabling. DC voltages were applied to the gates using SRS SIM928 isolated voltage sources, and a Keithley 2401 SourceMeter was used to apply the p–n forward bias to the ohmic contacts. The set-reset sequence was implemented using custom code written to interface with the voltage sources using a GPIB communication channel. Fig. 4.2 shows the electrical circuits used to operate the device.* Looking at the charge gas induced on just the left side of the device, it can be either floating or grounded, and due to the ambipolar nature of the device, either n-type (electrons, $V_{tgL} > 0$) or p-type (holes, $V_{tgL} < 0$). The charge gas on the right side will then be grounded or floating respectively, and p-type ($V_{tgR} < 0$) or n-type ($V_{tgR} > 0$) respectively. This yields four distinct measurement configurations, as shown in Table 4.1. These configurations will henceforth be referred to using their shorthands—LFN, LFP, LGN and LGP. Note that this nomenclature stays valid even when the device is operated in the Set-Reset mode, since they correspond to the device configuration in the ON state of each set-reset cycle.

* Note that the sample images have been reused from the previous chapter and are just representative.

left side	V_{tgL}	right side	V_{tgR}	shorthand
floating, n-type	> 0	grounded, p-type	< 0	LFN
floating, p-type	< 0	grounded, n-type	> 0	LFP
grounded, n-type	> 0	floating, p-type	< 0	LGN
grounded, p-type	< 0	floating, n-type	> 0	LGP

Table 4.1: Four distinct configurations the lateral 2D p–n junction devices can be measured in. Circuit diagrams for these configurations are shown in Fig. 4.2.

4.2 Experimental results

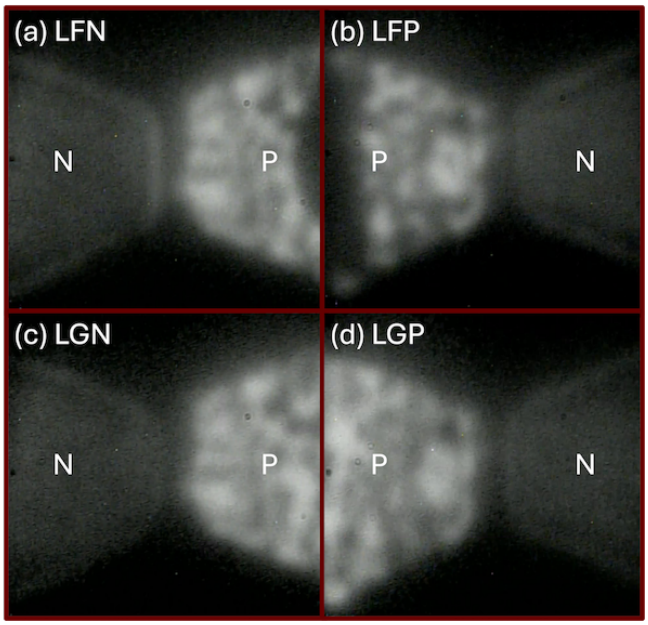

Figure 4.3: Still images from videos of the luminescing SHJI sample operated in set-reset mode in the (a) LFN, (b), LFP, (c) LGN, and (d) LGP measurement configurations. The images are captured from the center of the sample at the moment of peak emission brightness during a specific set-reset cycle. The left and right trapezoidal ITO topgates are clearly visible in each image, along with the small gap separating them. The width of each gate at the center is designed to be 5 µm.

When the SHJI dopant-free lateral p–n junction is operated in DC mode, it behaves similarly to its RQW counterpart. Once the forward bias crosses the diode turn-on threshold, the resulting EL and I_{pn} quenches in a matter of seconds, indicating that local parasitic charging is taking place here as well. The possible mechanisms for parasitic charging in the SHJI device are the same as those outlined for the RQW device (Section 3.7). By operating the device in the Set-Reset mode to clear away parasitic charges, EL quenching is circumvented. All the following results correspond to when the device is operated in

the Set-Reset mode.

From Fig. 4.3, it is evident that the p-type side emits brighter (albeit patchier) luminescence than the n-type side, regardless of whether the corresponding ohmic contacts are floating or grounded. The intuitive reason for this is that electrons have a higher mobility than holes due to their lower effective mass, and may be able to tunnel across the barrier at the intrinsic gap with a higher probability than holes. Note that for the RQW sample, the 2DEG region under the n-topgate was brighter, and all spectra were obtained from this side (Section 3.6.1). The reason for this difference is not immediately evident.

An important point to note is that the EL emitted from this device is *not* confined to the center, i.e., not localized. In fact, the EL is visible in patches along the entire edge of the topgate (facing the center) on both the n- and p-sides, and extends all the way to the *mesa* edge at the upper and lower regions of the device. This result was also observed for the RQW sample from Chapter 3. Briefly, we hypothesize this is due to two reasons—alternate current pathways through the *mesa*, and minority current under the edges of the majority carrier side topgate. This is of course not ideal; more details on these issues and ways to solve them are addressed in Chapter 5.

EL spectra were acquired at the device center from the n-side and p-side for all four measurement configurations (Fig. 4.4). Two emission peaks are clearly visible from the n-side around E =1.515 eV, whereas only one major peak is visible at that energy from the p-side. Of the two peaks from the n-side, we know that the higher energy must correspond to the neutral exciton X^0 emission and the lower energy to a charged exciton emission peak. Since the charged exciton peak is absent from the p-side spectra, we can infer that it must be a trion X^- peak, since there is a surplus of electrons on the n-side that could bind to neutral excitons and result in X^- emission (this follows the same reasoning as in Chapter 3). We also see the LH peak at around $E = 1.518$ eV in Fig. 4.4 (a).

The lower-energy broadband peak from the p-side in Fig. 4.4 (b) may be due to charge traps associated with background impurities getting optically excited by the emission from the SHJI (biased self-illumination). This is yet to be verified, but can be done via temperature dependence measurements—cooling down the sample from a higher temperature should result in the saturation of the intensity of the impurity peak, while the intensity of the other peaks should keep increasing. Alternatively, this peak could be due to indirect excitons; these can be identified via lifetime measurements since their lifetime will be much longer than the neutral exciton lifetime. This broadband peak on the p-side was absent in the spectra from the RQW device in Chapter 3, possibly since

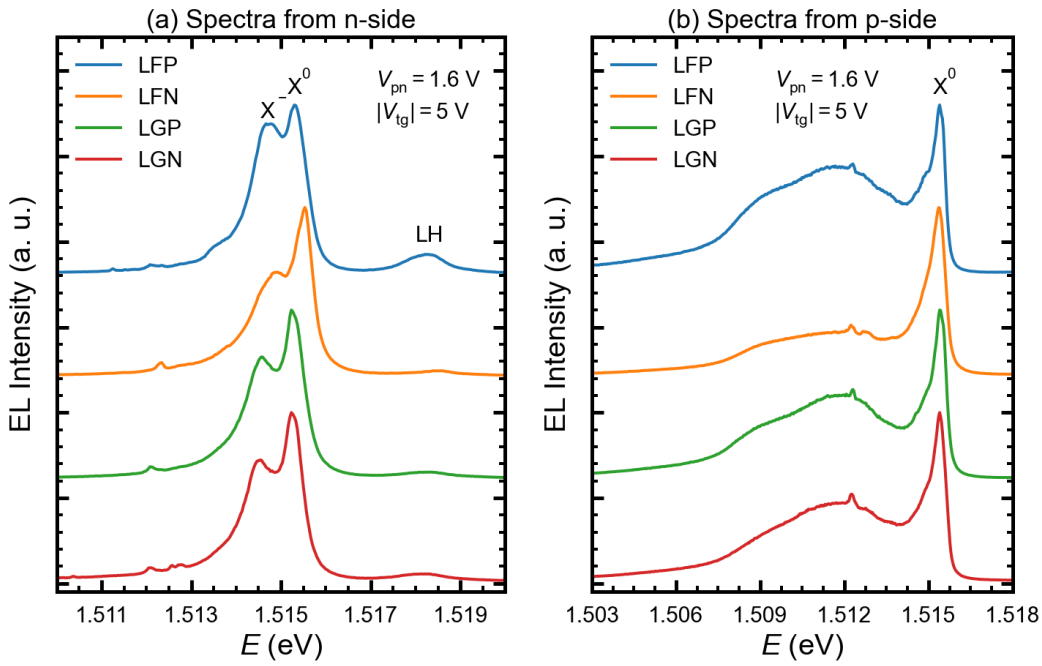

Figure 4.4: EL spectra from the (a) n-side and (b) p-side of the center of our device for the LFN, LFP, LGN and LGP measurement configurations. The X^0 and X^- peaks are clearly visible in the spectra from the n-side. The higher energy LH peak is also seen. The p-side emission has a broadband lower-energy peak in addition to the X^0 peak; the X^- peak is suppressed. Note that the spectra are normalized and vertically offset for clarity.

they were acquired only from the n-side for those devices. However, the spectra from the p-side of the SHJI device in Chapter 5 *does* show a similar energy (albeit narrow) peak (Fig. 5.13). This asymmetry between the n- and p-sides can be explained if we assume that the background impurities causing these lower-energy peaks are p-type—on the n-side, the effect of these impurities will be gated away, whereas this will not be the case on the p-side. An explanation for why the EL looks patchy on the p-side is that the inducing gate (ITO) may have non-uniform composition, and this non-uniformity may enhance the field in certain regions, which interacts with the p-type background impurities in the vicinity.

To study the effect of changing V_{pn} on the X^0 and X^- peaks, several spectra from the n-side were acquired at increasing values of V_{pn} using the same acquisition time (Fig. 4.5). $V_{pn} = 1.46\,V$ is below the diode turn-on ($\sim 1.5\,V$) and negligible counts are detected. For V_{pn} values above 1.54 V, the X^- peak intensity begins decreasing relative to the X^0 intensity, which stays relatively the same. The LH peak intensity varies with V_{pn} in a manner similar to the X^- peak.

Another point to note is that the spectral energy of the X^0 peak in this device

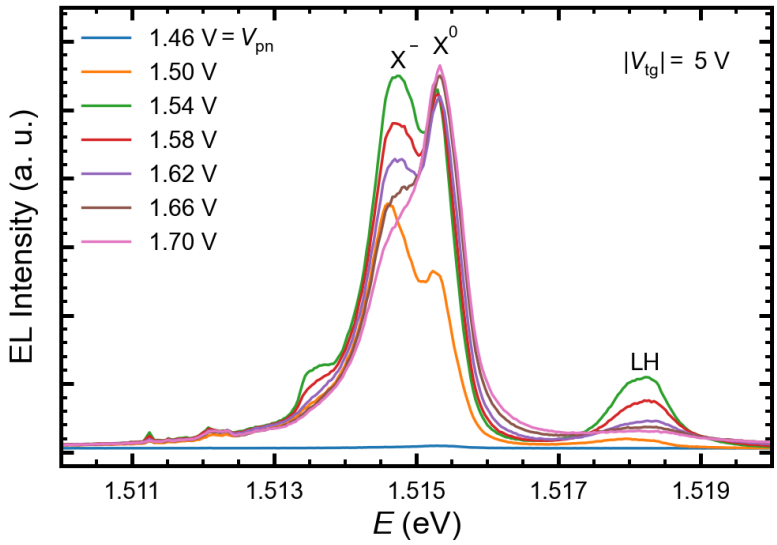

Figure 4.5: EL spectra from the n-side of the device as a function of V_{pn}. EL intensity counts are acquired over a period of 20 s and are *not* normalized. Below the turn-on threshold, the EL intensity is negligible ($V_{pn} = 1.46$ V). As V_{pn} increases, both X^0 and X^- peak intensities initially increase. Above $V_{pn} = 1.54$ V, the X^- peak intensity decreses while the X^0 intensity stays relatively constant. The LH peak intensity follows a similar trend as the X^- peak as a function of V_{pn}.

($E_{EL}(X^0) \sim 1.515$ eV) is smaller than that of our RQW devices (~ 1.534 eV), and also smaller than the bandgap of GaAs ($E_g = 1.519$ eV). Reproducing Eqn. 3.3 from Chapter 3,

$$E_{EL}(X^0) = E_g - \vec{p} \cdot \vec{E}_{ext} + E_{e\text{-}QW} + E_{h\text{-}QW} - E_{bx}, \tag{4.1}$$

where $E_{e\text{-}QW}$ and $E_{h\text{-}QW}$ are the bound state energies of the electrons and holes in the asymmetric triangular quantum well induced at the SHJI, E_{bx} is the X^0 binding energy, and $\vec{p} \cdot \vec{E}_{ext}$ is the small redshift due to the Franz-Keldysh effect; we assume this last term is negligible. We can then rewrite Eqn. 4.1 as

$$E_{bx} - (E_{e\text{-}QW} + E_{h\text{-}QW}) = E_g - E_{EL}(X^0) \approx 4\,\text{meV}. \tag{4.2}$$

Currently, we do not have an estimate for $E_{e\text{-}QW}$ and $E_{h\text{-}QW}$—these can be calculated by solving for the lowest bound state energy in an asymmetric triangular quantum well. For now, we cannot rule out the possibility that E_{bx} and $(E_{e\text{-}QW} + E_{h\text{-}QW})$ are both large (tens or hundreds of meV) or that both are small (a few meV).

4.3 Conclusion and outlook

To summarize, electron-hole recombination at GaAs/AlGaAs SHJIs is possible—we are the first to demonstrate this by fabricating and measuring the EL emission from a gated ambipolar dopant-free lateral 2D p–n junction, and operating it using the Set-Reset protocol. This bodes well since fabrication of SHJI devices, specifically the ohmic contacts, is easier and has a higher yield than RQW devices. The trade-off is that the spectra may be harder to analyze since the peak energies match closely to emissions one would expect from the substrate.

Our nano-LEDs are shown to be operable in four distinct measurement configurations, depending on whether the left or right side is n-type or p-type, and whether they are floating or grounded. Camera images of the device center show that the p-side of the device is consistently brighter than the n-side, in contrast to the RQW devices—the reason for this difference is not evident and needs to be studied. The emission is not confined the p–n junction interface, and is instead visible along the topgate edges facing the junction on both sides of the device. This is hypothesized to be due to alternate current pathways through the *mesa*. EL is also observed at locations where the topgates overlap the etched sidewall edges of the *mesa*—this is possibly due to minority currents under the edges of the majority carrier topgate. This delocalization of emission is also seen in the RQW devices, and solutions are proposed in Chapter 5.

The EL spectra from the n-side shows two distinct peaks that we believe to be the neutral (X^0) and charged (X^-) exciton peaks, similar to the n-side of the RQW devices. The broadband lower-energy peak from the p-side may be due to a light p-type impurity background in the wafer. The identities of these peaks can be confirmed through temperature dependence and power dependence measurements. The X^- peak decays at a lower temperature threshold than the X^0 peak. The linewidths of bound excitons due to impurities broaden at low temperatures, and their peak intensities increase with increasing excitation power faster than those of X^0 peaks. Like its RQW counterparts, the EL from the SHJI device also quenches quickly during DC mode operation. This may not only be due to local parasitic charging, but also charge movement due to biased self-illumination of the p-type background impurities.

5. Localization and time-stabilization of electroluminescence

When considering the requirements for a precursor to an efficient electrically-driven source of single and entangled photons, the nano-LEDs or dopant-free lateral 2D p–n junctions described in the previous chapters fall short in two major ways. First, the emission is unstable over short time intervals—this is due to parasitic charging, and although this is fixed by applying the Set-Reset protocol, the photon-statistics under this protocol are not time-stable at the single photon level, which is required for a quantum emitter. The second deficiency is that emission is not spatially localized to a single region. In fact, light is observed from regions under the topgate edges extending all the way to the edge of the *mesa*. There are two proposed reasons for these deficiencies—alternate current pathways through the device *mesa* away from the topgates, and minority charge carriers that travel along the topgate edges to recombine at the *mesa* edges. These faults would drastically reduce the emission and collection efficiencies of potential single photon emission. In this chapter, we attempt to address these shortcomings using a novel gate architecture. This architecture utilizes side surface gates—Ti/Pd gates deposited directly on the semiconductor surface above and below the p–n channel at the center.

A key point about the device described in this chapter is that the addition of the side surface gates creates many additional modes of operation, and the results obtained from most of these modes are very history-dependent, which makes explaining and understanding these results harder. The reader should treat this chapter like a puzzle—each section contributes a puzzle piece, but the bigger picture is visible only after collecting all pieces and completing the puzzle. In other words, it is important not to draw conclusions from results in a specific section of this chapter before reading the rest.

5.1 Experimental methods

5.1.1 Sample design and fabrication

The dopant-free lateral p–n junction described in this chapter was fabricated using the MBE-grown GaAs heterostructure wafer G0372, along the high-mobility crystal orientation $[1\bar{1}0]$. Top-down optical images of the device are shown in Fig. 5.1.

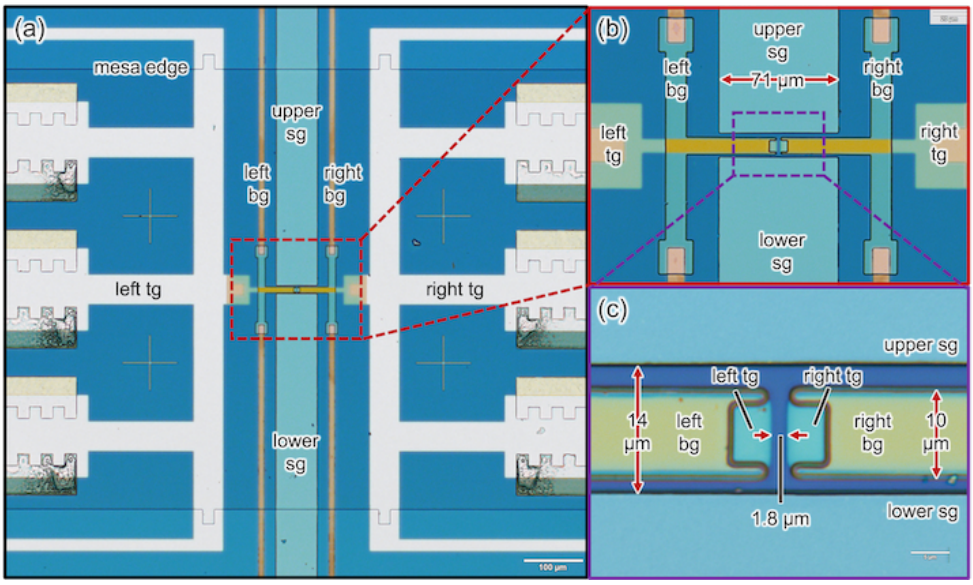

Figure 5.1: Top-down views of the fabricated sample at magnifications of (a) 5x (100 µm scale bar), (b) 20x (20 µm scale bar), (c) 100x (5 µm scale bar). The surface gates (sg) are ∼71 µm wide and ∼14 µm apart, while the topgates (tg)/barrier gates (bg) at the center are ∼10 µm wide, with a ∼1.8 µm tg gap.

The layer sequence of this wafer (starting from the substrate) is as follows (see Fig. 5.2): a 200 nm GaAs buffer, a 20-period smoothing superlattice made of a 2.5 nm GaAs layer and a 2.5 nm $Al_{0.3}Ga_{0.7}As$ layer, a 500 nm GaAs spacer, a 100 nm $Al_{0.3}Ga_{0.7}As$ top barrier, and a 10 nm GaAs cap layer. Carriers are induced at the SHJI at a depth of 110 nm. A control Hall bar (ambipolar induced HEMT) was also fabricated using the same wafer to characterize electron and hole transport.

The n-type and p-type ohmic contacts for this device were fabricated using the same recipe as outlined in Chapter 3 (see Appendix C). Annotated pattern masks for the lithography steps during fabrication are included in Appendix B. Prior to oxide deposition, two Ti/Pd gates (∼ 71 µm wide) were deposited on the surface of the device, with a ∼ 14 µm

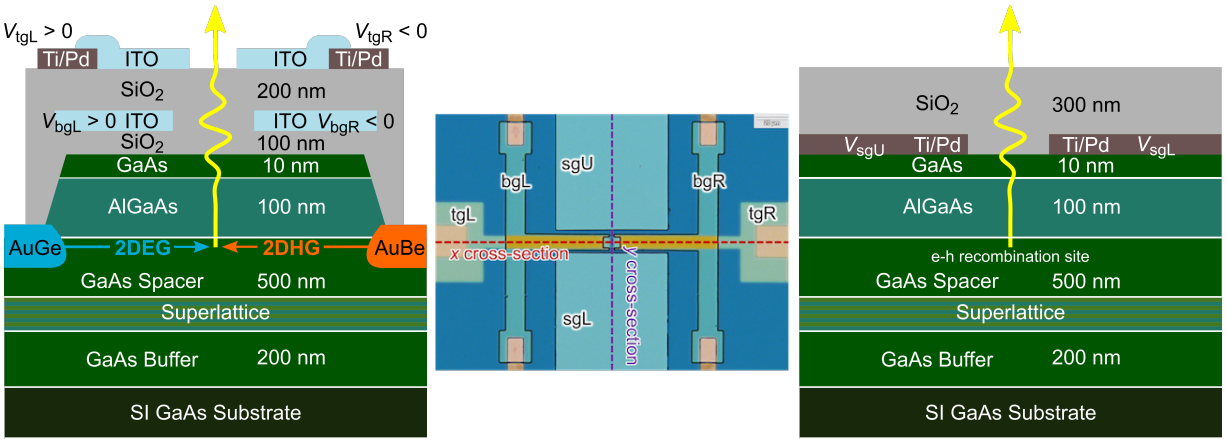

Figure 5.2: Schematic views of planes along the growth direction (z) for cross-sections passing through the device center along the x (LEFT) and y (RIGHT) directions of our fabricated ambipolar dopant-free lateral p–n junction showing the layers of the SHJI GaAs/AlGaAs heterostructure G0372, as well as the ohmic contacts and the gate structures. The top-view image in the middle shows the vertical cross-sectional lines along x (red, LEFT image) and y (purple, RIGHT image).

gap separating them. These gates run perpendicular to the channel direction. A 300 nm PECVD SiO_2 layer separates both the left and right inducing topgates from the surface. The topgate gap was measured to be ~ 1.8 µm. A left and right side 'barrier' gate—each with two pincers at the center—lies between the topgates and the surface, with 100 nm of SiO_2 below and 200 nm above. The topgates were designed to have an overhang of ~ 5 µm over the barrier gates along the channel direction, while the barrier gates overhang slightly relative to the topgates along the perpendicular direction. 30 nm semi-transparent ITO was used as the topgate and barrier gate materials close to the center of the device to allow EL to pass through, and Ti/Pd was used elsewhere.

The surface gates were included in the device design to address the issue of EL instability over time when operating in DC mode. Assuming a sizeable fraction of parasitic charge is built up close to the device surface, this charge could potentially be cleared away using a Schottky gate and lead to more stable emission. The actual implementation of EL time-stabilization using the surface gates and the conceptual model derived from the results differ from the above hypothesis.

The barrier gates were designed to solve the problem of localization. By applying a voltage on each barrier gate with the same polarity as the corresponding topgate, minority carriers would in theory be prevented from passing the potential barrier created by the barrier gates, and radiative recombination would be restricted to the center of the device. While this was the intended outcome, our measurements did not yield any confining

capabilities of the barrier gates, and they effectively behaved as topgates. A previous iteration of barrier gate architecture *did* successfully yield confinement, however this was due to the topgate overhang being longer and the width of the barrier gate being larger. Although the barrier gate did not work as expected, operating the device in a specific side gate voltage regime did yield interesting results with regards to localization; this will be discussed in Section 5.6.

5.1.2 Optical and electrical characterization

The sample was cooled to 1.6 K in an attocube attoDRY2100 closed-cycle optical cryostat. The objective lens used has a numerical aperture of 0.81 and a working distance of 0.70 mm. All EL spectra were frequency selected using a 1200 grooves/mm grating of a Princeton Instruments Acton Series SP-2750 optical spectrometer, before being captured on the integrated Princeton Instruments PIXIS 100 CCD camera thermoelectrically cooled to −70 °C. Data showing the change in emission intensity in counts/s as a function of time was also frequency selected by the grating and then detected using an Excelitas SPCM-AQRH APD.*

Optical video of the electroluminescing device was captured using a Watec WAT-910HX CCIR miniature camera with a 0.5 inch black and white CCD; still images from these videos are reported in this chapter. These images are qualitative, and are used as a way to infer the EL distribution over the device.

Transport characterization of the control Hall bar sample was conducted using a Janis pumped He–4 cryostat cooled to 1.65 K. The built-in electromagnet was used to apply an out-of-plane magnetic field of $B = \pm 0.1$ T; the Hall voltage was measured for each B–field value and their average taken. Note that the Hall bar sample does not possess surface or barrier gates.

Custom in-house electrical connections were used to connect the 2DPN device to voltage sources. DC voltages were applied to the topgates, barrier gates and surface gates using SRS SIM928 isolated voltage sources, and a Keithley 2401 SourceMeter was used to apply the p–n forward bias to the ohmic contacts. The Set-Reset sequence was implemented using custom code written to interface with the voltage sources using a GPIB communication channel. The device was operated in all four measurement configurations described in

* $\sim$ 60% detection efficiency around 800 nm, measured dark counts $\sim$ 200 cps

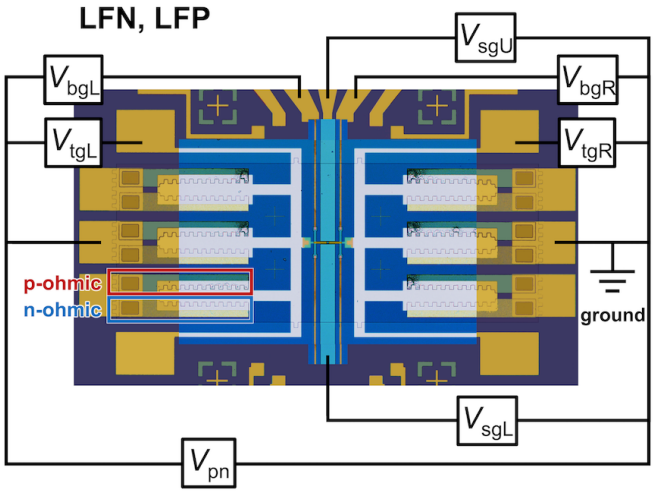

Figure 5.3: Circuit diagram for the measurement of our dopant-free lateral 2D p–n junction with surface gates, specifically for the LFN or LFP configuration. V_{pn} = diode forward bias; $V_{tg(L,R)}$ = topgate voltage (left, right); $V_{bg(L,R)}$ = barrier gate voltage (left, right); $V_{sg(U,L)}$ = surface gate voltage (upper, lower).

the previous chapter (see Fig. 4.2 and Table 4.1), but mainly in the LFN configuration (Fig. 5.3).

5.2 Transport characterization, mobility and density

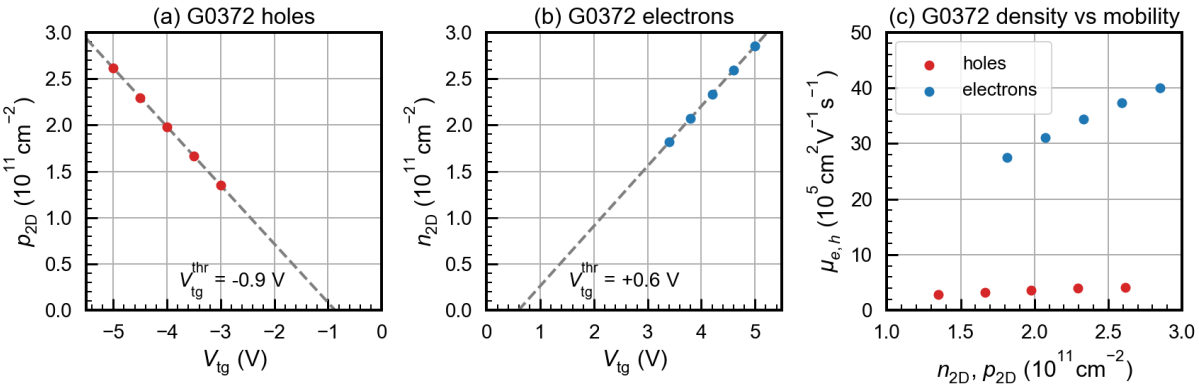

Figure 5.4: Four-terminal transport measurement results for wafer G0372. (a) Hole density (p_{2D}) as a function of topgate voltage (V_{tg}), $V_{tg}^{thr} = -0.9$ V. (b) Electron density (n_{2D}) as a function of V_{tg}, $V_{tg}^{thr} = +0.6$ V. (c) Hole and electron mobilities vs carrier density.

Fig. 5.4 shows the effect of the topgate voltage on the hole and electron densities in wafer G0372, plus the density vs. mobility relation for each carrier type. The V_{tg} vs. n_{2D}, p_{2D} relations are linear and reproducible, with no hysteresis or drift over time. The threshold topgate voltages for the holes ($V_{tg}^{thr} = -0.9\,V$) and electrons ($V_{tg}^{thr} = +0.6\,V$) are estimated from the intercept of the linear extrapolation of each curve with the V_{tg} axis.

The measured mobilities for this wafer are about $(3–4)10^6$ cm^2/Vs for electrons and $(3–4)10^5$ cm^2/Vs for holes, for densities of about $(1.5–3)10^{11}$ cm^{-2}. As expected, due to their lower effective mass, the electron mobilities exceed the hole mobilities (in this case by an order of magnitude). Since the 2DEG/2DHG is formed at the SHJI in G0372, there is less interface roughness and thus higher carrier mobility compared to wafers like G0375 or G0569 where carriers are induced inside a narrow 15 nm quantum well (see Fig. 3.3).

5.3 Ambipolar diode I–V traces

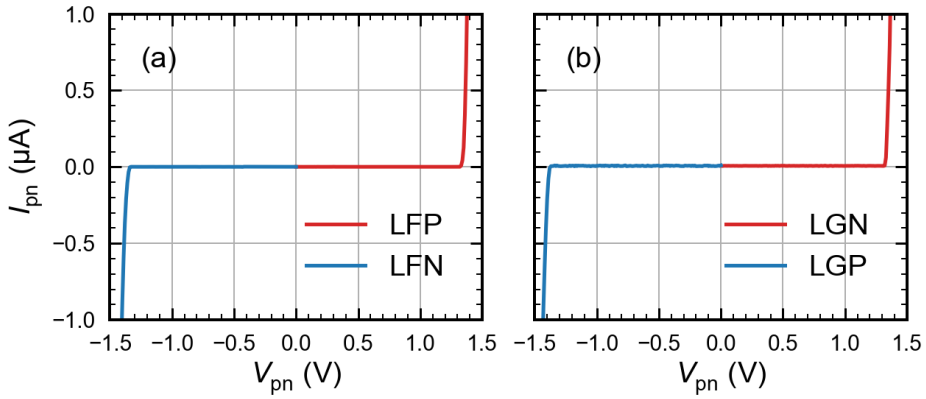

Figure 5.5: Diode current I_{pn} versus forward bias voltage V_{pn} (DC mode) for measurement configurations (a) LFP (red trace, positive V_{pn}) and LFN (blue trace, negative V_{pn}); (b) LGN (red trace, positive V_{pn}) and LGP (blue trace, negative V_{pn}). V_{pn} is applied to the floating side in each case. $|V_{tgL}| = |V_{tgR}| = 4.20\,V$ and $|V_{bgL}| = |V_{bgR}| = 2.00\,V$ for all traces. Additionally, the two surface gates are *disconnected* for these measurements. Note that reverse bias measurements are not shown for any configuration.

Like the SHJI device in Chapter 4, this ambipolar diode can also be operated in the measurement configurations LFN, LFP, LGN and LGP (Table 4.1). Fig. 5.5 shows typical I–V traces for the device in all four configurations. We choose the convention of applying the p–n bias to the floating side. The bias magnitude was ramped up from zero volts for all configurations (reverse bias measurements are not shown). The diode turns on close

to +1.5 V in the LFP and LGN configurations, and close to −1.5 V in the LFN and LGP configurations. These values match what is expected for GaAs ($E_g \sim 1.5$ eV). The nearly identical behaviour in all configurations shows that the device is symmetric. Additionally (like the devices from previous chapters), once the forward bias crosses the turn-on threshold, radiative emission due to electron-hole recombination begins but lasts only a few seconds before disappearing, implying that parasitic charging of the surrounding semiconductor material and the semiconductor/SiO_2 interface is taking place. Note that the device is being operated in the DC mode, using the nomenclature from Chapter 3.

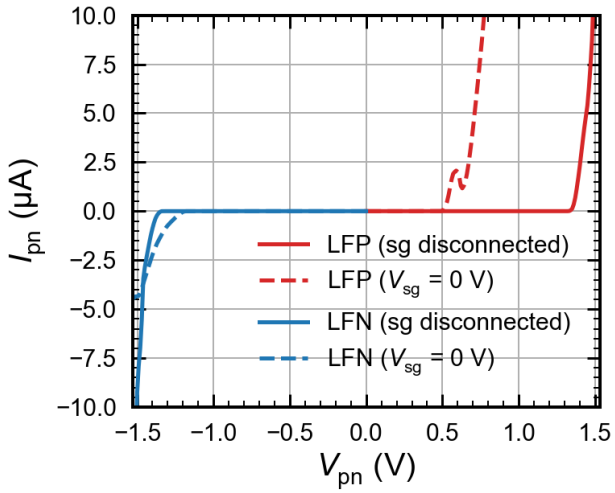

Figure 5.6: Diode current I_{pn} vs forward bias voltage V_{pn} (DC mode) for the LFP and LFN measurement configurations, when the surface gates (sg) are disconnected and connected to a voltage source set to 0 V. V_{pn} is applied to the floating side in each case. $|V_{tg(L,R)}| = 4.20$ V and $|V_{bg(L,R)}| = 2.00$ V for all traces. Note that reverse bias measurements are not shown for any configuration.

For the I–V traces in Fig. 5.5, the surface gates are not connected to any voltage source. Fig. 5.6 shows the effect of connecting the surface gates to a voltage source set to 0 V in the LFP and LFN configurations. The turn-on threshold is shifted to a lower value for both configurations, with a much larger shift for LFP. This indicates the presence of current leakage paths from the charge gases to the surface gates once they are connected, with holes leaking much more easily than electrons. No EL is emitted past these premature turn-on thresholds for either configuration.

5.4 Set-Reset operation

The Set-Reset (SR) mode clears away parasitic charges that build up during DC mode operation. As in DC mode, not only can the device be in one of the four main measurement configurations (LFN, LFP, LGN and LGP), the surface gates can also be connected to or disconnected from a voltage source (Table 5.1).

	LGN	**LFP**	**LFN**	**LGP**
$V_{sg} = 0\,V$	no EL	no EL	EL	EL
sg disconnected	EL	EL	EL	EL

Table 5.1: Mapping different measurement configurations to whether or not radiative EL emission is present. No EL is emitted in the LFP and LGN configurations when the surface gates are connected and $V_{sg} = 0\,V$.

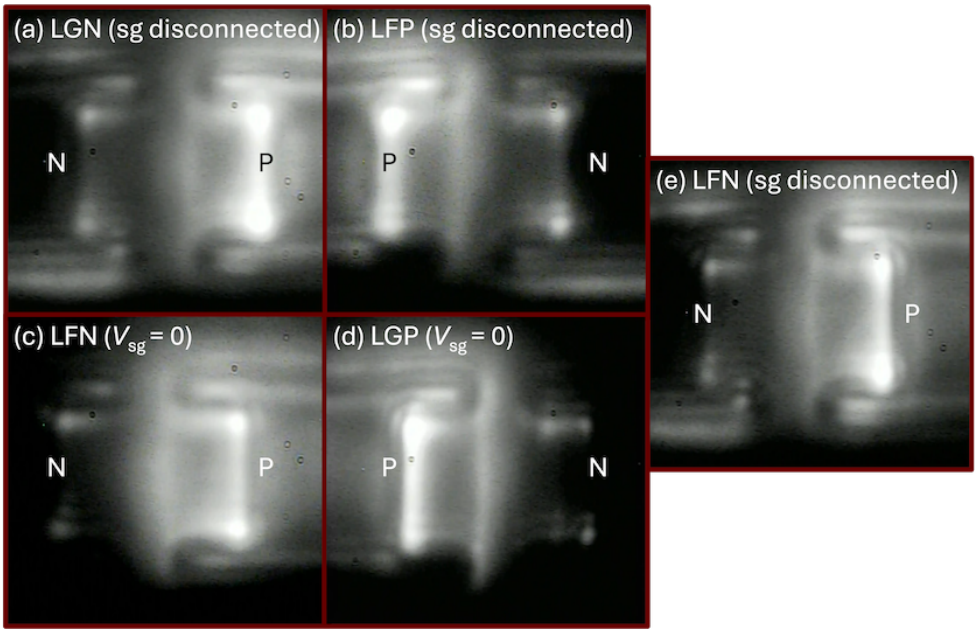

Figure 5.7: Still images from videos of the center of the device when operating in the configurations (a) LGN (sg disconnected), (b) LFP (sg disconnected), (c) LFN ($V_{sg} = 0\,V$), (d) LGP ($V_{sg} = 0\,V$), and (e) LFN (sg disconnected). Note that $|V_{pn}| = 1.59\,V$, $|V_{tg(L,R)}| = 4.20\,V$, and $|V_{bg(L,R)}| = 2.00\,V$ in all cases.

A few patterns emerge when observing EL from the device center in these various configurations (Table 5.1, Fig. 5.7), from which the following conclusions can be drawn:

– Connecting the surface gates and setting $V_{sg} = 0\,V$ eliminates EL emission for the LGN and LFP configurations, i.e. when the p-side is floating, whereas this is not the case

when the n-side is floating (Table 5.1). This is likely due to the ease of hole leakage to the surface gates in these configurations (as argued at the end of Section 5.3).

– Regardless of the measurement configuration (as long as there is radiative emission), EL is brighter and more concentrated on the p-side of the device, matching what was observed in the sample from the previous chapter. This implies that electrons are crossing the junction gap at a higher rate than holes, likely due to their higher mobility and larger tunneling probability across the junction gap.
– The EL distribution in Figs. 5.7 (a) and (e) are identical, implying that when the surface gates are disconnected, the device behaviour is independent of whether the left side is grounded or floating (with the right side being floating or grounded, respectively). In this sense, when the surface gates are disconnected, the device behaves like a dopant-free lateral p–n junction with *no* surface gates.
– Swapping from LGN [Fig. 5.7 (a)] to LFP [Fig. 5.7 (b)], or LFN [Fig. 5.7 (c)] to LGP [Fig. 5.7 (d)], results in the EL distribution undergoing a reflection transformation about a vertical line through the middle, implying bilateral symmetry of our junction.
– When the surface gates are disconnected [Figs. 5.7 (a, b)], more EL is visible on the n-side relative to when they are connected and $V_{sg} = 0\,\mathrm{V}$, but the EL is restricted to the edges of the topgate.
– Connecting the surface gates to a voltage source set to 0 V (and referenced to earth) with the n-side floating and the p-side grounded [Figs. 5.7 (c, d)] results in the overall brightness decreasing and the EL distribution becoming more asymmetric, i.e. dimmer on the n-side and more skewed toward the p-side. The brighter EL under the n-side topgate edge in Figs. 5.7 (a, b) could be a result of recombination of electrons with minority holes that have crossed the gap and are being drawn towards the n-type ohmic contacts by the forward bias along the region under the edges of the topgate. If we assume an excess of holes is present in the substrate due to p-type background impurities, connecting the surface gates to a voltage source set to 0 V may be enough to gate away the excess holes and reduce edge recombination under the n-side topgate.

A complete picture of how the EL distribution across the entire device is affected[‡] is outlined in Table 5.2 and the associated device map in Fig. 5.8. We first look at the results from SR operation. When the surface gates are disconnected, there is stray EL visible in several locations away from the center, namely the *mesa* edges on the n-side and p-side (locations 8 to 15), and along the edge of the p-side topgate (between 4 and 11, 5 and 15).

[‡] Specifically for the LFN configuration, but we assume this extends to LGP, taking into account reflective symmetry.

Map locations	SR mode (sg disconnected)	SR mode (V_{sg} = 0 V)	DC mode (sg disconnected)	DC mode (V_{sg} = 0 V)
1 to 6	very bright	bright	dim, quenches in 5 s	very dim, only at 1
7	dim	dark	dim, quenches in 5 s	dark
8 to 15	some EL	dark	some EL, quenches in 5 s	some EL, quenches in 5 s
lines connecting 4 – 11, 5 – 15	dim, patchy	dark	dark	dark
everywhere else	dark	dark	dark	dark

Table 5.2: EL distribution over the entire device in SR and DC modes when the surface gates are disconnected, or connected and set to 0 V. DC mode is entered into either by ramping up forward bias from below the turn-on threshold, or by switching into it directly from SR mode. Map locations are based on numbers in Fig. 5.8. Note that the device is operated in the LFN configuration.

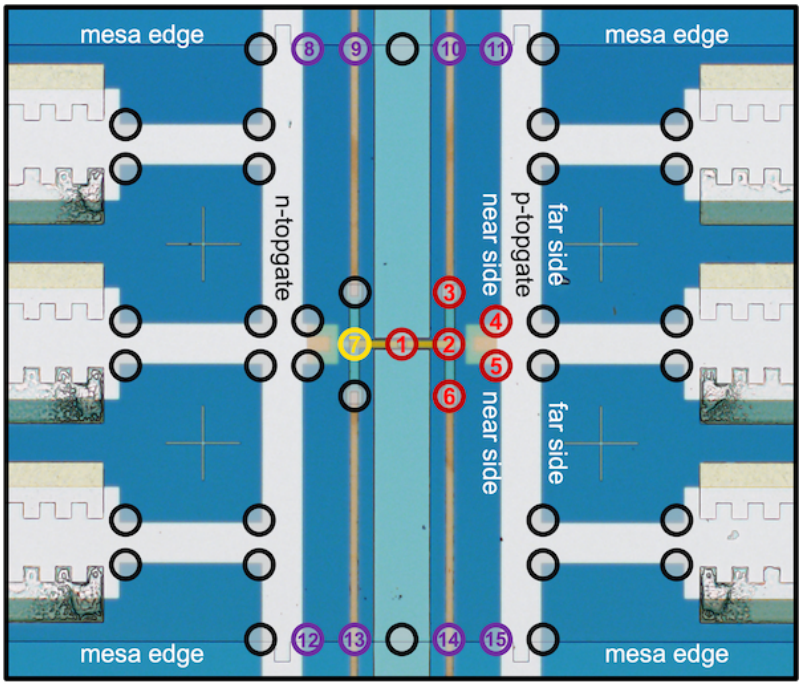

Figure 5.8: Top-down image of the device mapping out several key locations for the LFN configuration. The location numbers are colour-coded according to their groupings in Table 5.2—**red:** 1 to 6; **yellow:** 7; **purple:** 8 to 15; **black:** dark regions of special interest (corners, gate-*mesa* edge overlaps).

These locations are on the side of the n- and p-topgate facing the center of the sample (the near side), and not the far side. Essentially, minority electrons cross the gap and travel under the near side edges of the p-side topgate, moving all the way to the *mesa* edge in an attempt to reach the p-type ohmic contacts; minority holes do the same on the n-side of the device. Additionally, alternate current pathways for electrons through the *mesa* could be contributing to the EL along the near side edge of the p-topgate. The main vertical

arm of the p-side topgate acts as a barrier for the minority electrons, preventing them from reaching the region under the far side of the p-topgate and recombining. EL due to recombination at the *mesa* edges was observed to have lower energies than the EL from the device center; we can thus attribute the *mesa* edge recombination to charge traps at the etched surface. This energy difference was not seen for EL along the edge of the p-side topgate.

With the surface gates connected and $V_{sg} = 0\,\mathrm{V}$ in SR mode, light is only visible at the center and a few locations along the p-side topgate close to the center. Following the logic that setting $V_{sg} = 0\,\mathrm{V}$ may be gating *away* excess minority holes on the n-side, it could also be inducing a region of confinement for the minority electrons on the p-side, reducing their mobility and preventing them from traveling along the region under the p-topgate edge. Their positioning could also be blocking alternate current pathways for electrons through the *mesa* outside of the p–n channel.

For the results in the last two columns of Table 5.2, instead of entering DC mode operation directly by increasing the forward bias from below the turn-on threshold, the device is instead operated in SR mode and then *switched* into DC mode. This sequence of operations results in EL that lasts about 5 s post-switch. When the surface gates are not connected, this short-lived EL appears from mostly the same locations that EL is visible during SR operation—locations 1 through 15—but not along the near side edge of the p-topgate. This tells us that the phenomenon of alternate current pathways through the *mesa* could be a problem only during SR operation. When the surface gates are connected and $V_{sg} = 0\,\mathrm{V}$, the device in DC mode still emits light from points along the upper and lower *mesa* edges overlapping with the topgates, despite those locations being dark in SR operation. This indicates that even though V_{sg} is set to 0 V, minority carrier current pathways (both n- and p-type) are still forming under the edges of the topgates in an attempt to reach the ohmic contacts of the opposite polarity, instead reaching the charge traps along the *mesa* edge and recombining. The difference is that in this configuration they begin to radiate only after switching from SR mode to DC mode.

Fig. 5.9 shows EL spectra from the center of the device operated in the Set-Reset mode for three different configurations. The main peak from the LGP ($V_{sg} = 0\,\mathrm{V}$) and LGN (sg disconnected) spectra match in energy, and possibly correspond to the neutral exciton (X^0) peak. The LFP (sg disconnected) spectrum possesses an additional lower energy peak, likely a charged exciton peak. Measurements to verify peak identities will be completed in future work.

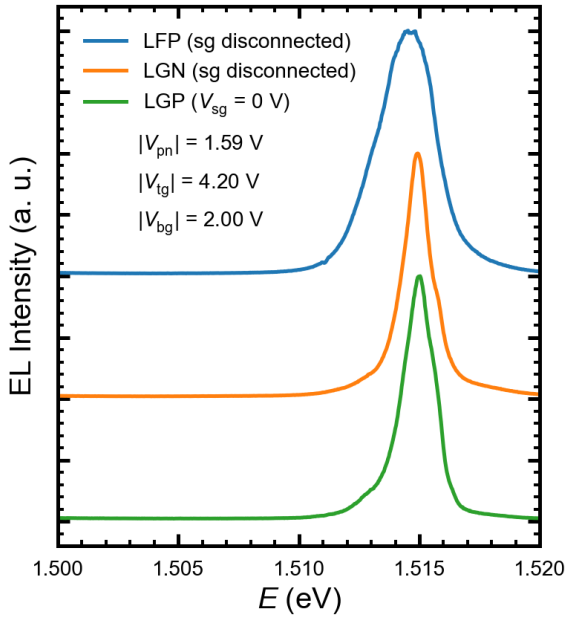

Figure 5.9: EL spectra for the device in SR mode for three different measurement configurations. The spectra are offset along the y-axis for clarity.

Summarizing the various conclusions in this section:

- A lateral dopant-free p–n junction device with *disconnected* surface gates behaves like a device with *no* surface gates.
- The device possesses bilateral symmetry. In other words, there is effective equivalency between the LFN and LGP configurations or the LGN and LFP configurations.
- In order to utilize the side surface gates, the p-side must be grounded and the n-side floating, i.e. the device must be operated in the LFN or LGP configuration. No EL is observed in the LFP or LGN configurations, likely due to hole leakage to the surface gates. For the remainder of this chapter, results from mainly the LFN configuration are reported.
- Electrons cross the junction gap from the n-side to the p-side to radiatively recombine with holes at a higher rate than holes crossing the gap to recombine with electrons.
- With the surface gates disconnected, alternate current pathways of minority carriers through the *mesa* and along the regions under edges of the majority side topgate causes delocalized emission along the near side edge of the p-topgate (in SR mode) and the overlap of the *mesa* edges with the n- and p-topgates (in SR and DC modes).
- When the surface gates are connected to a voltage source referenced to earth ($V_{sg} = 0\,\text{V}$), EL away from the center is completely removed in SR mode, but persists along the *mesa*

edges in DC mode.

An important point to note is that a device with a very similar gate architecture was operated in a majority of the various configurations detailed in this section, and was observed to exhibit behaviour that matches perfectly with the above results, indicating the replicability of these samples.

5.5 Non-zero surface gate potential

Like insulator-separated topgates, applying a positive (negative) potential on surface or Schottky gates can induce a 2DEG (2DHG) at a SHJI below them, assuming these carriers are available to populate. However, the absence of an insulator also means that these gates are more easily susceptible to carrier leakage past a certain voltage threshold.

We are already familiar with a scenario for parasitic local charging of our device (see Section 3.7) that results in EL decay and non-radiative electron-hole recombination. To recap, when applying a forward bias, charges escape confinement at the SHJI in the gap between the 2DEG and 2DHG. These escaped charges enter the surrounding GaAs/AlGaAs material, and some reach the surface.

We now propose a conceptual model to understand the effect of the side surface gates. When a small bias is applied to the surface gates, instead of escaping everywhere, the parasitic charge collects in the potential wells induced at the SHJI underneath the surface gates. Of course, this applies to only one type of charge carrier (electron or hole) at a time, since the polarity on the surface gates is the same. Additionally, since the surface gates are in close proximity to the topgates, increasing the magnitude of the surface gate bias could deplete the charge carrier gas under the topgate with the opposite polarity. This model can be used to explain the data in Fig. 5.10.[†]

Let us first tackle the $V_{sg} < 0$ regime. As V_{sg} is reduced from 0 V to −0.5 V, I_{pn} decreases marginally from 2.30 µA to 2.00 µA, while I_{sg} stays at 0, implying there is no leakage to the surface gates. This decrease in I_{pn} could be due to a reduction in the 2DEG density under the left topgate as V_{sg} becomes more negative. Meanwhile, a 2DHG comprised of holes that have escaped confinement forms below the surface gates. Below $V_{sg} = -0.5$ V, the surface gates begin to leak. This leakage current (I_{sg}) is *negative*, implying there is a flow of

[†] Note that the device is measured in DC mode in the LFN configuration (see Fig. 5.3), and has no prior history.

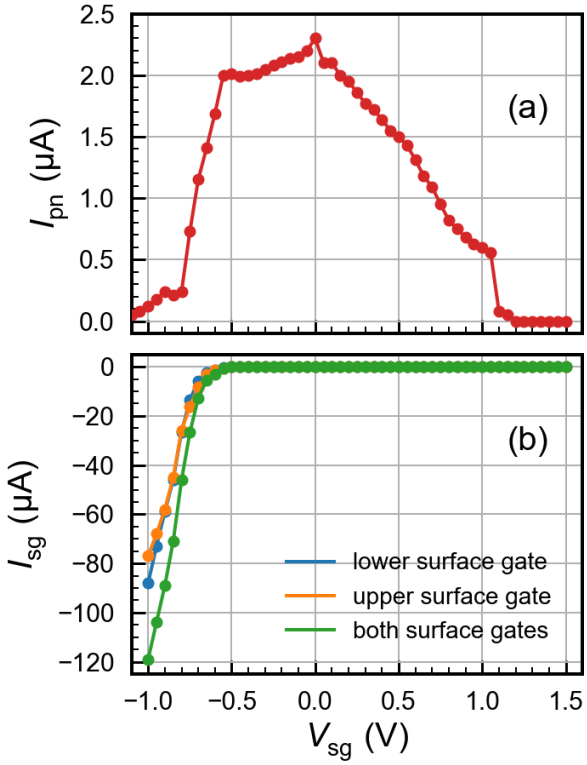

Figure 5.10: (a) I_{pn} and (b) I_{sg} as a function of V_{sg}. The device measured in DC mode in the LFN configuration, and is non-radiative for these measurements. The blue (orange) curve in (b) corresponds to when the lower (upper) surface gate is connected and the upper (lower) surface gate is disconnected. The green curve is when both upper and lower surface gates are connected to the same voltage source and ammeter. Note: $|V_{pn}| = 1.59\,\text{V}$, $|V_{tg(L,R)}| = 4.20\,\text{V}$, $|V_{bg(L,R)}| = 2.00\,\text{V}$.

positive charge away from the device. In other words, holes are leaking from the 2DHG to the surface gates. The magnitude of the leakage current does not decay with time, because there is a continuous supply of holes from the p-type ohmic contacts to the surface gates via the collective 2DHG under the p-topgate and the surface gates. There is simultaneously a sharp drop-off in I_{pn} for V_{sg} below $-0.5\,\text{V}$—as hole leakage increases, there are fewer holes left to recombine with electrons injected into the 2DHG. This continues until I_{pn} is fully pinched off at $V_{sg} = \text{-}1.2\,\text{V}$.

Moving onto the $V_{sg} > 0$ regime, we see a similar trend in I_{pn}. As V_{sg} increases, I_{pn} decreases due to the 2DHG density decreasing; the rate of decrease is sharper than in the $V_{sg} < 0$ regime. This sharper decrease makes sense if we assume that the majority of the p–n current is due to electron-hole recombination happening on the p-side.[‡] I_{pn}

[‡] Recall that the observed EL is concentrated on the p-side.

eventually pinches off at $V_{sg} = +1.2\,\text{V}$. The I_{sg} curve, however, does not show a similar trend in comparison to the $V_{sg} < 0$ regime. We have observed electron leakage to surface gates for voltages above 0.9 V in the past in our single-electron pumps (Fig. 2 (d) in Ref. [24]); however, no leakage of electrons to the surface gates was observed in the current device even for $V_{sg} = +1.5\,\text{V}$. Again, this could be due to a lightly p-doped background in the wafer substrate that prevents electrons from leaking (from the 2DEG under the n-topgate to the surface gates) for this voltage range when the device has had no history. Note also that the surface gates in Ref. [24] overlap the area of influence of the topgates, making gate leakage easier—that is not the case for our current device.

Set-Reset operation with *non-zero* V_{sg} yields fairly complex charge carrier dynamics. The behaviour of the device is very different in the $V_{sg} < 0$ and the $V_{sg} > 0$ regimes; this is discussed in the subsequent sections.

5.6 Localization

As discussed in Section 5.4, operating the device in SR mode with $V_{sg} = 0\,\text{V}$ yields EL that is not perfectly centered but concentrated on the p-side and spread out over a $\sim (150 \times 150)\,\mu\text{m}^2$ area. As V_{sg} is lowered and hole leakage from the 2DHG to the surface gates is increased, we observe the total EL intensity emitted per set-reset cycle drops, until it completely pinches off at $V_{sg} = -1.2\,\text{V}$ (this matches the pinch-off for I_{pn} when the device is operated in DC mode, see Fig. 5.10). More interestingly, the EL distribution shifts toward the center of the device prior to pinch-off, and becomes perfectly symmetric at around $V_{sg} = -0.9\,\text{V}$ (left image in Fig. 5.11). Scanning the rest of the sample in this state confirms there is no light emission from anywhere else on the device, and that the EL is restricted to location 1 on the sample map (see Fig. 5.8).

Let us understand the dynamics at play in this configuration. From our proposed conceptual model, as V_{sg} becomes more negative, the 2DEG density on the n-side decreases in the regions adjacent to the surface gates. Additionally, the 2DHG under the surface gates merges with the p-topgate 2DHG, and holes begin to leak to the surface gates. This merging is aided by the presence of p-type background impurities. For a sufficiently large magnitude of V_{sg}, the 2DEG is completely depleted at the center which instead becomes an extension of the 2DHG. Now, instead of crossing an insulating gap at the center, electrons driven by the forward bias meet a sea of holes at the center and recombine with them there, yielding a symmetric EL distribution. However, the EL is dim since a significant

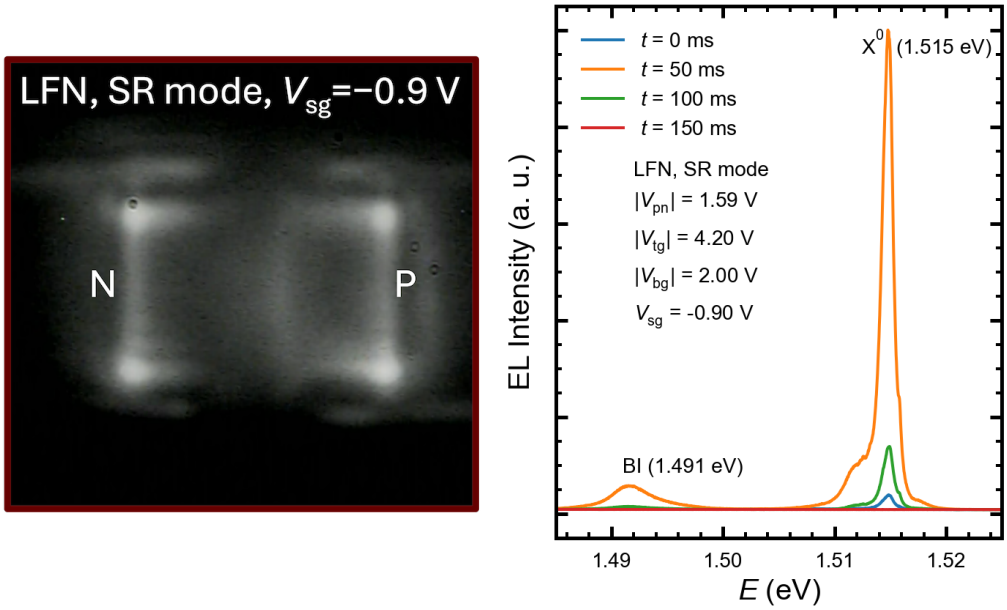

Figure 5.11: (LEFT) Still image from a video of the center of sample operated in SR mode in the LFN configuration with $V_{sg} = -0.90\,\text{V}$. The EL is localized, centered and symmetric, but dimmer than when $V_{sg} = 0\,\text{V}$. (RIGHT) EL spectra captured at four different times during a single set-reset cycle when $V_{sg} = -0.90\,\text{V}$. The intensity of the neutral exciton peak [$E(\text{X}^0) = 1.515\,\text{eV}$] reaches its maximum at $t = 50\,\text{ms}$ (orange curve). An additional small peak due to background impurities (BI) that appears due to self-illumination is seen at a lower energy [$E(\text{BI}) = 1.491\,\text{eV}$]. For these measurements, $|V_{\text{pn}}| = 1.59\,\text{V}$, $|V_{\text{tg(L,R)}}| = 4.20\,\text{V}$, and $|V_{\text{bg(L,R)}}| = 2.00\,\text{V}$.

fraction of the holes are lost to I_{sg} leakage and are not available to recombine with the electrons.

Why does radiative electron-hole recombination not take place further away from the center on the p-side? In other words, why is the EL localized to the center? When $V_{sg} = 0\,\text{V}$, EL is visible at locations 2 to 6 in addition to location 1 (see Fig. 5.8) due to minority electron current along the edges of the 2DHG under the p-topgate. This minority current is now blocked by a wide wall of holes running perpendicular to the channel, effectively centering and localizing the emission.

Switching from SR to DC mode with this gate voltage configuration and forward bias does not yield EL lasting even a few seconds; the device EL quenches *immediately*. I_{pn}, however, remains non-zero, indicating non-radiative recombination.

The graph on the right of Fig. 5.11 shows the EL spectrum neutral exciton peak for this measurement configuration. The exciton energy is unchanged from when $V_{sg} = 0\,\text{V}$.

5.7 Time-stabilization

Running the device in SR mode with $V_{sg} > 0$ does not shift the spatial distribution of EL emission. Instead, as V_{sg} increases, the device begins to 'blink'—over a measurement of several set-reset cycles, a fraction of them are found to be non-radiative. Additionally, while this blinking process appears to be stochastic to a degree, the average frequency of blinking measured over a duration of several cycles increases with increasing V_{sg}, until the device completely stops luminescing at $V_{sg} \sim +1.1\,\text{V}$. Each *off* state during blinking is associated with a large *positive* spike in surface gate leakage current ($I_{sg} \sim 80\,\mu\text{A}$[†]). In contrast, the leakage current during radiative emission is two orders of magnitude smaller ($I_{sg} \sim 0.80\,\mu\text{A}$). In other words, any large leakage of electrons to the surface gates during Set-Reset operation kills the possibility of radiative electron-hole recombination.

An interesting observation is that the measured values of I_{sg} and I_{pn} are exactly the same when the device is in the off state during blinking. Intuitively, one would assume that I_{pn} should tend to zero when the surface gates are leaking (as seen for the $V_{sg} < 0$ regime), since electrons would fail to cross the gap and reach the p-side, instead flowing directly to the surface gates. Looking at the LFN measurement circuit in Fig. 5.3 clears up this confusion. Rewording the scenario from the perspective of current, we can say that a positive current flows directly from the surface gates to the n-side of the junction, bypassing the p-side. Tracing the current path through the whole circuit, and keeping in mind there is no charge flow across the diode, we see that the current measured at the voltage source supplying forward bias must equal the sum of the currents measured by the sources supplying voltage to the two surface gates, i.e., $I_{pn} = I_{sgU} + I_{sgL} = I_{sg}$. Note that this means there is no actual current flow across the p–n junction. An observation that naturally follows this discussion is that setting a compliance (upper limit) of $\sim 30\,\mu\text{A}$ on I_{sg} completely eliminated blinking during Set-Reset operation.

Switching the device from SR mode to DC mode in the $V_{sg} > 0$ regime yields a result opposite to that obtained in the $V_{sg} < 0$ regime. Instead of the EL getting quenched immediately, we instead achieve *time-stable* EL emission in standard DC operation, without the need for the Set-reset protocol. This happens starting at $V_{sg} = 0.55\,\text{V}$. An important caveat is that the switchover from SR to DC mode must occur when the device is luminescing (i.e. in the *on* state) and *not* in the off state of the blinking process (which can be easily achieved by setting a compliance on I_{sg}). If the SR to DC switchover occurs when the

[†] Here, I_{sg} is the total current leaking through both upper and lower surface gates.

device is off, the device is stuck in this configuration, in which case the surface gates keep leaking ($I_{sg} \sim 80\,\mu A$) and there is no EL emission.

How does this measurement configuration and sequence of operations yield time-stable EL? To answer this, we return to our trusty conceptual model. As the device is operated in SR mode, electrons escape vertical confinement at the junction interface, according to the local parasitic charging mechanism. Some of these electrons get trapped in the induced triangular potential wells underneath the positively biased surface gates. For device operation over several set-reset cycles, the electrons stochastically leak to the surface gates for a certain fraction of these cycles, corresponding to the off state during blinking. If we switch over from SR to DC mode when the device is in this state, the device gets locked in this configuration—the electron current leakage path stays open, and we end up with no EL. Now, when the device is in the on state during SR operation, the surface gate leakage path is closed, and the p–n channel is open and conducting. An additional key point is that under each surface gate, there is a 2DEG present that is *not contiguous* with the 2DEG on the n-side. This non-contiguity could be due to the p-type impurity background in the substrate. These 2DEGs under the surface gates are formed from electrons that have escaped channel confinement during the off periods of blinking in previous cycles of the Set-Reset operation. If the device switches to DC mode in this state with the device luminescing, these 2DEGs stay trapped underneath the surface gates with nowhere to go. These static pools of electrons on either side of the channel are a strong presence of negative charge that can repel other electrons. Any electrons in the channel subsequently crossing the junction from the n-side to the p-side are corralled by the repelling Coulombic forces of the static pools on either side to stay in the channel and not escape gate-induced confinement as easily. This drastically slows down the rate of parasitic charging of the surrounding region, which would otherwise result in short-lived DC mode EL (as observed for $V_{sg} = 0\,V$, or in the absence of surface gates; see Fig. 3.5).

As mentioned, managing the device history is very important for particular modes of operation. Entering DC mode from SR mode in the manner described above is *essential* for achieving time-stabilization. We found that if the device is operated directly in DC mode and V_{sg} is set to, say, $0.60\,V$ prior to applying a forward bias, the device does not luminesce once V_{pn} crosses the turn-on threshold. This is because there has been no opportunity for the time-stabilizing pools of electrons to form and stay underneath the surface gates—this can occur only during the off state regimes of blinking during SR operation.

How stable, really, is the EL in this configuration? Figs. 5.12 (a, b, c) track I_{pn} and EL intensity measured at the device center using an APD over time for three different surface

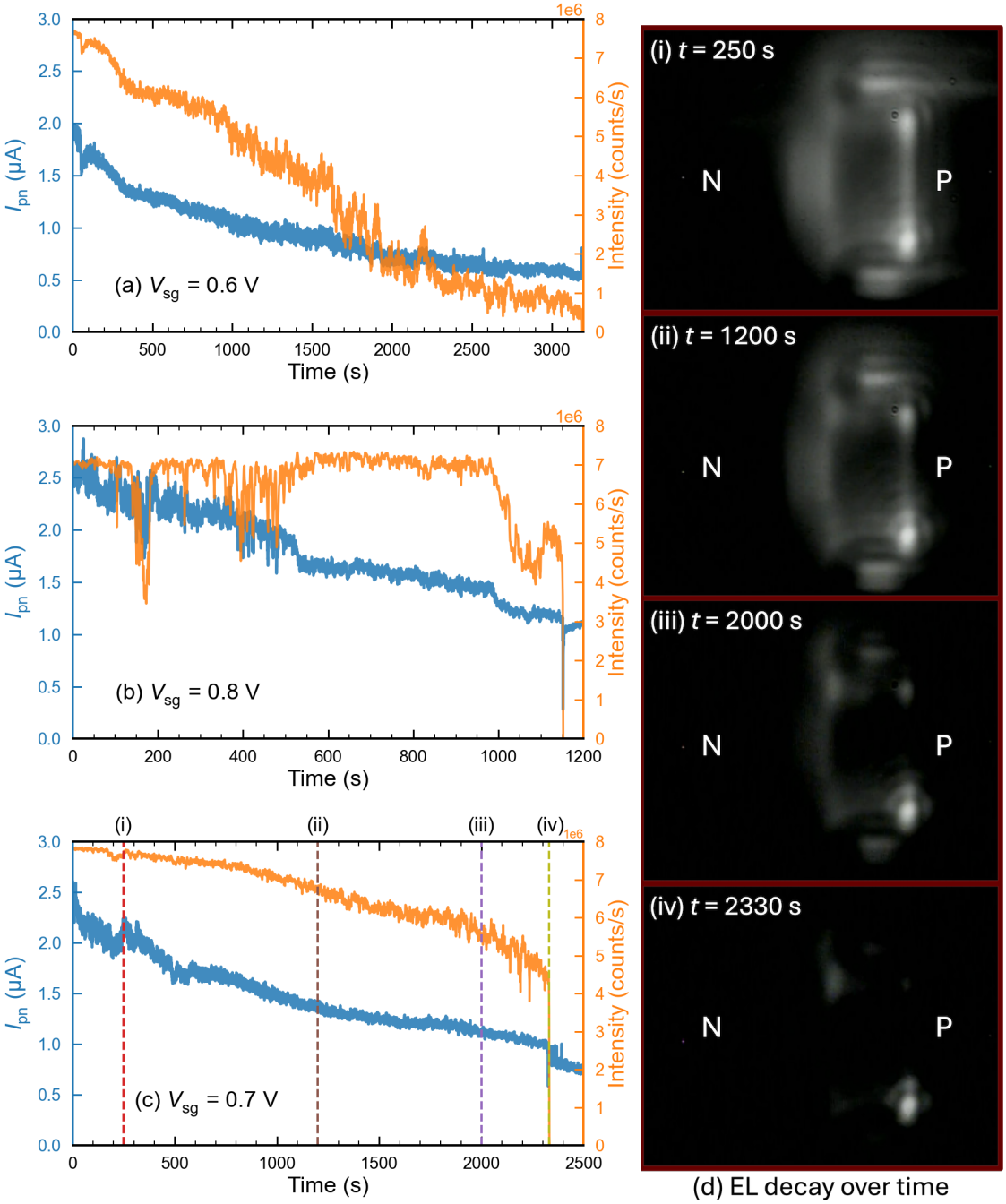

Figure 5.12: Tracking stability of I_{pn} and EL intensity over time for V_{sg} = (a) 0.6 V, (b) 0.8 V, (c) 0.7 V. (d) Images of device center for V_{sg} = 0.7 V showing decay of EL over time. Note: device is in the LFN configuration (EL is from the p-side on the right), with $|V_{pn}|$ = 1.59 V, $|V_{tg(L,R)}|$ = 4.20 V, $|V_{bg(L,R)}|$ = 2.00 V.

gate potentials. In all three cases, both EL and I_{pn} last much longer than we have previously recorded or known possible for such devices when measured in DC operation. The EL duration for V_{sg} = 0.6 V, V_{sg} = 0.7 V and V_{sg} = 0.8 V for these specific measurement

runs were approximately 50 min, 39 min and 19 min respectively. There is a fairly good correlation between the I_{pn} and intensity plots for each value of V_{sg}—fluctuations in the value of one of these parameters is mirrored in the other. The fact that both I_{pn} and EL intensity still decay over time implies there are still small leakage paths for parasitic charge into the surrounding substrate, but this leakage rate is very slow, allowing the EL to last a long time before quenching. Once EL quenches, I_{pn} persists but is non-radiative.

Fig. 5.12 (d) shows images of the device center captured at four different points in time during the $V_{sg} = 0.7\,V$ measurement run highlighted in Fig. 5.12 (c). The EL is restricted to the p-side, as is the case when $V_{sg} = 0$. Over time, the EL intensity drops everywhere uniformly, *except* for a spot at the concave corner of one of the 'pincer' features of the barrier gate [Fig. 5.12 (d) (iv)]. Interestingly, this state where the EL has decayed significantly can be artificially achieved even at $t = 0$ by throttling I_{pn}. A compliance of $\sim 0.90\,\mu A$ brings the device from the state in Fig. 5.12 (d) (i) to Fig. 5.12 (d) (iv) instantaneously, allowing us to study the emission from the isolated point at the pincer corner without having to wait. Also,this process is reversible—removing the compliance returns bright EL. Intuitively, it may be possible that operating the device with the throttled I_{pn} can increase the time-stability of emission—this would need to be investigated in future work.

The spectral curves in Fig. 5.13 show two distinct peaks. The neutral exciton peak ($E(X^0) = 1.515\,eV$) is present on the edge of the p-side topgate for both LFN and LGP configurations. Note that there is no emission from the n-side [see Fig. 5.12 (d)]. Also note the absence of a charged exciton peak—these are only visible in spectra from the n-side (and correspond to X^-) as seen in previous chapters. The lower energy peak at $E = 1.511\,eV$ corresponds to emission from location 'c', the same concave corner of the pincer feature of the barrier gate on the p-side (LFN configuration) where EL persists as seen in Fig. 5.12 (d) (iv). The fact that this peak is at a lower energy explains why EL emission persists from this spot after decaying everywhere else. Similar to the broadband lower-energy peak in Chapter 4, this peak is possibly due to the excitation of a charge trap state from a fixed background impurity in the substrate. This excitation may be amplified by the 'concentrated' electric field coming from the pincer corner. More research is required to understand these peaks better.

To report observations regarding the EL distribution across the entire device during time-stable operation, we must go back to the sample map in Fig. 5.8. As is the case when $V_{sg} = 0\,V$, switching the device from SR to DC mode when $V_{sg} = +0.60\,V$ results in EL at location 1 and at locations 8 through 15 along the *mesa* edges. The difference is that the EL persists—not only at location 1, as we have seen, but also along the *mesa* edges

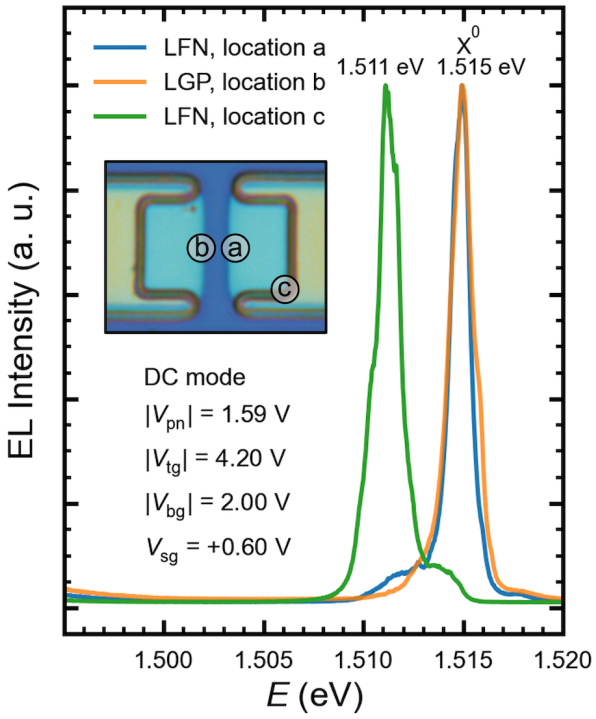

Figure 5.13: EL spectra captured at three different locations around the device center during DC operation with $V_{sg} = +0.60$ V. The peaks from locations a and b correspond to emission from the edge of the p-side topgate in the LFN and LGP configurations, respectively. Both these peaks coincide and correspond to X^0 ($E = 1.515$ eV). The peak from the the barrier gate pincer corner on the p-side (location c, LFN configuration) is at a lower energy ($E = 1.511$ eV), implying the possible presence of a charge trap.

(but *not* along the edges of the p-topgate). This indicates the presence of a persistent minority carrier current under the edges of the majority carrier topgate that is driven by the forward bias on *both sides* of the device. This is of course detrimental to the overall quantum efficiency of the device.

Routing the topgates to avoid the upper and lower *mesa* edges and instead directing them past the ohmic contacts would prevent *mesa* edge recombination increase the external quantum efficiency (EQE) by localizing the emission. The internal quantum efficiency (IQE) will technically reduce, since the contribution to radiative *mesa* edge recombination has become non-radiative. The only way for IQE to increase is to block the minority current paths entirely—this can be done by including an insulator-separated blocking gate on the p-side (see Fig. 1.2 in Section 1.2) whose confinement potential would prevent minority currents from flowing, in a manner similar to how the side surface gates work during localization. The difference is that this blocking gate would not be on the surface to avoid the issue of leakage currents. This needs to be tested in future work.

5.7.1 Calculating efficiencies

The data from Figs. 5.12 (a, b, c) can be used to calculate values for the IQE (η_{IQE}), EQE (η_{EQE}) and collection efficiency (η_{CE}). These efficiency numbers can be expressed as

$$\eta_{\text{IQE}} = \frac{\text{photons generated/s}}{\text{electrons supplied/s}} = \frac{\phi/\alpha}{I_{\text{pn}}/e} = \frac{\phi e}{I_{\text{pn}}\alpha}, \tag{5.1}$$

$$\eta_{\text{EQE}} = \frac{\text{photons extracted/s}}{\text{electrons supplied/s}} = \eta_{\text{IQE}} \times \eta_{\text{EE}}, \text{ and} \tag{5.2}$$

$$\eta_{\text{CE}} = \frac{\text{photons collected/s by objective}}{\text{photons generated/s}}. \tag{5.3}$$

Here, ϕ is the photon intensity or photon flux detected by the APD, I_{pn} is the current through the device, and e is the elementary charge. α is the fraction of generated photons detected by the APD after losses due to total internal reflection at the substrate–air interface, the collection angle of the objective lens, and the remaining optics in the collection path. η_{EE} is the extraction efficiency or the ratio of the rate of photon extraction from the device substrate to the rate of photon generation.

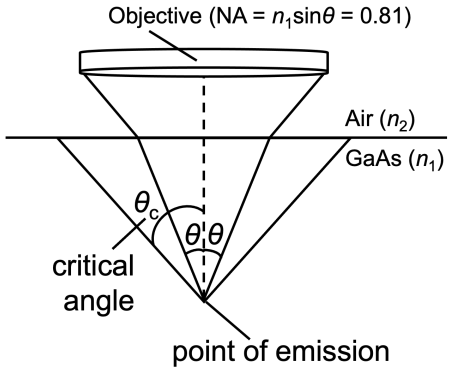

Figure 5.14: Cross-sectional schematic showing the cone of light accepted by the objective from a localized point of emission. θ is the angle corresponding to the NA of the objective. The substrate index (n_1) is assumed to be uniform and equal to that of GaAs for simplicity.

For the sake of simplicity, we assume that the emission is localized to a single point (see Fig. 5.14), and that the substrate is uniformly GaAs with the exciton dipole oriented in-plane (parallel to the substrate surface). A value for η_{EE} can be analytically estimated by first calculating the solid angle Ω_c corresponding to the critical angle θ_c for total internal

reflection at the substrate–air interface as per Snell's law—

$$\Omega_c = 4\pi \sin^2\left(\frac{\theta_c}{2}\right), \tag{5.4}$$

$$\text{where } \theta_c = \arcsin\left(\frac{n_2}{n_1}\right) = \arcsin\left(\frac{1}{3.5}\right). \tag{5.5}$$

We then find η_{EE} by taking the ratio of the surface area subtended by Ω_c to the total surface area of a sphere with radius r,

$$\eta_{EE} = \frac{\Omega_c r^2}{4\pi r^2} = \sin^2\left(\frac{\theta_c}{2}\right) = 2.08\% \tag{5.6}$$

η_{CE} is found in a manner similar to η_{EE}, but instead of using the critical angle, we use the angle θ corresponding to the numerical aperture (NA) of the objective lens (see Fig. 5.14). Our objective is part of attocube's LT-APO series and has an NA of 0.81. Using the well-known relation $\text{NA} = n_1 \sin\theta$, where n_1 is the refractive index of GaAs, we get

$$\theta = \arcsin\left(\frac{\text{NA}}{n_1}\right) = \arcsin\left(\frac{0.81}{3.5}\right), \tag{5.7}$$

and in turn, we calculate the efficiency of collection as

$$\eta_{CE} = \sin^2\left(\frac{\theta}{2}\right) = 1.36\%. \tag{5.8}$$

Here, we assume that the modal distribution in the far-field regime is uniform across momentum space.

These analytical estimations for η_{EE} and η_{CE} were corroborated with Lumerical FDTD simulations. Rather than assume uniform GaAs, wafer G0372 with the SHJI and other constituent layers was used in the model (see Section 5.1.1 for the detailed layer sequence). The emitter was assumed to be a localized, in-plane dipole source located 7.5 nm below the GaAs/AlGaAs SHJI. At the emission wavelength $\lambda \sim 818.4$ nm (corresponding to the neutral exciton emission energy of ~ 1.515 eV), a value of $\eta_{EE} \sim 1.64\%$ was obtained through simulation. From the simulated far-field emission profile in Fig. 5.15, the ratio η_{CE}/η_{EE} for the objective lens with $\text{NA} = 0.81$ is 80.64%. In turn, we get $\eta_{CE} \sim 1.32\%$. These simulated values for η_{EE} and η_{CE} match fairly well with the analytical estimations.

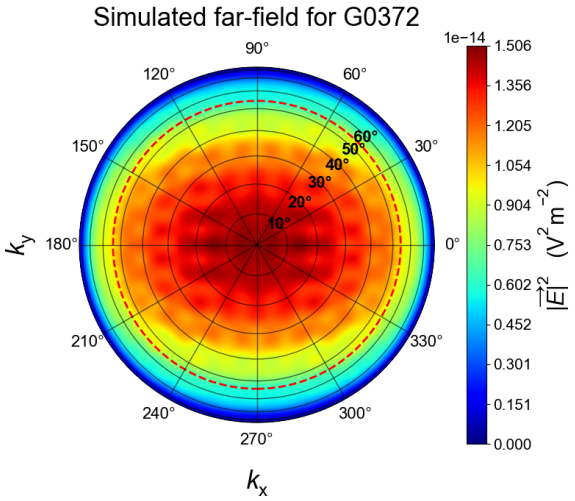

Figure 5.15: Simulated far-field emission profile for a dipole emitter in SHJI wafer G0372 for $\lambda \sim 818.4\,\text{nm}$ (corresponding to the neutral exciton energy, $\sim 1.515\,\text{eV}$). The dipole is oriented parallel to the substrate surface and is located 7.5 nm below the GaAs/AlGaAs SHJI. The dotted red circle corresponds to the collection angle of the objective lens with an NA of 0.81. From this profile, $\eta_{\text{CE}}/\eta_{\text{EE}}$ is found to be 80.64%.

η_{CE} can be boosted by incorporating a cavity around the emission region. A well-designed cavity shapes the emission into a single mode that is easier to collect (see Chapter 6).

optic	**efficiency**
objective lens	T = 0.850
silver mirrors 8×	R = 0.960
plate beamsplitter	T = 0.500
pellicle beamsplitter	T = 0.700
spectrometer	T = 0.268
lens at APD input	T = 0.998
APD detection efficiency	0.600
$\boldsymbol{\eta_{\text{optics}}}$ **(net)**	**3.44%**

Table 5.3: Efficiencies of all optics in the detection path. The spectrometer efficiency was *measured* and includes the transmission through the lenses at the input and output slits, as well as the reflection off the grating (1200 grooves/mm) and mirrors within the spectrometer. The efficiencies of the other optics were obtained from their respective data sheets. The calculated net efficiency η_{optics} based on these numbers is 3.44%.

To calculate η_{IQE} (and in turn η_{EQE}), we first estimate a value for α. This factor has two main contributions,

$$\alpha = \eta_{\text{CE}} \times \eta_{\text{optics}}, \tag{5.9}$$

where η_{CE} has been estimated analytically or through simulation, and η_{optics} is the effi-

ciency of the remaining optical elements in the detection path including mirrors, lenses, beamsplitters, the spectrometer grating and the APD. From Table 5.3, the net η_{optics} is $\sim 3.44\%$. Using this value, we can calculate upper bound estimates for α for our two cases: (i) when we use the analytical $\eta_{\text{CE}} = 1.36\%$, we get $\alpha \sim 4.68\times10^{-4}$; and (ii) for the simulated $\eta_{\text{CE}} = 1.32\%$, we get $\alpha \sim 4.54\times10^{-4}$. With these values of α, and using the measured current I_{pn} and photon intensity ϕ at time $t = 0$ obtained from the data in Figs. 5.12 (a, b, c), IQE and EQE for the device are calculated using Eqns. 5.1 and 5.2, respectively. Table 5.4 summarizes these results. The average IQE and EQE from these values are 1.19×10^{-3} and 1.95×10^{-5}, respectively.

			$\eta_{\text{EE}} = 2.08\%$, $\eta_{\text{CE}} = 1.36\%$		$\eta_{\text{EE}} = 1.64\%$, $\eta_{\text{CE}} = 1.32\%$	
V_{sg} (V)	I_{pn} (μA)	ϕ ($10^6 s^{-1}$)	η_{IQE}	η_{EQE}	η_{IQE}	η_{EQE}
0.6	1.9	7.7	1.39×10^{-3}	2.89×10^{-5}	1.43×10^{-3}	2.35×10^{-5}
0.7	2.5	7.0	9.58×10^{-4}	1.99×10^{-5}	9.88×10^{-4}	1.62×10^{-5}
0.8	2.4	7.8	1.11×10^{-3}	2.31×10^{-5}	1.15×10^{-3}	1.88×10^{-5}

Table 5.4: IQE (η_{IQE}) and EQE (η_{EQE}) calculated using data in Figs. 5.12 (a, b, c) for $V_{\text{sg}} = 0.6$ V, 0.7 V and 0.8 V. Two sets of values are shown in each case. The fourth and fifth columns show values corresponding to the analytically obtained $\eta_{\text{CE}} = 1.36\%$, while the last two columns correspond to the simulated $\eta_{\text{CE}} = 1.32\%$.

The efficiency of our devices can be improved in multiple ways, some of which have been mentioned already. Any improvement to the localization of EL increases η_{CE}. EL along the edges of the topgates facing the junction can be eliminated using the side gates discussed in this chapter. Delocalized EL due to recombination at the *mesa* edges as a result of minority currents under the edges of the majority carrier topgate may be mitigated by rerouting the topgates to go past the ohmics instead of over the *mesa* edge. However, this reduces but does not completely eliminate non-radiative electron-hole recombination, resulting in only a minor improvement in η_{IQE}. Minority currents may be completely eliminated using the potential from an additional blocking gate, placed perpendicular to the channel just past the site of recombination. Ideally, all radiative electron-hole recombination should be localized to a single point—this can be achieved using a cavity structure comprised of a lateral grating and a bottom mirror. Such a structure enhances the spontaneous emission rate via the Purcell effect, boosting η_{IQE} and η_{EQE}. The cavity would also couple the emissions into a single guided mode, enhancing η_{CE}. Chapter 6 discusses cavity enhancement in detail.

5.8 Conclusion and outlook

We have fabricated a dopant-free lateral 2D p–n junction or nano-LED with a novel gate architecture that combines topgates with channel-adjacent gates deposited on the surface. By changing the magnitude and polarity of the surface gate voltage, the device can be operated in different regimes. Operation with floated surface gates is equivalent to operating a nano-LED without surface gates. With zero volts applied to the surface gates, the device emits light only when the n-side is floating and the p-side is grounded. This has implications for a future quantum emitter, since our quantized charge pumps rely on surface-deposited quantum point contact (QPC) gates. For compatibility, a new pump design with QPC gates separated from the surface by a thin insulator must be tested.

For negative voltages ($V_{sg} \sim -0.9\,\mathrm{V}$), EL emission is localized during Set-Reset operation—the light is centered and symmetric about the junction. *Mesa* edge radiative recombination is curbed since the surface gates induce a wide barrier of holes that prevent minority electrons from forming currents under the p-topgate. Also, EL from the topgate edges facing the device center is quenched since alternate current pathways through the *mesa* are blocked by the barrier of holes. These are interesting results but this architecture is not practical for quantum light emission since the surface gates constantly leak and the emission cannot be localized in DC operation. Instead, we can learn from and adapt this design by using an insulator-separated blocking gate that induces the barrier of holes to create confinement and localization of emission.

For positive voltages ($V_{sg} \sim +0.6\,\mathrm{V}$) in DC operation, the EL emission is stable in time—the light lasts over several tens of minutes (600 times longer than a standard nano-LED), with the device internal quantum efficiency being $\sim 1.19\times10^{-3}$. From our conceptual model formulated to understand the behaviour of the device, the stabilization of emission over time occurs due to the formation of static pools of electrons under the surface gates that corral the channel electrons, reducing the rate of parasitic charging. The surface gates in this case are prone to leakage as well, so future designs can use insulator separated side gates that induce static pools of electrons via their own n-type ohmic contacts.

A nano-LED combining the usage of insulated side gates and a blocking gate would potentially extend the lifetime of stable emission and localize the emission area, and achieve this using just one operating regime. This would be very beneficial in the development of an electrically-driven quantum emitter fabricated using these materials.

6. Enhancing the emission, extraction and collection efficiencies

The lateral 2D p–n junctions described in the previous chapters emit light omnidirectionally. If we are successful in integrating a source of charge quantization into these p-n junctions to obtain a source of single photons, this omnidirectionality would be detrimental since we require high photon extraction efficiencies for bright quantum emitters. An obvious way to roughly double the count rate of collected photons is to integrate a mirror below the emission region. Based on fabrication constraints, a Bragg mirror[†] made of alternating semiconducting layers of contrasting refractive indices is the ideal option. This would require precise growth capabilities of an MBE chamber, but unlike metallic mirrors, this would avoid the need for flip-chip fabrication.

In addition to a bottom mirror, modifying the environment around the emission region to shape the emitted mode and enhance the rate of spontaneous emission via the Purcell effect would further boost the extraction efficiency. CBGs have been a long-standing candidate for this task when it comes to quantum dot emitters. We adapt these structures to be compatible with the existing architecture of our lateral planar LEDs.

6.1 Sample characterization methods

Room temperature reflectance measurements of samples were conducted using two different setups. Measurements of bare unpatterned wafers [see Fig. 6.3 (b)] were done using a Filmetrics F50 thin-film measurement tool. The remaining reflectance measurements were done using an optical setup consisting of a YSL Photonics SC-OEM broadband

[†] Also called a distributed Bragg reflector (DBR)

supercontinuum laser as the source, and a Princeton Instruments PIXIS 100 CCD camera thermoelectrically cooled to −70 °C as the detector. Reflected light was frequency selected using a 1200 grooves/mm grating of a Princeton Instruments Acton Series SP-2750 optical spectrometer before reaching the camera. Due to the oscillatory nature of the supercontinuum laser spectrum, a Savitsky-Golay filter was applied programmatically to the measured data before plotting (see Fig. D.2 in the appendix for a comparison of the data before and after filtering).

PL spectra were collected from a sample placed in an attocube attoDRY2100 optical cryostat cooled to 1.6 K. The built-in sample heater in the cryostat allowed for PL measurements at different temperatures. The sample was excited using a Thorlabs Stabilized Red HeNe Laser emitting at 632.992 nm.

Scanning Electron Microscopy (SEM) images of samples were captured using a JEOL JSM-7200F SEM (Fig. 6.10).

6.2 Distributed Bragg Reflectors

6.2.1 Design and simulation

Bragg mirrors consist of alternating layers of two materials with contrasting refractive indices. By choosing the right materials and thicknesses, the mirror can be made reflective over the desired wavelength range. For a DBR reflection stopband to be centered at a given wavelength λ_0, the thickness of each layer in the DBR should be

$$d = \frac{\lambda_0}{4n}, \tag{6.1}$$

where n is the absolute refractive index of the material comprising that layer. In other words, each layer must be one quarter-wavelength thick. For normal incidence, this allows the reflected light waves at each material interface to be all in phase and constructively interfere. Eqn. 6.1 is known as the Bragg condition.

For a DBR with p pairs of alternating materials, the reflectivity R at the center of the stopband is

$$R(p) = \left(\frac{1 - \frac{n_s}{n_i}\left(\frac{n_l}{n_h}\right)^{2p}}{1 + \frac{n_s}{n_i}\left(\frac{n_l}{n_h}\right)^{2p}} \right)^2, \tag{6.2}$$

where n_l and n_h are the refractive indices of the low-index and high-index materials in the Bragg mirror stack, and n_i and n_s are the refractive indices of the incident medium and the substrate on the other side of the Bragg stack.[138] The spectral width of the stopband is approximately

$$\Delta\lambda_0 \approx \frac{4\lambda_0}{\pi}\arcsin\left(\frac{n_h - n_l}{n_h + n_l}\right) \approx \frac{4\lambda_0}{\pi}\left(\frac{n_h - n_l}{n_h + n_l}\right), \tag{6.3}$$

assuming $(n_h + n_l) \gg (n_h - n_l)$.

To maximize R and $\Delta\lambda_0$, we would need to maximize the index contrast between the two materials comprising the Bragg stack, and also maximize the number of pairs p. In GaAs/AlGaAs heterostructures, this would mean using GaAs and AlAs as the mirror stack materials. We were, however, faced with a few constraints that excluded this design. For one, an induced device made with a wafer consisting of a GaAs QW and a bottom GaAs/AlAs Bragg mirror could have charge carriers induced in the GaAs layers of the Bragg stack, leading to parallel conduction. This can be avoided by using $Al_xGa_{1-x}As$ with a low Al ratio x. A limitation of the MBE growth chamber yielded a lower limit of $x = 0.2$. Secondly, AlAs as a material is very prone to corrosion. Certain fabrication steps involve etching into the substrate; if the etch goes past the AlAs layers, these layers can corrode and potentially delaminate if the etched sidewall is exposed to air. Although it is also susceptible to corrosion, using $Al_xGa_{1-x}As$ with a high Al ratio instead of AlAs mitigates this issue to an extent. For our purposes, we chose $x = 0.9$. To summarize, the designed DBR stack uses $Al_{0.9}Ga_{0.1}As$ as the low-index material and $Al_{0.2}Ga_{0.8}As$ as the high-index material.

Choosing the thickness d for each material in the Bragg stack depends on the refractive index n of each material, which in turn depends on the wavelength λ_0. The emission wavelength from our induced devices with rectangular GaAs QWs sandwiched between AlGaAs barriers depends on the thickness of the QW. Fig. 6.1 shows the measured PL peak wavelengths for some of our wafers with different QW widths, ranging from 10 nm to 30 nm. For our new wafer, we chose to go with a QW width of 15 nm—this corresponds to an emission wavelength $\lambda_e = 807.96$ nm. Therefore, the values of n and d must be found for $\lambda_0 = \lambda_e = 807.96$ nm.

Ref. [139] gives us an expression for the real part of the refractive index of $Al_xGa_{1-x}As$ as a function of x and λ. From this expression, and for $\lambda = \lambda_e$, we obtain the refractive indices for $Al_{0.2}Ga_{0.8}As$ and $Al_{0.9}Ga_{0.1}As$ as $n_h = 3.54$ and $n_l = 3.08$, respectively. Using Eqn. 6.1, we then calculate the corresponding layer thicknesses as $d_h = 57.06$ nm and

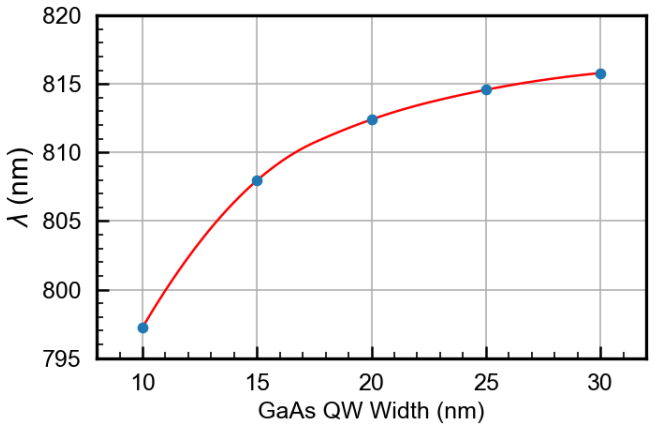

Figure 6.1: Measured peak PL emission wavelengths for GaAs heterostructure wafers with five different QW widths, ranging from 10 nm to 30 nm. The red interpolating line is to guide the eye. Note that this figure is identical to Fig. 3.11 (c)

$d_l = 65.58$ nm. Also, Eqn. 6.3 tells us the spectral width of the stopband $\Delta\lambda_0 \sim 71.5$ nm, and Eqn. 6.2 yields reflectivity values of $R(p = 20) = 98.48\%$, $R(p = 25) = 99.62\%$ and $R(p = 30) = 99.91\%$. Thirty periods in the DBR result in a reflectivity of over 99.9%, which we deemed sufficient for our needs. Note that for the sake of convenience, these calculations assume the extinction coefficient κ of each material in the DBR (given by the imaginary part of the refractive index) is zero. In reality, this value is finite and reduces the peak reflectivity achievable from these DBRs. At cryogenic temperatures, the value of κ is reduced relative to its room temperature value, but is still above zero.

While these calculations were useful as an intial proof of principle for our design, there were some additional requirements that necessitated a full simulation using the Lumerical FDTD solver. One requirement from MBE growth was for a thin 2.45 nm GaAs layer to be inserted after every $Al_{0.9}Ga_{0.1}As$ layer in each period of the stack to 'smoothen' the transitions between the lattices. A thin 1 nm protective GaAs layer was also needed between the Bragg stack and the bottom AlGaAs barrier to reduce trapping of background impurities as growth chamber conditions were varied. In general, the effect of including all layers of the heterostructure wafer stack on R and $\Delta\lambda_0$ needed to be calculated. Given all these conditions, the final wafer design is shown in Fig. 6.2 (a). There are 30 periods in the Bragg stack, consisting of 55 nm thick $Al_{0.2}Ga_{0.8}As$ and 65.8 nm thick $Al_{0.9}Ga_{0.1}As$ layers. The grating is designed for $\lambda_0 = 807.96$ nm. Fig. 6.2 (b) shows the reflectivity values for this wafer, as well as a similar wafer with no DBR. The peak value of R at $\lambda = \lambda_0$ is 99.94%, and $\Delta\lambda_0 \sim 67$ nm. Note that once again, the values of the extinction coefficients κ for the materials in this simulation are set to zero.

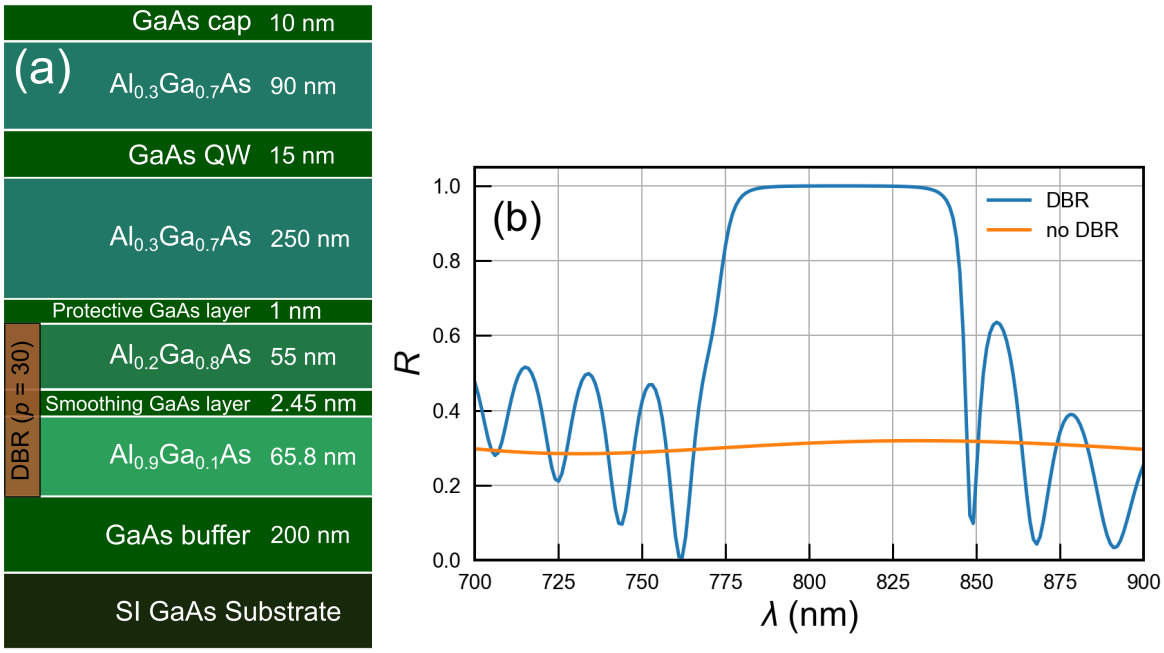

Figure 6.2: (a) Wafer stack of the designed GaAs/AlGaAs heterostructure with a 15 nm GaAs QW and a DBR consisting of 30 pairs. (b) Simulated reflectivity R of this wafer stack as a function of wavelength λ, along with that of a similar wafer stack with no DBR. The reflectivity stopband is clearly visible when the DBR is present. The stopband is centered at $\lambda_0 = 807.96\,\text{nm}$ with width $\Delta\lambda_0 \sim 67\,\text{nm}$

6.2.2 Measurement and design validation

The designed wafer specifications from the previous section were supplied to the MBE grower, and the grown wafer (ID G0708) was tested. Unfortunately, XRD measurements revealed a few deviations in the layer thicknesses from expected values, some of which affected the reflection spectrum. Fig. 6.3 (a) shows the wafer stack for G0708, with layer thicknesses measured using XRD. One main difference from the design is that the grown GaAs QW width is slightly smaller—14.59 nm instead of 15 nm—due to some Ga flux contributing to a calibration measurement. This difference is enough to shift the emission wavelength from $\lambda_e = 807.96\,\text{nm}$ to $\lambda_e \sim 806.5\,\text{nm}$, based on Fig. 6.1.

Another key difference is that the low-index $Al_xGa_{1-x}As$ in the DBR stack ended up with $x = 0.94$ instead of $x = 0.9$ due to a lower than expected Ga flux rate during this step, which also caused the layer thickness to be smaller—62.27 nm instead of 65.8 nm. This in turn shifted the center of the stopband to 780.5 nm, 26 nm lower than the QW emission wavelength. The blue and orange curves in Fig. 6.3 (b) show the simulated and

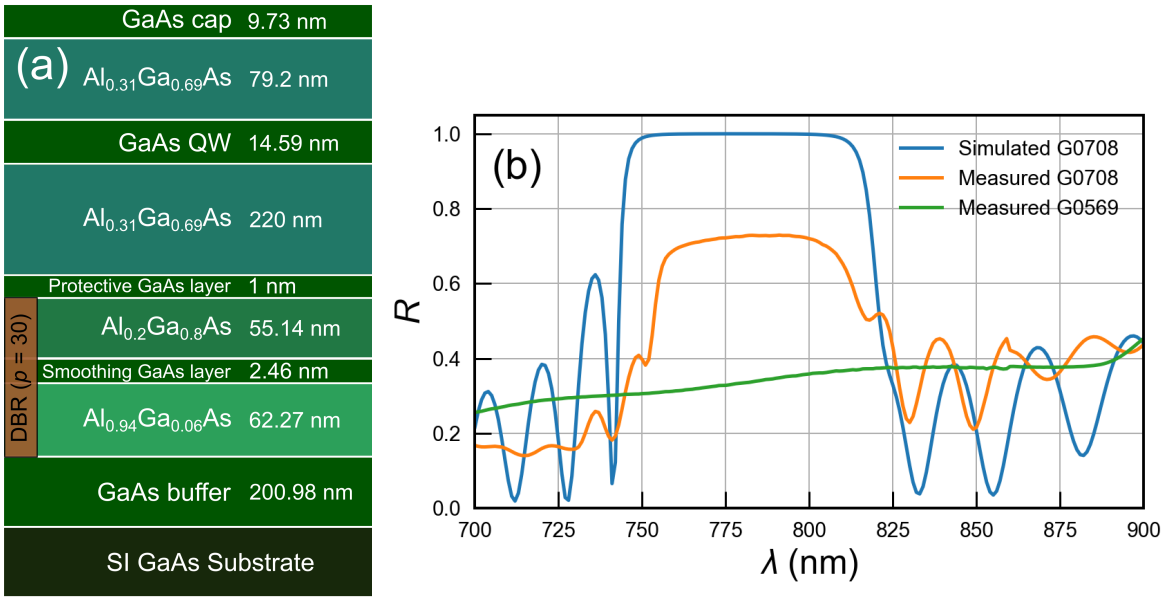

Figure 6.3: (a) Wafer stack of the MBE-grown GaAs/AlGaAs heterostructure (wafer ID G0708) with a 14.59 nm GaAs QW and a DBR consisting of 30 pairs. (b) Measured and simulated reflectivity R of G0708, along with a measurement of R from G0569, a similar wafer with no DBR. Measurements were conducted at room temperature corresponding to a high extinction coefficient κ, which explains the diminished peak reflectivity relative to simulation.

measured stopbands for wafer G0708.[†] The centre of the measured reflection stopband matches fairly well with that of simulation. The peak reflectivity is lower, since these room temperature measurements involve optical attenuation (defined by non-zero extinction κ) through the layers as the light travels to and from the DBR. Also, the spectral width of the measured reflectivity stopband is smaller—$\Delta\lambda_0 \sim 55$ nm instead of ~ 69 nm. This is likely due to small variations in the DBR layer thicknesses across all the repeats. The measured reflection spectrum from another MBE-grown GaAs/AlGaAs heterostructure wafer with ID G0569 (green curve) is also shown for comparison—G0569 *does not* have a bottom DBR. Differences between designed and expected values of any other layer thicknesses (AlGaAs barriers, GaAs cap layer) are assumed to have a negligible effect on the reflection spectrum.

Fig. 6.4 shows measured PL spectra for a sample chip from G0708 as a function of increasing temperature T, normalized to what is assumed to be the neutral exciton (X^0) peak. The peak identities can be confirmed using this temperature dependence measurement. As the temperature increases, the wavelengths of all peaks are red-shifted. Focusing on

[†] Note that the oscillatory behaviour of the reflectivity outside the stopband is a typical feature of Bragg mirrors.[140]

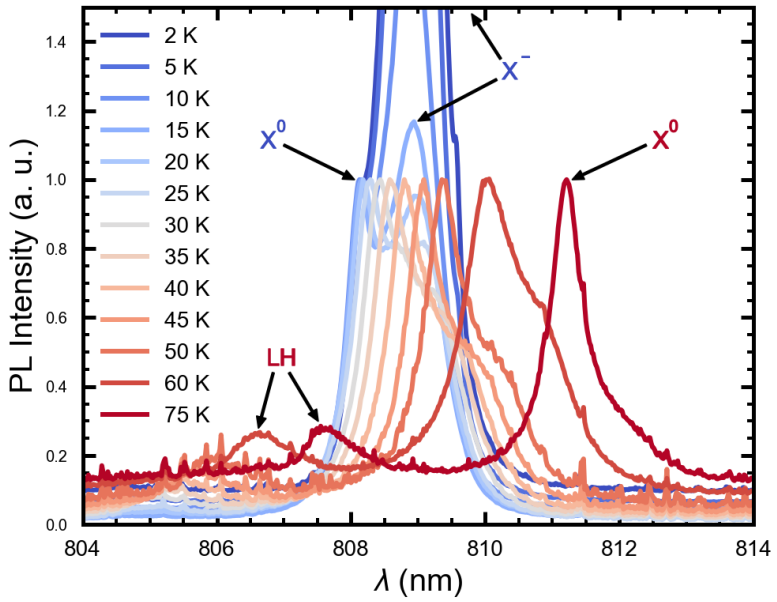

Figure 6.4: PL intensity as a function of wavelength from wafer G0708 for sample temperatures ranging from 2 K to 75 K. The sample was excited using a red HeNe laser emitting at ∼ 633 nm .

the two high intensity peaks, the higher wavelength (lower energy) peak decays relative to the lower wavelength (higher energy) peak as T increases, until it is no longer visible at $T = 75$ K. This behaviour is characteristic of the charged exciton X^- emission. The higher wavelength peak is therefore the X^- peak. By the process of elimination, the lower wavelength peak is the neutral X^0 peak. At higher temperatures, an even higher energy (lower wavelength) peak appears, corresponding to light holes (LH). These temperature dependence results match similar spectral data from Chapter 3 (Fig. 3.13). The PL spectra in Fig. 3.11 also corroborate these peak identities. Another important takeaway from Fig. 6.4 is that the measured X^0 peak at $T = 2$ K is at $\lambda = \lambda_e \sim 808.25$ nm, which does not correspond to the value of $\lambda_e = 806.5$ nm extracted from Fig. 6.1. With this in mind, an average value of 807.5 nm for the emission wavelength λ_e was assumed when designing the CBGs in Section 6.3.

The simulated far-field emission profile for an in-plane dipole emitter located in the GaAs QW layer of wafer G0708 is shown in Fig. 6.5. The red dotted circle in Fig. 6.5 corresponds to the collection angle of the objective lens with NA = 0.81. It is evident from the mode shape that the majority of the emission lies outside the collection angle of the objective. In fact, the theoretical ratio of the collection efficiency η_{CE} and the extraction

	η_{EE}/η_{CE}	η_{EE}	η_{CE}
G0372	80.64%	1.64%	1.32%
G0708	22.22%	2.60%	0.58%

Table 6.1: Extraction and collection efficiencies for wafers G0372 and G0708. A SHJI nano-LED made using wafer G0372 is discussed in Chapter 5 (see specifically Section 5.7.1). Wafer G0708 has a GaAs RQW located above the DBR stack. The DBR enhances η_{EE} but changes the mode shape such that η_{CE} reduces.

efficiency η_{EE}* is just 22.22%. In comparison, for the SHJI wafer G0372, $\eta_{CE}/\eta_{EE} = 80.64\%$, which is ~ 3.6 times larger. From the same model, an estimation for η_{EE} at the emission wavelength ~ 807.5 nm is found to be 2.60%. Using this value, η_{CE} is calculated as 0.58%.

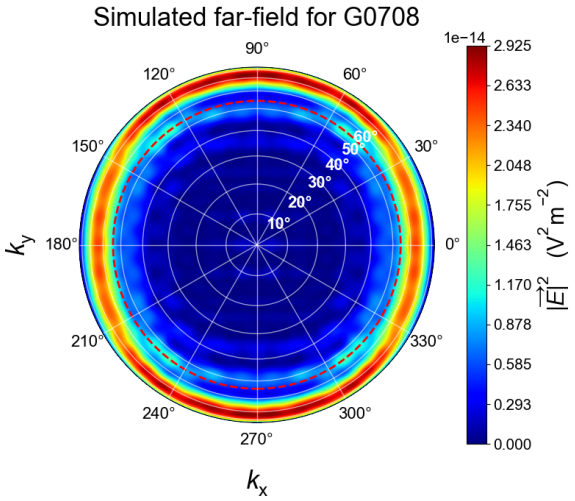

Figure 6.5: Simulated far-field emission profile for an in-plane dipole emitter located in the RQW above the DBR in wafer G0708. The red dotted circle indicates the collection angle of the objective lens (NA = 0.81). Most of the mode lies outside the collection angle ($\eta_{CE}/\eta_{EE} = 22.22\%$).

Table 6.1 summarizes the above simulated values for η_{EE} and η_{CE}. Although the presence of a bottom DBR enhances η_{EE} (by a factor of ~ 1.6 for these specific wafers), the shape of the mode is such that η_{CE} is diminished (in this case by a factor of ~ 0.4). Shaping the emission into a single mode that can be easily collected by the objective is crucial for improving η_{CE}. Combining our DBR with the CBGs discussed in the next section allows for mode shaping, and also boosts η_{IQE} and η_{EQE} via the Purcell effect.

* η_{CE} is the ratio of the photon flux at the first optic (the objective lens) to the generated photon flux, while η_{EE} is the ratio of the extracted power from the device to the source power (see Section 5.7.1)

6.3 Circular Bragg Gratings

While a bottom DBR aids in boosting the extraction efficiency η_{EE} of EL emissions, our devices still emit omnidirectionally into multiple modes, resulting in poor collection efficiency η_{CE}. Engineering a cavity in the environment around the emission region can shape the emission into a single mode directed perpendicularly outward from the device substrate, enhancing η_{CE}. This lateral cavity combined with the bottom Bragg mirror will also boost the internal and external quantum efficiencies (η_{IQE} and η_{EQE}) by enhancing the spontaneous emission rate via the Purcell effect. A variety of structures have been used to enhance these efficiencies in the case of quantum dot emitters, including photonic crystals,[141] tapered nanowires,[142] micropillar cavities,[143] solid immersion lenses[14,144] and CBGs.[145,30,29,146,147] Nanowires and micropillars are incompatible with our structure since they do not offer a route for carriers to flow in and recombine. Solid immersion lenses could be incorporated into our nano-LEDs but only boost collection without offering Purcell enhancement. Etching structures into our substrate so that they surround the emission region is necessary—photonic crystals and CBGs are two possible candidates. Of these two candidates, CBGs offer a better out-of-plane extraction efficiency and a better mode shape than photonic crystals. Conveniently, there is recent literature specifying how to tune the CBG design for different wavelengths and material properties.[148,149,150] CBGs have also been used to extract guided modes for conventional LEDs[151], and are the most promising candidate for our sources.

CBGs are essentially a circular analogue of planar DBRs. Moving radially outwards in any direction from a central point, the refractive index periodically alternates between two values. An emitter placed at the center of the resulting concentric rings benefits from mode-shaping and Purcell enhancement. These concentric rings are usually created by patterning and etching the substrate around the emission region. To prevent photon loss into the substrate, the CBG can be patterned in a suspended membrane, but such structures are quite fragile and hard to fabricate. Instead, we can pair the CBGs with a bottom mirror—in our case, the DBR.

The magnitude of Purcell enhancement afforded by a cavity with quality factor Q and mode volume V is given by the Purcell factor,

$$F_{\text{P}} = \frac{\gamma_{\text{c}}}{\gamma_0} = \frac{3}{4\pi^2}\left(\frac{\lambda_0}{n}\right)^3 \frac{Q}{V}, \tag{6.4}$$

where γ_c and γ_0 are the spontaneous emission rates in the cavity and in bulk; also, λ_0 is the vacuum wavelength and n is the cavity refractive index, making (λ_0/n) the wavelength inside the cavity. η_{IQE} is the ratio of the radiative emission rate to the sum total of the radiative and non-radiative emission rates,

$$\eta_{IQE} = \frac{\gamma_{rad}}{\gamma_{tot}} = \frac{\gamma_{rad}}{\gamma_{rad} + \gamma_{non\text{-}rad}}. \tag{6.5}$$

γ_{rad} is modified by Purcell enhancement as $\gamma'_{rad} = F_P \gamma_{rad}$. The modified IQE η'_{IQE} is then[152]

$$\eta'_{IQE} = \frac{F_P \eta_{IQE}}{(F_P - 1)\eta_{IQE} + 1}. \tag{6.6}$$

We see from the above equation that η'_{IQE} increases with F_P. Note that $F_P > 1$ necessitates a higher injection current. For CBGs, both Q and V (and in turn F_P) depend on various design parameters for the concentric rings—the number of rings N_{rings}, central disk radius r_i, ring width w, ring period p, and ring depth or ring height h.

6.3.1 Design and simulation

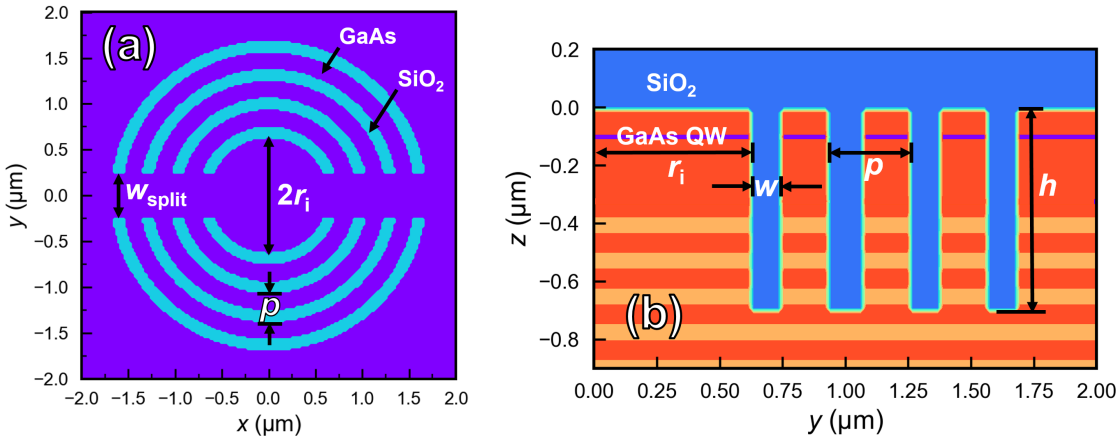

Figure 6.6: (a) Horizontal and (b) vertical cross-sections of a split CBG etched into the DBR wafer G0708. The horizontal cross-section is at the height of the GaAs QW. The vertical cross section is for positive values of y at $x = 0$. The rings are etched past the DBR and filled with deposited SiO_2.

Fig. 6.6 shows our design for CBGs in the wafer G0708, modelled using Lumerical FDTD. To make them compatible with our lateral 2D p–n junctions, a split in the rings with width $w_{split} = 500\,\text{nm}$ was added to the design, which allows n- and p-type carriers

to be brought to the center by inducing gates to form exciton dipoles before radiatively recombining. Following the detailed design method for CBG cavities in Ref. [148], values of the other design parameters were obtained as follows: number of rings $N_{\text{rings}} = 4$, ring height $h = 700\,\text{nm}$, ring width $w = 130\,\text{nm}$, ring period $p = 312\,\text{nm}$, and central disk radius $r_{\text{i}} = 2p = 624\,\text{nm}$. This simulated design assumed a single exciton dipole emitter located at the center of the grating with an emission wavelength of $\lambda_e = 807.5\,\text{nm}$.

Simulated Purcell factors (F_{P}) as a function of wavelength for exciton dipole emitter orientations varying from $\phi = 0°$ to $\phi = 90°$ are shown in Fig. 6.7. When $\phi = 0°$, the exciton dipole is parallel to the split in the CBG, and F_{P} is at its maximum value (5.33) at a wavelength $\lambda_0 = 807.36\,\text{nm}$ that is close to the expected emission wavelength ($\lambda_e = 807.5\,\text{nm}$). As the dipole rotates, the value of F_{P} at $\lambda = \lambda_0$ reduces from 5.33 at $\phi = 0°$ to nearly unity at $\phi = 90°$ (see inset of Fig. 6.7). The probability of an exciton radiatively recombining at

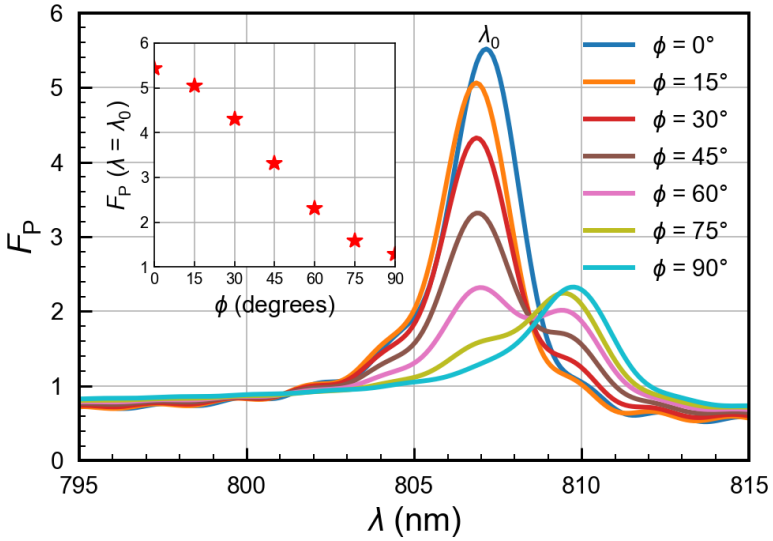

Figure 6.7: Simulated Purcell factor distribution for varying dipole emitter angle ϕ in a split-ring CBG in wafer G0708. (INSET) As ϕ increases from 0° to 90°, $F_{\text{P}}(\lambda = \lambda_0 = 807.36\,\text{nm})$ reduces to nearly unity.

a certain dipole orientation is weighted by the Purcell factor for that dipole orientation at the emission wavelength. It follows that any exciton dipole located at the center of the split CBG recombines at the $\phi = 0°$ orientation with the highest probability, boosting the collection efficiency of photons that are linearly polarized along the split in the CBG. We set the convention that this orientation corresponds to horizontal polarization (H). Photons emitted due to the recombination of exciton dipoles oriented along $\phi = 90°$ are vertically polarized (V).

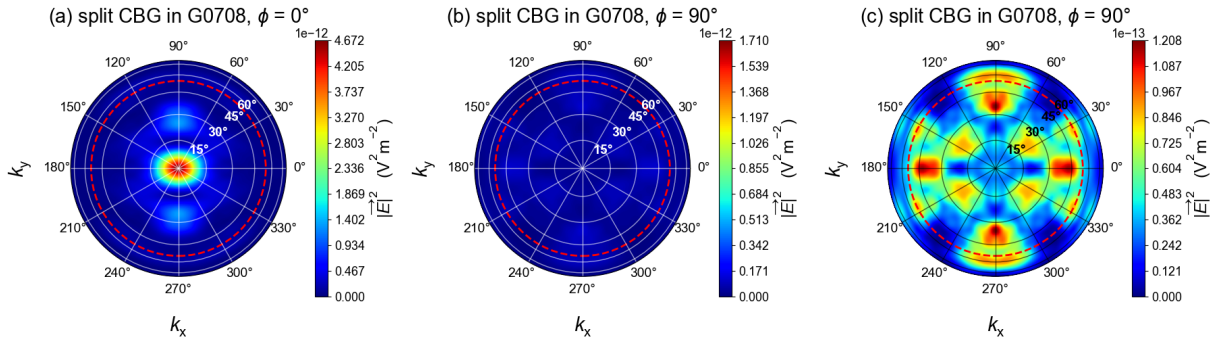

Figure 6.8: Simulated far-field emission profiles for an exciton dipole emitter in wafer G0708 oriented (a) parallel ($\phi = 0°$), and (b, c) perpendicular ($\phi = 90°$) to the split in a split CBG, corresponding to H- and V-polarized emission respectively. The contour color bars for (a) and (b) are scaled to the same maximum extent for comparison. (b) and (c) are identical except the color bar in (c) has been scaled to view the mode shape. The dotted red circles overlaid onto the profiles correspond to the numerical aperture (0.81) of the objective lens. The mode shape when $\phi = 0°$ (H polarized) is an elliptical Gaussian, and 92.76% of the extracted photons are collected by the objective. The peak emission intensity (proportional to $|\vec{E}|^2$) when $\phi = 90°$ (V polarized) is an order of magnitude lower than the peak intensity when $\phi = 0°$ and the mode shape is completely destroyed, with only 76.11% extracted photons collected by the objective. This indicates birefringence and polarized light emission.

Fig. 6.8 (a) shows the simulated far-field emission profile for the split-ring CBG when $\phi = 0°$. The shape of the single mode is an elliptical Gaussian, which is typical for CBGs.[153,29,154,145] The mode lies comfortably within the collection angle of our objective lens, which has an NA of 0.81 (represented by the dotted red circle). The ratio η_{CE}/η_{EE} is calculated from the data in Fig. 6.8 (a) as 92.76%. When the exciton dipole is oriented perpendicular to the ring split ($\phi = 90°$), the mode is completely destroyed—the peak intensity drops by over an order of magnitude, and there is no longer any single-mode Gaussian nature to the far-field profile [Figs. 6.8 (b, c)]. In this case, η_{CE}/η_{EE} drops to 76.11%. These simulations support the result that our split-CBG cavity acts as a source of effective birefringence, polarizing the extracted and collected mode.

Simulated Purcell factors F_P and extraction efficiencies η_{EE} for four different cases are shown in Fig. 6.9: whole rings, split rings when $\phi = 0°$ (H polarization), split rings when $\phi = 90°$ (V polarization), and no rings. The lineshapes and peak wavelengths for the simulated F_P are similar to their η_{EE} counterparts. Note that whole-ring CBGs are incompatible with our gated quantum emitters, and their simulated data are included only for the sake of comparison. For a whole-ring CBG with ring dimensions identical to our split CBG, F_P reaches a maximum of 6.59 at $\lambda = 806.45$ nm. The peak F_P for the split CBG (H polarization) is 5.33, but this is at the slightly larger wavelength of $\lambda = 807.36$ nm. The bandwidth of this Purcell distribution is ~ 3.7 nm or ~ 7.04 meV.

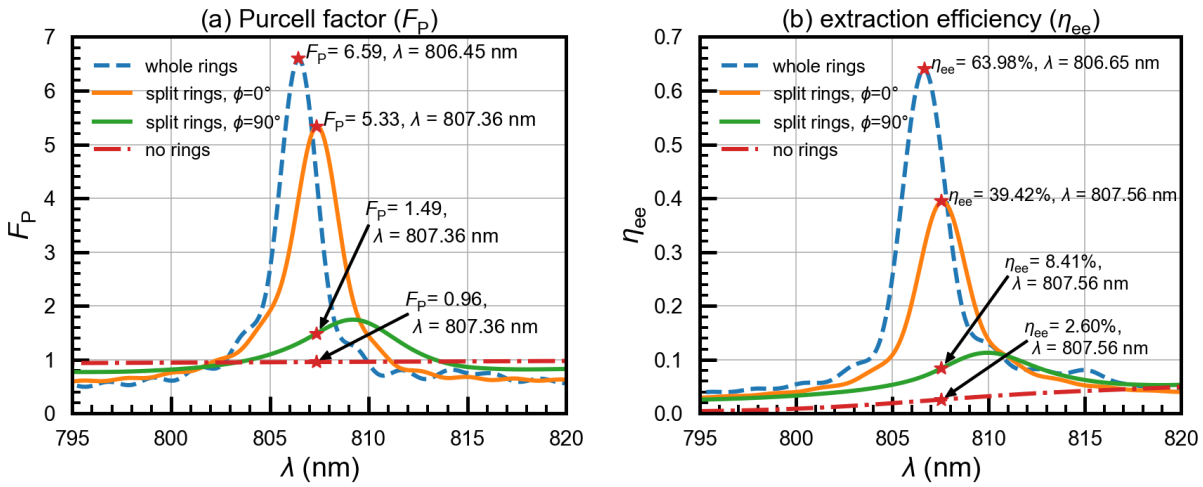

Figure 6.9: (a) Simulated Purcell factor F_P and (b) simulated extraction efficiency η_{EE} as a function of wavelength λ for the whole ring CBGs (dashed, blue), our split-ring CBGs when $\phi = 0°$ (solid, orange), our split-ring CBGs when $\phi = 90°$ (solid, green), and no rings (dash-dotted, red) in wafer G0708. For the split rings, F_P peaks at 5.3 ($\lambda = 807.36$ nm) and η_{EE} at 0.39 ($\lambda = 807.56$ nm). Please see the text for a detailed explanation.

Also, the corresponding peaks for η_{EE} (63.98% for whole rings, 39.42% for split rings, H-polarized emission) are shifted by 0.2 nm relative to their F_P counterparts. To compare the split-CBG H-polarization case with the V-polarization and no-CBG cases, we choose values of F_P and η_{EE} that are at the same wavelengths as the peak F_P and η_{EE} for H polarization. Both F_P and η_{EE} are significantly lower for a dipole emitter oriented perpendicular to the CBG split. In the absence of a CBG, there is no Purcell enhancement of the spontaneous emission rate—$F_P \sim 1$ across the entire simulated wavelength range. With these values of η_{EE} along with the ratios η_{CE}/η_{EE} obtained from the far-field plots (Figs. 6.5 and 6.8), the collection efficiency η_{CE} can be calculated. Table 6.2 summarizes these results.

	F_P	η_{EE}	η_{CE}	η_{CE}/η_{EE}
split CBG (H)	5.33	39.42%	36.57%	92.76%
split CBG (V)	1.49	8.41%	6.40%	76.11%
no CBG	0.96	2.60%	0.58%	22.22%

Table 6.2: F_P, η_{EE}, η_{CE} and η_{CE}/η_{EE} for three cases: the split CBG for H polarization ($\phi = 0°$), the split CBG for V polarization ($\phi = 90°$), and the DBR wafer G0708 with no patterned CBG.

The weighting of the probability of exciton recombination along a specific dipole orientation by the corresponding Purcell factor allows us to derive an expression for effective efficiencies for our split CBGs. Given the efficiency numbers η_H and η_V corresponding to

H-polarized and V-polarized photon emission, the effective efficiency is

$$\eta = \frac{F_{\mathrm{P_H}}\eta_{\mathrm{H}} + F_{\mathrm{P_V}}\eta_{\mathrm{V}}}{F_{\mathrm{P_H}} + F_{\mathrm{P_V}}}, \tag{6.7}$$

where $F_{\mathrm{P_H}}$ and $F_{\mathrm{P_V}}$ are the Purcell factors for H- and V-polarized emission, respectively. With this expression, we find the effective extraction and collection efficiencies for the split CBG—$\eta_{\mathrm{EE}} = 32.65\%$ and $\eta_{\mathrm{CE}} = 29.98\%$. These numbers are respectively ~ 13 times and ~ 52 times the efficiencies for a device with no rings.

The effect of the split CBG and DBR on the IQE and EQE can also be calculated. We start with an average value of $\eta_{\mathrm{IQE}} = 1.19\times10^{-3}$ from the data for our nano-LED in SHJI wafer G0372 in Section 5.7.1. Using Eqn. 6.6, we calculate the modified η_{IQE} for H-polarized and V-polarized emission as 6.31×10^{-3} and 1.77×10^{-3}, respectively. Substituting these values into Eqn. 6.7 gives us an effective IQE of 5.32×10^{-3}, corresponding to an enhancement factor of ~ 4.5 relative to the device without the DBR and split CBG. To find the effective EQE for our split CBG, we simply multiply the effective values for η_{IQE} and η_{EE}. This gives us an effective value of $\eta_{\mathrm{EQE}} = 1.74\times10^{-3}$, corresponding to a significant enhancement factor of ~ 89. See Table 6.3 for a summary of these efficiencies.

	η_{EE}	η_{CE}	η_{IQE}	η_{EQE}
G0372	1.64%	1.32%	1.19×10^{-3}	1.95×10^{-5}
G0708	2.60%	0.58%	1.14×10^{-3}	2.96×10^{-5}
G0708 + split CBG	32.65%	29.98%	5.32×10^{-3}	1.74×10^{-3}

Table 6.3: Extraction and collection efficiencies as well as internal and external quantum efficiencies for G0372, G0708, and G0708 with a split CBG. The combination of the DBR and CBG enhances the IQE by a factor of ~ 4.5 and the EQE by a factor of ~ 89, relative to wafer G0372.

How does the presence of our cavity affect the entanglement fidelity of our source? To recap the discussion on entanglement from Chapter 1, when electron pumps are operated in the $n = 2$ regime, they can emit spin-entangled singlet pair states. This spin singlet electron pair would reach the p-side and recombine with holes to yield entangled photons, assuming there is no spin-dephasing. The presence of our split-CBG cavity would affect this entangled photon generation process. Our cavity is polarization selective—H-polarized light is extracted more efficiently compared to V-polarized light, and recombination into this mode is preferred due to the Purcell effect. This would completely destroy entanglement fidelity. Alternate designs for the CBG cavity may alleviate this issue. For one, a narrower split and more rings would reduce the birefringence of the cavity. A

narrow split would, however, require narrow topgates, which would need to be placed closer to the semiconductor to be able to effectively induce a 2DEG or 2DHG. CBGs with zig-zag or spiral-shaped splits have been studied,[154] and would also reduce birefringence, but fabricating compatible topgates would be difficult.

6.3.2 Fabrication

The general fabrication recipe for the CBGs can be found in Appendix C. Based on the simulated design parameters, a fabrication run was conducted involving an Electron-Beam Lithography (EBL) dose test—a pattern consisting of 20 rows of CBGs of increasing ring width, with each row containing 5 repeats, was exposed using 16 different doses, yielding an array of 1600 CBGs in total. Each CBG was assigned the label DαRβCγ, with α, β and γ being the dose, row, and column number of the CBG respectively. The ring widths as per the .gds pattern file were increased from 80 nm (R1) to 99 nm (R20). The average of the inner and outer radii (the radial halfway point) of each ring was fixed based on the design parameters. In other words, going down the column, the ring period remained the same while the ring width increased and the central disk radius decreased, thus decreasing the effective cavity size. Note that these ring width values (80–99 nm) were chosen with the assumption that the actual pattern would be overexposed, shifting the window of values to include the expected ring width of 130 nm. The patterns were written using ZEP520A, a robust positive tone resist that was also used as the etch mask during Reactive Ion Etching (RIE) of the pattern. With a base dose of 300 µC/cm^2, the dose multiplication factor was varied from 0.7x to 1.45x in steps of 0.5x. Increasing the dose also increases the effective ring widths and decreases the central disk radius of the patterns; however the sharpness and reproducibility of features is also dose-dependent. The goal of this dose test was to determine an optimal dose at which the ring features comprising the CBGs were sharp, reproducible, and matched the design parameters.

A couple of fabricated CBGs etched in G0708 are shown in Fig. 6.10. At first glance, the etched features look very clean and uniform. However, these images are representative of how most rings looked—it was difficult to distinguish differences in sharpness of features or observe non-uniformity among the repeats just by eye.

Since there were a very large number of CBGs fabricated for this dose test (320 distinct patterns with 5 repeats per pattern), only CBGs from the first and last row of each dose were imaged using SEM. Ring widths for these rows were measured using the

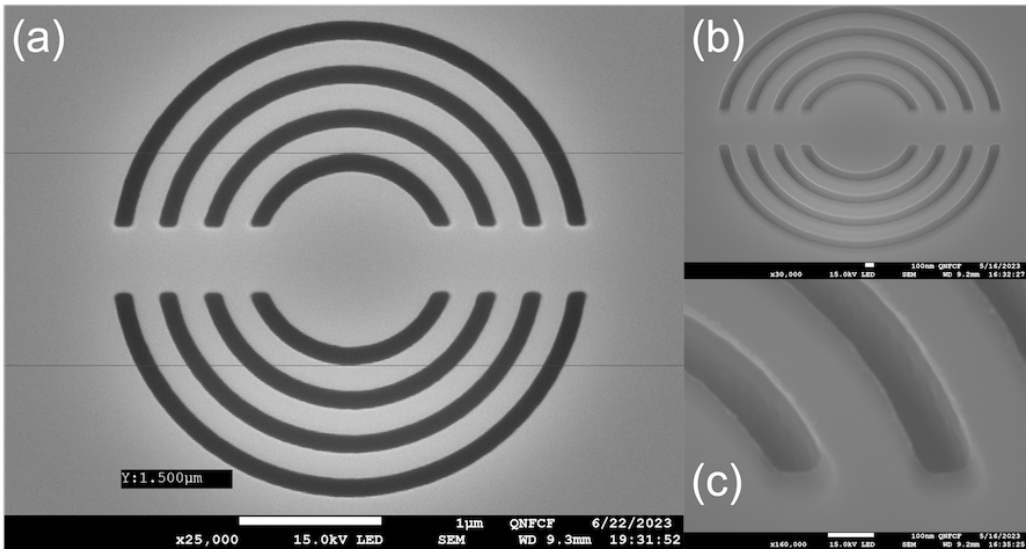

Figure 6.10: SEM images of etched CBG structures in the wafer G0708, fabricated as part of the dose test. (a) Top-down view. (b) 30° tilted view. (c) 30° tilt + magnified view.

scale bar on the SEM images, and the ring widths of the remaining CBGs were estimated using linear interpolation. The measured ring widths for R1 ranged from 113 nm (D1) to 125.5 nm (D16), while those for R20 ranged from 130.2 nm (D1) to 144.6 nm (D16). Thus, the assumption that overexposure would shift the window of ring width values to include the design parameter of 130 nm was accurate.

Post SEM imaging but prior to further testing, 300 nm of SiO_2 was deposited on top of the substrate—this oxide filled in the etched rings.

6.3.3 Measurement and design validation

It is natural to expect deviations between simulation and reality when designing and fabricating structures such as our CBGs. This makes measurement for design validation essential. Since choosing the best dose and .gds pattern file ring width was not possible purely by looking at several SEM images, another means of design validation was necessary.

A tried and tested method involves measuring the reflection spectrum from the CBGs.[146,145,154] At the wavelength corresponding to the cavity mode of the CBG, we expect a dip in the reflection spectrum due to a phenomenon known as Fano resonance.[155] An asymmetry in the line shape of the dip is characteristic of Fano resonance. An important point about our CBGs is that the split in the middle of the CBG makes the shape of the

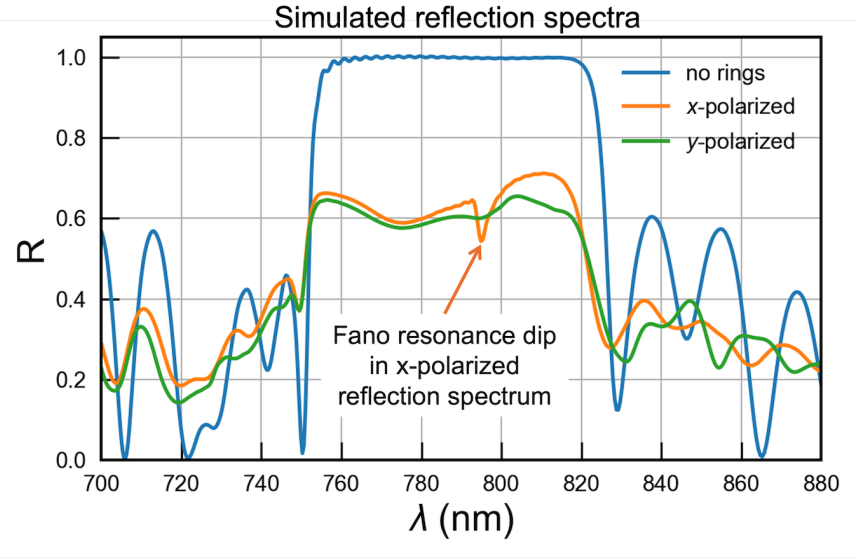

Figure 6.11: Simulated reflection spectra from a split CBG on G0708, with 300 nm of SiO_2 on top, and SiO_2 filling the etched rings. Incident light is polarized parallel (x-polarized, orange) and perpendicular (y-polarized, green) to the split. A characteristic Fano resonance dip is present when the incident light is x-polarized, and absent when the light is y-polarized. The simulated reflection spectrum from bare G0708 (no rings, blue) with 300 nm of SiO_2 on top is also shown for comparison.

reflection spectrum dependent on the polarization of the incident light, as seen in the simulated reflection spectra in Fig. 6.11. The Fano dip is most prominent when the incident light on the CBGs is x-polarized, i.e. polarized parallel to the ring split (orange curve), and is absent when the incident light is y-polarized, i.e. polarized perpendicular to the ring split (green curve).

The measurement of Fano resonances for our split CBGs was conducted by passing light from the broadband supercontinuum laser through a linear polarizer, followed by a half-wave plate (HWP) to control the polarization angle, before directing it to the sample (Fig. A.2 in Appendix A). An angle of 0° or 90° on the HWP corresponds to y-polarization, while 45° corresponds to x-polarization. All reflection spectra were normalized to the intrinsic intensity distribution of the broadband supercontinuum laser (after Savitsky-Golay filtering), obtained by observing the reflection from gold (Fig. D.1). The reflected intensity from CBG D14R20C1 (Fig. 6.12) shows a clear dip at $\lambda = 778.6$ nm when the incident light is x-polarized (45°), while the y-polarized curves (0° and 90°) overlap and show no Fano dip. This polarization dependence was reproduced for other CBGs as well (see Fig. 6.13).

A noticeable difference between the simulated and measured reflection spectra is that the linewidth of the measured Fano resonance dip for x-polarization is broader than that

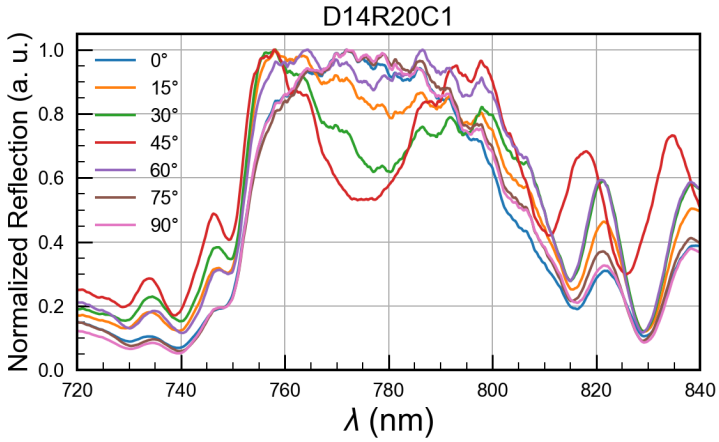

Figure 6.12: Measured reflection spectra (normalized) from split CBG D14R20C1. The different spectra correspond to increasing angle of the HWP, that rotates the polarization from y (0°) to x (45°) and back to y (90°). A clear Fano resonance dip is visible at $\lambda = 778.6\,\text{nm}$ when the incident light is x-polarized.

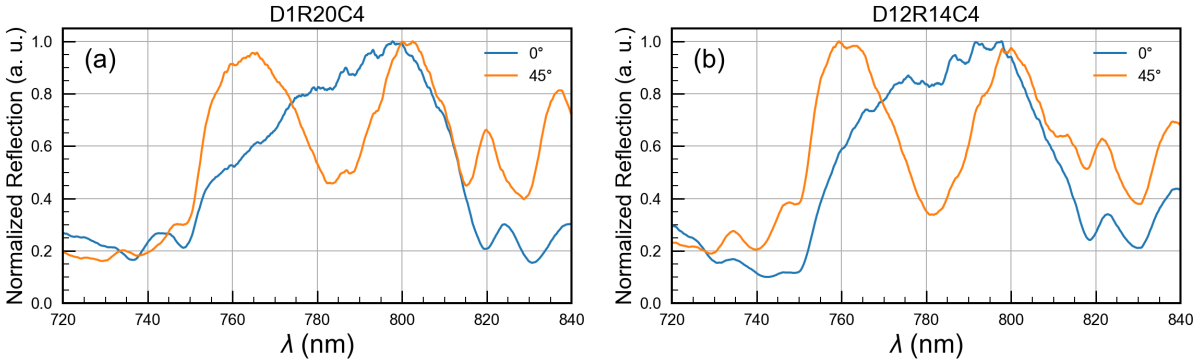

Figure 6.13: Measured reflection spectra (normalized) from CBGs (a) D1R20C4 and (b) D12R14C4 for y-polarization (0°) and x-polarization (45°) of incident light. Cavity mode dips are present (at $\lambda = 786.3\,\text{nm}$ for (a) and $\lambda = 782.4\,\text{nm}$ for (b)) when the incident light is x-polarized, but absent for y-polarization.

of simulation. This broadening was thought to be due to errors and variations in the ring widths that occur during lithography. An attempt to simulate the effect of these errors was made (see Fig. D.3). Although the linewidth increases when errors in the ring width are introduced in the simulation, the resonance dip is also more washed out, unlike what is observed experimentally. It is not fully understood why the measured resonance linewidth is broad without loosing depth.

As the ring width increases, the central disk radius decreases—this decreases the effective size of the cavity. Intuitively, we should expect a decrease in the dip wavelength of the Fano resonance as the cavity size decreases. The measured reflection spectra in Fig. 6.14 show just this. For all three doses (D1, D12, D16), as the row number increases,

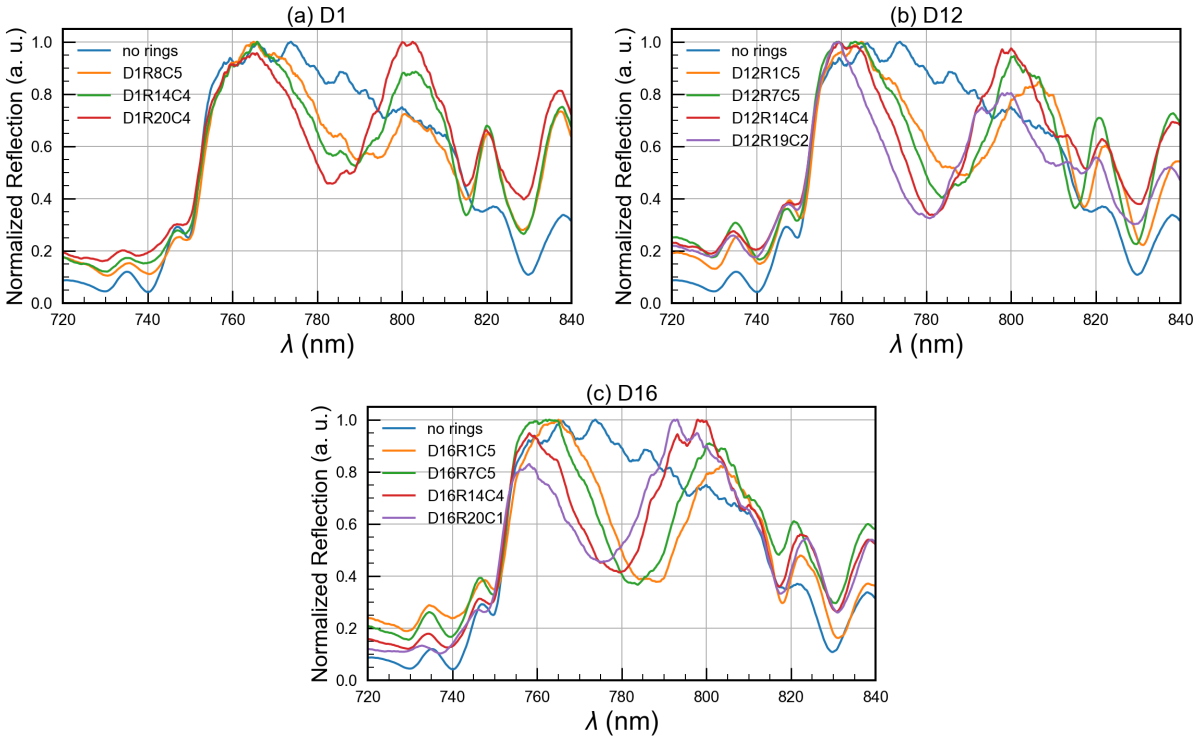

Figure 6.14: Measured reflection spectra (normalized) from CBGs in different rows for three different doses: (a) D1 (210 µC/cm^2), (b) D12 (375 µC/cm^2), and (c) D16 (435 µC/cm^2). Incident light is x-polarized for all measurements. Dip wavelength decreases for increasing ring width in all cases.

the ring width increases, decreasing the cavity size and the dip wavelength.

By plotting the measured dip wavelengths vs measured ring widths and comparing the trend to the dip wavelengths acquired from simulation, we can contrast the difference between simulation and measurement and find a way to correlate design parameters to actual measurement results. These plots are shown in Fig. 6.15. Both plots show a linear trend, and have nearly identical slopes. The key takeaway is that for a given ring width, there is a systematic offset of about 16.3 nm between the simulated and measured dip wavelengths.[†] From the linear fit of the measured dip wavelengths (red dashed line), a fabricated ring width of $\sim$94.8 nm is needed to achieve a dip wavelength of 807.5 nm, which corresponds to the X^0 emission line from the QW of G0708.

[†] This number is calculated by taking the difference of the intercepts of the two line fits.

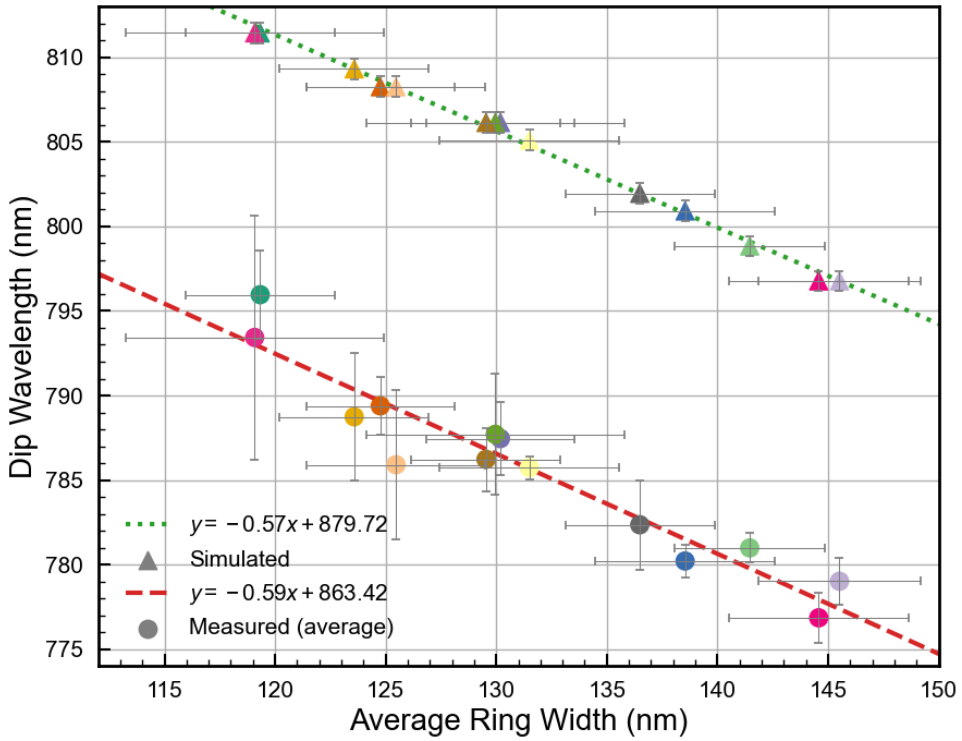

Figure 6.15: Simulated (triangles) and measured (circles) dip wavelengths as a function of ring widths for 14 different CBGs of different dose and row numbers. The measured dip wavelengths are averaged over the 5 repeats in each row. Ring widths are interpolated from the average ring widths of the first and last rows of each dose. Error bars are shown in grey. The green dotted line and the red dashed line correspond to the linear fits for the simulated and measured data.

6.4 Conclusion and outlook

Combining a bottom Bragg mirror and a CBG is an effective way to boost the emission, extraction and collection efficiencies from quantum light sources via Purcell enhancement and mode shaping. By adapting the DBR and CBG structures to be compatible with current fabrication restrictions for our nano-LEDs, we create the opportunity to integrate these structures with a future quantum light source based on the combined architectures of the nano-LED and quantized charge pump.

From theoretical simulations, the maximum Purcell factor F_p when the dipole emitter is parallel to the split in the CBG is 5.33 at $\lambda = 807.36$ nm. For a dipole oriented perpendicular to the split, $F_\mathrm{p} = 1.49$ at the same wavelength. This fact coupled with the contrast between the far-field profiles for the two dipole orientations indicates polarization selectivity of our cavity. This destroys any entanglement between photons that may be created within

the cavity. However, the extraction and collection efficiencies for single photons is still significantly boosted, by factors of ~ 13 and ~ 52, respectively relative to a device without any CBG. In comparison to the nano-LED from Chapter 5, the IQE and EQE of a device made using DBR wafer G0708 and a split CBG would be enhanced by factors of ~ 4.5 and ~ 89, respectively.

The fabricated CBG prototypes of varying ring widths were validated using polarized reflection measurements to observe the Fano resonance dips. The CBG ring width varied linearly with dip wavelength for both simulation and measurement. Interestingly, the linear fits for the simulated and measured data were offset by $\sim 16.3\,\text{nm}$. Based on the measured data, a ring width of of $\sim 94.8\,\text{nm}$ is needed to achieve a resonance dip wavelength matching the emission from the QW ($\sim 807.5\,\text{nm}$). With this information, a new dose test with tighter windows for the dose and ring width would reveal the ideal design parameters for a CBG compatible with wafer G0708. Additionally, a future MBE growth run could correct the error in the stopband position seen in wafer G0708, and new CBGs can be designed for this new wafer.

7. Conclusion

7.1 Summary of experimental results

The work presented in this thesis contributes to a project whose broader goal is to develop a stable, high-rate, deterministic, electrically-driven quantum light source by combining the architectures of a nano-LED (or gate-defined lateral planar p–n junction) with a single-parameter quantized charge pump using dopant-free GaAs/AlGaAs heterostructures as the material system. Although this ultimate goal is yet to be achieved, the individual structures of the nano-LED and quantized charge pump have been independently realized.* Before the two devices can be integrated, some obstacles due to deficiencies in the nano-LEDs need to be addressed. Chapters 3, 4, 5 and 6 of this thesis highlight these deficiencies, propose solutions, and implement them to a degree. These contributions move us further along the development roadmap.

We identified the following obstacles that need to be overcome with respect to our nano-LEDs:

(i) quenching of device EL and time-instability of emissions due to parasitic charge accumulation, necessitating thermal cycling to reset the device;
(ii) alternate current pathways (both radiative and non-radiative) through the device *mesa* that reduce both internal and external quantum efficiency;
(iii) delocalized emission at *mesa* edges due to minority currents under the topgate edges, affecting extraction efficiency and position-controllability; and
(iv) multimode emission and slow rate of spontaneous emission that reduce extraction and collection efficiencies.

The specific solutions for each of these problems were uncovered by us over the course of experimentation, modelling, design and intuitive thinking, yielding the experimental

* The results from our quantized charge pumps are not a part of this thesis; see Refs. [24, 102].

results collected in this thesis. Before listing these solutions at the end of this section, we will first summarize these experimental results.

Nano-LEDs using quantum well (QW) substrates (Chapter 3), and for the first time single heterojunction interface (SHJI) substrates (Chapters 4, 5) were fabricated and tested electrically and optically. The nano-LEDs in Chapters 3 and 4 possess standard basic architectures that include ambipolar ohmic contacts on the left and right sides of the device and two insulator-separated topgates above each set of ohmics that induce charge of opposite polarity, forming the p–n junction. Conventional forward-bias operation resulted in short-lived light emission from the device center and also from other regions such as gate and *mesa* edges. The quenching of EL is due to localized parasitic charge accummulation, contributed to by electrons/holes that escape the confinement of the p–n channel.

The existence of our working SHJI devices disproves a recent theoretical study[31] stating that such devices are impossible to achieve. Currently, the fabrication yield for our SHJI devices—specifically for the p-type and n-type ohmic contacts—is higher than that of QW devices, making them a useful alternative for prototyping. There are some fundamental advantages to QWs, however. The spectra are easier to identify and analyze in QWs since the energies of the emission peaks are different from the expected emission energies from the substrate, unlike in SHJIs. Confinement from a QW would result in stronger electron-hole overlap, increasing the emission efficiency or brightness. The electron-hole recombination lifetime can be fine-tuned by tuning the QW thickness during MBE growth; this is not possible for SHJIs.

We found that the EL from under the topgate on the p-side is brighter than on the n-side for our SHJI devices, likely due to the higher mobility and higher probability of tunneling across the junction for electrons compared to holes. This is perfect for designing a quantum emitter that integrates a lateral p–n junction and a quantized charge pump since it is much easier to construct and operate a quantized electron pump than a quantized hole pump. The QW devices in Chapter 3 showed brighter emission from the n-side; the reason for this difference is not immediately evident.

The Set-Reset (SR) protocol introduced in Chapter 3 solves the problem of EL quenching due to localized parasitic charge accumulation in both QW and SHJI devices. Parasitic charging enhances non-radiative recombination, or gates the channel and suppresses the current due to the forward bias. Parasitic charging may occur due to charges escaping the channel confinement potential, or due to biased self-illumination that excites carriers

in the 2DEG/2DHG or in charge traps from background impurities. SR operation avoids the need for thermal cycling—warming up samples from cryogenic to room temperature to dissipate frozen parasitic charge before cooling them back down—thus saving a lot of time. The SR protocol is useful for resetting parasitic charge in a photon source *between* few-photon experiments, which is a major improvement compared to thermal cycling. A method of achieving *in-situ* time-stable operation is still needed for performing few-photon experiments; this is satisfied by the 'time-stabilization' regime of operation from Chapter 5 (discussed below).

In contrast to the basic architecture of the devices from Chapters 3 and 4, the nano-LED architecture in Chapter 5 additionally incorporates two wide *side surface gates* placed laterally and adjacent to the p–n channel. SR operation with the surface gates disconnected is identical to that of a device without surface gates. Connecting to these gates and applying zero volts was sufficient to alter the dynamics of charge transport and recombination in DC and SR operation. Applying negative and positive potentials yielded operating regimes corresponding to localization (SR mode) and time-stabilization (DC mode). When operating the SHJI device in conventional DC mode, hole current leakage from the side surface gates was observed for surface gate voltages below -0.5 V, but no electron leakage was observed for positive voltages up to +1.5 V, suggesting the possibility of the substrate having p-type background impurities. SR operation when zero volts are applied to the surface gates yields *no* EL when the p-side is floating and n-side is grounded, again due to hole leakage through the surface gates. This will be a problem when it comes to operating our quantum emitter, since operating our quantized charge pump requires the n-side to be grounded. Even in the absence of the side surface gates, the pump still requires quantum point contact (QPC) gates that are placed directly on the semiconductor substrate surface, which means they could potentially leak. This problem may be fixed by including a thin insulating region between the QPC gates and the semiconductor surface.

For the devices without surface gates, delocalized EL emission was observed during SR operation in addition to DC operation. In the device *with* side surface gates, SR operation for surface gate voltages of -0.9 V yielded localized emission for two reasons: (i) electrons driven by the forward bias encounter a wide barrier of holes, preventing minority electrons from forming currents under the p-topgate that could lead to radiative recombination at the *mesa* edges; (ii) alternate current pathways through the *mesa* are blocked—these currents could otherwise result in radiative recombination along the p-topgate edges facing the center of the device. SR operation for positive surface gate voltages resulted in *stochastic blinking* in the EL that went up in frequency for higher voltages, until complete quenching

above +1.1 V. The off state of this blinking process was associated with electron leakage from the surface gates, whose current value ($\sim 80\,\mu A$) was two orders of magnitude larger than the leakage current when the device was in the on state ($\sim 0.80\,\mu A$). Limiting the surface gate leakage current by setting a compliance of $\sim 30\,\mu A$ eliminated blinking during Set-Reset operation.

Switching the device from SR to DC mode during a period of luminescence (on state) during blinking yielded time-stable EL[†] that lasted for a duration on the order of tens of minutes. The longest duration was about 600 times the duration of EL in a nano-LED without side surface gates. We hypothesize that electrons escape the p–n channel as a part of the parasitic charging process and accumulate in the potential confinement regions under the surface gates over several set-reset cycles. During the switchover from SR to DC operation, these electrons become fixed, forming static pools of negative charge that do not electrically contact the channel 2DEG. Instead, these static electron pools guide and corral the *channel* electrons across the p–n junction and reduce the rate at which channel electrons escape by repelling them. Decay of the EL (and the strongly correlated channel current I_{pn}) does still occur, but the rate is much slower than in devices without side surface gates. After fully quenching, the device can be fully reset by operating briefly in SR mode with zero volts on the surface gates and no forward bias. The internal and external quantum efficiencies of the nano-LED in this configuration were estimated to be $\sim 1.19\times10^{-3}$ and $\sim 1.95\times10^{-5}$, respectively.

Operating one of our QW devices using the Set-Reset protocol yielded the narrowest EL linewidths observed to date (0.70 meV) in either doped or undoped lateral p–n junctions. Spectra were obtained from the n-side, which was brighter. We identified the heavy-hole free exciton (X^0), the light-hole free exciton (LH) and the negatively charged exciton (X^-) peaks from the EL spectra, whose energies are similar to corresponding PL values from literature. Unlike most other papers detailing dopant-free lateral p–n junctions,[89,90,91] we have fabricated several working samples, indicating the reproducibility of our fabrication recipe.

Spectra from our SHJI devices were also studied. In Chapter 4, the presence of a broadband emission peak from under the p-topgate that sits at an energy below what is assumed to be the neutral exciton (~ 1.515 eV) indicates the possible presence of low-density p-type background impurities in the substrate. The potential traps associated with these impurities are activated due to localized parasitic charging as well as biased

[†] for surface gate voltages above +0.55 V and below +1.1 V

self-illumination. The activation of these impurities in turn causes EL decay and quenching during DC operation, necessitating SR operation to avoid the need for thermal cycling. Similar to the QW sample, two peaks were observed from the n-side, assumed to be the X^0 and X^- peaks. The peak intensity of the X^- and LH peaks relative to X^0 decreased with increasing forward bias above 1.54 V, demonstrating a degree of control over the relative peak intensities. For the SHJI device in Chapter 5 with side surface gates, the assumed neutral exciton peak lies at the same energy (~ 1.515 eV). A lower energy EL peak (~ 1.511 eV) was observed at a concave gate corner feature, that persisted longer than the rest of the device during time-stable operation. The lower energy is possibly due to a fixed charge trap or background impurity being excited by the 'concentrated' field from the gate corner.

Our devices are compatible with RF operation (~ 1 GHz) as shown by performing time-resolved EL measurements on our QW nano-LED and extracting an exciton lifetime of 237 ± 0.8 ps, which is smaller than the PL lifetime (419 ± 5.2 ps) and is reaching our limit of ~ 200 ps set by the timing jitter of our single-photon detector. Moving to a material system with a higher spin-orbit coupling such as InGaAs/GaAs could yield even shorter lifetimes, necessitating a single-photon detection method with less jitter. RF compatibility is essential for an integrated quantum emitter since our quantized charge pump operates at these frequencies.

In Chapter 6, we modeled, fabricated, and validated the design for a photonic structure compatible with our projected quantum emitter that can boost the IQE and collection efficiency. The structure incorporates a bottom Bragg mirror with a lateral CBG cavity. The Bragg mirror effectively doubles the extraction by reflecting downward propagating emissions back up. The rings of the cavity have a split in the middle to allow charges to be funnelled into the center via inducing topgates. The CBG cavities combined with the bottom Bragg mirror boost the spontaneous emission rate at the center via the Purcell effect; this increase is measured by the Purcell factor F_P. For an exciton dipole oriented parallel to the split in the rings ($\phi = 0°$), $F_\mathrm{P} = 5.33$ from simulation. When the dipole is oriented perpendicular to the ring split ($\phi = 90°$), $F_\mathrm{P} = 1.49$, indicating a degree of linear polarization to the emission. Simulations of the far-field also confirm polarized emission—light emits into a single elliptical Gaussian mode when $\phi = 0°$, whereas the mode is destroyed when $\phi = 90°$. The effective extraction and collection efficiencies (for an objective lens with NA = 0.81) are 32.65% and 29.98%, respectively ~ 13 and ~ 52 times greater than that of a device without a split-CBG cavity. Also, the measured values of IQE and EQE will be boosted by factors of ~ 4.5 and ~ 89, respectively.

Reflection measurements of the Bragg mirror yielded results that matched fairly well with simulation. Reflection measurements of several etched CBG cavities with varying ring widths yielded cavity resonance dip wavelengths that were offset from simulation by a fixed value of ~ 16.3 nm. The resonance dips were only observed for incident light polarized parallel to the split in the rings. The observed linear trend of cavity mode wavelength vs fabricated ring width points us to a ring width of ~ 94.8 nm (all other parameters being the same) to match the mode to the QW emission line of ~ 807.5 nm.

The solutions for the various obstacles outlined at the top of this section are summarized below:

(i) Device operation using the Set-Reset protocol solves the problem of EL quenching. *In-situ* time-stability is achieved by applying a positive potential of about 0.6 V on channel-adjacent surface gates.

(ii) The surface gates also prevent alternate current pathways (both radiative and non-radiative) through the device mesa.

(iii) *Mesa* edge recombination due to minority currents under the topgate edges can be fixed by using a blocking gate just past the site of recombination.

(iv) An integrated bottom Bragg mirror along with a CBG cavity can boost the efficiency of emission, extraction and collection by boosting the rate of spontaneous emission via the Purcell effect and guiding emissions into a single elliptical Gaussian mode.

7.2 Future work

The results summarized in the previous section are significant, and pave the way for the realization of our ultimate goal—the development of a high-rate, electrically-driven quantum emitter based on our proposed design (see Section 1.2). This section lays out suggestions for the rest of the development roadmap that can be followed to achieve our end goal, as well as other experiments that may yield interesting results. A summary of the recommended future work can be found at the end of this section.

Chapter 3 does a thorough job of identifying the various peaks in the EL spectra, comparing them with PL, calculating the EL binding energies, and performing lifetime measurements. This degree of thoroughness must be extended to the spectra from Chapters 4 and 5. This will help us better understand the exciton dynamics at single heterojunction interfaces, and explain why we see electron-hole recombination despite the absence of a

quantum well confinement potential. Peak identification can be achieved through temperature dependence measurements as well as power dependence measurements. Temperature dependence can reveal the identity of a charged exciton (X^-) peak relative to a neutral (X^0) peak, since the temperature threshold above which the X^- peak decays is much lower than that of the X^0 peak. The identity of bound excitons can also be found through temperature dependence, as well as power dependence—their linewidths broaden at low temperatures, and their peak intensities quickly increase relative to the X^0 peak with increasing excitation power.[156] These measurements can help confirm the identity of the lower energy peaks in Chapters 4 and 5 as being due to background impurity charge traps. Since the lower energy peak from the device in Chapter 5 (Fig. 5.13) is *not* broadband, and in fact has a very similar linewidth to the X^0 peak, we could fabricate another junction with a gate structure similar to this one to intentionally create a localized emission site. Integrating a charge pump with this junction could yield a localized quantum emitter that emits at the bound state energy. The EL from this region also lasts longer than the rest of the device, making it easier to characterize using $g^{(2)}$ measurements.

The effect of grounding or floating the p- and n-side was investigated only in the SHJI devices. Observing the differences, if any, in QW devices would be a useful experiment. Also, the distribution of EL across the device should be measured for more QW devices, including whether the n-side or p-side is brighter.

The polarization of emission from different points in our nano-LEDs should also be investigated. Polarized emission would indicate a significant non-zero electric field pointing along the direction of the p–n current. This would have a positive impact on single photon emission from a device with our polarization-sensitive CBG.

Chapter 5 introduced a large gate voltage parameter space within which to operate a lateral p–n junction. However, the effect of non-zero surface gate bias including the regimes of localization and time-stabilization were only studied in one device. These results need to be replicated in a device with an identical or similar gate architecture. Some similar devices that were part of the same fabrication batch are already known to work, and can be tested without delay (Fig. 7.1).

The results from Chapter 5 give us many ideas on how to change the device architecture for future fabrication runs. One major issue for devices with surface gates is gate leakage—future devices should avoid using surface gates if possible.[‡] Also, surface gates require the

[‡] In an integrated quantum emitter device, the QPC gates of the electron pump will have to be insulator-separated instead of on the surface due to the same gate leakage issue.

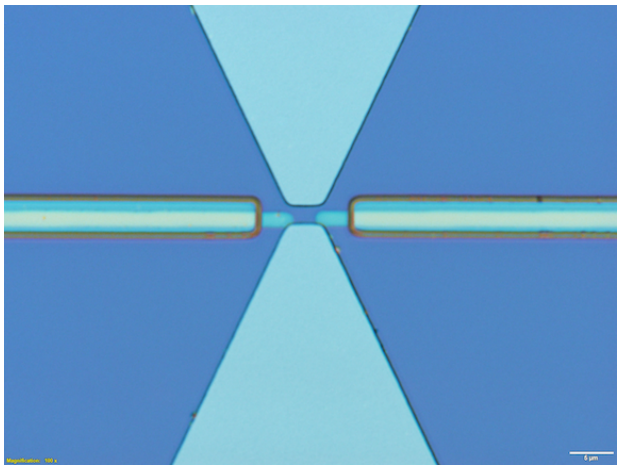

Figure 7.1: Optical image of a lateral p–n junction with surface gates. The gate shapes and dimensions are slightly different relative to the device in Chapter 5.

n-side to be floating, which is not compatible with our electron pumps that need the n-side to be grounded. Instead of surface gates, we can try to achieve the same corralling effect of the static pools of electrons in time-stable operation by gate-inducing them directly using insulator-separated side topgates and n-type ohmic contacts. The 2DEGs under these side gates would not contribute to p–n channel current when an appropriate bias is applied to the corresponding ohmic contacts. Since these inducing gates will not be on the surface, there is a negligible probability of gate leakage. Devices with different side gate separations can be tested to see how the corralling and time-stabilizing effect changes—potentially indefinite DC operation may be possible. Of course, a downside is that adding steps to the fabrication process increases complexity and lowers yield.

An easy fix for radiative recombination at the *mesa* edge is to place the bondpads for the topgates behind those of the ohmic contacts, thus routing minority carriers to rejoin the p–n circuit instead of recombining at defect states at the *mesa* edges. However, this could still compromise IQE due to some fraction of the minority carriers recombining non-radiatively. Implementing a wide blocking gate and a topgate with a longer overhang over the blocking gate could suppress non-radiative current while keeping the emission localized.

The fabrication of confining structures around the region of emission is a necessary step prior to the successful integration of a lateral p–n junction and a quantized charge pump. In anticipation of that, we fabricated prototypes for a bottom Bragg mirror and CBG microcavity. Due to a growth error, the centre of the stopband of our Bragg mirror was offset relative to the expected QW emission wavelength. This can be corrected in a

future MBE wafer growth. Using this wafer, an array of CBGs with updated ring widths should be fabricated and tested to see if the cavity resonance dip wavelengths match more closely with the QW emission. A final design validation of the rings can be conducted and the perfected fabrication recipe should be recorded. Once a near-ideal cavity is fabricated, polarization dependent PL lifetime measurements should be performed to observe Purcell enhancement. Prior to incorporating into a nano-LED device, LED prototypes with narrow topgates should be tested, since the p–n channel within the cavity is only 500 nm wide. The left and right topgates would ideally be deposited at different heights so that they can overlap; this would reduce the junction gap to the smallest possible value. Operating a nano-LED with an integrated CBG will definitively tell us how sensitive the EL emission is to the split in the rings. In a fully integrated device, the CBGs will serve the role of localizing the single photon emission to a small region. However, stray EL outside the cavity due to alternate current pathways cannot be prevented by a CBG, making the use of blocking gates still necessary. Also, the presence of charge traps associated with defects along the etched sidewalls of the rings could be a problem.

Once the quantized charge pump and nano-LED are successfully integrated to create a quantum emitter device, the following properties can be characterized—antibunching and second-order correlation function dip $g^{(2)}(0)$ to characterize sub-Poissonian behaviour and single-photon purity; linewidth, lifetime, and count rate to characterize source brightness. The effect of changing the electric field distribution (by tuning the topgate and forward bias potentials) on the EL spectra can be explored. The effect of an external magnetic field on the spectra should also be investigated.

In summary, we recommend the following experimental work be conducted (both device fabrication and measurement) to bring us closer to our goal:

(i) temperature and power dependence measurements to identify EL peaks in spectra from SHJI devices;
(ii) characterization of the EL distribution from several QW nano-LEDs measured using the four measurement configurations introduced in Chapter 4;
(iii) investigation of the possibility of polarized emission from our nano-LEDs;
(iv) measurement of other devices with side surface gates from the same fabrication batch as the device in Chapter 5 to test replicability;
(v) fabrication and measurement of devices with insulator-separated side gates (with varying separations) and corresponding n-type ohmic contacts;
(vi) rerouting of topgates for all future nano-LEDs to connect to their respective bondpads *behind* the ohmic contacts instead of going off-*mesa*;

(vii) fabrication and measurement of nano-LEDs with narrow overlapping topgates for compatibility with the CBGs;
(viii) fabrication of CBGs with the correct ring widths estimated from our reflection measurements;
(ix) MBE growth of a new DBR wafer with the stopband center matching the emission wavelength from the QW;
(x) fabrication and measurement of a nano-LED with an integrated CBG and blocking gates;
(xi) fabrication of an integrated quantum emitter device using a DBR wafer that combines the nano-LED, quantized charge pump, CBG, side gates, and blocking gates;
(xii) optical measurement of the quantum emitter to characterize sub-Poissonian behaviour, single-photon purity, linewidth, lifetime, and brightness; and
(xiii) tuning external electric and magnetic fields and observing their influence on the spectra from the quantum emitter.

Letters of copyright permission

AIP PUBLISHING LICENSE TERMS AND CONDITIONS

Jun 25, 2024

This Agreement between Nachiket S Sherlekar ("You") and AIP Publishing ("AIP Publishing") consists of your license details and the terms and conditions provided by AIP Publishing and Copyright Clearance Center.

License Number	5798911030322
License date	May 30, 2024
Licensed Content Publisher	AIP Publishing
Licensed Content Publication	Journal of Applied Physics
Licensed Content Title	Distinguishing persistent effects in an undoped GaAs/AlGaAs quantum well by top-gate-dependent illumination
Licensed Content Author	Fujita, Takafumi; Hayashi, Ryota
Licensed Content Date	Jun 15, 2021
Licensed Content Volume	129
Licensed Content Issue	23
Type of Use	Thesis/Dissertation
Requestor type	Student
Format	Print and electronic
Portion	Figure/Table
Number of figures/ tables	1
Will you be translating?	No
Title of new work	Towards Gated Quantum Emitters from Undoped Nano-LEDs
Institution name	University of Waterloo
Expected presentation date	Jun 2024
Portions	Figure 1. a.
Requestor Location	Nachiket S Sherlekar RAC1 475 Wes Graham Way Waterloo, ON N2L6R2 Canada Attn: Mr. Nachiket Sherlekar
Total	**0.00 CAD**

AIP PUBLISHING LICENSE TERMS AND CONDITIONS

Jun 25, 2024

This Agreement between Nachiket Sherlekar ("You") and AIP Publishing ("AIP Publishing") consists of your license details and the terms and conditions provided by AIP Publishing and Copyright Clearance Center.

License Number	5816091258174
License date	Jun 25, 2024
Licensed Content Publisher	AIP Publishing
Licensed Content Publication	Applied Physics Letters
Licensed Content Title	Undoped high mobility two-dimensional hole-channel GaAs⁄AlxGa1−xAs heterostructure field-effect transistors with atomic-layer-deposited dielectric
Licensed Content Author	Lu, T. M.; Luhman, D. R.
Licensed Content Date	Mar 16, 2007
Licensed Content Volume	90
Licensed Content Issue	11
Type of Use	Thesis/Dissertation
Requestor type	Student
Format	Print and electronic
Portion	Figure/Table
Number of figures/tables	1
Will you be translating?	No
Title of new work	Towards Gated Quantum Emitters from Undoped Nano-LEDs
Institution name	University of Waterloo
Expected presentation date	Jun 2024
Portions	Fig. 1
The Requesting Person / Organization to Appear on the License	Nachiket Sherlekar
Requestor Location	Nachiket S Sherlekar RAC1 475 Wes Graham Way Waterloo, ON N2L6R2 Canada Attn: Mr. Nachiket Sherlekar
Billing Type	Invoice
Billing Address	Nachiket S Sherlekar RAC1 475 Wes Graham Way Waterloo, ON N2L6R2 Canada Attn: Mr. Nachiket Sherlekar
Total	**0.00 CAD**

AIP PUBLISHING LICENSE TERMS AND CONDITIONS

Jun 25, 2024

This Agreement between Nachiket Sherlekar ("You") and AIP Publishing ("AIP Publishing") consists of your license details and the terms and conditions provided by AIP Publishing and Copyright Clearance Center.

License Number	5816101099282
License date	Jun 25, 2024
Licensed Content Publisher	AIP Publishing
Licensed Content Publication	Journal of Applied Physics
Licensed Content Title	Formation of two-dimensional electron and hole gases in undoped $Al_xGa_{1-x}As/GaAs$ heterostructures
Licensed Content Author	Hirayama, Y.
Licensed Content Date	Jul 1, 1996
Licensed Content Volume	80
Licensed Content Issue	1
Type of Use	Thesis/Dissertation
Requestor type	Student
Format	Print and electronic
Portion	Figure/Table
Number of figures/tables	1
Will you be translating?	No
Title of new work	Towards Gated Quantum Emitters from Undoped Nano-LEDs
Institution name	University of Waterloo
Expected presentation date	Jun 2024
Portions	Fig. 1 (c)
The Requesting Person / Organization to Appear on the License	Nachiket Sherlekar
Requestor Location	Nachiket S Sherlekar RAC1 475 Wes Graham Way Waterloo, ON N2L6R2 Canada Attn: Mr. Nachiket Sherlekar
Billing Type	Invoice
Billing Address	Nachiket S Sherlekar RAC1 475 Wes Graham Way Waterloo, ON N2L6R2 Canada Attn: Mr. Nachiket Sherlekar
Total	**0.00 CAD**

AIP PUBLISHING LICENSE TERMS AND CONDITIONS

Jun 25, 2024

This Agreement between Nachiket Sherlekar ("You") and AIP Publishing ("AIP Publishing") consists of your license details and the terms and conditions provided by AIP Publishing and Copyright Clearance Center.

License Number	5816101272856
License date	Jun 25, 2024
Licensed Content Publisher	AIP Publishing
Licensed Content Publication	Applied Physics Letters
Licensed Content Title	Fabrication of high-quality one- and two-dimensional electron gases in undoped GaAs/AlGaAs heterostructures
Licensed Content Author	Harrell, R. H.; Pyshkin, K. S.
Licensed Content Date	Apr 19, 1999
Licensed Content Volume	74
Licensed Content Issue	16
Type of Use	Thesis/Dissertation
Requestor type	Student
Format	Print and electronic
Portion	Figure/Table
Number of figures/tables	1
Will you be translating?	No
Title of new work	Towards Gated Quantum Emitters from Undoped Nano-LEDs
Institution name	University of Waterloo
Expected presentation date	Jun 2024
Portions	Fig. 1
The Requesting Person / Organization to Appear on the License	Nachiket Sherlekar
Requestor Location	Nachiket S Sherlekar RAC1 475 Wes Graham Way Waterloo, ON N2L6R2 Canada Attn: Mr. Nachiket Sherlekar
Billing Type	Invoice
Billing Address	Nachiket S Sherlekar RAC1 475 Wes Graham Way Waterloo, ON N2L6R2 Canada Attn: Mr. Nachiket Sherlekar
Total	**0.00 CAD**

AIP PUBLISHING LICENSE TERMS AND CONDITIONS

Jun 25, 2024

This Agreement between Nachiket Sherlekar ("You") and AIP Publishing ("AIP Publishing") consists of your license details and the terms and conditions provided by AIP Publishing and Copyright Clearance Center.

License Number	5816101437216
License date	Jun 25, 2024
Licensed Content Publisher	AIP Publishing
Licensed Content Publication	Journal of Applied Physics
Licensed Content Title	Formation of a two-dimensional electron gas in an inverted undoped heterostructure with a shallow channel depth
Licensed Content Author	Kawaharazuka, A.; Saku, T.
Licensed Content Date	Jan 15, 2000
Licensed Content Volume	87
Licensed Content Issue	2
Type of Use	Thesis/Dissertation
Requestor type	Student
Format	Print and electronic
Portion	Figure/Table
Number of figures/tables	1
Will you be translating?	No
Title of new work	Towards Gated Quantum Emitters from Undoped Nano-LEDs
Institution name	University of Waterloo
Expected presentation date	Jun 2024
Portions	Fig. 1 (a)
The Requesting Person / Organization to Appear on the License	Nachiket Sherlekar
Requestor Location	Nachiket S Sherlekar RAC1 475 Wes Graham Way Waterloo, ON N2L6R2 Canada Attn: Mr. Nachiket Sherlekar
Billing Type	Invoice
Billing Address	Nachiket S Sherlekar RAC1 475 Wes Graham Way Waterloo, ON N2L6R2 Canada Attn: Mr. Nachiket Sherlekar
Total	**0.00 CAD**

AIP PUBLISHING LICENSE TERMS AND CONDITIONS

Jun 25, 2024

This Agreement between Nachiket Sherlekar ("You") and AIP Publishing ("AIP Publishing") consists of your license details and the terms and conditions provided by AIP Publishing and Copyright Clearance Center.

License Number	5816110087538
License date	Jun 25, 2024
Licensed Content Publisher	AIP Publishing
Licensed Content Publication	Applied Physics Letters
Licensed Content Title	Demonstration and characterization of an ambipolar high mobility transistor in an undoped GaAs/AlGaAs quantum well
Licensed Content Author	Croxall, A. F.; Zheng, B.
Licensed Content Date	Feb 27, 2013
Licensed Content Volume	102
Licensed Content Issue	8
Type of Use	Thesis/Dissertation
Requestor type	Student
Format	Print and electronic
Portion	Figure/Table
Number of figures/tables	1
Will you be translating?	No
Title of new work	Towards Gated Quantum Emitters from Undoped Nano-LEDs
Institution name	University of Waterloo
Expected presentation date	Jun 2024
Portions	Fig. 1 (a)
The Requesting Person / Organization to Appear on the License	Nachiket Sherlekar
Requestor Location	Nachiket S Sherlekar RAC1 475 Wes Graham Way Waterloo, ON N2L6R2 Canada Attn: Mr. Nachiket Sherlekar
Billing Type	Invoice
Billing Address	Nachiket S Sherlekar RAC1 475 Wes Graham Way Waterloo, ON N2L6R2 Canada Attn: Mr. Nachiket Sherlekar
Total	**0.00 CAD**

AIP PUBLISHING LICENSE TERMS AND CONDITIONS

Jun 25, 2024

This Agreement between Nachiket Sherlekar ("You") and AIP Publishing ("AIP Publishing") consists of your license details and the terms and conditions provided by AIP Publishing and Copyright Clearance Center.

License Number	5816110269038
License date	Jun 25, 2024
Licensed Content Publisher	AIP Publishing
Licensed Content Publication	Applied Physics Letters
Licensed Content Title	Non-adiabatic single-electron pumps in a dopant-free GaAs/AlGaAs 2DEG
Licensed Content Author	Buonacorsi, B.; Sfigakis, F.
Licensed Content Date	Sep 13, 2021
Licensed Content Volume	119
Licensed Content Issue	11
Type of Use	Thesis/Dissertation
Requestor type	Student
Format	Print and electronic
Portion	Figure/Table
Number of figures/tables	1
Will you be translating?	No
Title of new work	Towards Gated Quantum Emitters from Undoped Nano-LEDs
Institution name	University of Waterloo
Expected presentation date	Jun 2024
Portions	Fig. 2 (e)
The Requesting Person / Organization to Appear on the License	Nachiket Sherlekar
Requestor Location	Nachiket S Sherlekar RAC1 475 Wes Graham Way Waterloo, ON N2L6R2 Canada Attn: Mr. Nachiket Sherlekar
Billing Type	Invoice
Billing Address	Nachiket S Sherlekar RAC1 475 Wes Graham Way Waterloo, ON N2L6R2 Canada Attn: Mr. Nachiket Sherlekar
Total	**0.00 CAD**
Terms and Conditions	

AIP Publishing -- Terms and Conditions: Permissions Uses

AIP Publishing hereby grants to you the non-exclusive right and license to use and/or distribute the Material according to the use specified in your order, on a one-time basis, for the specified term, with a maximum distribution equal to the number that you have ordered. Any links or other content accompanying the Material are not the subject of this license.

1. You agree to include the following copyright and permission notice with the reproduction of the Material:"Reprinted from [FULL CITATION], with the permission of AIP Publishing." For an article, the credit line and permission notice must be printed on the first page of the article or book chapter. For photographs, covers, or tables, the notice may appear with the Material, in a footnote, or in the reference list.
2. If you have licensed reuse of a figure, photograph, cover, or table, it is your responsibility to ensure that the material is original to AIP Publishing and does not contain the copyright of another entity, and that the copyright notice of the figure, photograph, cover, or table does not indicate that it was reprinted by AIP Publishing, with permission, from another source. Under no circumstances does AIP Publishing purport or intend to grant permission to reuse material to which it does not hold appropriate rights.
   You may not alter or modify the Material in any manner. You may translate the Material into another language only if you have licensed translation rights. You may not use the Material for promotional purposes.
3. The foregoing license shall not take effect unless and until AIP Publishing or its agent, Copyright Clearance Center, receives the Payment in accordance with Copyright Clearance Center Billing and Payment Terms and Conditions, which are incorporated herein by reference.
4. AIP Publishing or Copyright Clearance Center may, within two business days of granting this license, revoke the license for any reason whatsoever, with a full refund payable to you. Should you violate the terms of this license at any time, AIP Publishing, or Copyright Clearance Center may revoke the license with no refund to you. Notice of such revocation will be made using the contact information provided by you. Failure to receive such notice will not nullify the revocation.
5. AIP Publishing makes no representations or warranties with respect to the Material. You agree to indemnify and hold harmless AIP Publishing, and their officers, directors, employees or agents from and against any and all claims arising out of your use of the Material other than as specifically authorized herein.
6. The permission granted herein is personal to you and is not transferable or assignable without the prior written permission of AIP Publishing. This license may not be amended except in a writing signed by the party to be charged.
7. If purchase orders, acknowledgments or check endorsements are issued on any forms containing terms and conditions which are inconsistent with these provisions, such inconsistent terms and conditions shall be of no force and effect. This document, including the CCC Billing and Payment Terms and Conditions, shall be the entire agreement between the parties relating to the subject matter hereof.

This Agreement shall be governed by and construed in accordance with the laws of the State of New York. Both parties hereby submit to the jurisdiction of the courts of New York County for purposes of resolving any disputes that may arise hereunder.

V1.2

Questions? E-mail us at customercare@copyright.com.

American Physical Society
Reuse and Permissions License

25-Jun-2024

This license agreement between the American Physical Society ("APS") and Nachiket Sherlekar ("You") consists of your license details and the terms and conditions provided by the American Physical Society and SciPris.

Licensed Content Information

License Number:	**RNP/24/JUN/080636**
License date:	25-Jun-2024
DOI:	10.1103/PhysRevLett.110.126803
Title:	Counting Statistics for Electron Capture in a Dynamic Quantum Dot
Author:	Lukas Fricke et al.
Publication:	Physical Review Letters
Publisher:	American Physical Society
Cost:	USD $ 0.00

Request Details

Does your reuse require significant modifications: No

Specify intended distribution locations:	Worldwide
Reuse Category:	Reuse in a thesis/dissertation
Requestor Type:	Student
Items for Reuse:	Figures/Tables
Number of Figure/Tables:	1
Figure/Tables Details:	Fig. 4
Format for Reuse:	Print and Electronic
Total number of print copies:	Up to 1000

Information about New Publication:

University/Publisher:	University of Waterloo
Title of dissertation/thesis:	Towards Gated Quantum Emitters from Undoped Nano-LEDs
Author(s):	Nachiket Sunil Sherlekar
Expected completion date:	Jun. 2024

License Requestor Information

Name:	Nachiket Sherlekar
Affiliation:	Individual
Email Id:	nsherlek@uwaterloo.ca
Country:	Canada

American Physical Society
Reuse and Permissions License

TERMS AND CONDITIONS

The American Physical Society (APS) is pleased to grant the Requestor of this license a non-exclusive, non-transferable permission, limited to Print and Electronic format, provided all criteria outlined below are followed.

1. You must also obtain permission from at least one of the lead authors for each separate work, if you haven't done so already. The author's name and affiliation can be found on the first page of the published Article.
2. For electronic format permissions, Requestor agrees to provide a hyperlink from the reprinted APS material using the source material's DOI on the web page where the work appears. The hyperlink should use the standard DOI resolution URL, http://dx.doi.org/{DOI}. The hyperlink may be embedded in the copyright credit line.
3. For print format permissions, Requestor agrees to print the required copyright credit line on the first page where the material appears: "Reprinted (abstract/excerpt/figure) with permission from [(FULL REFERENCE CITATION) as follows: Author's Names, APS Journal Title, Volume Number, Page Number and Year of Publication.] Copyright (YEAR) by the American Physical Society."
4. Permission granted in this license is for a one-time use and does not include permission for any future editions, updates, databases, formats or other matters. Permission must be sought for any additional use.
5. Use of the material does not and must not imply any endorsement by APS.
6. APS does not imply, purport or intend to grant permission to reuse materials to which it does not hold copyright. It is the requestor's sole responsibility to ensure the licensed material is original to APS and does not contain the copyright of another entity, and that the copyright notice of the figure, photograph, cover or table does not indicate it was reprinted by APS with permission from another source.
7. The permission granted herein is personal to the Requestor for the use specified and is not transferable or assignable without express written permission of APS. This license may not be amended except in writing by APS.
8. You may not alter, edit or modify the material in any manner.
9. You may translate the materials only when translation rights have been granted.
10. APS is not responsible for any errors or omissions due to translation.
11. You may not use the material for promotional, sales, advertising or marketing purposes.
12. The foregoing license shall not take effect unless and until APS or its agent, Aptara, receives payment in full in accordance with Aptara Billing and Payment Terms and Conditions, which are incorporated herein by reference.
13. Should the terms of this license be violated at any time, APS or Aptara may revoke the license with no refund to you and seek relief to the fullest extent of the laws of the USA. Official written notice will be made using the contact information provided with the permission request. Failure to receive such notice will not nullify revocation of the permission.
14. APS reserves all rights not specifically granted herein.
15. This document, including the Aptara Billing and Payment Terms and Conditions, shall be the entire agreement between the parties relating to the subject matter hereof.

Bibliography

[1] M. Planck, "Ueber das Gesetz der Energieverteilung im Normalspectrum", Annalen der Physik **309**, 553–563 (1901).

[2] A. Einstein, "Über einen die Erzeugung und Verwandlung des Lichtes betreffenden heuristischen Gesichtspunkt", Annalen der Physik **322**, 132–148 (1905).

[3] C. Cohen-Tannoudji, J. Dupont-Roc, and G. Grynberg, *Photons and atoms: introduction to quantum electrodynamics*, Physics Textbook (Wiley-VCH, Weinheim, 2004), 468 pp.

[4] M. D. Eisaman, J. Fan, A. Migdall, and S. V. Polyakov, "Invited Review Article: Single-photon sources and detectors", Review of Scientific Instruments **82**, 071101 (2011).

[5] P. Senellart, G. Solomon, and A. White, "High-performance semiconductor quantum-dot single-photon sources", Nature Nanotechnology **12**, 1026–1039 (2017).

[6] D. Huber, M. Reindl, J. Aberl, A. Rastelli, and R. Trotta, "Semiconductor quantum dots as an ideal source of polarization-entangled photon pairs on-demand: a review", Journal of Optics **20**, 073002 (2018).

[7] I. Aharonovich, D. Englund, and M. Toth, "Solid-state single-photon emitters", Nature Photonics **10**, 631–641 (2016).

[8] L.-M. Duan, M. D. Lukin, J. I. Cirac, and P. Zoller, "Long-distance quantum communication with atomic ensembles and linear optics", Nature **414**, 413–418 (2001).

[9] J. Yang, Z. Jiang, F. Benthin, J. Hanel, T. Fandrich, R. Joos, S. Bauer, S. Kolatschek, A. Hreibi, E. P. Rugeramigabo, M. Jetter, S. L. Portalupi, M. Zopf, P. Michler, S. Kück, and F. Ding, "High-rate intercity quantum key distribution with a semiconductor single-photon source", Light: Science & Applications **13**, 150 (2024).

[10] X. Ma, C.-H. F. Fung, and H.-K. Lo, "Quantum key distribution with entangled photon sources", Physical Review A **76**, 012307 (2007).

[11] C. McDonald, G. Moody, S. W. Nam, R. P. Mirin, J. M. Shainline, A. McCaughan, S. Buckley, and K. L. Silverman, "III-V photonic integrated circuit with waveguide-coupled light-emitting diodes and WSi superconducting single-photon detectors", Applied Physics Letters **115**, 081105 (2019).

[12] V. Scarani, H. de Riedmatten, I. Marcikic, H. Zbinden, and N. Gisin, "Four-photon correction in two-photon Bell experiments", The European Physical Journal D **32**, 129–138 (2005).

[13] X.-L. Wang, L.-K. Chen, W. Li, H.-L. Huang, C. Liu, C. Chen, Y.-H. Luo, Z.-E. Su, D. Wu, Z.-D. Li, H. Lu, Y. Hu, X. Jiang, C.-Z. Peng, L. Li, N.-L. Liu, Y.-A. Chen, C.-Y. Lu, and J.-W. Pan, "Experimental Ten-Photon Entanglement", Physical Review Letters **117**, 210502 (2016).

[14] Y. Chen, M. Zopf, R. Keil, F. Ding, and O. G. Schmidt, "Highly-efficient extraction of entangled photons from quantum dots using a broadband optical antenna", Nature Communications **9**, 2994 (2018).

[15] N. Somaschi, V. Giesz, L. De Santis, J. C. Loredo, M. P. Almeida, G. Hornecker, S. L. Portalupi, T. Grange, C. Antón, J. Demory, C. Gómez, I. Sagnes, N. D. Lanzillotti-Kimura, A. Lemaítre, A. Auffeves, A. G. White, L. Lanco, and P. Senellart, "Near-optimal single-photon sources in the solid state", Nature Photonics **10**, 340–345 (2016).

[16] X. Ding, Y.-P. Guo, M.-C. Xu, R.-Z. Liu, G.-Y. Zou, J.-Y. Zhao, Z.-X. Ge, Q.-H. Zhang, H.-L. Liu, L.-J. Wang, M.-C. Chen, H. Wang, Y.-M. He, Y.-H. Huo, C.-Y. Lu, and J.-W. Pan, *High-efficiency single-photon source above the loss-tolerant threshold for efficient linear optical quantum computing*, (Nov. 28, 2023) `http://arxiv.org/abs/2311.08347`, pre-published.

[17] N. Tomm, A. Javadi, N. O. Antoniadis, D. Najer, M. C. Löbl, A. R. Korsch, R. Schott, S. R. Valentin, A. D. Wieck, A. Ludwig, and R. J. Warburton, "A bright and fast source of coherent single photons", Nature Nanotechnology **16**, 399–403 (2021).

[18] M. Anderson, T. Müller, J. Skiba-Szymanska, A. B. Krysa, J. Huwer, R. M. Stevenson, J. Heffernan, D. A. Ritchie, and A. J. Shields, "Gigahertz-Clocked Teleportation of Time-Bin Qubits with a Quantum Dot in the Telecommunication *C* Band", Physical Review Applied **13**, 054052 (2020).

[19] N. Mizuochi, T. Makino, H. Kato, D. Takeuchi, M. Ogura, H. Okushi, M. Nothaft, P. Neumann, A. Gali, F. Jelezko, J. Wrachtrup, and S. Yamasaki, "Electrically driven single-photon source at room temperature in diamond", Nature Photonics **6**, 299–303 (2012).

[20] S. Guo, S. Germanis, T. Taniguchi, K. Watanabe, F. Withers, and I. J. Luxmoore, "Electrically Driven Site-Controlled Single Photon Source", ACS Photonics **10**, 2549–2555 (2023).

[21] G. Shooter, Z.-H. Xiang, J. R. A. Müller, J. Skiba-Szymanska, J. Huwer, J. Griffiths, T. Mitchell, M. Anderson, T. Müller, A. B. Krysa, R. M. Stevenson, J. Heffernan, D. A. Ritchie, and A. J. Shields, "1GHz clocked distribution of electrically generated entangled photon pairs", Optics Express **28**, 36838–36848 (2020).

[22]F. Hargart, C. A. Kessler, T. Schwarzbäck, E. Koroknay, S. Weidenfeld, M. Jetter, and P. Michler, "Electrically driven quantum dot single-photon source at 2 GHz excitation repetition rate with ultra-low emission time jitter", Applied Physics Letters **102**, 011126 (2013).

[23]T.-K. Hsiao, A. Rubino, Y. Chung, S.-K. Son, H. Hou, J. Pedrós, A. Nasir, G. Éthier-Majcher, M. J. Stanley, R. T. Phillips, T. A. Mitchell, J. P. Griffiths, I. Farrer, D. A. Ritchie, and C. J. B. Ford, "Single-photon emission from single-electron transport in a SAW-driven lateral light-emitting diode", Nature Communications **11**, 917 (2020).

[24]B. Buonacorsi, F. Sfigakis, A. Shetty, M. C. Tam, H. S. Kim, S. R. Harrigan, F. Hohls, M. E. Reimer, Z. R. Wasilewski, and J. Baugh, "Non-adiabatic single-electron pumps in a dopant-free GaAs/AlGaAs 2DEG", Applied Physics Letters **119**, 114001 (2021).

[25]T. Wenz, J. Klochan, F. Hohls, T. Gerster, V. Kashcheyevs, and H. W. Schumacher, "Quantum dot state initialization by control of tunneling rates", Physical Review B **99**, 201409 (2019).

[26]A. V. Kuhlmann, J. H. Prechtel, J. Houel, A. Ludwig, D. Reuter, A. D. Wieck, and R. J. Warburton, "Transform-limited single photons from a single quantum dot", Nature Communications **6**, 8204 (2015).

[27]J. Waldie, P. See, V. Kashcheyevs, J. P. Griffiths, I. Farrer, G. A. C. Jones, D. A. Ritchie, T. J. B. M. Janssen, and M. Kataoka, "Measurement and control of electron wave packets from a single-electron source", Physical Review B **92**, 125305 (2015).

[28]L. Tian, F. Sfigakis, A. Shetty, H.-S. Kim, N. Sherlekar, S. Hosseini, M. C. Tam, B. van Kasteren, B. Buonacorsi, Z. Merino, S. R. Harrigan, Z. Wasilewski, J. Baugh, and M. E. Reimer, "Stable electroluminescence in ambipolar dopant-free lateral p–n junctions", Applied Physics Letters **123**, 061102 (2023).

[29]H. Wang, H. Hu, T.-H. Chung, J. Qin, X. Yang, J.-P. Li, R.-Z. Liu, H.-S. Zhong, Y.-M. He, X. Ding, Y.-H. Deng, Q. Dai, Y.-H. Huo, S. Höfling, C.-Y. Lu, and J.-W. Pan, "On-Demand Semiconductor Source of Entangled Photons Which Simultaneously Has High Fidelity, Efficiency, and Indistinguishability", Physical Review Letters **122**, 113602 (2019).

[30]C. Nawrath, R. Joos, S. Kolatschek, S. Bauer, P. Pruy, F. Hornung, J. Fischer, J. Huang, P. Vijayan, R. Sittig, M. Jetter, S. L. Portalupi, and P. Michler, "Bright Source of Purcell-Enhanced, Triggered, Single Photons in the Telecom C-Band", Advanced Quantum Technologies **6**, 2300111 (2023).

[31]D.-H. Kim, J.-H. Lee, and S.-K. Son, "Band-structure simulations for overlap wave functions between electrons and holes for recombination in undoped GaAs/AlGaAs heterostructures", Journal of the Korean Physical Society, 161–166 (2022).

[32]T. Ando, A. B. Fowler, and F. Stern, "Electronic properties of two-dimensional systems", Reviews of Modern Physics **54**, 437–672 (1982).

[33]R. A. Kiehl, P. M. Solomon, and D. J. Frank, "Heterojunction FETs in III–V compounds", IBM Journal of Research and Development **34**, 506–529 (1990).

[34]W. W. Y. Mak, "Transport Experiments in Undoped GaAs/AlGaAs Heterostructures" (University of Cambridge, 2013).

[35]T. Mimura, "Development of High Electron Mobility Transistor", Japanese Journal of Applied Physics **44**, 8263 (2005).

[36]B. E. Kane, L. N. Pfeiffer, K. W. West, and C. K. Harnett, "Variable density high mobility two-dimensional electron and hole gases in a gated GaAs/$Al_xGa_{1-x}As$ heterostructure", Applied Physics Letters **63**, 2132–2134 (1993).

[37]S. Peters, L. Tiemann, C. Reichl, and W. Wegscheider, "Gating versus doping: Quality parameters of two-dimensional electron systems in undoped and doped GaAs/AlGaAs heterostructures", Physical Review B **94**, 045304 (2016).

[38]A. F. Croxall, B. Zheng, F. Sfigakis, K. Das Gupta, I. Farrer, C. A. Nicoll, H. E. Beere, and D. A. Ritchie, "Demonstration and characterization of an ambipolar high mobility transistor in an undoped GaAs/AlGaAs quantum well", Applied Physics Letters **102**, 082105 (2013).

[39]P. Harrison and A. Valavanis, *Quantum Wells, Wires and Dots: Theoretical and Computational Physics of Semiconductor Nanostructures* (Wiley, 2016).

[40]E. Garmire, "Chapter 2 - Optical Nonlinearities in Semiconductors Enhanced by Carrier Transport", in *Semiconductors and Semimetals*, Vol. 58, edited by E. Garmire and A. Kost, Nonlinear Optics in Semiconductors I (Elsevier, Jan. 1, 1998), 55–173.

[41]B. E. Kane, L. N. Pfeiffer, and K. W. West, "High mobility GaAs heterostructure field effect transistor for nanofabrication in which dopant-induced disorder is eliminated", Applied Physics Letters **67**, 1262–1264 (1995).

[42]Y. Hirayama, K. Muraki, and T. Saku, "Two-dimensional electron gas formed in a back-gated undoped heterostructure", Applied Physics Letters **72**, 1745–1747 (1998).

[43]T. Sajoto, M. Santos, J. J. Heremans, M. Shayegan, M. Heiblum, M. V. Weckwerth, and U. Meirav, "Use of superlattices to realize inverted GaAs/AlGaAs heterojunctions with low-temperature mobility of 2×10^6 $cm^2/V\,s$", Applied Physics Letters **54**, 840–842 (1989).

[44]T. Fujita, R. Hayashi, M. Kohda, J. Ritzmann, A. Ludwig, J. Nitta, A. D. Wieck, and A. Oiwa, "Distinguishing persistent effects in an undoped GaAs/AlGaAs quantum well by top-gate-dependent illumination", Journal of Applied Physics **129**, 234301 (2021).

[45]T. M. Lu, D. R. Luhman, K. Lai, D. C. Tsui, L. N. Pfeiffer, and K. W. West, "Undoped high mobility two-dimensional hole-channel GaAs/$Al_xGa_{1-x}As$ heterostructure field-effect transistors with atomic-layer-deposited dielectric", Applied Physics Letters **90**, 112113 (2007).

[46]Y. Hirayama, "Formation of two-dimensional electron and hole gases in undoped $Al_xGa_{1-x}As$/GaAs heterostructures", Journal of Applied Physics **80**, 588–590 (1996).

[47]R. H. Harrell, K. S. Pyshkin, M. Y. Simmons, D. A. Ritchie, C. J. B. Ford, G. A. C. Jones, and M. Pepper, "Fabrication of high-quality one- and two-dimensional electron gases in undoped GaAs/AlGaAs heterostructures", Applied Physics Letters **74**, 2328–2330 (1999).

[48]A. Kawaharazuka, T. Saku, Y. Hirayama, and Y. Horikoshi, "Formation of a two-dimensional electron gas in an inverted undoped heterostructure with a shallow channel depth", Journal of Applied Physics **87**, 952–954 (2000).

[49]S. J. MacLeod, A. M. See, A. R. Hamilton, I. Farrer, D. A. Ritchie, J. Ritzmann, A. Ludwig, and A. D. Wieck, "Hybrid architecture for shallow accumulation mode AlGaAs/GaAs heterostructures with epitaxial gates", Applied Physics Letters **106**, 012105 (2015).

[50]Y. Ashlea Alava, D. Q. Wang, C. Chen, D. A. Ritchie, A. Ludwig, J. Ritzmann, A. D. Wieck, O. Klochan, and A. R. Hamilton, "Ultra-Shallow All-Epitaxial Aluminum Gate GaAs/$Al_xGa_{1-x}As$ Transistors with High Electron Mobility", Advanced Functional Materials **32**, 2104213 (2022).

[51]D. Taneja, F. Sfigakis, A. F. Croxall, K. D. Gupta, V. Narayan, J. Waldie, I. Farrer, and D. A. Ritchie, "N-type ohmic contacts to undoped GaAs/AlGaAs quantum wells using only front-sided processing: application to ambipolar FETs", Semiconductor Science and Technology **31**, 065013 (2016).

[52]J. Scharnetzky, P. Baumann, C. Reichl, H. Karl, W. Dietsche, and W. Wegscheider, "Donor implanted back-gates in GaAs for MBE-grown highest mobility two-dimensional electron systems", Semiconductor Science and Technology **36**, 085012 (2021).

[53]R. L. Willett, L. N. Pfeiffer, and K. W. West, "Simple-layered high mobility field effect heterostructured two-dimensional electron device", Applied Physics Letters **89**, 242107 (2006).

[54]N. Braslau, J. B. Gunn, and J. L. Staples, "Metal-semiconductor contacts for GaAs bulk effect devices", Solid-State Electronics **10**, 381–383 (1967).

[55]D. W. Langer, A. Ezis, and A. K. Rai, "Structure and lateral diffusion of ohmic contacts in AlGaAs/GaAs high electron mobility transistors and GaAs devices", Journal of Vacuum Science & Technology B: Microelectronics Processing and Phenomena **5**, 1030–1032 (1987).

[56]E. J. Koop, M. J. Iqbal, F. Limbach, M. Boute, B. J. van Wees, D. Reuter, A. D. Wieck, B. J. Kooi, and C. H. van der Wal, "On the annealing mechanism of AuGe/Ni/Au ohmic contacts to a two-dimensional electron gas in GaAs/$Al_xGa_{1-x}As$ heterostructures", Semiconductor Science and Technology **28**, 025006 (2013).

[57]W. Y. Mak, K. Das Gupta, H. E. Beere, I. Farrer, F. Sfigakis, and D. A. Ritchie, "Distinguishing impurity concentrations in GaAs and AlGaAs using very shallow undoped heterostructures", Applied Physics Letters **97**, 242107 (2010).

[58]W. Y. Mak, F. Sfigakis, K. Das Gupta, O. Klochan, H. E. Beere, I. Farrer, J. P. Griffiths, G. A. C. Jones, A. R. Hamilton, and D. A. Ritchie, "Ultra-shallow quantum dots in an undoped GaAs/AlGaAs two-dimensional electron gas", Applied Physics Letters **102**, 103507 (2013).

[59]J. C. H. Chen, D. Q. Wang, O. Klochan, A. P. Micolich, K. Das Gupta, F. Sfigakis, D. A. Ritchie, D. Reuter, A. D. Wieck, and A. R. Hamilton, "Fabrication and characterization of ambipolar devices on an undoped AlGaAs/GaAs heterostructure", Applied Physics Letters **100**, 052101 (2012).

[60]R. P. Taylor, P. T. Coleridge, M. Davies, Y. Feng, J. P. McCaffrey, and P. A. Marshall, "Physical and electrical investigation of ohmic contacts to AlGaAs/GaAs heterostructures", Journal of Applied Physics **76**, 7966–7972 (1994).

[61]S. J. Sarkozy, K. D. Gupta, F. Sfigakis, H. Beere, I. Farrer, R. Harrell, D. Ritchie, and G. Jones, "Overcoming Contact Hurdles for Investigating Lower Dimensional Structures in Undoped Heterostructures", ECS Transactions **11**, 75 (2007).

[62]T. Saku, K. Muraki, and Y. Hirayama, "High-Mobility Two-Dimensional Electron Gas in an Undoped Heterostructure: Mobility Enhancement after Illumination", Japanese Journal of Applied Physics **37**, L765–L767 (1998).

[63]Y. Hirayama, K. Muraki, A. Kawaharazuka, K. Hashimoto, and T. Saku, "Backgated layers and nanostructures", Physica E: Low-dimensional Systems and Nanostructures **11**, 155–160 (2001).

[64]E. H. Linfield, A. R. Hamilton, N. Iredale, D. A. Ritchie, and G. A. C. Jones, "Transport properties of a two-dimensional electron gas closely separated from an underlying n^+ GaAs layer: The fabrication of independent ohmic contacts using molecular beam epitaxial regrowth and in situ focused ion beams", Journal of Vacuum Science & Technology B: Microelectronics and Nanometer Structures Processing, Measurement, and Phenomena **11**, 982–984 (1993).

[65]S. Sarkozy, K. D. Gupta, C. Siegert, A. Ghosh, M. Pepper, I. Farrer, H. E. Beere, D. A. Ritchie, and G. A. C. Jones, "Low Temperature Transport in Undoped Mesoscopic Structures", Applied Physics Letters **94**, 172105 (2009).

[66]T.-M. Chen, C.-T. Liang, M. Y. Simmons, G.-H. Kim, and D. A. Ritchie, "Transport and quantum lifetime dependence on electron density in gated GaAs/AlGaAs heterostructures", Physica E: Low-dimensional Systems and Nanostructures, 15th International Conference on Electronic Propreties of Two-Dimensional Systems (EP2DS-15) **22**, 312–315 (2004).

[67]D. Q. Wang, J. C. H. Chen, O. Klochan, K. Das Gupta, D. Reuter, A. D. Wieck, D. A. Ritchie, and A. R. Hamilton, "Influence of surface states on quantum and transport lifetimes in high-quality undoped heterostructures", Physical Review B **87** (2013).

[68] A. Shetty, F. Sfigakis, W. Y. Mak, K. Das Gupta, B. Buonacorsi, M. C. Tam, H. S. Kim, I. Farrer, A. F. Croxall, H. E. Beere, A. R. Hamilton, M. Pepper, D. G. Austing, S. A. Studenikin, A. Sachrajda, M. E. Reimer, Z. R. Wasilewski, D. A. Ritchie, and J. Baugh, "Effects of biased and unbiased illuminations on two-dimensional electron gases in dopant-free GaAs/AlGaAs", Physical Review B **105**, 075302 (2022).

[69] D. Taneja, I. Shlimak, V. Narayan, M. Kaveh, I. Farrer, and D. Ritchie, "Reappearance of linear hole transport in an ambipolar undoped GaAs/AlGaAs quantum well", Journal of Physics: Condensed Matter **29**, 185302 (2017).

[70] A. Matthiessen and A. C. C. Vogt, "IV. On the influence of temperature on the electric conducting-power of alloys", Philosophical Transactions of the Royal Society of London **154**, 167–200 (1997).

[71] D. Laroche, S. Das Sarma, G. Gervais, M. P. Lilly, and J. L. Reno, "Scattering mechanism in modulation-doped shallow two-dimensional electron gases", Applied Physics Letters **96**, 162112 (2010).

[72] S. Das Sarma and E. H. Hwang, "Screening and transport in 2D semiconductor systems at low temperatures", Scientific Reports **5**, 16655 (2015).

[73] T. Fujisawa and Y. Hirayama, "Charge noise analysis of an AlGaAs/GaAs quantum dot using transmission-type radio-frequency single-electron transistor technique", Applied Physics Letters **77**, 543–545 (2000).

[74] Y. Ashlea Alava, D. Q. Wang, C. Chen, D. A. Ritchie, O. Klochan, and A. R. Hamilton, "High electron mobility and low noise quantum point contacts in an ultra-shallow all-epitaxial metal gate GaAs/$Al_xGa_{1-x}As$ heterostructure", Applied Physics Letters **119**, 063105 (2021).

[75] E. H. Hwang and S. Das Sarma, "Limit to two-dimensional mobility in modulation-doped GaAs quantum structures: How to achieve a mobility of 100 million", Physical Review B **77**, 235437 (2008).

[76] A. M. See, A. R. Hamilton, A. P. Micolich, M. Aagesen, and P. E. Lindelof, "Using light and heat to controllably switch and reset disorder configuration in nanoscale devices", Physical Review B **91**, 085417 (2015).

[77] P. O. Vaccaro, H. Ohnishi, and K. Fujita, "A light-emitting device using a lateral junction grown by molecular beam epitaxy on GaAs (311)A-oriented substrates", Applied Physics Letters **72**, 818–820 (1998).

[78] F. J. Ahlers, N. E. Fletcher, J. Ebbecke, and T. J. B. M. Janssen, "Surface acoustic wave driven quantized current transport", Current Applied Physics **4**, 529–533 (2004).

[79] B. Kaestner and V. Kashcheyevs, "Non-adiabatic quantized charge pumping with tunable-barrier quantum dots: a review of current progress", Reports on Progress in Physics **78**, 103901 (2015).

[80]C. Bäuerle, D. C. Glattli, T. Meunier, F. Portier, P. Roche, P. Roulleau, S. Takada, and X. Waintal, "Coherent control of single electrons: a review of current progress", Reports on Progress in Physics **81**, 056503 (2018).

[81]S. P. Giblin, A. Fujiwara, G. Yamahata, M.-H. Bae, N. Kim, A. Rossi, M. Möttönen, and M. Kataoka, "Evidence for universality of tunable-barrier electron pumps", Metrologia **56**, 044004 (2019).

[82]A. Sh. Achoyan, A. É. Yesayan, É. M. Kazaryan, and S. G. Petrosyan, "Two-dimensional p-n junction under equilibrium conditions", Semiconductors **36**, 903–907 (2002).

[83]A. North, J. Burroughes, T. Burke, A. Shields, C. Norman, and M. Pepper, "The two-dimensional lateral injection in-plane laser", IEEE Journal of Quantum Electronics **35**, 352–357 (1999).

[84]M. Cecchini, V. Piazza, F. Beltram, M. Lazzarino, M. B. Ward, A. J. Shields, H. E. Beere, and D. A. Ritchie, "High-performance planar light-emitting diodes", Applied Physics Letters **82**, 636–638 (2003).

[85]B. Kaestner, D. A. Williams, and D. G. Hasko, "Nanoscale lateral light emitting *p–n* junctions in AlGaAs/GaAs", Microelectronic Engineering, Proceedings of the 28th International Conference on Micro- and Nano-Engineering **67–68**, 797–802 (2003).

[86]J. R. Gell, P. Atkinson, S. P. Bremner, F. Sfigakis, M. Kataoka, D. Anderson, G. a. C. Jones, C. H. W. Barnes, D. A. Ritchie, M. B. Ward, C. E. Norman, and A. J. Shields, "Surface-acoustic-wave-driven luminescence from a lateral p-n junction", Applied Physics Letters **89**, 243505 (2006).

[87]C. P. Dobney, A. Nasir, P. See, C. J. B. Ford, J. P. Griffiths, C. Chen, D. A. Ritchie, and M. Kataoka, "Formation of a lateral p–n junction light-emitting diode on an n-type high-mobility GaAs/$Al_{0.33}Ga_{0.67}As$ heterostructure", Semiconductor Science and Technology **38**, 065001 (2023).

[88]T. Lunghi, G. De Simoni, V. Piazza, C. A. Nicoll, H. E. Beere, D. A. Ritchie, and F. Beltram, "Anti-bunched photons from a lateral light-emitting diode", Applied Physics Letters **99**, 131103 (2011).

[89]G. De Simoni, V. Piazza, L. Sorba, G. Biasiol, and F. Beltram, "Acoustoelectric luminescence from a field-effect n-i-p lateral junction", Applied Physics Letters **94**, 121103 (2009).

[90]V.-T. Dai, S.-D. Lin, S.-W. Lin, J.-Y. Wu, L.-C. Li, and C.-P. Lee, "Lateral Two-Dimensional p–i–n Diode in a Completely Undoped GaAs/AlGaAs Quantum Well", Japanese Journal of Applied Physics **52**, 014001 (2013).

[91]V.-T. Dai, S.-D. Lin, S.-W. Lin, Y.-S. Lee, Y.-J. Zhang, L.-C. Li, and C.-P. Lee, "High-quality planar light emitting diode formed by induced two-dimensional electron and hole gases", Optics Express **22**, 3811 (2014).

[92]Y. Chung, H. Hou, S.-K. Son, T.-K. Hsiao, A. Nasir, A. Rubino, J. P. Griffiths, I. Farrer, D. A. Ritchie, and C. J. B. Ford, "Quantized charge transport driven by a surface acoustic wave in induced unipolar and bipolar junctions", Physical Review B **100**, 245401 (2019).

[93]F. A. Chaves and D. Jiménez, "The gate tunable 2D *pn* junction driven out-of-equilibrium", Journal of Applied Physics **130**, 174505 (2021).

[94]F. A. Chaves, A. Pacheco-Sanchez, and D. Jiménez, "Gate Tunable Lateral 2D *Pn* Junctions: An Analytical Study of Its Electrostatics", IEEE Transactions on Nanotechnology **22**, 52–57 (2023).

[95]L. P. Kouwenhoven, A. T. Johnson, N. C. van der Vaart, C. J. P. M. Harmans, and C. T. Foxon, "Quantized current in a quantum-dot turnstile using oscillating tunnel barriers", Physical Review Letters **67**, 1626–1629 (1991).

[96]J. M. Shilton, V. I. Talyanskii, M. Pepper, D. A. Ritchie, J. E. F. Frost, C. J. B. Ford, C. G. Smith, and G. A. C. Jones, "High-frequency single-electron transport in a quasi-one-dimensional GaAs channel induced by surface acoustic waves", Journal of Physics: Condensed Matter **8**, L531 (1996).

[97]M. Kataoka, J. D. Fletcher, P. See, S. P. Giblin, T. J. B. M. Janssen, J. P. Griffiths, G. A. C. Jones, I. Farrer, and D. A. Ritchie, "Tunable Nonadiabatic Excitation in a Single-Electron Quantum Dot", Physical Review Letters **106**, 126801 (2011).

[98]C. L. Foden, V. I. Talyanskii, G. J. Milburn, M. L. Leadbeater, and M. Pepper, "High-frequency acousto-electric single-photon source", Physical Review A **62**, 011803 (2000).

[99]V. Kashcheyevs and B. Kaestner, "Universal Decay Cascade Model for Dynamic Quantum Dot Initialization", Physical Review Letters **104**, 186805 (2010).

[100]L. Fricke, M. Wulf, B. Kaestner, V. Kashcheyevs, J. Timoshenko, P. Nazarov, F. Hohls, P. Mirovsky, B. Mackrodt, R. Dolata, T. Weimann, K. Pierz, and H. W. Schumacher, "Counting Statistics for Electron Capture in a Dynamic Quantum Dot", Physical Review Letters **110**, 126803 (2013).

[101]M. D. Blumenthal, B. Kaestner, L. Li, S. Giblin, T. J. B. M. Janssen, M. Pepper, D. Anderson, G. Jones, and D. A. Ritchie, "Gigahertz quantized charge pumping", Nature Physics **3**, 343–347 (2007).

[102]B. Buonacorsi, "Quantum dot devices in silicon and dopant-free GaAs/AlGaAs heterostructures", Doctoral Thesis (University of Waterloo, Jan. 29, 2021).

[103]N. S. Sherlekar, "Next-Generation Solid-State Quantum Emitters", MA thesis (University of Waterloo, Jan. 31, 2019).

[104]S. Birner, T. Zibold, T. Andlauer, T. Kubis, M. Sabathil, A. Trellakis, and P. Vogl, "Nextnano: General Purpose 3-D Simulations", IEEE Transactions on Electron Devices **54**, 2137–2142 (2007).

[105] A. Trellakis, T. Zibold, T. Andlauer, S. Birner, R. K. Smith, R. Morschl, and P. Vogl, "The 3D nanometer device project nextnano: Concepts, methods, results", Journal of Computational Electronics **5**, 285–289 (2006).

[106] E. H. Bogardus and H. B. Bebb, "Bound-Exciton, Free-Exciton, Band-Acceptor, Donor-Acceptor, and Auger Recombination in GaAs", Physical Review **176**, 993–1002 (1968).

[107] L. Pavesi and M. Guzzi, "Photoluminescence of $Al_xGa_{1-x}As$ alloys", Journal of Applied Physics **75**, 4779–4842 (1994).

[108] G. Oelgart, M. Proctor, D. Martin, F. Morier-Genaud, F.-K. Reinhart, B. Orschel, L. C. Andreani, and H. Rhan, "Experimental and theoretical study of excitonic transition energies in GaAs/$Al_xGa_{1-x}As$ quantum wells", Physical Review B **49**, 10456–10465 (1994).

[109] D. Birkedal, J. Singh, V. G. Lyssenko, J. Erland, and J. M. Hvam, "Binding of Quasi-Two-Dimensional Biexcitons", Physical Review Letters **76**, 672–675 (1996).

[110] J. L. Osborne, A. J. Shields, M. Pepper, F. M. Bolton, and D. A. Ritchie, "Photoluminescence due to positively charged excitons in undoped GaAs/$Al_xGa_{1-x}As$ quantum wells", Physical Review B **53**, 13002–13010 (1996).

[111] A. J. Shields, C. L. Foden, M. Pepper, D. A. Ritchie, M. P. Grimshaw, and G. A. C. Jones, "Electron-density-dependent optical spectra of a remotely-doped GaAs/$Al_{0.33}Ga_{0.67}As$ single quantum well", Superlattices and Microstructures **15**, 355 (1994).

[112] G. Finkelstein, H. Shtrikman, and I. Bar-Joseph, "Optical Spectroscopy of a Two-Dimensional Electron Gas near the Metal-Insulator Transition", Physical Review Letters **74**, 976–979 (1995).

[113] R. Kumar, A. S. Vengurlekar, S. S. Prabhu, J. Shah, and L. N. Pfeiffer, "Measurements of frequency upconversion and picosecond excitation-correlation luminescence spectra in GaAs quantum wells and determination of time constants describing exciton dynamics", Journal of Applied Physics **80**, 5921–5931 (1996).

[114] A. Manassen, E. Cohen, A. Ron, E. Linder, and L. N. Pfeiffer, "Trion dephasing by electron scattering in GaAs/AlAs quantum wells", JOSA B **13**, 1372–1375 (1996).

[115] M. Hayne, C. L. Jones, R. Bogaerts, C. Riva, A. Usher, F. M. Peeters, F. Herlach, V. V. Moshchalkov, and M. Henini, "Photoluminescence of negatively charged excitons in high magnetic fields", Physical Review B **59**, 2927–2931 (1999).

[116] A. Esser, E. Runge, R. Zimmermann, and W. Langbein, "Photoluminescence and radiative lifetime of trions in GaAs quantum wells", Physical Review B **62**, 8232–8239 (2000).

[117] A. L. Stancik and E. B. Brauns, "A simple asymmetric lineshape for fitting infrared absorption spectra", Vibrational Spectroscopy **47**, 66–69 (2008).

[118]M. Cecchini, G. De Simoni, V. Piazza, F. Beltram, H. E. Beere, and D. A. Ritchie, "Surface acoustic wave-driven planar light-emitting device", Applied Physics Letters **85**, 3020–3022 (2004).

[119]T. Hosey, V. Talyanskii, S. Vijendran, G. A. C. Jones, M. B. Ward, D. C. Unitt, C. E. Norman, and A. J. Shields, "Lateral n–p junction for acoustoelectric nanocircuits", Applied Physics Letters **85**, 491–493 (2004).

[120]S. A. Lourenço, I. F. L. Dias, J. L. Duarte, E. Laureto, E. A. Meneses, J. R. Leite, and I. Mazzaro, "Temperature dependence of optical transitions in AlGaAs", Journal of Applied Physics **89**, 6159–6164 (2001).

[121]J. Batey and S. L. Wright, "Energy band alignment in GaAs:(Al,Ga)As heterostructures: The dependence on alloy composition", Journal of Applied Physics **59**, 200–209 (1986).

[122]Y. Wang, F. Zahid, Y. Zhu, L. Liu, J. Wang, and H. Guo, "Band offset of GaAs/$Al_xGa_{1-x}As$ heterojunctions from atomistic first principles", Applied Physics Letters **102**, 132109 (2013).

[123]A. V. Filinov, C. Riva, F. M. Peeters, Yu. E. Lozovik, and M. Bonitz, "Influence of well-width fluctuations on the binding energy of excitons, charged excitons, and biexcitons in GaAs-based quantum wells", Physical Review B **70**, 035323 (2004).

[124]R. Winkler, "Excitons and fundamental absorption in quantum wells", Physical Review B **51**, 14395–14409 (1995).

[125]W. Franz, "Einfluß eines elektrischen Feldes auf eine optische Absorptionskante", Zeitschrift für Naturforschung A **13**, 484–489 (1958).

[126]L. V. Keldysh, "Behaviour of non-metallic crystals in strong electric fields", JETP Letters **6**, 763 (1958).

[127]W. Langbein and J. M. Hvam, "Localization-enhanced biexciton binding in semiconductors", Physical Review B **59**, 15405–15408 (1999).

[128]L. C. Andreani and A. Pasquarello, "Accurate theory of excitons in GaAs-$Ga_{1-x}Al_xAs$ quantum wells", Physical Review B **42**, 8928–8938 (1990).

[129]T. Saito, T. Nakaoka, and Y. Arakawa, "Effect of lateral electric field on the transition energies of neutral and charged excitons in $In_{0.5}Ga_{0.5}As$/GaAs quantum dots", Physical Review B **91**, 115306 (2015).

[130]R. Pässler, "Temperature dependence of fundamental band gaps in group IV, III–V, and II–VI materials via a two-oscillator model", Journal of Applied Physics **89**, 6235–6240 (2001).

[131]R. Pässler, "Dispersion-related description of temperature dependencies of band gaps in semiconductors", Physical Review B **66**, 085201 (2002).

[132]A. Shields, M. Pepper, D. Ritchie, M. Simmons, and G. Jones, "Quenching of excitonic optical transitions by excess electrons in GaAs quantum wells", Physical Review B **51**, 18049–18052 (1995).

[133]A. D. Platt, M. J. Kendrick, M. Loth, J. E. Anthony, and O. Ostroverkhova, "Temperature dependence of exciton and charge carrier dynamics in organic thin films", Physical Review B **84**, 235209 (2011).

[134]A. Shields, J. Osborne, M. Simmons, M. Pepper, and D. Ritchie, "Magneto-optical spectroscopy of positively charged excitons in GaAs quantum wells", Physical Review B **52**, R5523–R5526 (1995).

[135]G. T. Dang, H. Kanbe, and M. Taniwaki, "Photoluminescence of an Al0.5Ga0.5As/GaAs multiple quantum well in the temperature range from 5 to 400 K", Journal of Applied Physics **106**, 093523 (2009).

[136]J. Kundrotas, A. Čerškus, G. Valušis, M. Lachab, S. P. Khanna, P. Harrison, and E. H. Linfield, "Radiative recombination spectra of p-type delta-doped GaAs□AlAs multiple quantum wells near the Mott transition", Journal of Applied Physics **103**, 123108 (2008).

[137]S.-D. Lin, private communication (November 2020).

[138]H. Benisty, H. De Neve, and C. Weisbuch, "Impact of planar microcavity effects on light extraction-Part II: selected exact simulations and role of photon recycling", IEEE Journal of Quantum Electronics **34**, 1632–1643 (1998).

[139]S. Adachi, "GaAs, AlAs, and $Al_xGa_{1-x}As$: Material parameters for use in research and device applications", Journal of Applied Physics **58**, R1–R29 (1985).

[140]H. Benisty, H. De Neve, and C. Weisbuch, "Impact of planar microcavity effects on light extraction-Part I: basic concepts and analytical trends", IEEE Journal of Quantum Electronics **34**, 1612–1631 (1998).

[141]D. Dovzhenko, I. Martynov, P. Samokhvalov, E. Osipov, M. Lednev, A. Chistyakov, A. Karaulov, and I. Nabiev, "Enhancement of spontaneous emission of semiconductor quantum dots inside one-dimensional porous silicon photonic crystals", Optics Express **28**, 22705–22717 (2020).

[142]A. Fognini, A. Ahmadi, M. Zeeshan, J. T. Fokkens, S. J. Gibson, N. Sherlekar, S. J. Daley, D. Dalacu, P. J. Poole, K. D. Jöns, V. Zwiller, and M. E. Reimer, "Dephasing Free Photon Entanglement with a Quantum Dot", ACS Photonics **6**, 1656–1663 (2019).

[143]H. Wang, Y.-M. He, T.-H. Chung, H. Hu, Y. Yu, S. Chen, X. Ding, M.-C. Chen, J. Qin, X. Yang, R.-Z. Liu, Z.-C. Duan, J.-P. Li, S. Gerhardt, K. Winkler, J. Jurkat, L.-J. Wang, N. Gregersen, Y.-H. Huo, Q. Dai, S. Yu, S. Höfling, C.-Y. Lu, and J.-W. Pan, "Towards optimal single-photon sources from polarized microcavities", Nature Photonics **13**, 770–775 (2019).

[144]Y. Ma, P. E. Kremer, and B. D. Gerardot, "Efficient photon extraction from a quantum dot in a broad-band planar cavity antenna", Journal of Applied Physics **115**, 023106 (2014).

[145]K. Xiong, X. Li, Y. Wei, W. Wu, C. Zhang, J. Liu, Y. Chen, and P. Chen, "Efficient generation of single photons by quantum dots embedded in bullseye cavities with backside dielectric mirrors", Optics Express **31**, 19536–19543 (2023).

[146]J. Liu, R. Su, Y. Wei, B. Yao, S. F. C. da Silva, Y. Yu, J. Iles-Smith, K. Srinivasan, A. Rastelli, J. Li, and X. Wang, "A solid-state source of strongly entangled photon pairs with high brightness and indistinguishability", Nature Nanotechnology **14**, 586–593 (2019).

[147]M. Davanço, M. T. Rakher, D. Schuh, A. Badolato, and K. Srinivasan, "A circular dielectric grating for vertical extraction of single quantum dot emission", Applied Physics Letters **99**, 041102 (2011).

[148]C.-W. Shih, S. Rodt, and S. Reitzenstein, "Universal design method for bright quantum light sources based on circular Bragg grating cavities", Optics Express **31**, 35552–35564 (2023).

[149]S. Ji, T. Tajiri, H. Kiyama, A. Oiwa, and S. Iwamoto, "Design of bull's-eye optical cavity toward efficient quantum media conversion using gate-defined quantum dot", Japanese Journal of Applied Physics **60**, 102003 (2021).

[150]A. Barbiero, J. Huwer, J. Skiba-Szymanska, T. Müller, R. M. Stevenson, and A. J. Shields, "Design study for an efficient semiconductor quantum light source operating in the telecom C-band based on an electrically-driven circular Bragg grating", Optics Express **30**, 10919–10928 (2022).

[151]M. Y. Su and R. P. Mirin, "Enhanced light extraction from circular Bragg grating coupled microcavities", Applied Physics Letters **89**, 033105 (2006).

[152]H.-Y. Ryu, "Modification of internal quantum efficiency and efficiency droop in GaN-based flip-chip light-emitting diodes via the Purcell effect", Optics Express **23**, A1157–A1166 (2015).

[153]L. Rickert, T. Kupko, S. Rodt, S. Reitzenstein, and T. Heindel, "Optimized designs for telecom-wavelength quantum light sources based on hybrid circular Bragg gratings", Optics Express **27**, 36824–36837 (2019).

[154]Q. Buchinger, S. Betzold, S. Höfling, and T. Huber-Loyola, "Optical properties of circular Bragg gratings with labyrinth geometry to enable electrical contacts", Applied Physics Letters **122**, 111110 (2023).

[155]U. Fano, "Effects of Configuration Interaction on Intensities and Phase Shifts", Physical Review **124**, 1866–1878 (1961).

[156]V. Srinivas, Y. J. Chen, and C. E. C. Wood, "Bound exciton induced photoluminescence linewidth broadening in GaAs quantum wells", Solid State Communications **89**, 611–614 (1994).

Appendix

A. Experimental setups

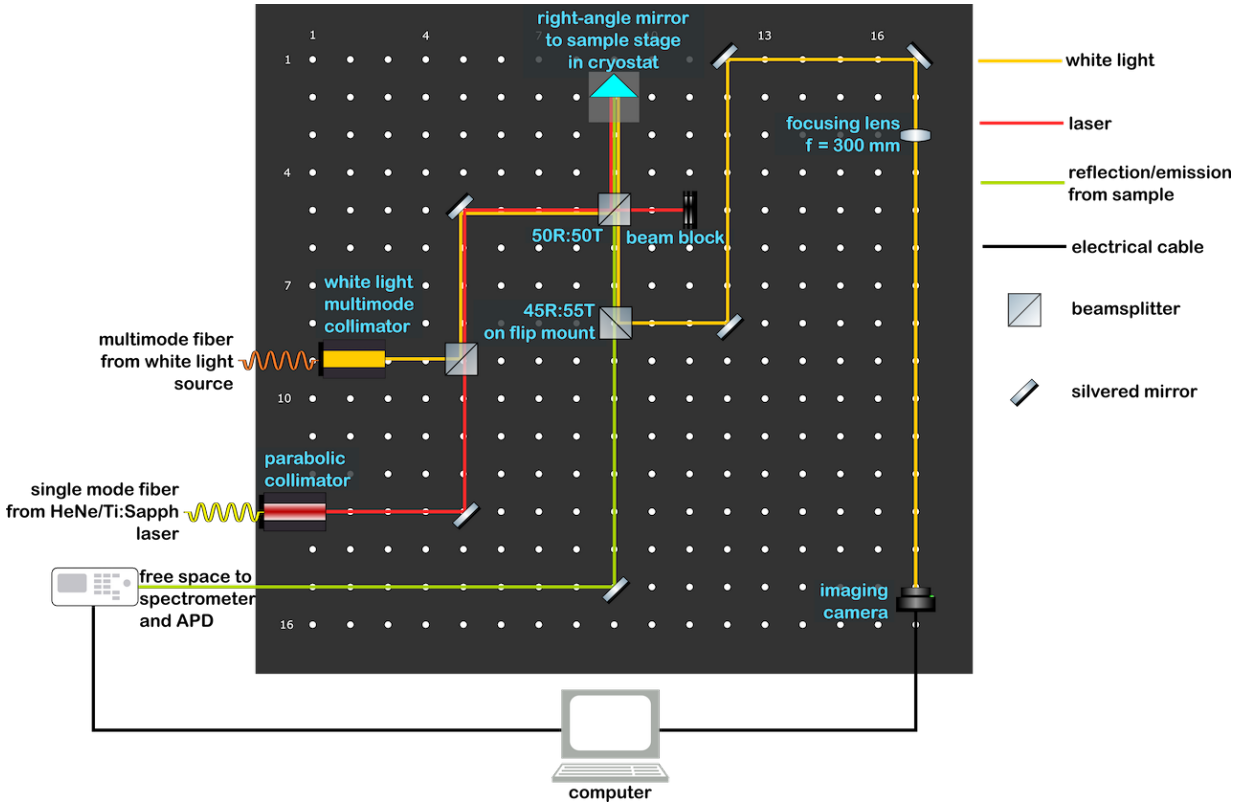

Figure A.1: Optical measurement setup for Chapters 3, 4 and 5, and for PL measurements in Chapter 6. The input paths include red/NIR laser (HeNe/Ti:Sapph) and white light. The output paths end at the imaging camera and the spectrometer.

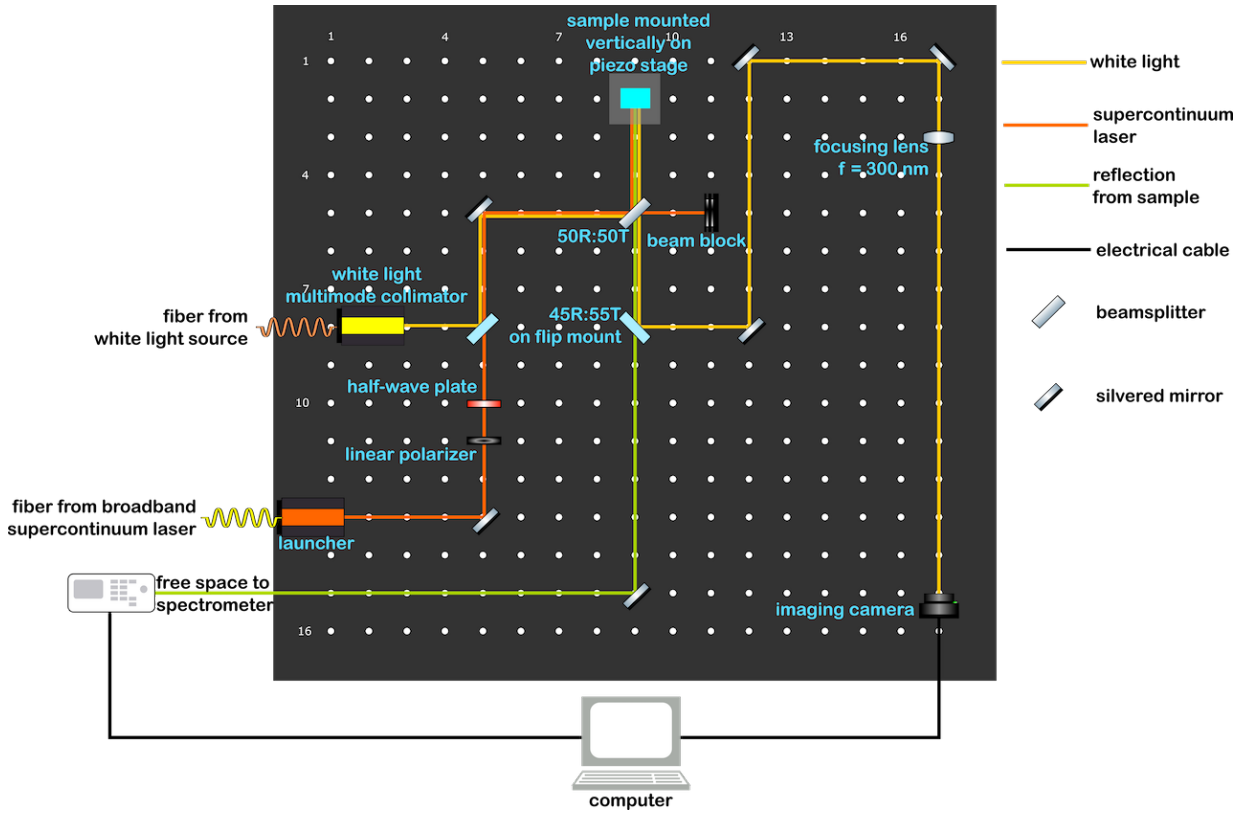

Figure A.2: Reflection measurement setup for Chapter 6. The input paths include a broadband supercontinuum laser and white light. The output reflection paths end at the imaging camera and the spectrometer. A linear polarizer polarizes the supercontinuum input, and a half-wave plate allows for control of the input polarization on the CBGs. Rotating the half-wave plate changes the reflection spectra from the CBGs. When the polarization is aligned to the CBG split, there is a dip in the reflection. As the polarization is rotated, the dip wanes until it disappears for orthogonal polarization.

B. Fabrication pattern masks with dimensions

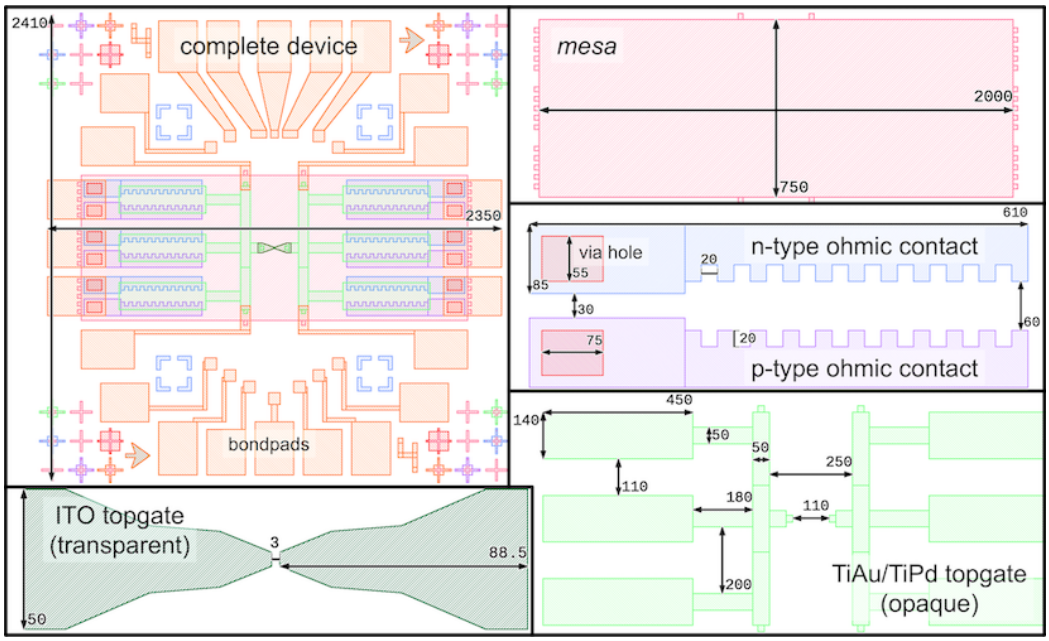

Figure B.1: Pattern masks for the lateral p–n junctions in Chapters 3 and 4 with annotated dimensions. All dimensions are in microns. (TOP LEFT) Overlay of patterns for all layers of the device. The bondpads are indicated in orange. (TOP RIGHT) Device *mesa*. The rest of the wafer is etched to well past the SHJI/QW. (MIDDLE RIGHT) n-type and p-type ohmic contacts, as well as oxide via holes to connect bondpads to them. (BOTTOM RIGHT) Opaque topgate pattern for either TiAu or TiPd. (BOTTOM LEFT) Transparent ITO topgate at the device center. The left and right topgate separation varies for different devices.

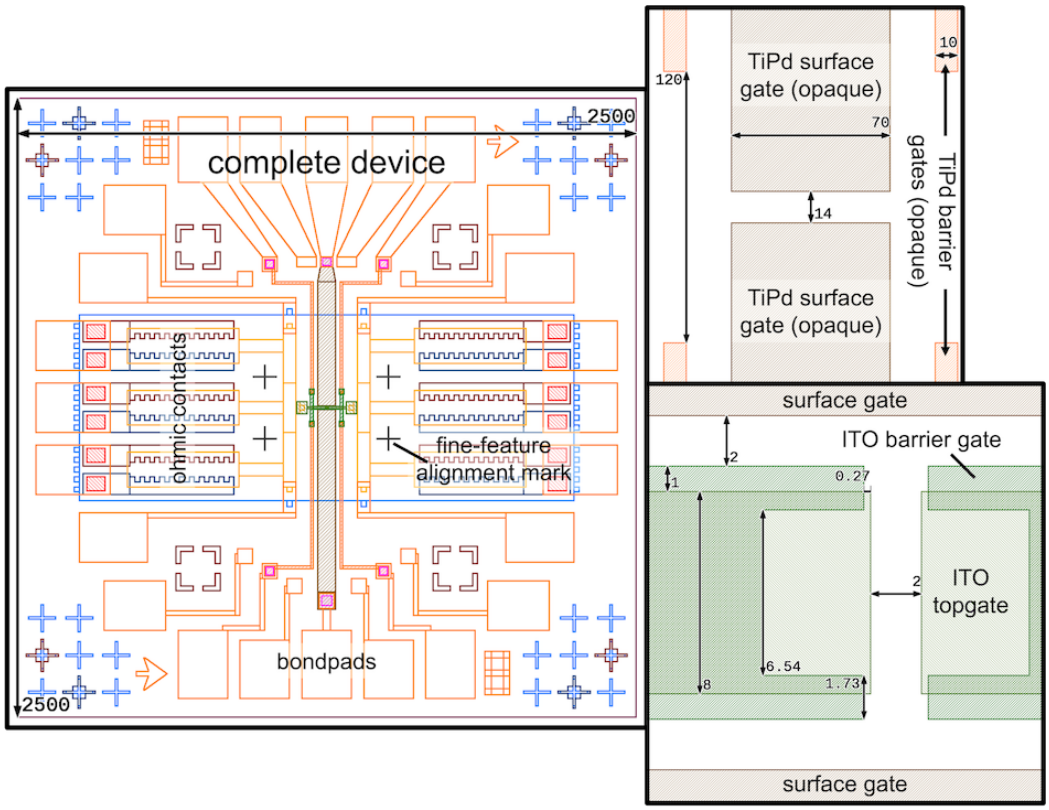

Figure B.2: Pattern masks for the lateral p–n junction in Chapter 5 with annotated dimensions. All dimensions are in microns. The patterns for the *mesa*, ohmic contacts and opaque topgate are the same as in Fig. B.1. (LEFT) Overlay of patterns for all layers of the device. The bondpads are indicated in orange. The fine-feature alignment marks are also indicated. (TOP RIGHT) Opaque TiPd side surface gates and TiPd barrier gate leads for the transparent ITO barrier gate. (BOTTOM RIGHT) Transparent ITO barrier gates with pincer features and ITO topgates at the device center. The surface gates are also indicated at the top and bottom.

C. Fabrication recipes

C.1 Lateral planar p–n junctions

C.1.1 Mesa

1. Clean a ~ 8 mm by 10 mm wafer piece by sonicating in Acetone and Isopropyl Alcohol (IPA) for 5 min each.
2. Etch the native oxide by dipping in buffered oxide etchant (BOE, 1:10 HF:NH_4F) for 30 s
3. Spin-coat S1811 resist monolayer, expose *mesa* pattern, develop, ash.*
   (a) Spin-coat at 5000 rpm for 60 s
   (b) Bake for 90 s at 120 °C
   (c) Expose UV-lithography *mesa* pattern
   (d) Develop for 60 s in MF-319
   (e) Ash for 10 s
4. Etch the *mesa*:
   (a) Prepare 1:8:120 solution of H_2SO_4:H_2O_2:H_2O
   (b) Calibrate etch rate of solution
   (c) Dip sample in BOE for 1 min followed by 1 min in H_2O
   (d) Dip sample in the H_2SO_4:H_2O_2:H_2O etch solution for 60-80 s, followed by 1 min in H_2O.
5. Strip the resist by submerging in Acetone or hot Remover PG and sonicating for 5–7 min.

* Ensure transport direction is along high-mobility axis of the wafer.

C.1.2 p-type ohmic contacts

1. Prepare an etch solution of 1:1:20 H_3PO_4:H_2O_2:H_2O.
2. Dip the sample in BOE for 1 min before spin-coating resist.
3. Spin-coat S1811 on the sample, expose p-ohmics pattern, develop, ash (same recipe as for *mesa*).
4. Reflow bake resist for 5 min at 150 °C
5. Calibrate the etch rate, etch ohmic recesses and deposit p-type material.
   (a) Calibrate the etch rate of the solution using a test piece, then etch the recesses for the ohmic contacts[†]
   (b) Ash for about 90 s
   (c) Dip in BOE for 1 min
   (d) Deposit 160–200 nm of AuBe using thermal evaporation with the sample tilted to 45°
6. Perform metal liftoff in Remover PG.
7. Cap the ohmics with 300 nm of SiO_2 using the PECVD.
8. Anneal the ohmics—several min purge with N_2 gas followed by heating in Ar at 520 °C for 3 min).
9. Etch away the oxide cap using BOE.

C.1.3 n-type ohmic contacts for SHJI

1. Prepare a 1:1:20 H_3PO_4:H_2O_2:H_2O etch solution.
2. Clean a test etch sample and prepare it alongside the main sample.
3. Dip main sample for 1 min in BOE followed by a several minute rinse in H_2O.
4. Spin-coat S1811 on the sample, expose n-ohmics pattern, develop, ash (same recipe).
5. Reflow bake the sample at 150 °C for 5 min.
6. Calibrate etch rate, etch ohmic recesses and deposit n-type material.
   (a) Calibrate the etch rate of the solution using a test piece, then etch the recesses for the ohmic contacts
   (b) Ash for about 330 s
   (c) Dip in BOE for 1 min

[†] The target etch depth is 15–20 nm above the heterojunction interface or quantum well.

(d) Deposit 10/250/120 nm of Ni/AuGe/Ni at a rate of 0.5/2.0/1.5 A/s with the sample tilted to 60°

7. Perform metal liftoff in Remover PG.
8. Anneal the ohmics—several min purge with N_2 followed by heating in Ar at 450 °C for 3 min.

C.1.4 n-type ohmic contacts for QW

1. Prepare a 1:1:20 H_3PO_4:H_2O_2:H_2O etch solution.
2. Clean a test etch sample and prepare it alongside the main sample.
3. Dip main sample for 1 min in BOE followed by a several minute rinse in H_2O.
4. Spin-coat S1811 on the sample, expose n-ohmics pattern, develop, ash (same recipe).
5. Reflow bake the sample at 120 °C for 5 min.
6. Calibrate etch rate, etch ohmic recesses and deposit n-type material.
   (a) Calibrate the dry and wet etch rates (RIE an etch solution) using a test piece
   (b) Perform dry etch using metal-RIE targeting an etch depth of 50–100 nm below the QW
   (c) Perform wet etch to etch an additional 35–70 nm
   (d) Deposit 10/250/120 nm of Ni/AuGe/Ni at a rate of 0.5/2.0/1.5 A/s with the sample tilted to 60°
7. Perform metal liftoff in Remover PG.
8. Anneal the ohmics—several min purge with N_2 followed by heating in Ar at 450 °C for 3 min.

C.1.5 Oxide insulator and via-holes

1. Deposit 300 nm of PECVD SiO_2 with silane as the precursor.
2. Spin-coat S1811 monolayer, expose via-hole pattern, develop, ash.
3. Dip in BOE for 3 min to etch away oxide from the vias.
4. Place the sample in Remover PG and heat to 80 °C for 10 min. Rinse and dry the sample.

C.1.6 Top gate and bond pads

1. Spin-coat PMGI/S1811 bilayer, expose top gate and bond pad patterns, develop, observe for undercut, ash.
2. Prepare solution of 1:4 HCl:H_2O.
3. Dip sample in HCl solution to remove any oxide from ashing.
4. Deposit 20/80 nm of Ti/Au or Ti/Pd (0.5/2.0 A/s deposition rate) using e-beam evaporation.
5. For ITO topgates, sputter 30 nm of ITO.
6. Perform metal liftoff in Remover PG.

C.2 Circular Bragg gratings

C.2.1 Resist mask

1. Prepare 1:1 solution of ZEP520A:Anisole, allow it to warm to room temperature.
2. Clean a wafer piece by sonicating in Acetone and IPA for 5 min each.
3. Etch the native oxide by dipping in buffered oxide etch (BOE, 1:10 HF:NH_4F) for 30 s.
4. Pattern CBGs using electron-beam lithography.
   (a) Spin-coat diluted ZEP520A at 2000 rpm for 60 s
   (b) Bake sample at 180 °C for 3 min
   (c) Expose resist pattern using electron-beams
   (d) Develop in ZED-N50 for 90 s and rinse in IPA for 30 s

C.2.2 Pattern etching

1. Perform dry etching using RIE to etch 700 nm into the substrate (calibration test etch required).
2. Place wafer in Remover PG overnight to strip the resist.

D. Reflection spectra

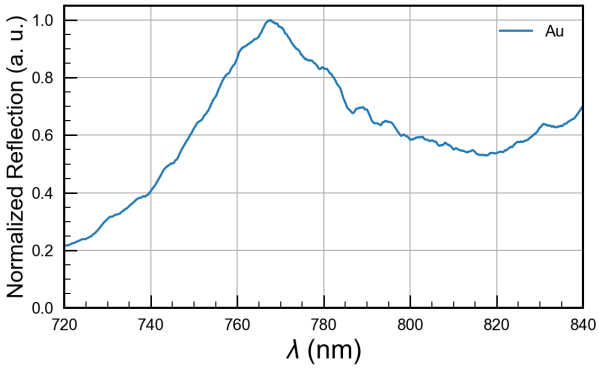

Figure D.1: Reflection of the broadband supercontinuum laser spectrum from a gold (Au) feature on the sample, indicating the intensity distribution of the laser over wavelength. The spectrum has been passed through a Savitsky-Golay filter. All measured reflection spectra in Chapter 6 have been normalized to this spectrum.

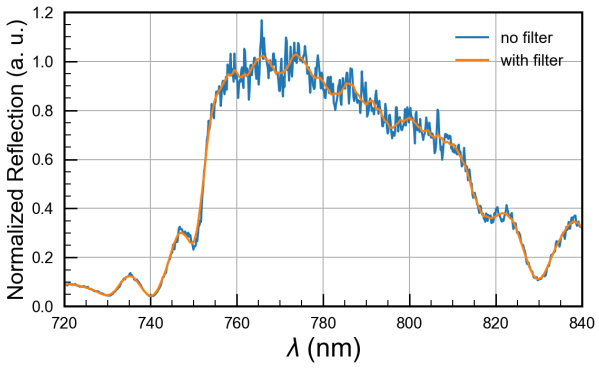

Figure D.2: Reflection of the broadband supercontinuum laser spectrum from the DBR wafer G0708 before and after applying the Savitsky-Golay filter. The spectra have been normalized to the filtered reflection spectrum off of Au (Fig. D.1).

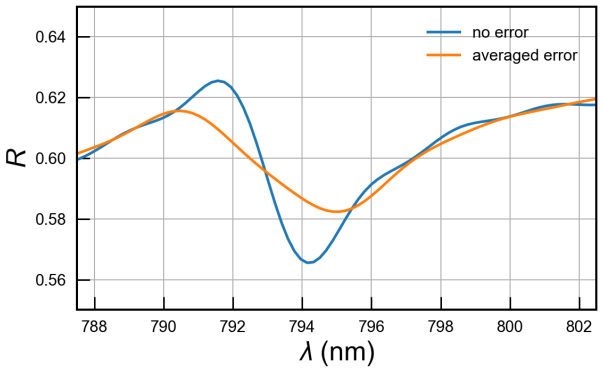

Figure D.3: Fano resonance dip in the simulated reflection spectrum from a CBG with and without errors in the ring width. The broadened resonance is obtained by averaging spectra from CBGs with no error, 1% error (positive and negative), and 2% error (positive and negative).